

**IRON AND SULFUR CONTROL DURING PRESSURE LEACHING OF SULFIDE
CONCENTRATES IN THE PRESENCE OF CHLORIDE IONS AT 150°C**

by

Baseer Abdul

B.Tech., National Institute of Technology Warangal, 2003

M.S., University of Utah, 2007

A THESIS SUBMITTED IN PARTIAL FULFILLMENT OF THE REQUIREMENTS FOR

THE DEGREE OF

DOCTOR OF PHILOSOPHY

in

THE FACULTY OF GRADUATE AND POSTDOCTORAL STUDIES

(Materials Engineering)

THE UNIVERSITY OF BRITISH COLUMBIA

(Vancouver)

November 2019

© Baseer Abdul, 2019

The following individuals certify that they have read, and recommend to the Faculty of Graduate and Postdoctoral Studies for acceptance, the dissertation entitled:

IRON AND SULFUR CONTROL DURING PRESSURE LEACHING OF SULFIDE CONCENTRATES IN THE PRESENCE OF CHLORIDE IONS AT 150°C

submitted by BASEER ABDUL in partial fulfillment of the requirements for

the degree of DOCTOR OF PHILOSOPHY

in MATERIALS ENGINEERING

Examining Committee:

DR. EDOUARD ASSELIN

Supervisor

DR. DAVID DREISINGER

Supervisory Committee Member

DR. MAREK PAWLIK

Supervisory Committee Member

Dr. BERN KLIEN

University Examiner

Dr. TOM TROCZYNSKI

University Examiner

Abstract

TECK and Vale operate their medium temperature copper and nickel sulfide concentrate leaching processes at 150°C. “Medium temperature” is used to describe a variety of processes that operate above the melting point of sulfur (119°C) but below the temperature where sulfur become highly viscous (159°C).

During leaching, and depending upon various process parameters, iron (Fe) may precipitate as hematite, goethite, jarosite or other oxyhydroxide compounds. Hematite is the favored precipitate because it is the most environmentally (thermodynamically) stable and does not adsorb as much copper (Cu), nickel (Ni), or other solution constituents during precipitation. A better understanding of the formation and structure of these iron precipitates may elucidate key factors that would ultimately result in lower valuable metal losses and more stable leach residues.

This thesis details the experimental work performed to clarify the conditions under which the precipitation of highly crystalline hematite occurs during medium temperature leaching of copper sulfide concentrates. Various process parameters at the lab scale were studied and classical, as well as newly developed, methods to identify the optimal conditions for hematite precipitation were employed.

Higher acid concentrations resulted in increased copper extractions and favor the formation of hematite during concentrate leaching, rather than other metastable phases. Seeding with synthetic hematite resulted in more crystalline residues. Furthermore, commercially available water displacement formula ‘WD40[®]’ and other novel reagents (benzene sulfonic acid, phenyl

phosphonic acid, decane, mineral oil) affect Fe precipitation and sulfur chemistry, leading to very different process outcomes such as improved extractions (from 98.0 to 99.2%) and larger, more easily separated, sulfur particles (from 20 μm to 1 mm).

The solubility of ferrihydrite (and its main transformation product, hematite) increased with increasing acid concentration. The solid-state transformation of ferrihydrite to hematite was found to be the major mechanism. These results indicate that the ferrihydrite formed in the CESL process will eventually transform into hematite, but that solution potential will play an important role in the nature of iron oxide residue. Ferrihydrite transformation was not complete within the time (60 min) that is typically used in medium temperature leaching for the simple system studied here.

Lay summary

This dissertation investigates the reduction of undesirable copper and nickel losses during the process of copper extraction from sulfide concentrates in autoclave pressure leaching. The losses of copper and nickel were found to be related to the poorly formed iron oxide phase in the leach residue. To this end, copper sulfide leaching experiments were performed in a benchtop autoclave with various process conditions and reagent additions. Some novel reagents were shown to make better residues by reducing the poorly crystalline iron oxide phases and thereby reducing the loss of copper to the leach residue. The rust prevention formula ‘WD40®’ is one such novel reagent as applied here. The solubility of an iron oxyhydroxide and its transformation to more stable forms of iron was also studied. It is shown that this transformation does not occur to completion within the time scales used in the typical extraction process.

Preface

The objectives of this research were defined in consultations with Teck Resources and Vale Canada, both UBC Hydrometallurgy Chair Sponsors, together with me and my thesis supervisor, Prof. Edouard Asselin. The strategy for investigating the effects of process conditions on iron and sulfur control during pressure leaching of sulfide concentrates as well as the experimental design and the development of analytical methods were formulated and carried out by me. Chemical analyses for feed materials, solution samples, and leach residues were performed at the Cominco Engineering Services Laboratory (CESL). X-ray diffraction phase analysis was performed by Dr. Mati Raudsepp, at the Electron Microbeam and X-ray Diffraction Facility at UBC. Mössbauer spectroscopy was performed by Dr. Dominic Ryan at McGill University. Transmission electron microscopy (TEM) work was performed by me at 4D Labs at Simon Fraser University, and the scanning electron microscopy (SEM) was performed at the Materials Electron Microscopy Lab at UBC. The sequential extraction experiments featured in Chapter 4 were performed in collaboration with a fellow Ph.D. student, Dr. Tasawar Javed, and the X-ray diffraction analysis presented in Chapter 5 was performed with assistance from a fellow Ph.D. student, Dr. Matteo Pernechele.

The publications listed below have been prepared from the data presented in this dissertation. I am the primary contributor to these publications, prepared with the guidance of Dr. Edouard Asselin, my thesis advisor. The dissertation was composed by me with manuscript edits by Dr. Edouard Asselin.

Peer-reviewed Journal Papers:

Baseer Abdul, Edouard Asselin, 2016. Novel reagents for iron and sulfur control in medium temperature leaching of sulfide concentrates. *Canadian Metallurgical Quarterly* 56(4), 382-392.

Tasawar Javed, **Baseer Abdul**, Dominic Ryan, Matti Raudsepp, Edouard Asselin, 2016. Amorphous iron phases in medium temperature leach residues and associated metal loss, *International Journal of Mineral Processing* 148, 65-71.

Baseer Abdul, Edouard Asselin. Solubility of metastable ferrihydrite in sulfate-chloride solution at 150°C (*in preparation*)

Peer-reviewed Conference Proceeding:

Baseer Abdul, Matteo Pernechele, Dominic Ryan, Edouard Asselin, 2014. Mössbauer studies of synthetic jarosites doped with Copper, in: Asselin, E., Dixon, D.G., Doyle, F.M., Dreisinger, D.B., (Eds.), *Proceedings of 7th International Symposium on Hydrometallurgy*. Victoria, pp. 213-224

Conference Presentations:

Baseer Abdul, Edouard Asselin, 2017. Novel reagents for iron and sulfur control in medium temperature leaching of sulfide concentrates. Conference of Metallurgists, COM-2017, Vancouver, BC, Canada.

Baseer Abdul, Edouard Asselin, 2015. Assessing the effects of new reagents for iron control in medium temperature sulfide concentrate leaching. International Chemical Congress of Pacific Basin Societies, PACIFICHEM-2015, Hawaii, USA.

Baseer Abdul, Dominic Ryan, Edouard Asselin, 2014. Mössbauer studies of iron phases in hydrometallurgical residues, Canadian Material Science Conference, CMSC-2014, Saskatoon, SK, Canada.

Baseer Abdul, Tasawar Javed, Dominic Ryan, Matti Raudsepp, Edouard Asselin, 2013. Characterization of medium temperature sulfide concentrate leach residue. Canadian Material Science Conference, CMSC-2013, Montreal, QC, Canada.

Invention disclosure:

New surfactants for medium temperature pressure leaching. Inventors: Baseer Abdul and Edouard Asselin. Technology ID: 17-039, Agreement ID: 17-0152. University-Industry Liaison Office, UILO, UBC. June 27, 2016.

Table of contents

Abstract.....	iii
Lay summary.....	v
Preface.....	vi
Table of contents	ix
List of tables.....	xvi
List of figures.....	xx
List of symbols.....	xxviii
List of abbreviations	xxix
Acknowledgments	xxxii
Dedication	xxxiv
Chapter 1: Introduction	1
1.1 Background.....	1
1.2 Thesis outline.....	4
Chapter 2: Literature review	6

2.1	Hydrometallurgical leaching processes	10
2.2	CESL and VALE medium temperature leaching.....	16
2.3	Iron behavior in aqueous solution.....	20
2.4	Iron phases in leach residues.....	29
2.5	Crystallization theory of precipitation	36
2.6	Crystal growth modification in iron precipitation	47
2.7	Transformation of ferrihydrite	48
2.8	Solubility of ferrihydrite, goethite, and hematite.....	53
2.9	Sulfur and sulfur dispersing agents in leaching processes.....	60
2.9.1	O-Phenylenediamine and reaction products	63
2.9.2	Effect of organic reagents on the viscosity of sulfur	68
2.9.3	Effect of organic reagents on sulfur polymerization.....	70
2.10	Summary.....	73
Chapter 3: Research objectives		76
Chapter 4: Evaluation of crystallinity in CESL and Vale leach residues.....		78

4.1	Introduction to iron phases in leach residues	79
4.2	Samples and leaching conditions	80
4.3	Quantitative X-ray powder diffraction (QXRPD)	82
4.4	Iron phases by sequential extraction	84
4.5	Iron analysis comparison	91
4.6	Determination of HaHC soluble amorphous phases	92
4.7	Transmission electron microscope.....	94
4.7.1	Phase identification.....	98
4.7.2	Elemental mapping	102
4.8	Mössbauer spectroscopy	104
4.8.1	Mössbauer spectrometer and parameters	105
4.8.2	Mössbauer spectra of leach residues.....	107
4.8.3	Impact of HaHC treatment.....	109
4.8.4	Phase identification in leach residues	112
4.8.5	Indication of jarosite contributions	114

4.9	Conclusions.....	115
Chapter 5: Evaluation of crystallinity in synthetic jarosites		117
5.1	Precipitation of synthetic jarosites	117
5.2	Chemical characterization of synthetic jarosites.....	118
5.3	Powder X-ray diffraction (PXRD) of synthetic jarosites.....	120
5.4	Mössbauer spectroscopy of synthetic jarosites	123
5.5	Conclusions.....	128
Chapter 6: Pressure leaching of sulfide concentrates.....		130
6.1	Introduction.....	130
6.2	Experimental	131
6.2.1	Materials and sample preparation	131
6.2.2	Quantitative phase analysis.....	132
6.2.3	HaHC extraction	134
6.2.4	Pressure leaching autoclave	134
6.2.5	Pressure leaching procedure	135

6.2.6	Atmospheric leaching procedure	135
6.3	Results and discussion	138
6.3.1	Acid concentration	138
6.3.2	Seeding and residue recycle.....	147
6.3.3	Novel reagent for iron and sulfur control	154
6.3.3.1	Water displacement formula WD40®	165
6.3.3.2	Effect of organic additives on hematite	168
6.3.3.3	Iron complexation by benzene sulfonic and phenyl phosphonic acids.....	169
6.4	Conclusions.....	170
Chapter 7: Solubility of metastable ferrihydrite in sulfate-chloride solutions at 150°C.....		173
7.1	Experimental.....	174
7.1.1	Ferrihydrite synthesis.....	174
7.1.2	Quantitative X-ray powder diffraction (QXRPD)	175
7.1.3	HaHC extraction	176
7.1.4	Electrolyte preparation for ORP tests	177

7.1.5	Experimental procedure for solubility measurements	178
7.2	Results and discussion	181
7.2.1	Titanium corrosion.....	207
7.2.2	Fe(II) catalyzed transformation.....	217
7.3	Conclusions.....	220
Chapter 8: Conclusions and recommendations		222
8.1	Conclusions.....	222
8.1.1	Analysis of the leach residue from CESL and Vale processes	222
8.1.2	Leaching of sulfide concentrates	223
8.1.3	Novel reagent(s) for iron and sulfur control	224
8.1.4	Solubility of metastable ferrihydrite under CESL conditions at 150°C	224
8.2	Recommendations for future work	225
References.....		228
Appendices.....		265
	Appendix A : Multi-acid digestion procedure	265

Appendix B : X-Ray amorphous determination scheme	267
Appendix C : Calculations for HaHC soluble and Cu extraction	270
Appendix D : X-Ray spectrum of ferrihydrite	271
Appendix E : Ferrihydrite solubility	272

List of tables

Table 2-1: Summary of the studies characterizing iron residues precipitated at $T > 100^{\circ}\text{C}$	35
Table 2-2: Melting and boiling points of phenylenediamines	64
Table 4-1: Mineralogy of concentrates pertaining to leach residues S1, S2, and S3.....	81
Table 4-2: Leaching conditions that generated leach residues S1, S2, and S3	81
Table 4-3: Comparison of phases in samples S1, S2, and S3 as determined by XRD and QXRPD	83
Table 4-4: Distributions of Fe, Cu, As, Ca and Ni in mass percent determined by the 1 st and 2 nd stages of sequential extraction and compared to Digestion & ICP-MS of the dried as-received solids	89
Table 4-5: Comparison of ratios of Cu/Fe and Ni/Fe during 1 st and 2 nd stage extractions.....	90
Table 4-6: Comparison of total Fe from Digestion & ICP-MS, QXRPD, 1 st and 2 nd stage extraction for S1, S2, S3	91
Table 4-7: QXRPD analysis of samples S1, S2 and S3; as received (R), after 1 st stage extraction (R1) and 2 nd stage extraction (R2)	93
Table 4-8: Summary of the morphology of naturally occurring iron oxides and oxyhydroxides	98
Table 4-9: Description of Mössbauer parameters.....	107

Table 5-1: Chemical composition of synthetic jarosite samples	119
Table 5-2: Unit cell parameters and amorphous content obtained by Rietveld refinement.....	123
Table 6-1: Chemical analysis of copper sulfide concentrate	132
Table 6-2: QXRPD phase analysis of copper concentrate.....	133
Table 6-3: Pressure leaching experimental matrix.....	137
Table 6-4: Effect of acid on HaHC soluble phase (Cu SD: 0.02% and HaHC SD: 0.5%).....	138
Table 6-5: Cu and Fe in leach residue at varying free acid concentration (Cu and Fe SD: 0.02%)	140
Table 6-6: Amount of Cu and Fe recovered by HaHC treatment of the residue at varying acid concentrations (Cu and Fe SD: 0.02%).....	141
Table 6-7: Effect of synthetic hematite seed (Cu extn SD: 0.02%).....	148
Table 6-8: Effect of synthetic hematite seed on calculated HaHC soluble phase (HaHC SD: 0.5%)	149
Table 6-9: Effect of seed recycle on HaHC soluble phase (HaHC SD: 0.5%).....	149
Table 6-10: Effect of residue recycle on HaHC soluble phase (HaHC SD: 0.5%)	150
Table 6-11: Effect of WD40 [®] , nonane and cyclohexane (Cu extraction SD: 0.02%).....	155

Table 6-12: Effect of decane and mineral oil (Cu extraction SD: 0.02%).....	156
Table 6-13: Effect of NS, BS, MS, and PP (Cu extraction SD: 0.02%).....	157
Table 6-14: Effect of reagents on QXRPD of the residue from the standard copper concentrate leaching experiments	162
Table 6-15: Effect of reagents on HaHC soluble phase (HaHC SD: 0.5%)	163
Table 6-16: Ion exchange resins	170
Table 7-1: Ferric to ferrous ratio of synthetic solutions containing chloride, copper and nickel in 10g/L H ₂ SO ₄ at 25°C	197
Table 7-2: The oxidation-reduction potential of solutions from the hematite solubility experiments	198
Table 7-3: Ferric to ferrous ratio in hematite solubility solutions at 25°C at varying acid concentrations (12 g/L Cu and 12 g/L Ni added only at 10 g/L H ₂ SO ₄)	199
Table 7-4: QXRPD of the residues from the ferrihydrite solubility experiments after 6 h in sulfate-chloride solutions at 150°C (HaHC SD: 0.5%)	212
Table 7-5: Solid-state transformation of ferrihydrite (where percentages are with respect to the total amount of Fe put into the system as ferrihydrite).....	215

Table 7-6: Comparison of initial and final molar acid equivalents for ferrihydrite solubility solutions (error: ~ 2.0%)..... 215

List of figures

Figure 2-1: Illustration of three types of leaching processes based on temperature regimes	13
Figure 2-2: CESL process basic flowsheet	19
Figure 2-3: Eh-pH diagram for the Fe-H ₂ O system at 25°C and unit solute activity	22
Figure 2-4: Eh-pH diagram for the Fe-H ₂ O system at 150°C and unit solute activity	22
Figure 2-5: Eh-pH diagram for the S-H ₂ O system at 25°C and unit solute activity	24
Figure 2-6: Eh-pH diagram for the S-H ₂ O system at 150°C and unit solute activity	24
Figure 2-7: Metastable Eh-pH diagram for the Fe-H ₂ O-S system at 25°C and unit solute activity	25
Figure 2-8: Eh-pH diagram for the Fe-H ₂ O-S system at 150°C and unit solute activity	26
Figure 2-9: Experimental temperature versus pH diagram for Fe(III) - Fe ₂ O ₃ -H ₂ O system	27
Figure 2-10: Hydroxide precipitation diagram for Fe(III), Cu(II), and Ni(II) at 25°C	28
Figure 2-11: Hydroxide precipitation diagram for Fe(III), Cu(II), and Ni(II) at 150°C	29
Figure 2-12: Model of the two structural components of ferrihydrite	31
Figure 2-13: Kinetic processes involved in precipitation	38

Figure 2-14: Classification of the nucleation mechanism.....	38
Figure 2-15: Generalized nucleation diagram describing the characteristic differences between homogeneous, heterogeneous and surface nucleation as a function of supersaturation	40
Figure 2-16: Crystal growth mechanism by movement of the solvated solute molecule	41
Figure 2-17: Separation of precipitation regimes based on rate versus saturation ratio relationships	42
Figure 2-18: Crystallization rate of the metastable and stable phase as a function of saturation ratio	44
Figure 2-19: Dissolution-recrystallization process for phase transformation.....	45
Figure 2-20: First-order reaction plot for the transformation of ferrihydrite at various pH values plotted for the ratio of Fe_o (oxalate soluble Fe) to Fe_t (total iron) versus time.....	50
Figure 2-21: Solubility of ferrihydrite, goethite and 'soil-Fe' versus pH.....	54
Figure 2-22: <i>o</i> -phenylenediamine (OPD)	63
Figure 2-23: Positioning of the amine on the benzene ring	64
Figure 2-24: Reactions of <i>o</i> -phenylenediamine to form benzimidazole and 2,3-diaminophenazine	65
Figure 2-25: Oxidation of <i>o</i> -phenylenediamine.....	66

Figure 2-26: Synthesis <i>o</i> -phenylenediamine from <i>o</i> -nitroaniline	66
Figure 2-27: Synthesis <i>o</i> -phenylenediamine from <i>o</i> -dichlorobenzene	67
Figure 2-28: Synthesis <i>o</i> -phenylenediamine from <i>o</i> -chloroaniline	67
Figure 2-29: Sulfonation of aniline.....	68
Figure 2-30: Effect of various reagents on the viscosity of sulfur.....	69
Figure 2-31: Schematic for (a) thermal ring opening of S ₈ into polymeric sulfur diradical forms (b) copolymerization of S ₈ with DIB to form chemically stable sulfur copolymers.....	71
Figure 2-32: Schematic for copolymerization of S ₈ with limonene to form chemically stable sulfur copolymers.....	72
Figure 2-33: Thermally induced and the lithium-initiated reaction of dichlorobenzene and sulfur to generate polysulfides	73
Figure 4-1: Sequential extraction scheme for the determination of HaHC soluble and crystalline iron oxides phases.....	87
Figure 4-2: Fe and Cu dissolved by HaHC extraction for the samples S1, S2, and S3	90
Figure 4-3: TEM image of 2-line ferrihydrite and diffraction pattern from sample S1	100
Figure 4-4: TEM image of 6-line ferrihydrite and diffraction pattern from sample S1	100

Figure 4-5: TEM image of acicular goethite nanorods from sample S2.....	101
Figure 4-6: TEM image of rounded hematite particles from sample S3	101
Figure 4-7: High-resolution TEM image of sample S1 with overlaid EDS mapping of S, Fe, and Cu.....	103
Figure 4-8: Spectrum from electron diffraction of sample S1	104
Figure 4-9: Basic elements of Mössbauer spectroscopy.....	105
Figure 4-10: Hyperfine interactions for ^{57}Fe nuclei and resulting Mössbauer spectrum.....	106
Figure 4-11: Room temperature Mössbauer spectra of the samples S1, S2, and S3	109
Figure 4-12: Room temperature Mössbauer spectra before (top, S1) and after (bottom, S1–R1) HaHC leaching.....	110
Figure 4-13: Room temperature Mössbauer spectra of samples S2 and S3 taken before (black bars) and after (solid red lines) HaHC leaching.....	111
Figure 4-14: Mössbauer spectra of samples S1-R1 and S3-R3 (post- HaHC leaching) taken at 11K	113
Figure 4-15: Iron atoms forming a kagome lattice in jarosites.....	114
Figure 5-1: SEM micrographs of Na-Jarosite doped with Cu	120

Figure 5-2: Experimental X-ray powder diffraction patterns for the four jarosite samples	122
Figure 5-3: Room temperature Mössbauer spectra of the jarosite doped with Cu and HaHC leached residue sample.....	124
Figure 5-4: Mössbauer spectra of the Cu-doped sodium Jarosite taken at 50 K and below.....	125
Figure 5-5: Mössbauer spectra of the S1-R1 sample taken at 60 K and below	127
Figure 6-1: Final acid (g/L) versus pH	139
Figure 6-2: HaHC soluble mass (wt%) versus free acid (g/L).....	140
Figure 6-3: Effect of temperature and pH on the stability of the Fe compounds	142
Figure 6-4: Effect of acid concentration on the morphology of hematite precipitate.....	144
Figure 6-5: Schematic representation of calculating HaHC soluble phase.....	147
Figure 6-6: Effect of hematite seed, seed recycle and residue recycle on HaHC soluble phase	151
Figure 6-7: Effect of OPD on sulfur in the leach residue (no visible sulfur prills)	158
Figure 6-8: Effect of WD40 [®] +OPD on sulfur in the leach residue	159
Figure 6-9: Effect of benzene sulfonic acid on sulfur in the leach residue.....	159
Figure 6-10: Effect of phenyl phosphonic acid on sulfur in the leach residue	160

Figure 6-11: Effect of phenyl phosphonic acid on sulfur (crushed) in the leach residue	160
Figure 6-12: Effect of various reagents on the pyrite recovery in the leach residue	161
Figure 6-13: Synthetic hematite in the absence of WD40 [®]	164
Figure 6-14: Synthetic hematite in the presence of WD40 [®]	164
Figure 6-15: Schematic diagram of the proposed mechanism for the formation of hematite particles from sulfate-chloride solutions in the presence of WD40 [®] at 150°C	167
Figure 7-1: SEM micrographs of synthetic ferrihydrite aggregates	175
Figure 7-2: X-Ray diffraction pattern of the as-synthesized ferrihydrite via the solvent deficient method.....	176
Figure 7-3: Synthetic ferrihydrite solubility in HaHC at 50°C.....	177
Figure 7-4: Percent of Fe dissolved from the total initial Fe put into the system as synthetic ferrihydrite (20 g/L) at various initial sulfuric acid concentrations (inset legend) in sulfate-chloride (12 g/L) solutions at 150°C.....	182
Figure 7-5: Percent of Fe dissolved in the presence of Cu and Ni from the total initial Fe put into the system as synthetic ferrihydrite at 10 g/L initial sulfuric acid, 12 g/L chloride solutions at 150°C	188

Figure 7-6: Comparison of solubility data from sulfate-chloride solutions with Umetsu et al. (1977), Sasaki et al. (1993) and Reid and Papangelakis (2006)	190
Figure 7-7: PHREEQC calculated equilibrium Fe(III) species of the solution at 150°C in the presence of 11 g/L Fe(III) and 12 g/L Cl ⁻ added as LiCl	195
Figure 7-8: PHREEQC calculated equilibrium Fe(III) species of the solution at 150°C in the presence of 11 g/L Fe(III) and in the absence of added Cl ⁻	195
Figure 7-9: Concentration of total iron, ferric and ferrous iron dissolved from hematite in sulfate-chloride solutions at 150°C for 0 g/L initial acid. Chloride ion added as LiCl.	200
Figure 7-10: Fe-Cl speciation diagram for 0 g/L initial acid concentration, pH 1.68 at the end of 6 h and the measured ORP of 0.76 V at 25°C (SHE)	201
Figure 7-11: Concentration of total iron, ferric and ferrous iron dissolved from hematite in sulfate-chloride solutions at 150°C for 5 g/L initial acid.....	202
Figure 7-12: Concentration of total iron, ferric and ferrous iron dissolved from hematite in sulfate-chloride solutions at 150°C for 10 g/L initial acid.....	202
Figure 7-13: Concentration of total iron, ferric and ferrous iron dissolved from hematite in sulfate-chloride solutions at 150°C for 15 g/L initial acid.....	203
Figure 7-14: Concentration of total iron, ferric and ferrous iron dissolved from hematite in sulfate-chloride solutions at 150°C for 20 g/L initial acid.....	204

Figure 7-15: Concentration of total iron, ferric and ferrous iron dissolved from hematite in sulfate-chloride solutions at 150°C for 25 g/L initial acid..... 205

Figure 7-16: Concentration of total iron, ferric and ferrous iron dissolved from hematite in sulfate-chloride solutions at 150°C for 10 g/L initial acid in presence of 12 g/L Cu ions 206

Figure 7-17: Concentration of total iron, ferric and ferrous iron dissolved from hematite in sulfate-chloride solutions at 150°C for 10 g/L initial acid in the presence of 12 g/L Ni ions 206

Figure 7-18: Percentage of ferric and ferrous iron relative to the total iron concentration at various final acid concentration for hematite in sulfate-chloride solutions at 150°C..... 218

List of symbols

am	Amorphous
aq	Aqueous
B_{hf}	Magnetic hyperfine field
c	Crystalline
G	Growth rate
k_B	Boltzmann constant
K_{sp}	Solubility product
l	Liquid
P_{80}	80% passing size
s	Solids
S	Saturation ratio
S^*	Critical saturation ratio
S°	Elemental Sulfur
$S_\lambda, S_\mu, \text{ and } S_\pi$	Allotropes of Sulfur
ΔE_Q	Electric quadrupole interaction
ΔG°	Standard free energy
\dot{J}	Nucleation rate
δ	Electric monopole interaction
Ω	Attachment frequency

List of abbreviations

AA-UBC	Anglo American - The University of British Columbia
BS	Benzene sulfonic acid
CBD	Citrate bicarbonate dithionite
CBED	Convergent-beam electron diffraction
CDS	Carbon disulfide
CESL	Cominco engineering services limited
CIM	Canadian Institute of mining, metallurgy, and petroleum
ED	Electron diffraction
EDTA	Ethylenediaminetetraacetic acid
EDX	Energy-dispersive X-ray spectroscopy
EW	Electrowinning
EXAFS	Extended X-ray absorption fine structure
HAADF	High-angle annular dark-field imaging
HaHC	Hydroxylamine hydrochloride
HSC	Enthalpy (H), entropy (S), and heat capacity (C)
HT	High temperature
ICDD	International centre for diffraction data
ICNG	Internation Nickel Study Group
ICP-MS	Inductively coupled plasma mass spectrometry
ICSD	Inorganic crystal structures database

ICSG	International Copper Study Group
LLE	Liquid-liquid extraction
LT	Low temperature
MPD	Meta-phenylenediamine
MS	Methane sulfonic acid
MT	Medium temperature
NIST	The national institute of standards and technology
NS	Nonane sulfonic acid
NSC	Nitrogen species catalyzed
NSERC	Natural sciences and engineering research council of Canada
NTA	Nitrilotriacetic acid
OPD	Ortho-phenylenediamine
ORP	Oxidation-reduction potential
PDF	The pair distribution function
PGE	Platinum group elements
PP	Phenyl phosphonic acid
PPD	Para-phenylenediamine
PTFE	Polytetrafluoroethylene
PXRD	Powder X-ray diffraction
PZC	Point of zero charge
QS	Quadrupole splitting

QXRPD	Quantitative X-ray powder diffraction
SAED	Selected area electron diffraction
SD	Standard deviation
SDA	Sulfur dispersing agent
SEM	Scanning electron microscope
SHE	Standard hydrogen electrode
STEM	Scanning transmission electron microscope
SX	Solvent extraction
TEM	Transmission electron microscopy
TPOX	Total pressure oxidation
XRD	X-ray diffraction

Acknowledgments

I have always found research to be fascinating, exhilarating, and rewarding. Through this particular research work, I finally found a long-term passion that promises always to enthrall my mind. For this gift, and for allowing me the benefit of his esteemed guidance, I am forever indebted to my advisor, Dr. Edouard Asselin. This thesis would not have been possible without his generous support, patient and persistent guidance, and unwavering faith in my abilities.

I would like to thank the members of my supervisory committee, Dr. David B. Dreisinger and Dr. Marek Pawlik for providing me with invaluable insights and direction, throughout the course of my research project. I am also grateful to Dr. Berend Wassink, for helping me build robust foundations with his ingenious course on hydrometallurgy, experimental procedures, and laboratory safety.

I extend a special thank you to Mr. Henry Salomon-De-Friedberg, Superintendent of New Technologies and Mr. Keith Mayhew, Manager, Teck-Cominco Engineering Services Limited (CESL), for their valuable input throughout the course of this work. I am also thankful to Dr. Indje Mihaylov, Section Head of Hydrometallurgy, Vale Canada Limited, for his useful suggestions and astute reviews of my work on several occasions. I gratefully acknowledge the financial support of

my endeavors by CESL (a subsidiary of Teck Resources), Vale Limited, and Natural Science and Engineering Research Council of Canada (NSERC).

I am incredibly grateful to Dr. Dominic Ryan from the Department of Physics at McGill University for his support with the Mössbauer analysis, Dr. Mati Raudsepp from the Department of Earth, Ocean and Atmospheric Sciences (EOAS) at the University of British Columbia, for the quantitative X-ray analysis, and to Mr. John MacIntosh, from Teck-CESL for help with the numerous chemical analyses presented in this work.

Last but not least, I acknowledge my family and friends whose unfaltering support saw me through the most challenging of times. I am grateful to my friends Richa Anand, Amit Kumar, and Vinoth Kumar for their unconditional friendship. I am infinitely thankful to my parents and sisters for loving me unconditionally and supporting me in every imaginable way. I am particularly indebted to them for their altruistic wisdom in letting me spread my wings and go across continents to fulfill my destiny, and for the sacrifices they have made to see me succeed. I sincerely thank each and everyone that have helped me achieve my goal. I wish them all the best and hope I can return their kindness in any measure possible.

Dedicated
to
My Beloved
Parents

CHAPTER 1: INTRODUCTION

1.1 Background

Iron present in mineral concentrates typically dissolves in hydrometallurgical processes along with the target metals of economic interest and must be eliminated from solution. This is usually achieved by precipitation as iron oxide/oxyhydroxides. These phases, however, have an adsorptive capacity that can prove to be disadvantageous when it results in loss of valuable metals from process solutions (Sahu and Asselin, 2011). The iron precipitates can be metastable, difficult to settle, thicken and filter due to poor crystallinity, nanoscale size, high surface area, and moisture levels. Adequate iron control and removal from acidic sulfate solutions require a filterable (and low moisture), low cost and “environmentally friendly” precipitate (Dutrizac, 1987, 1979).

Copper oxides and primary and secondary copper sulfides are the essential sources of copper. It is easier to recover copper from copper oxides ores using hydrometallurgical methods. About 90% of copper extraction can be obtained in only a few weeks of leaching in heaps using nothing but a dilute sulfuric acid solution. As the copper oxide reserves continue to deplete, the heap leaching process is being applied to secondary copper sulfide ores such as chalcocite (Cu_2S) and covellite (CuS). These ores are dissolved with ferric sulfate. This is usually improved upon with the use of iron-oxidizing microbes and injection of air at the base of the heap. Copper extraction from sulfide ores takes much longer (months instead of weeks) than from oxide ores. The dissolution of primary sulfides, on the other hand, is slow and incomplete under the same leaching conditions applied to the secondary copper sulfides. This is a problem that needs to be resolved since primary copper

sulfides are the main source of copper and chalcopyrite (CuFeS_2) alone accounts for about 80% of total copper reserves (Singer, 2017).

There are, however, alternative routes to recover copper from the primary sulfides. The most common being a pyrometallurgical route which involves concentrating via froth flotation followed by smelting, converting and electrolytic refining. This process results in high purity cathodes of over 99.99% copper. Copper pyrometallurgy in the past had a major disadvantage over copper hydrometallurgy due to the production of large amounts of toxic gases (primarily SO_2) to smelt the chalcopyrite concentrates. In recent times, modern smelters have largely overcome this problem with the use of more efficient reactors and gas collection systems. In comparison to old reverberatory furnace technology, modern smelters use flash fusion, autogenous bath fusion, and oxy-fuel burner technology. These new techniques generate comparatively lower volumes of higher strength off-gas, which are treated efficiently to produce sulfuric acid as a valuable byproduct.

Despite all these improvements, there are other factors that have kept researchers active in the search for a new and affordable method to treat chalcopyrite concentrates using hydrometallurgy. The capital investment required for smelters is significant. Furthermore, smelters need to handle large quantities of material to remain economic, and it is not clear that shipping concentrates across the globe to a handful of large smelters will be possible in future due to regulatory changes related to import restrictions on certain elements, such as arsenic, antimony and mercury (Fountain, 2008; George et al., 2018; Salomon-de-Friedberg and Robinson, 2015). Indeed, the presence of these impurities render some copper concentrates less suitable for smelting as strict regulations and

penalties are imposed by governments and environmental agencies (Berezowsky and Trytten, 2002; Dreisinger, 2006). Furthermore, there may also be radioactive constituents to some concentrates that preclude shipment (Ciobanu et al., 2013; Fountain, 2013; Weidenbach et al., 2016). The high throughput requirement is also a significant disadvantage when compared to hydrometallurgical plants, which can be built and operated on-site on a smaller scale with less capital, and which take advantage of the selectivity inherent in hydrometallurgical operations. On-site processing also enables the return of waste products to the mine site, avoiding potentially large disposal costs in more-populated areas. Other concerns with smelters relate to the emission of gases (especially fugitive emissions) as well as storage and transport difficulties associated with the onsite production of sulfuric acid.

Cominco Engineering Services Limited (CESL) has developed a hydrometallurgical process for base metal sulfide concentrates, notably those of copper and nickel. Defreyne et al. (2006) explain the role of iron in this process in detail. The basis of CESL technology is the chloride assisted medium temperature ($\sim 150^{\circ}\text{C}$) leaching of chalcopyrite concentrates. This process has technical and economic advantages such as the capacity to treat a variety of sulfide concentrates including low-grade bulk concentrates at low capital and operating costs, flexibility in terms of production scale and the ability to recover by-products. The main advantage of the process is that it uses a medium temperature which eliminates the need for ultrafine grinding of the chalcopyrite mineral but still produces elemental sulfur thus minimizing oxygen consumption. Less sulfate (SO_4^{2-}) is produced, so neutralization requirements are also diminished. Medium temperature leaching, such as the CESL leach recovers between 95 and 99% copper depending on the mineralogy and the

grade of the concentrate. The unrecovered copper represents an economic opportunity. It is in the residue, generated during chalcopyrite leaching, that copper losses are incurred although it is unclear as to which mechanisms are responsible for the losses.

One goal of this work is to identify the factors causing the loss of valuable metal to the leach residues produced under the CESL conditions. This is accomplished by performing pressure oxidation batch tests at CESL conditions in an autoclave reactor under various process conditions to reduce the valuable metal (copper) loss to the residue.

1.2 Thesis outline

The chapters of this study are organized as follows:

Chapter 2 presents a comprehensive literature review covering all aspects of iron precipitation in hydrometallurgical processes, leaching of sulfide concentrates, CESL and Vale processes, hematite precipitation and nucleation theory of crystallization, the solubility and transformation of ferrihydrite, hematite growth modifications and sulfur dispersing agents.

Chapter 3 defines the objectives of this study.

Chapter 4 presents the results of the characterization studies performed on leach residue samples from the CESL and Vale. An evaluation of crystallinity and a correlation between amorphous iron phases and associated Cu/Ni loss to the residue is established with the help of sequential extraction and various characterization techniques including quantitative X-ray powder diffraction (QXRPD), Transmission electron microscopy (TEM) and Mössbauer spectroscopy.

Chapter 5 further extends the Mössbauer spectroscopy studies into synthetic jarosite. Chemical synthesis of jarosite doped with copper and nickel was performed, and Mössbauer spectroscopy was applied to evaluate the crystallinity.

Chapter 6 presents the results from pressure oxidation leaching of sulfide concentrate at CESL condition in a benchtop autoclave. The effect of supersaturation control by varying acid concentration and promoting nucleation and growth of hematite in the presence of seed is discussed. This chapter also reveals the discovery of novel reagent(s) for iron and sulfur control in the CESL process.

Chapter 7 discusses the transformation of synthetic ferrihydrite and the solubility of the transformation product (hematite) under CESL conditions.

Finally, Chapter 8 provides a summary of the findings from this work and explores the topics for future work required to extend the outcomes of the current results.

CHAPTER 2: LITERATURE REVIEW

Iron is the fourth most abundant element in the earth's crust. It is believed that the earth's core consists mainly of iron. Metallic iron occurs free in nature, but it is comparatively rare. This is because of the readiness with which the metal is oxidized in moist air. Combined iron is exceedingly common, occurring as it does in hundreds of minerals - oxides, hydrated oxides, carbonates, silicates, sulfides, etc. It is so common, indeed, that a vast number of minerals owe their color to the presence of a small proportion of admixed iron compounds. Huay (1801), the father of modern mineralogy, rightly commented that "When nature takes up her brush, iron oxide is almost always on her palette". Alchemists commonly used the term 'Mars' for iron; for example, *crocus martis* is the name for anhydrous ferrous sulfate (FeSO_4) (Mellor, 1932). Iron was essential to the development of early life on Earth. The atmosphere was initially oxygen deficient, and iron was present in the ferrous oxidation state (Fe(II)) in all water bodies (oceans, lakes, etc.). A few billion years ago, photosynthetic bacteria began producing oxygen which induced the precipitation of iron oxide/oxyhydroxides, due to the extremely low solubility of the ferric (Fe(III)) ion. After depletion of Fe(II), the Earth's oxygen atmosphere began to form, and this event is evidenced in the intensely red iron oxide deposits found on several continents (Mielczarek and McGrayne, 2000). Because of oxygen, iron oxides and oxyhydroxides are everywhere in nature and impact all scientific disciplines (Cornell and Schwertmann, 1996). In the industrial processes related to mining and extractive metallurgy, iron is present in hydrometallurgical process liquors, waste or acid mine drainage and must be removed from these solutions (Dutrillac, 1987; Lee et al., 2002;

Meng et al., 2001; Qiang et al., 2003; Riveros et al., 2001; Sasowsky et al., 2000; Tufekci et al., 2000).

Copper was the most useful metal from the beginning of recorded history until the end of the medieval period. The use of copper marked the transition in the progress of human civilization from the stone age to the metal age. Every ancient metal culture was introduced by the use of copper even though gold was unquestionably the first metal to attract man's attention owing to its beauty, sparkling color, luster, resistance to corrosion and its native state. Iron may have been used before copper in the form of meteorites (Rickard, 1932). Copper was used initially for ornaments, statues, domestic utensils and implements of war. It was used for every purpose in which its properties proved superior to other materials. When ferrous metals attained large-scale production, their widespread use eclipsed copper. Then came the age of electricity, which introduced new requirements for materials to be used in the generation and transmission of electrical energy.

Copper is readily precipitated from solutions of its salts by iron. Alchemists regarded this as evidence of transmutation of metals. The pure metal was historically obtained from Cyprus under the name *aes cyprium*, which later became cuprum with the symbol Cu. Finally, this was anglicized as copper. Gold was the lure that attracted the miners to the deposits. The prospectors soon turned from gold to the silver-bearing quartz veins and from silver to copper. These mines have yielded hundreds of millions of pounds of copper per year and only small amounts of silver and gold. Hence the old saying: "A man is likely to go to the poor house with a gold mine on his hands, may make a fair living from a silver mine, but easily becomes wealthy when he finds a good copper mine" (Howard, 1929).

Nickel is also an essential metal for humanity. It has been found in metallic artifacts dating back more than 2,000 years. Nickel, a naturally occurring, lustrous, silvery-white metallic element, is the fifth most common element in the earth's crust. However, most of the nickel is inaccessible as it is present in the core of the planet. It was first identified and isolated as an element by the Swedish chemist, Axel Cronstedt, in 1751 (Gusenius, 1969). In the 19th century, nickel was used in plating and in alloys such as “nickel silver” (commonly known as German silver) in which it is alloyed with copper and zinc. This alloy was named for its silvery color and did not actually contain any silver. The name “Nickel” name comes from the Saxon term 'Kupfernickel' or Devils' Copper, as the 15th-century miners thought the ore looked red-brown like copper, but it was too difficult to mine, and they also believed it was poisoning them (it was, in fact, arsenic poisoning). In 1857, the coins in the US first used nickel alloyed with copper. The “nickel” was not a pure nickel, but in 1881, pure nickel was used for coins in Switzerland (Howard-White, 1963). Stainless steels were discovered in the early 20th century, and nickel was found to have a very beneficial role in many common grades, a situation which continues to this day. Alloys based on nickel have excellent corrosion resistance and high-temperature resistance, which made them suitable for chemical plants and allowed the practical realization of the jet engine. Because of these developments, nickel enjoyed strong growth in demand in the 20th century and continued to do so.

A growing world population combined with an increase in the standard of living, especially in countries with emerging economies is causing an increase in the global consumption of metals. The global demand for copper has been growing continuously. The world’s refined copper usage has more than tripled in the last 50 years due to the ever-expanding sectors such as electrical and

electronic products, building construction, industrial machinery and equipment, transportation equipment, consumer and general products and more recently electric cars. This is because copper has the second highest conductivity of all the elements, good ductility and resistance to corrosion. According to the International Copper Study Group (ICSG), in 2019, the world mine production of copper was expected to reach 21.0 million tonnes (Mt) (ICSG, 2019). The growth in copper demand is expected to continue as copper is essential to the economic activity of modern technological society. Infrastructural development in China and India will continue to sustain growth in copper demand. Moreover, according to the International Nickel Study Group (INSG) world, primary nickel production is projected to increase to around 2.4 Mt (INSG, 2019).

Copper metal production is carried out mainly by two routes, i.e., conventional pyrometallurgical and more recent hydrometallurgical techniques. Conventional pyrometallurgical techniques comprise crushing, grinding, flotation, smelting, converting and refining/electro-refining. The slag, which is the by-product from copper smelting and converting furnaces contains significant amounts of copper (4-8 Cu% in converting slag and 1-2% Cu in smelting slag) that remains unrecovered (Davenport et al., 2002). The presence of such large amounts of copper in the slag necessitates a slag cleaning step. Slag cleaning is achieved using various pathways such as employing slag cleaning electric furnaces, cooling of slag followed by crushing/grinding and flotation. The tailings from the slag cleaning step still contain about 0.4 to 1.0 % Cu, which is lost when slag is discarded.

Nickel production comes from two types of ores, sulfide ores or laterite (oxidized) ores and cobalt is a byproduct of nickel processing. Nickel sulfide ore comes from hard rock type deposits, mined

by open pit and underground mining techniques. Laterite ores are found as clay-rich 'soft' deposits, which are the result of prolonged tropical weathering of ultramafic rocks (Boldt, 1967). The sulfide ore bodies comprise about 30% of the world's nickel mineralization and account for about 60% of the world's nickel production, while laterites account for over 70% of the nickel resources and only 40% of nickel production (Dalvi et al., 2004). Generally, the sulfide ores are treated by a combination of mineral processing and pyrometallurgy to produce matte.

The conventional pyrometallurgical treatment of nickel concentrates includes roasting, smelting, and converting. Roasting drives off sulfur as sulfur dioxide and part of the iron is oxidized. Smelting involves melting the roaster product with a siliceous flux. The siliceous flux and the oxidized iron produce two immiscible phases, a solution of molten sulfides, which contains the metal values, and a liquid silicate slag, which can be discarded. In the converting operation, more sulfur is driven off as sulfur dioxide from the sulfide melt, and the remaining iron is oxidized and fluxed for removal as silicate slag, leaving a high-grade nickel copper sulfide matte. In several modern operations the nickel sulfide concentrate is treated directly in the smelter and the roasting step has been eliminated (Habashi, 1997). Sulfide Matte refining is done hydrometallurgically, which comprises grinding, leaching and reduction.

2.1 Hydrometallurgical leaching processes

One hydrometallurgical alternative to smelting is the high temperature (>180°C) total pressure oxidation (TPOX) process, which is ideally suited to copper-gold concentrates. This is because all sulfides are oxidized to sulfate and no cyanide-consuming sulfur reports to the residue, which

would allow easy and economic recovery of the precious metals. Furthermore, iron is rejected as a stable hematite phase, which is the preferred hydrometallurgical process residue. However, total sulfur oxidation implies considerable acid generation, which requires a great deal of neutralization. The cost associated with sulfate removal may become obstructive unless the copper and/or gold grade is high enough to justify such a neutralization expense. Another drawback of the TPOX process is that the autoclave heat balance requires the reactor to run moderately diluted, i.e., at relatively low pulp densities. The Platsol process (Dreisinger, 2003), is a variation of the TPOX process and could allow in situ platinum group element (PGE) extraction due to the presence of ~6 g/L chloride.

A host of low temperature (LT; <115°C) processes have been proposed. These can be grouped according to the media used: the sulfate, chloride, ammoniacal and nitric acid processes. The sulfate processes include the Sherritt Gordon process (Vizsolyi et al., 1967), Activox process (Corrans et al., 1993), Albion process (Hourn et al., 1996), BioCOP process (Batty and Rorke, 2006), Galvanox process (Dixon et al., 2008), Jetti process (Dixon et al., 2018) and the JX iodine process (Granata et al., 2019). The chloride processes are the Cymet process (McNamara et al., 1980), Clear process (Schweitzer and Livingstone, 1978), Cuprex (Dalton et al., 1991), Intec (Moyes et al., 2002) and HydroCopper process (Hyvärinen and Hämäläinen, 2005). The ammoniacal processes are: the Anaconda Arbiter (Kuhn et al., 1978) and Escondida processes (Duyvesteyn, 1995) and the nitric acid process is the NSC process (Anderson, 2003).

These processes may be attractive in terms of their economics and potentially lower capital investment. However, most low-temperature processes do not deal well with harmful elements,

are complex and tend to produce residues that are environmentally unstable (Steyl, 2012). In terms of both economic factors and risk factors associated with new technologies, the TPOX processes, such as the one at Freeport McMoran's Bagdad Operation in Arizona, US (Brewer, 2004; Marsden et al., 2003), may be the most viable option for higher grade ore bodies. However, if the oxide source required for acid neutralization is limited and a spare capacity exists in a downstream refining circuit of solvent extraction (SX) and electrowinning (EW) unit operations, a medium temperature (115-160°C) autoclave process may become an attractive alternative.

The different operating regimes are schematically illustrated in Figure 2-1. The low temperature (LT) processing options generally fall in a temperature region below the melting point of sulfur, whereas the high temperature (HT) processing options drive all sulfide sulfur to the sulfate form. Most of the difficulties associated with medium temperature (MT) operation are a result of liquid molten sulfur. Surfactants or fine coal are used in MT processes to disperse liquid sulfur, while ultra-fine grinding of concentrate and high oxygen pressures are applied to reduce the overall autoclave residence time. However, it would also be economically beneficial to operate the primary leaching SX circuit close to acid neutral, i.e., to prevent excessive acid neutralization or addition. This aspect depends heavily on the mineralogy of a specific concentrate, the temperature, the oxygen overpressure and the effectiveness of the surfactant(s). The upper-temperature boundary is limited by the sulfur transition region as shown in Figure 2-1 which is associated with a rapid increase in the viscosity of liquid sulfur, followed by a rapid decrease in the overall elemental sulfur yield. If the economics of the MT process demand operation close to this transition

point due to the slow chalcopyrite leaching rate, which is also related to the total available surface area, i.e., the cost of grinding, the elemental sulfur yield would be lower and more variable.

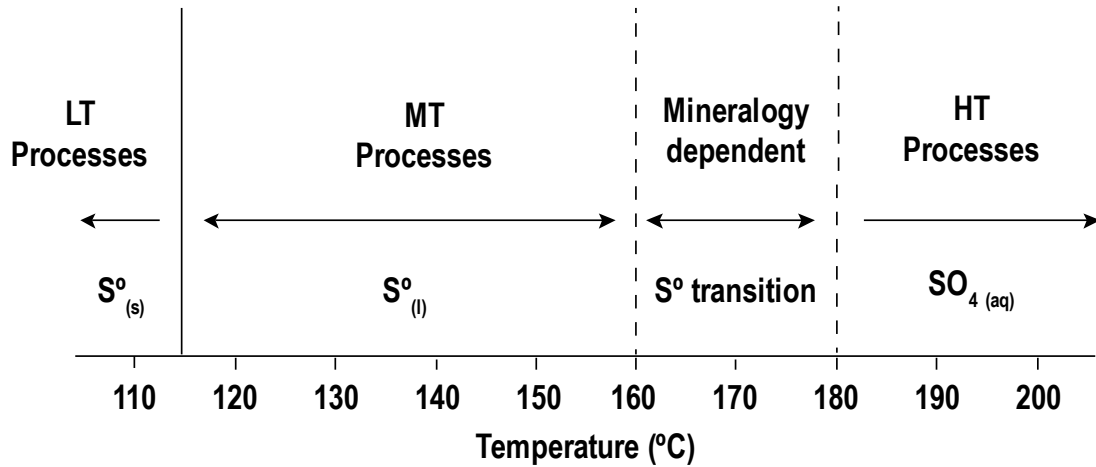


Figure 2-1: Illustration of three types of leaching processes based on temperature regimes
(Modified from Steyl, 2012)

Since the exact transition temperature depends on sulfur, which is difficult to disperse, only MT operation below $\sim 160^{\circ}\text{C}$ would generally be considered. MT processes that have come close to commercial success are the “Anglo American-The University of British Columbia” (AA-UBC) process (Dempsey and Dreisinger, 2003), a similar process applied by Freeport McMoRan Copper & Gold Inc. at the Morenci operation (Marsden et al., 2007a, 2007b, 2007c, 2007d) and Cominco Engineering Services Laboratory (CESL) process (Defreyne et al., 2008, 2004). These processes are similar, except for the lower surfactant (<3 kg/t) and ~ 12 g/L chloride additions in the case of the CESL process (McDonald and Muir, 2007a). The major difference is the presence of the chloride ion. The chloride anion complexes with the cuprous ion and activates the cupric/cuprous couple (Jones, 1974; Lundström et al., 2005; Muir, 2002). The kinetics of mineral oxidation with

the cupric/cuprous couple has been reported to increase linearly in proportion to the combined cupric/cuprous concentration (Hirato et al., 1987). There is also speculation that chloride ion helps sulfur dispersion as per the work of McDonald and Muir (2007a) and the therein cited paper of Brown and Papangelakis (2005).

The chloride ion relaxes the ultra-fine grinding and particle size requirement of the AA-UBC process (P_{90} :10 μm) to a P_{80} of about 20 to 40 μm . The presence of chlorides also results in a higher than 80% sulfide to sulfur conversion compared to the 50-70% in the AA-UBC process (Dreisinger et al., 2002; McDonald and Muir, 2007b). The AA-UBC, Dynatec and CESL processes could be very competitive, as they produce a more concentrated pregnant leach solution (PLS) as compared to both TPOX and LT processes (Berezowsky and Trytten, 2002) and pose a low environmental risk (Taylor and Jansen, 1999). Medium temperature operating conditions typically produce one-third of the acid compared to TPOX, consume about half the oxygen and need one third more reaction time (~ 90 min). CESL requires 60 minutes or less for chalcopyrite, but 90 minutes for enargite. Another important observation from these MT processes is that different surfactants and additives (e.g., chlorides or coal) may result in significant changes in the sulfide oxidation rate, elemental sulfur yield and post-leach cyanide consumption (Berezowsky and Trytten, 2002; McDonald and Muir, 2007b). The Dynatec process uses fine coal as a surfactant, which not only better withstands degradation, but also renders elemental sulfur at a slightly lower ($\sim 5\%$) yield and consumes $\sim 50\%$ less cyanide as compared to the AA-UBC process (Berezowsky and Trytten, 2002).

Many hydrometallurgical processes have also been developed to treat nickel sulfide concentrates. Sherritt International operates a pressure leaching process in ammonia-ammonium sulfate media that was developed in 1954. Hydrogen gas is used to precipitate nickel metal. The plant continues to be in operation in Fort Saskatchewan, Alberta (Forward, 1951; Forward and Warren, 1960; Kerfoot and Cordingley, 1997). Similar plants were built at Kwinana in Australia (Honey et al., 1997) and Springs in South Africa. The BioNIC process, which relies on the biological oxidation of ferrous to ferric, was developed by BHP Billiton (Miller et al., 1997).

The PLATSOL process, a high-temperature pressure oxidation process, was developed at SGS Lakefield by International PGM Technologies Limited to treat NorthMet bulk copper-nickel-PGM concentrate (Ferron et al., 2001). It involves high temperature ($>220^{\circ}\text{C}$) pressure oxidation of the bulk concentrate in the presence of chloride. The basic difference between the PLATSOL process and conventional high-temperature pressure oxidation is the addition of chloride ions to the autoclave feed. It was discovered that the addition of chloride at concentrations as low as ~ 3 g/L (5 g/L NaCl) resulted in the dissolution of most of the PGM's in the autoclave along with copper and nickel.

The Activox process was developed by Western Minerals Technology (WMT) for the oxidative leaching of sulfide concentrates (Palmer and Johnson, 2005). The process involves activation of the mineral surfaces by ultra-fine grinding typically to a P_{80} of ~ 10 μm , followed by a low-temperature (100°C – 110°C), low-pressure (1,000 kPa) oxidative leach to break down the sulfide matrix. The HIKO process was developed by Outokumpu (Nyman et al., 1992). The process involves autoclave leaching using an oxygen pressure of 5 bars, the temperature of 110°C or below

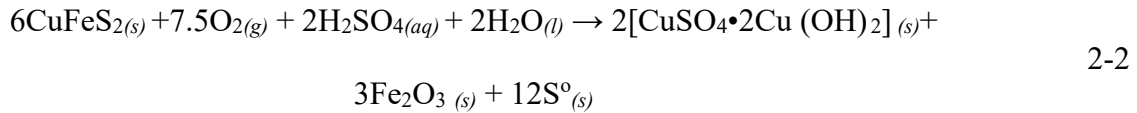
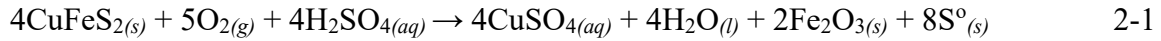
the melting point of sulfur and mixing capable of giving sufficient contact among gas, liquid, and solid particles. Much of the design effort was focused on good oxygen dispersion and ways to create strong intersecting surface flows to draw oxygen from the gas volume back into the intensively mixed slurry.

The other processes include the Sumimoto process in which the mixed cobalt-nickel sulfides are leached under air pressure in sulfuric acid solution at 150°C to 160°C. The Nippon process wherein the mixed sulfide are pressure leached at 140°C to 170°C in sulfate solution under air pressure, to dissolve nickel and cobalt, together with other base metals (Kerfoot and Weir, 1988) and the CESL nickel process (Jones and Moore, 2001). Vale recently commissioned a full-scale plant in Long Harbor, Newfoundland to treat the Voisey Bay sulfide concentrate. These pressures leaching process are intended to minimize the conventional smelting routes.

2.2 CESL and VALE medium temperature leaching

Since the early 1990s, TECK (Formerly Cominco) has been developing a medium temperature pressure leaching process to extract copper and other valuable metals from sulfide concentrate. This process has been successfully and extensively piloted. It has also been demonstrated at the industrial scale in Brazil in cooperation with Vale. The leaching process occurs at *ca.* 150°C with a chloride “catalyst” in an autoclave and requires only a light concentrate regrind of P₉₅ at 45 µm. All copper minerals in the pressure leach step are oxidized within 60 minutes to either soluble copper (Reaction 2-1) or acid soluble copper salts (Reaction 2-2) such as basic copper sulfate

(antlerite), depending on the level of free acid in the leach (Defreyne et al., 2006; McDonald and Muir, 2007b).



The iron presented to the pressure leach, originating either from the chalcopyrite or from other sulfides such as pyrrhotite or pyrite, was ideally rejected to residue as hematite. Sulfide sulfur was mainly (>80%) oxidized to elemental sulfur while the remaining fraction converted to sulfate. The solids produced from the pressure leach were filtered and washed. They were subsequently treated by enhanced atmospheric leaching (EAL), where the residues were re-leached in dilute sulfuric acid at atmospheric conditions to generate copper sulfate (Reaction 2-3):



The high tenor copper sulfate solution was then processed through traditional solvent extraction/electrowinning to recover high-grade copper cathodes. It is to be noted that the iron precipitate formed in the pressure leach is expected to react minimally during the EAL step. The residue from EAL, which contains iron, sulfur, and precious metals, was then sent for further processing if required. The CESL process generalized flowsheet is shown in Figure 2-2.

Vale, from 1998 to 2008 developed, piloted and demonstrated a process for the recovery of Ni, Co, and Cu from nickel sulfide concentrate that was being produced from the Voisey's Bay nickel

sulfide (primarily pentlandite: $(\text{Fe,Ni})_9\text{S}_8$) deposit in Newfoundland and Labrador. The demonstration plant was in Argentina, and the commercial-scale facility is in Long Harbour. The pressure leaching process operates under similar conditions to those employed by CESL for copper concentrates, also in a sulfate-chloride solution. In the Vale process, hematite is the predominant and preferred form for iron precipitation in the pressure leach residue.

Both Teck and Vale are therefore, interested in further understanding the nature of the iron precipitates that are generated during this leaching process, and the leach conditions that will be most favorable for the precipitation of iron as hematite.

Iron precipitation is a critical step in most hydrometallurgical operations. The chemical and physical nature of iron residues generated through any hydrometallurgical operations is of significant concern for two reasons:

1. The precipitate generated during the leach must have limited capability to adsorb valuable metals or other solution species (such as sulfate) as that can affect economic and environmental aspects of the process.
2. The precipitate is typically impounded as tailings and must be in a chemically stable form to reduce any tendency for its reaction with the environment.

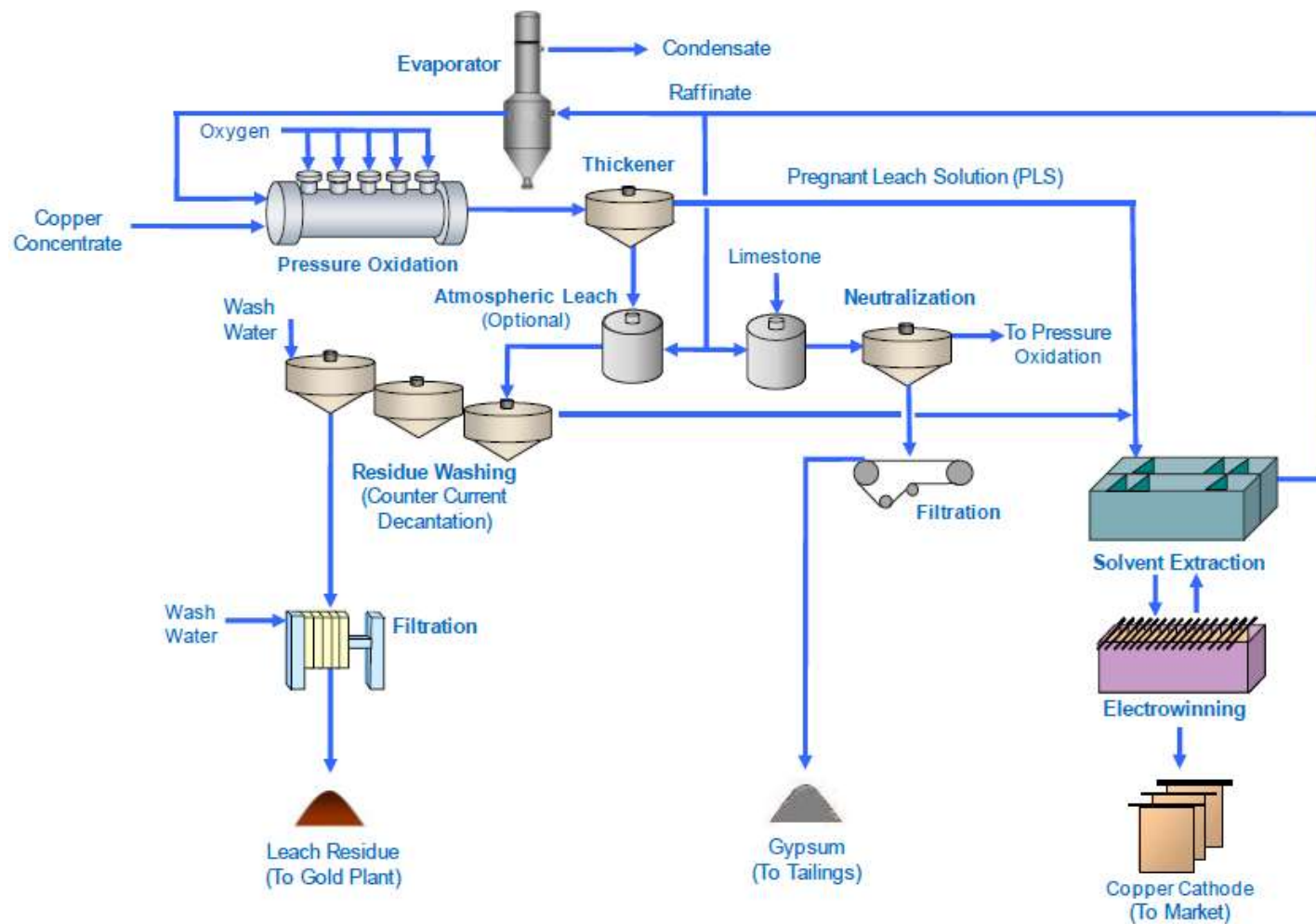


Figure 2-2: CESL process basic flowsheet
 (retrieved from www.cesl.com)

For both reasons, hematite is the preferred iron product of medium temperature sulfide concentrate leaching. Unfortunately, it is clear from the literature that leaching does not produce the ideal hematite iron residue. These residues are usually a mixture of hematite, goethite, jarosite and other iron oxyhydroxides that can affect long-term residue stability as well as copper and nickel recoveries.

2.3 Iron behavior in aqueous solution

The behavior of any hydrometallurgical system is determined by the associated thermodynamics and by kinetic considerations that influence the steady state conditions of the leaching system. The thermodynamic data for most metal-water systems at 25°C have been presented by Pourbaix (Pourbaix, 1966) in the form of Eh-pH diagrams. The use of such diagrams in hydrometallurgy has been discussed by Burkin (1966). Eh-pH diagrams are a convenient way of showing the thermodynamic equilibria that may be approached in aqueous systems, i.e., these diagrams do not account for kinetics. The lines parallel to the x-axis represent reactions in which H^+ and OH^- ions do not take part, and those which run parallel to the y-axis represent reactions in which there is no change of valency (such as ferric hydrolysis). The thermodynamically stable state at any given value of Eh and pH can readily be seen, and the superimposition of diagrams enables the interactions between various systems to be assessed. The lines for the reduction of oxygen at 1 atmosphere and the oxidation of hydrogen at 1 atmosphere are almost always superimposed and represent the limits of stability of water. From these diagrams, it is possible to see at a glance whether the oxidized or reduced state is the thermodynamically stable one at specific values of Eh-pH. The Eh-pH diagrams given by Pourbaix are all at 25°C, but most hydrometallurgical reactions

occur at elevated temperatures to improve reaction rates. However, limited thermodynamic data are available for aqueous systems at temperatures above 100°C, and therefore, several groups of workers have used extrapolative techniques to yield estimated values up to 300°C. The Criss-Cobble method has been used by Biernat and Robins (1972) and Townsend (1970) to produce Eh-pH diagrams for the Fe-H₂O system

The Eh-pH diagrams constructed by Biernat and Robins (1972) for the Fe-H₂O system at 25°C and 150°C are presented in Figure 2-3 and Figure 2-4, respectively. For the Fe-H₂O system, the aqueous species considered were Fe²⁺, FeOH⁺, HFeO²⁻, Fe³⁺, FeOH²⁺, Fe₂(OH)₂⁴⁺, Fe(OH)₂⁺ and FeO₄²⁻. The solids considered were Fe, FeO, Fe(OH)₂, Fe(OH)₃, FeOOH, Fe₂O₃, and Fe₃O₄. The stable iron species change at different temperatures. At ambient temperature, the iron is in solution at low pH and hydrolyzed at high pH. According to the diagram, the dominant species at 25°C are Fe, Fe²⁺, FeOH⁺, HFeO²⁻, Fe³⁺, FeOH²⁺, Fe(OH)₂⁺ and FeO₄²⁻. These authors chose to present the condensed metastable species Fe(OH)₂ and Fe(OH)₃ at 25°C, which is consistent with many experimental observations (Loan et al., 2002). Increasing temperature to 150°C, the stability regions of almost all ionic species decreases, which is to be expected as their solubility decreases. The exception is Fe(OH)₂⁺ and FeO₄²⁻, where the stability region increases; however, it is unlikely that these species are formed. Two new phases have also formed at this temperature: Fe₂(OH)₂⁴⁺ and Fe₂O₃. Fe₂O₃ replaces the ferric hydroxide phase indicating that metastable ferric hydroxide phases have transformed into the more stable hematite phase at 150°C.

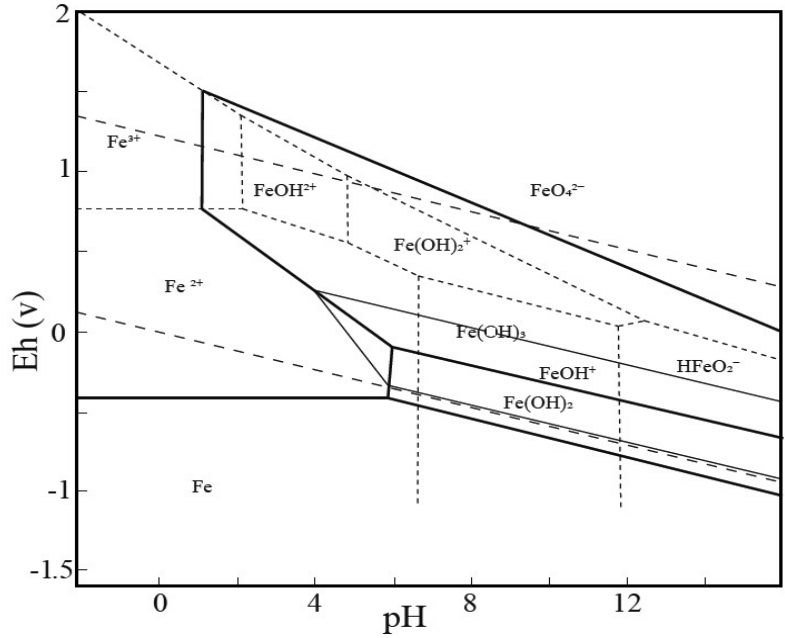


Figure 2-3: Eh-pH diagram for the Fe-H₂O system at 25°C and unit solute activity
(Redrawn from Biernat and Robins, 1972)

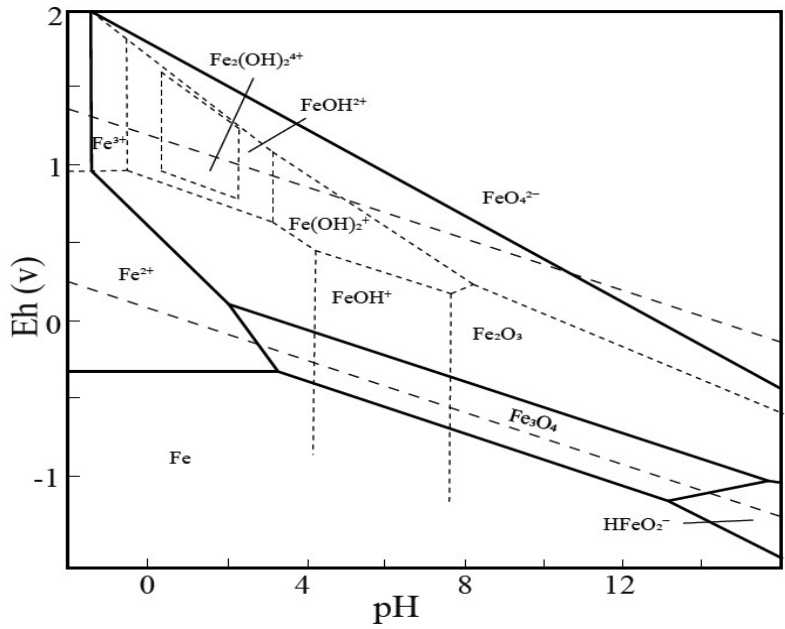


Figure 2-4: Eh-pH diagram for the Fe-H₂O system at 150°C and unit solute activity
(Redrawn from Biernat and Robins, 1972)

Biernat and Robins (1969) also developed S-H₂O Eh-pH diagrams at 25 and 150°C. The sulfur species and phases that were considered are H₂S, HS⁻, S²⁻, S_(s), S_(l), HSO₄⁻, and SO₄²⁻. As shown in Figure 2-5 and Figure 2-6, the same six species remain stable in the sulfur-water system even as temperature changes but the stability regions for some phases change. The stability region for H₂S remains relatively constant, and that of S_(s) has a minor decrease in its predominance area with increasing temperature. Significant changes can be seen for the ion stability regions. With increasing temperature, the stability region of HS⁻ decreases, while that of S²⁻ increases and the stability area where SO₄²⁻ is dominant decreases while that of HSO₄⁻ increases. Indeed, bisulfate is increasingly stable with temperature and the protonation of the sulfate anion reduces “at temperature acidity”. This phenomenon is well known in the nickel laterite industry where excess acid must be added in part to account for the increased stability of bisulfate (Rubisov and Papangelakis, 1999). Chapter 6 further discusses how Ni and Cu sulfate will affect the “at temperature acidity”.

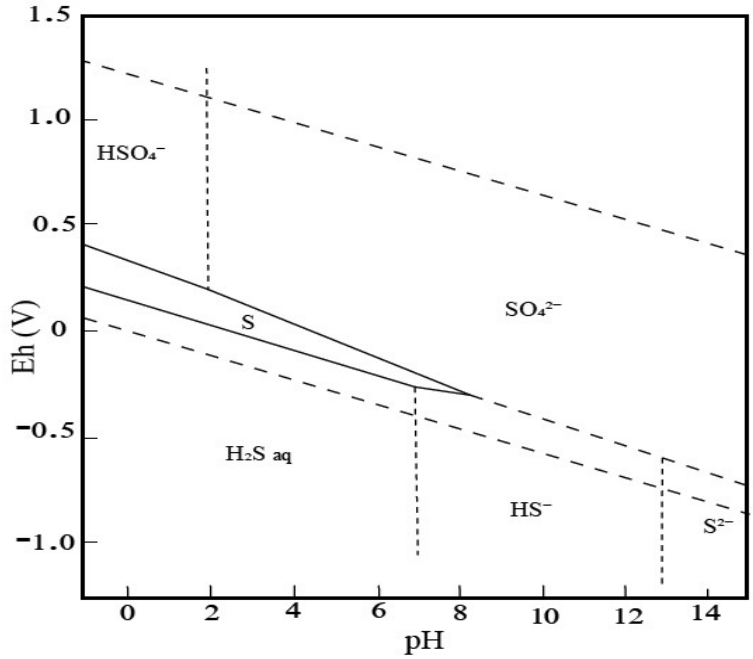


Figure 2-5: Eh-pH diagram for the S-H₂O system at 25°C and unit solute activity
(Redrawn from Biernat and Robins, 1969)

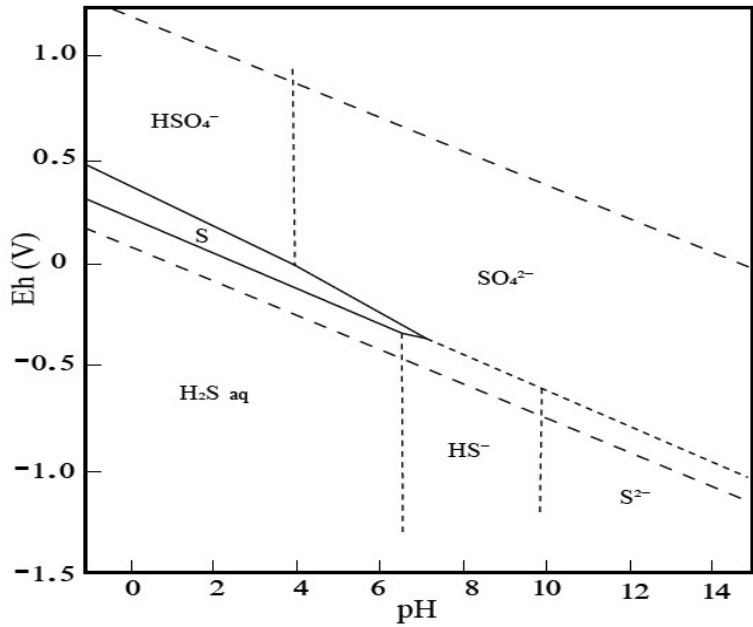


Figure 2-6: Eh-pH diagram for the S-H₂O system at 150°C and unit solute activity
(Redrawn from Biernat and Robins, 1969)

The Fe-H₂O and S-H₂O systems can be superimposed to predict the stable phases that exist in the Fe-S-H₂O system at different temperatures, as shown in Figure 2-7 and Figure 2-8. The new species that are formed from the superimposition are the solid phases FeS and FeS₂. This diagram does not consider sulfato-hydroxo complexes that form due to the lack of thermodynamic data for these complex phases. The high-temperature Eh-pH diagrams that include these phases have not been constructed or published. These are the species that lead to complex phases such as jarosite and basic ferric sulfate.

Finally, it is important to note that elemental sulfur is metastable as explained by Peters (1976) across a much broader Eh-pH region than is shown in Figures 2-5 and 2-6. This enables the production of elemental sulfur, rather than S(VI) species, under CESL and VALE conditions.

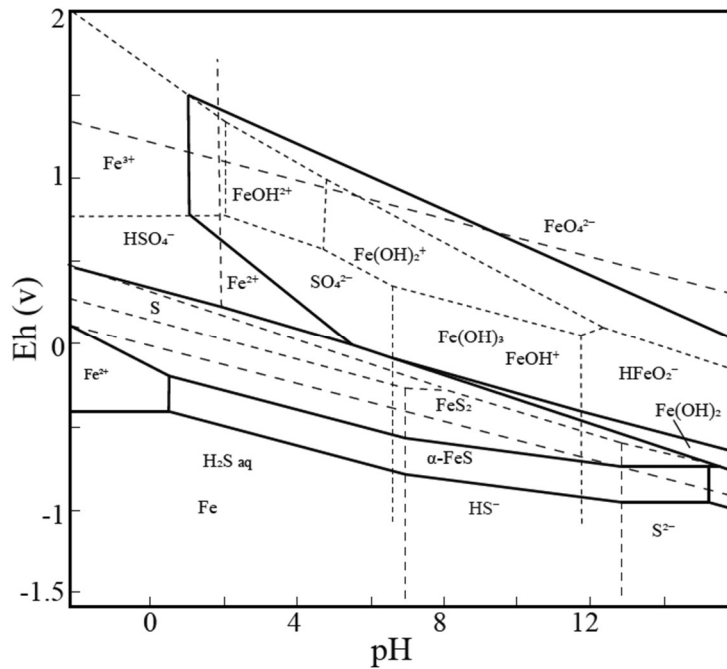


Figure 2-7: Metastable Eh-pH diagram for the Fe-H₂O-S system at 25°C and unit solute activity
(Redrawn from Biernat and Robins, 1972)

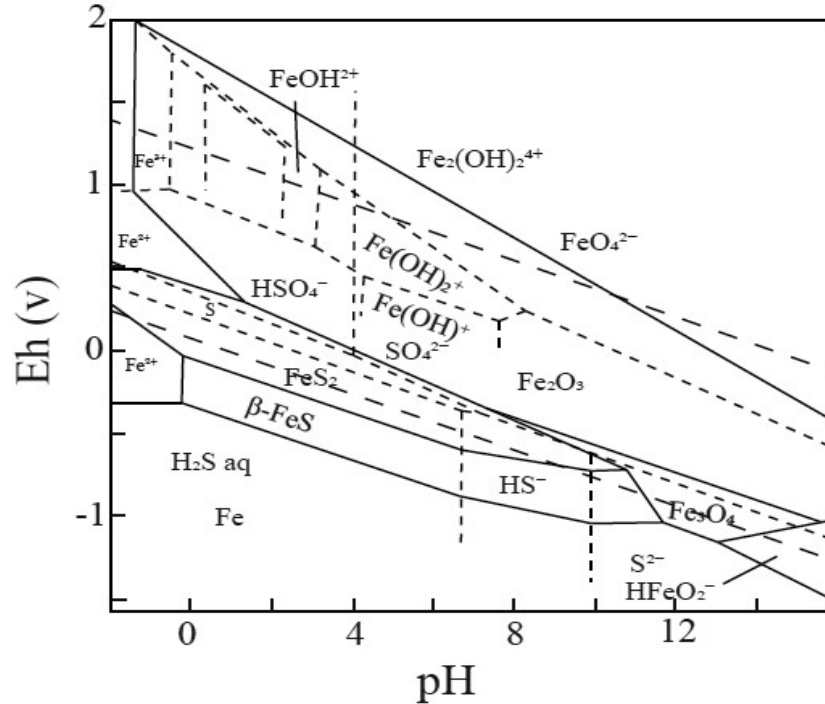


Figure 2-8: Eh-pH diagram for the Fe-H₂O-S system at 150°C and unit solute activity
 (Redrawn from Biernat and Robins, 1972)

Another useful method of presenting thermodynamic data related to the hydrolysis of metal species at elevated temperatures is the use of temperature/pH diagrams. At constant concentration, a linear relationship is obtained with intersections marking the temperatures of transformation between hydrates. Robins (1967) has constructed a number of such diagrams and the one for Fe(III)-H₂O is shown in Figure 2-9. The temperature-pH dependence of the particular phases when the Fe(III) is at unit molal concentration, with the effect of decreased molal concentrations indicated by the numeral in square brackets. By way of illustration, it can be seen that 0.2 molal solutions of pH 1.2 should precipitate FeOOH at 150°C.

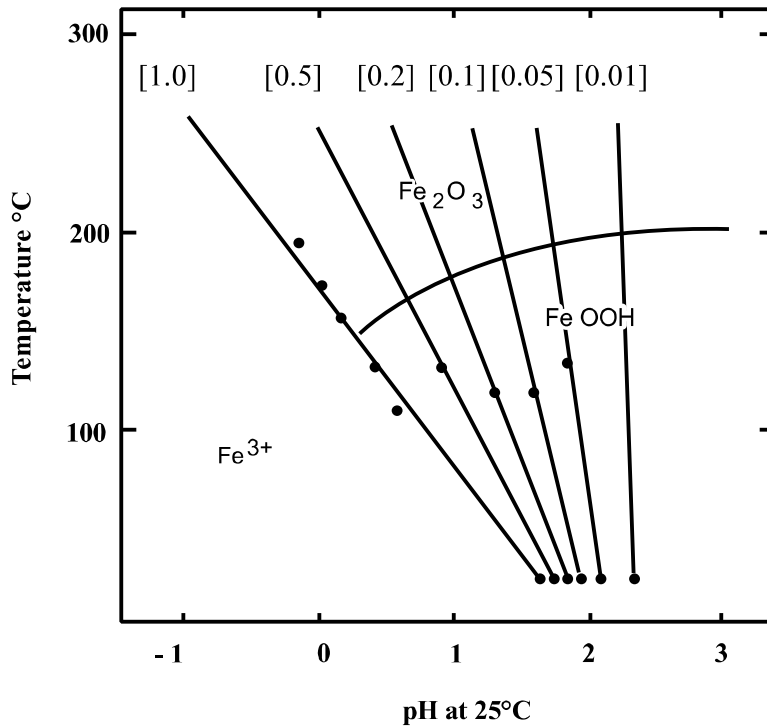


Figure 2-9: Experimental temperature versus pH diagram for Fe(III) - Fe₂O₃-H₂O system
(Robins, 1967)

The control of pH for selective precipitation of aqueous ions is often practiced as a separation technique in hydrometallurgy. In CESL and Vale processes, iron is removed from the solution by precipitating as hematite in the autoclaves. Monhemius (1977) presented several precipitation diagrams. A hydroxide precipitation diagram for iron, copper, and nickel at 298 K (25°C) was recalculated and plotted in Figure 2-10. The extent of precipitation is a function of both solution pH and metal ion concentration. For a given element, the metal ions remain in the solution for all the pH values to the left of the line and the metal ions precipitate out of solution as hydroxides for pH values to the right of the line. The ferric and copper precipitation lines are relatively distant, meaning that an effective Fe(III) and Cu(II) separation should be thermodynamically possible. For example, referring to Figure 2-10 at pH 2, Fe(III) solubility is approximately 3×10^{-3} M whereas Cu(II)

solubility is well above 1 M. Thus copper losses from solution and into Fe(III) hydroxide phases are more likely to be due to surface adsorption and/or solution occlusion within precipitating or forming Fe(III) solids, rather than co-precipitation. A similar argument can be made for Ni(II) as its line is even further from the Fe(III) line.

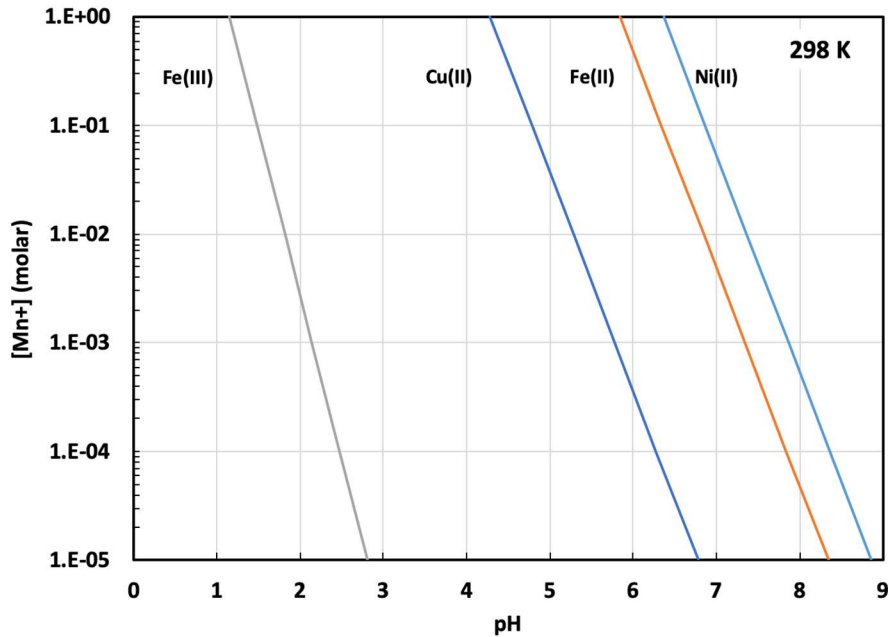


Figure 2-10: Hydroxide precipitation diagram for Fe(III), Cu(II), and Ni(II) at 25°C

The hydroxide precipitation diagram at 423 K (150°C) was calculated using the Monhemius method but with free energies calculated using the Criss-Cobble entropy correspondence principle and data collected from the NBS tables (Wagman, 1982) (with the exception of the data for Cu(OH)₂, which was taken from Beverskog and Puigdomenech, 1995). This diagram is presented in Figure 2-11. As discussed above with respect to Figures 2-3 and 2-4, the solubility of the various metal ions in equilibrium with their hydroxides decreases as temperature is increased. Thus, acidic solutions, which are generated during the pressure leaching of sulfides at 150°C, can effectively

reject Fe(III) as hydroxide phases (as metastable species). These phases would be expected to transform to more stable hematite given enough time.

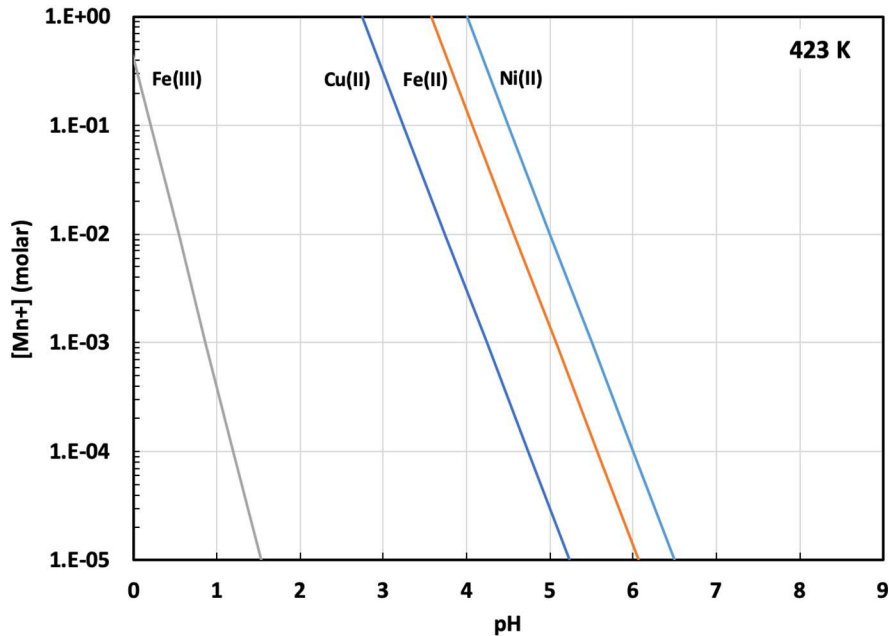


Figure 2-11: Hydroxide precipitation diagram for Fe(III), Cu(II), and Ni(II) at 150°C

2.4 Iron phases in leach residues

In 2011, Sahu and Asselin attempted a systematic characterization of leach residues generated during the processing of a variety of chalcopyrite concentrates under CESL conditions. Chemical analyses of the residues revealed the presence of 0.5 to 2.76% copper that accounts for 2 to 11% loss of copper during the processing of chalcopyrite. An ‘amorphous’ component was identified in the CESL residues by SEM/EDX, QXRPD/ Digestion & ICP-MS (inductively coupled plasma mass spectroscopy), Electron microprobe and Sequential extraction. This component was assumed

to be 'ferrihydrite.' In thirteen different residue samples, the ferrihydrite content was found to vary between 2 and 46%, and it had 5-times more Cu associated with it (Sahu and Asselin, 2011).

It is important to describe ferrihydrite and closely related schwertmannite. Ferrihydrite has been reviewed by Jambor and Dutrizac (2008) and is a disordered and metastable Fe(III) oxyhydroxide mineral approximated by $5\text{Fe}_2\text{O}_3 \cdot 9\text{H}_2\text{O}$, although the structure is excessively hydrous. The term 'ferrihydrite' most widely used in recent works, actually refers to a range of similar phases. Ferrihydrite is generally classified based on the number of X-ray diffraction lines which the precipitate yields. Hence, "two-line ferrihydrite" describes materials exhibiting little crystallinity and "six-line ferrihydrite" characterizes precipitates that are better crystallized.

The small grain size and poor crystallinity have so far prevented the direct determination of the crystal structure of ferrihydrite. It has been an object of many studies, and several structures have been proposed (Jambor and Dutrizac, 1998). The model of Towe and Bradley (1967) involves a defective hematite structure based on a hexagonal close-packed array of anions with vacant Fe(III) ions and a considerable amount of water. The Fe(III) ions are distributed randomly over the interstices, and there is more OH^- and H_2O and less Fe(III) in ferrihydrite than in hematite, i.e., there is a lower Fe/O atomic ratio ($<2/3$).

Further refinements of the structure were proposed by Drits et al. (1993) based on the agreement between experimental and simulated XRD data and by Manceau and Drits (1993) based on the structural data from EXAFS spectra. According to these refinements, 6-line ferrihydrite contains three intergrown structural components as shown in Figure 2-12 (Jansen et al., 2002).

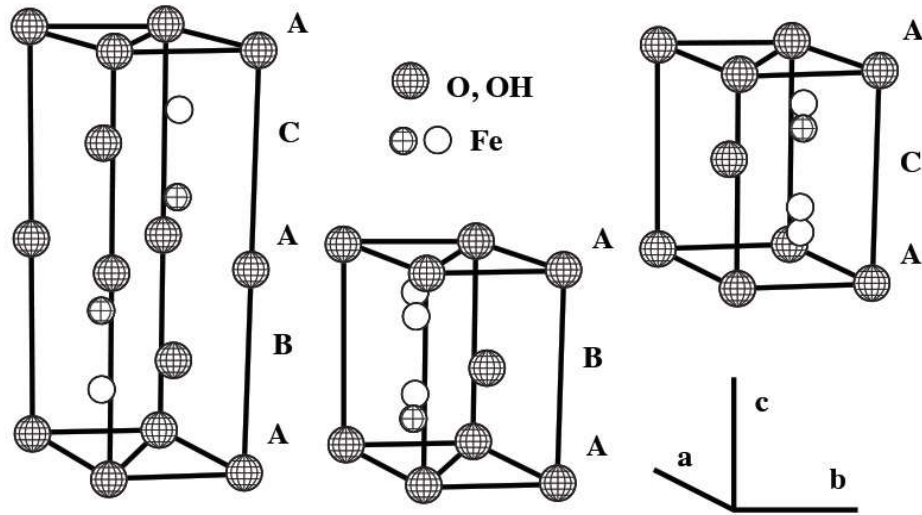


Figure 2-12: Model of the two structural components of ferrihydrite

(a) defect-free ABACA phase; (b) and (c) two defective ABA and ACA phases. Open circles represent vacant Fe sites (Jansen et al., 2002)

The low-equilibrium solubility of the Fe (III) ion dictates hydrolysis at pH ~3 to form ferrihydrite. If hydrolysis proceeds rapidly, the gelatinous 2-line ferrihydrite will precipitate; however, with slower hydrolysis, the more crystalline and larger 6-line ferrihydrite will form. The rapid coalescence of primary ferrihydrite crystals to form aggregates (up to 100 μm in size) creates both internal and interparticular micro-porosity; surface areas are typically 200 m^2/g . Hence ferrihydrite is known to absorb a wide range of inorganic and organic species (Jambor and Dutrizac, 1998). Ferrihydrite is also metastable and transforms into more crystalline products of goethite ($\alpha\text{-FeOOH}$) and hematite ($\alpha\text{-Fe}_2\text{O}_3$), mostly affected by changes in pH, temperature and water activity.

The sulfate-containing schwertmannite ($\text{Fe}_{16}\text{O}_{16}(\text{SO}_4)_2(\text{OH})_{12}$) is now regarded to be similar in structure, occurrence, and formation to ferrihydrite (Loan et al., 2006). Interestingly,

schwertmannite has a distinct and different morphology to ferrihydrite, forming hedge-hog-type aggregates with nano-dimension whiskers, although the two phases have been found to precipitate together (Loan et al., 2006). The historical difficulties in characterizing ferrihydrite and schwertmannite produced references to a variety of iron phases, unfortunately, including ferric hydroxide $[\text{Fe}(\text{OH})_3]$. Loan et al. (2002) suggested that the considerable hydrometallurgical literature documenting the formation of $\text{Fe}(\text{OH})_3$ under various pseudonyms refers to ferrihydrite (2- or 6-line), or alternatively schwertmannite. It is to be noted that $[\text{Fe}(\text{OH})_3]$ is crystalline.

Loan et al. (2006) explained that hydrometallurgical precipitation involving ferrihydrite or goethite formation is a complex and intricate process, as it involves the nucleation and aggregation of exceptionally small primary crystallites to significantly larger particles. Chen et al. (2006) performed the characterization of the iron-rich residues generated during the pressure leaching of Voisey's Bay nickel sulfide concentrate generated from a batch and mini-pilot testing using XRPD, microprobe and SEM/EDX. It was concluded that the leach residues consisted predominantly of hematite and elemental sulfur, with minor amounts of goethite. The elemental sulfur is present as large spheroids and irregular masses, commonly agglomerated with tiny particles of hematite and goethite. The hematite and goethite occur as thin spheroids and larger bubble-like particles. Moreover, although the solutions contained up to 15 g/L sodium, Na-jarosite particles were only rarely detected in a few of the continuous leach residues. The hematite 'seed' produced during the early stages of leaching was assumed to play a key role in promoting the precipitation of hematite, at the expense of Na-jarosite.

Chen and Dutrizac (2009) studied the factors affecting the precipitation of hematite rather than jarosite in nickel sulfide concentrates leached under autoclave conditions and concluded the following:

- i. Increased retention times (5-6 h) at 150°C resulted in increased precipitation of hematite,
- ii. Increased temperature promoted precipitation and improved crystallinity of hematite,
- iii. Increased chloride concentration slightly decreased the amount of hematite precipitated but did not affect its composition,
- iv. Increased H₂SO₄ concentrations dramatically reduced the amount of precipitate, but had no effect on the composition of the hematite formed,
- v. Increased concentrations of Fe(SO₄)_{1.5} augmented the amount of hematite precipitated but did not affect its composition,
- vi. Increased NiSO₄ concentrations resulted in an increased precipitate, but the composition remained constant,
- vii. Even modest concentrations of Na₂SO₄ resulted in extensive precipitation of sodium jarosite,
- viii. The presence of hematite seed suppressed the jarosite precipitation,
- ix. Autoclave leach residue which contains significant amounts of hematite is an effective seed material for hematite precipitation, and
- x. Regardless of the experimental conditions, the hematite precipitates were poorly crystallized.

A summary of the work by various researchers and the comparison of the test conditions and the various parameters is given in Table 2-1. The discussion highlights the complexity of iron precipitation in hydrometallurgy and the need to further understand the parameters (temperature, pressure, seeding, retention time, mixing, aging) affecting the precipitation of ferrihydrite, and to be able to identify and quantify the ‘amorphous’ phases in the medium temperature Cu-Ni leaching system.

Table 2-1: Summary of the studies characterizing iron residues precipitated at T > 100°C

	Chen et al., 2006	Dutrizac and Chen, 2009	Sahu and Asselin, 2011	Žic et al., 2011	Javed and Asselin, 2015
Study type	Batch and mini-pilot	Controlled lab scale, reagents	Industrial, various concentration	Controlled lab scale, reagent	Controlled lab scale, reagent, reagent
Background	H ₂ SO ₄	H ₂ SO ₄	H ₂ SO ₄	NaOH	H ₂ SO ₄
Crystallinity	Not quantified	Poor, not quantified	Very poor, quantified	Varying (amorphous to crystalline)	Varying, quantified
Effect of Na	No effect found	Extensive jarosite precipitation	Not known	Not tested	Tested along with other impurities
Effect of T	150°C, not tested	110-180°C improves crystallinity	150-205°C, none apparent	160°C, not tested	150-220°C, tested and quantified
Effect of time	Increases mass of precipitate	Increases mass of precipitate	None apparent	Ferrihydrite at the beginning (1h) then hematite	Hematite and amorphous (up to 2h) then hematite
Seed	Changes in morphology	Effective for fast hematite precipitation	Not tested	Not tested	Effective for fast hematite precipitation
[SO ₄] with hematite	5-7%	5-7%	Not measured	None, but altered morphology	5-9%
Effect of surfactant	Not mentioned	Not tested	Unknown	Ammonium Amidosulfonate suppressed hematite formation	Not tested
Increasing free acid	Not tested	Reduces precipitate mass otherwise no effect	Appears to reduce the amount of amorphous phase	Not tested	Increases hematite yield and reduces the amorphous phase
Effect of chloride	Not tested	The slight decrease in hematite yield	None	Not tested	Same effect as free acid

2.5 Crystallization theory of precipitation

According to crystallization literature (Dirksen and Ring, 1991; Mullin, 1993; Sohnel and Garside, 1992), precipitation is defined as “reactive crystallization,” to emphasize the product of the process. Some key characteristics of precipitation are: precipitates are usually highly insoluble, high supersaturation is associated with precipitation, supersaturation is generated by chemical reaction(s), the rate of primary nucleation is usually fast, and many fine particles develop that readily form aggregates.

Precipitation occurs when the concentration of a solute in solution exceeds the solubility value, i.e., the solution is supersaturated. Supersaturation can be considered as the driving force, which causes the crystallization of a species from an aqueous solution. Supersaturation may be defined as the concentration of a solute exceeding the saturation concentration (equilibrium concentration). The degree of supersaturation is represented by saturation ratio, S (Equation 2-4).

$$S = \frac{\alpha}{\alpha^*} \quad 2-4$$

Where S = saturation ratio, α = activity of the solute, α^* = activity of the saturated solution

Precipitation may be defined as the production of a crystal generated from an irreversible chemical reaction between reactants present in a system. According to thermodynamics, precipitation will occur when the reaction is spontaneous, that is the free energy change is < 0 as shown in Equation 2-5.

$$\Delta G = -RT \ln \left(\frac{\alpha}{\alpha^*} \right) = -RT \ln (S) < 0 \quad 2-5$$

The saturation ratio S may be approximated as Equation 2-6.:

$$S = \frac{C}{C^*} = \frac{m}{m^*} \quad 2-6$$

Where C = solute concentration (mol/L of solution), C^* = solute concentration at equilibrium for the given temperature and pressure (mol/L of solution), and m represents the concentration in terms of molality (mol/Kg of solvent).

Using the solubility product and assuming activities are equal to concentrations (Equation 2-7 to 2-9):



$$K_{SP} = [A^+]_{eq} [B^-]_{eq} \quad 2-8$$

$$S = \frac{[A^+][B^-]}{K_{SP}} \quad 2-9$$

Where K_{sp} = the solubility product of the precipitate, AB .

To form a solid, the state of supersaturation must be achieved as well as the availability of microscopic bodies or nuclei (seed or embryos) to act as centers of crystallization. Precipitation involves several kinetic processes such as the creation of supersaturation, followed by primary nucleation and crystal growth. The secondary changes such as recrystallization, aging, aggregation, and secondary nucleation overlap crystal growth as shown in Figure 2-13. The extent

to which these processes occur and their relative rates dictate the resultant morphologies and particle size distribution of the precipitates.

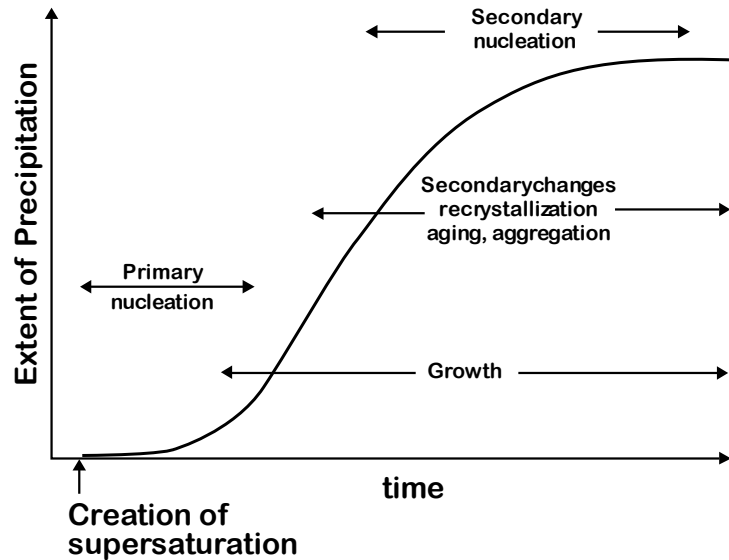


Figure 2-13: Kinetic processes involved in precipitation

(Sohnel and Garside, 1992)

The process of nucleation can be divided into three main categories: (i) primary homogeneous, (ii) primary heterogeneous nucleation, and (iii) secondary nucleation as shown in Figure 2-14.

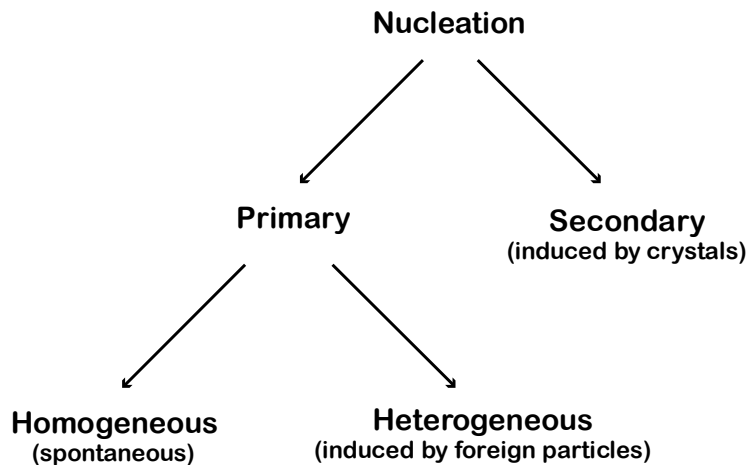
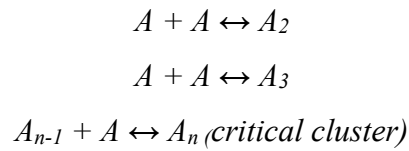


Figure 2-14: Classification of the nucleation mechanism

Primary homogeneous nucleation occurs spontaneously in the absence of a solid interface in a supersaturated solution. As the concentration of a solution containing ionized species increases, ionization decreases, and solvated ion pairs appear in solution to form clusters of solute molecules or liquid crystals with the same crystal structure as the solid. It was proposed by Mullin (1993), that a stable nucleus could arise from a sequence of bimolecular additions according to the scheme:



Further additions of molecules to the critical cluster would result in nucleation and subsequent growth of the nucleus. The nucleus is thermodynamically unstable at low supersaturations; therefore, this process occurs in regions of high supersaturation. High supersaturation results in the formation of poorly crystallized ultrafine particles with a high degree of aggregation and a high chance of impurity uptake. The nucleation rate J is defined as the number of nuclei formed per unit time per unit volume can be represented by Equation 2-10.

$$J = A \exp \left[- \left(\frac{\Delta G}{kT} \right) \right] \tag{2-10}$$

As indicated earlier (Equation 2.5), ΔG is related to the saturation ratio S , and the nucleation rate J is dependent on supersaturation. This is shown in Figure 2-15.

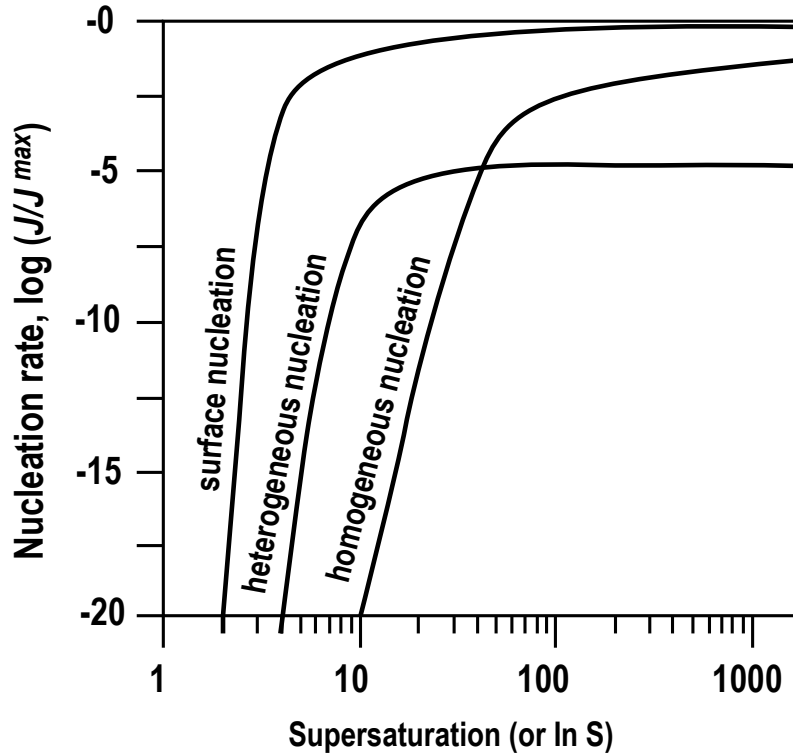


Figure 2-15: Generalized nucleation diagram describing the characteristic differences between homogeneous, heterogeneous and surface nucleation as a function of supersaturation
(Dirksen and Ring, 1991)

Primary heterogeneous nucleation is induced by the presence of foreign particles which serve as a “catalyst” lowering the required supersaturation to a level lower than that required for homogeneous nucleation (see Figure 2-15 and Figure 2-15). The extent of precipitation by heterogeneous nucleation mechanism is limited by the number of foreign particles (hetero-nuclei) that are present. Secondary nucleation results from the presence of “solute” particles in solution with the ones being precipitated and have been classified into three categories: apparent (the nuclei are introduced into the system due to the fragmentation of produced crystals), true or surface (seed crystals are added to the solution), and contact (collisions between crystals or between crystals and

the crystallizer). In general, for substances that are sparingly soluble, secondary nucleation may occur to a small extent or does not take place at all (Sohnel and Garside, 1992).

Crystal growth involves the integration of a solute species (so-called growth unit) into a growing crystal structure on two types of surface sites called ‘steps’ and ‘kinks.’ The crystal growth occurs through a series of stages: (i) interfacial transport of solute, (ii) adsorption on the particle surface, (iii) surface diffusion, (iv) attachment to a step, (v) diffusion along a step, (vi) integration into the crystal at a kink site (surface reaction), and (vii) de-solvation and/or diffusion of solvent molecules away from the surface. These stages are shown in Figure 2-16.

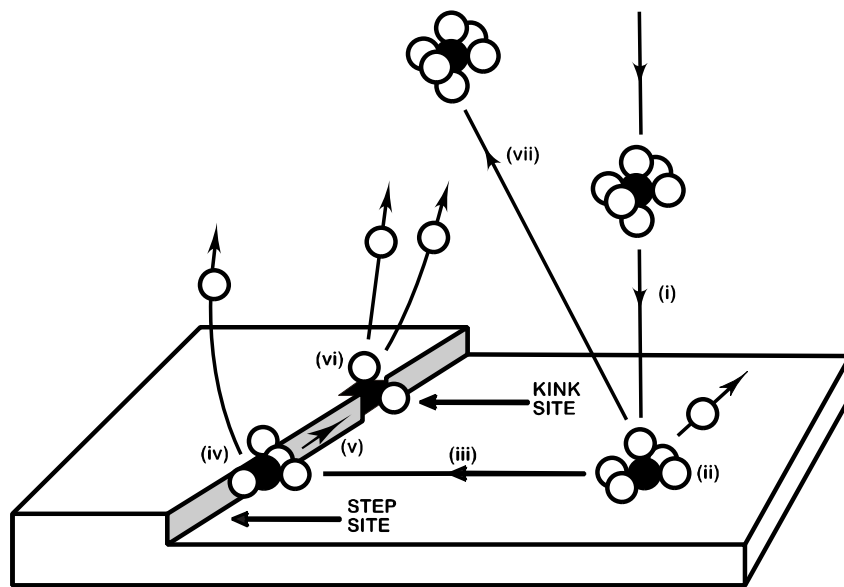


Figure 2-16: Crystal growth mechanism by movement of the solvated solute molecule
(Dirksen and Ring, 1991)

When the de-solvation process is complete, and the enthalpy of crystallization liberated, the solute molecule becomes part of a crystal (Dirksen and Ring, 1991). Many physical processes control the rate of crystal growth. The rate-limiting step is system-dependent (e.g., temperature, mixing rate,

reactor types), and can vary from diffusion-controlled growth to chemical reaction controlled (if a chemical reaction is used to induce supersaturation).

In addition to nucleation rate J , the growth rate G is a function of supersaturation as well. The degrees of dependency of G and J on supersaturation are different as shown in Figure 2-17. Two distinctly different precipitation regimes are defined based on S (Demopoulos, 1993, 2009). For $S < S_{hom}^*$, growth dominates, and well-grown crystals are expected to produce if the seed is used. On the other hand, for $S > S_{hom}^*$, homogeneous nucleation prevails, thus resulting in the production of ultrafine particles. In the region where $S \gg S_{hom}^*$, growth is not expected even in the presence of seed.

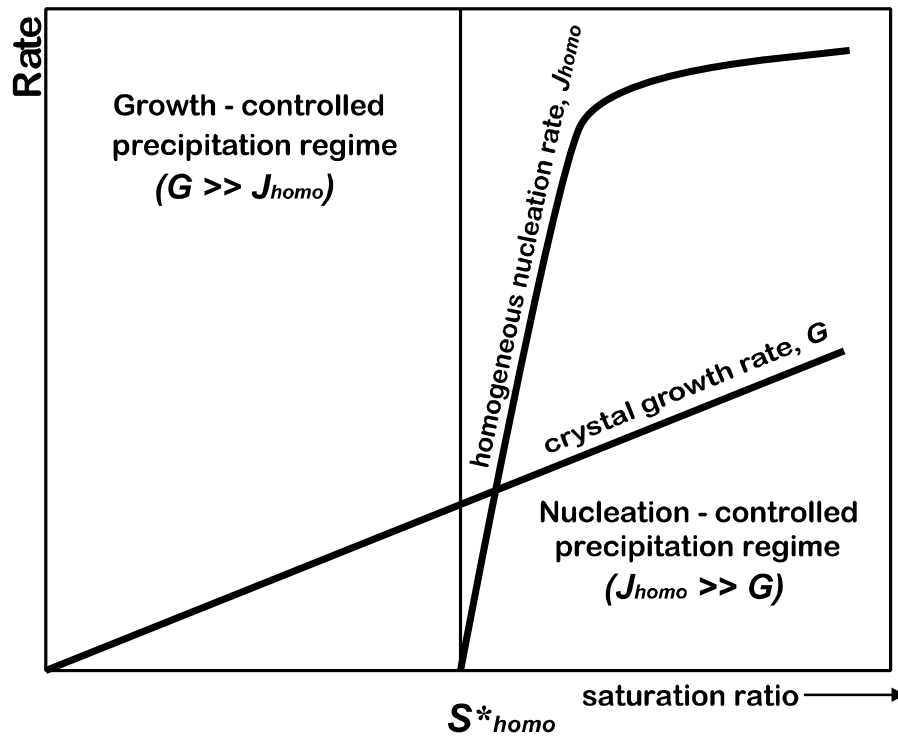


Figure 2-17: Separation of precipitation regimes based on rate versus saturation ratio relationships (Demopoulos, 1993, 2009)

Stranski's rule states that if the homogeneous nucleation prevails, the least stable or the so-called 'metastable phase' nucleates first (Blesa and Matijevic, 1989). The nucleation rate of metastable phase J_{met} can be expressed in terms of saturation ratio in this general form as shown by the Equation 2-11 (Nyvlt, 1995).

$$J_{met} = \Omega_{met} \left[\frac{-C_{met}}{(\ln S_{met})^2} \right] \quad 2-11$$

Where Ω is the attachment frequency (1/second), energetical term C relates to work of formation of the critical nucleus of the corresponding phase and J is the nucleation rate (particles /m²/s).

It is believed that fewer restrictions are required for a successful attachment in the metastable phase such that $\Omega_{met} > \Omega_{st}$ (wherein subscripts *met* denote metastable and *st* denotes stable phase). The interfacial energy requirements are also less stringent for the metastable phase, $C_{met} < C_{st}$. The exponential term in Equation 2.11 diminishes when precipitation occurs at high supersaturation because the saturation ratio S and the energy C oppose each other. The attachment frequency thus dominates the nucleation rate. The metastable phase becomes kinetically favorable in the region of high supersaturation, where homogeneous nucleation prevails as shown in Figure 2-18.

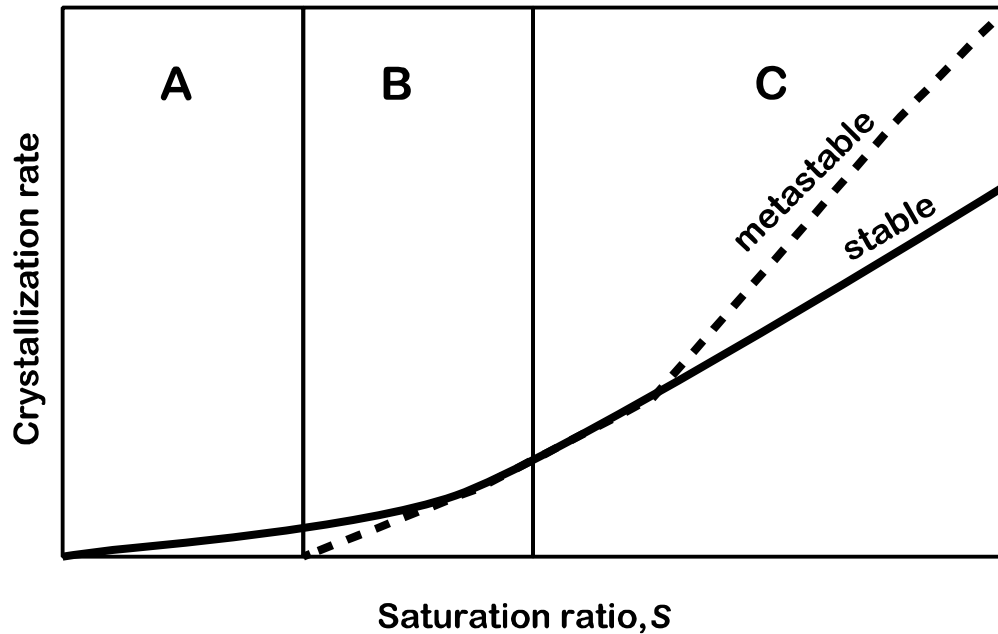
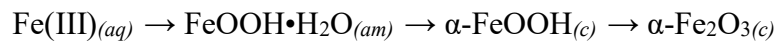


Figure 2-18: Crystallization rate of the metastable and stable phase as a function of saturation ratio
(Nyvlt, 1995)

The hydrolysis of inorganic Fe(III) salts at initially high supersaturation (e.g. 1.0 M Fe(NO₃)₃), which begins with the formation of a least stable amorphous phase (FeOOH·H₂O) that transforms to a more stable intermediate crystal phase(α-FeOOH) and finally to a most stable crystal phase (α-Fe₂O₃) is a good manifestation of Stranski's rule (Blesa and Matijevic, 1989), and is illustrated as follows:



Such a transformation process follows the dissolution-recrystallization mechanism as shown in Figure 2-19 (Blesa and Matijevic, 1989).

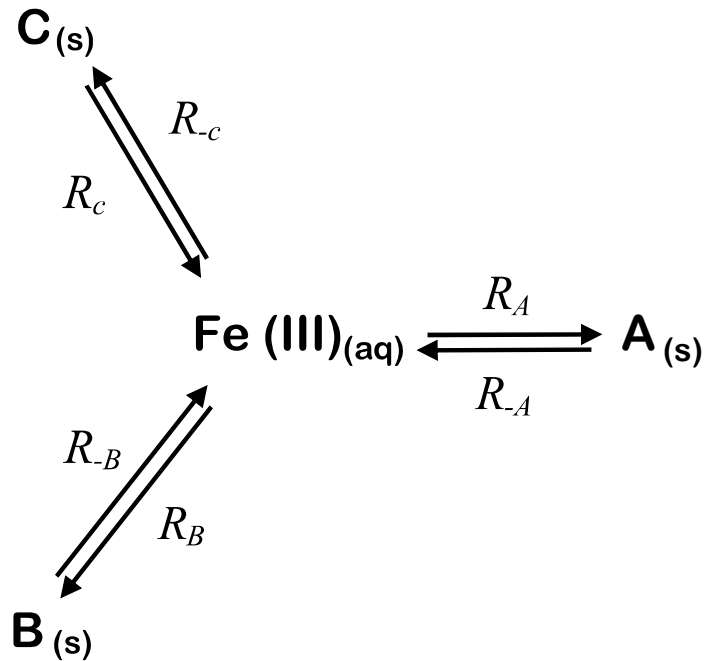
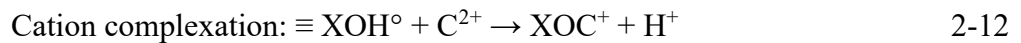


Figure 2-19: Dissolution-recrystallization process for phase transformation
(Blesa and Matijevic, 1989)

According to Stranski's rule the rate of initial precipitation of various phases A , B , and C follow the order of the solubilities $C_{A, \text{aq}} > C_{B, \text{aq}} > C_{C, \text{aq}}$ (i.e., $R_A > R_B > R_C$) (Blesa and Matijevic, 1989). The least stable phase A serves as a reservoir which slowly releases $\text{Fe(III)}_{\text{aq}}$ to maintain a constant Fe(III) concentration, $C_{A, \text{aq}}$ (Figure 2-19). And once the induction period related to the nucleation of phase B is completed, the growth rate of B is limited by the dissolution rate of phase A (R_{-A}); similar trend applies to the transformation from phase B to C . The rate of formation of crystalline phases is generally much faster at high temperatures, and particularly in acidic media. If an increase in R_B is substantial as compared to R_A , less amount of amorphous phase would be generated, and therefore noticeable enhancement of crystallinity is normally achieved with an increase in temperature.

Precipitation in uncontrolled batch reactors results in an extensive aggregation due to initial high supersaturation condition. The high supersaturation triggers precipitation via homogeneous nucleation, which generates many fine particles and as their population density increases, aggregation is favored. Aggregation becomes the main cause of growth in precipitation systems which are dominated by homogeneous nucleation, and it can be prevented using surfactants. The selection of surfactant, either cationic, anionic, or nonionic, depends on the particle-solution interface properties (Dzombak and Morel, 1990).

In addition to surfactants, other soluble species might also adsorb on the surface of the precipitating solid and interfere with the precipitation process. In the aqueous precipitation of inorganic compounds, hydration of surface cations followed by hydrolysis leads to the formation of a hydroxylated surface $\equiv\text{XOH}^\circ$ (oxide surface site), and ultimately to surface complexation reactions involving cations and/or anions as shown in Equation 2-12 and 2-13 (Dzombak and Morel, 1990):



The surface complexes in many cases are inner sphere complexes involving covalent bonding. Because of such adsorption reactions, the particle growth mode is altered, and impurities are incorporated into the solid product. As deduced from these adsorption reactions, cation sorption is favored at high pH while anion sorption is favored at low pH. The chemisorption of sulfate (anion) on hematite appears to follow the surface complexation reaction as shown in Equation 2-13.

In order to produce well grown and stable crystals, precipitation should be carried out under low supersaturation ($S < S_{homo}^*$), and in the presence of seed as shown in Figure 2-17. Under this condition, the consequences of Stranski's rule are avoided. By keeping low supersaturation (low S), the crystallization temperature can be effectively reduced. This has been clearly demonstrated in the cases of hematite precipitation from chloride solution at temperatures less than 100°C in the presence of hematite seed (Dutrizac and Riveros, 1999).

The matrix anion and co-existing impurity elements could be incorporated into the precipitate, lowering its purity. The different mechanisms of impurity incorporation into the precipitate, are co-precipitation as a distinct phase, substitution or adsorption. Adsorptive incorporation of impurities as shown in Equation 2-12 and 2-13, can be suppressed by reducing the specific surface area via growth of large and smooth particles, and thereby enhancing the crystallinity of the precipitate, simultaneously preventing aggregation (Demopoulos, 1993; Mullin, 1993; Sohnel and Garside, 1992).

2.6 Crystal growth modification in iron precipitation

Iron oxide particles of various morphologies were prepared by the forced hydrolysis of ferric chloride solutions with careful control of reaction conditions (Bailey et al., 1993; Matijević and Scheiner, 1978; Sugimoto and Muramatsu, 1996). Micron-sized spherical, cubic or ellipsoidal hematite particles formed at moderate concentrations of $FeCl_3$, while rhombohedral hematite single-crystals, of nanometer dimensions, formed in solutions with low $FeCl_3$ concentrations of <0.02 M and pH of about 1.5 (Kan et al., 1996). In these systems, the presence of phosphate even

in minor amounts has been shown to have a strong influence on the morphology of the resultant hematite particles (Morales et al., 1992; Ocaña et al., 1995). This change in morphology is a result of the binding of phosphate to certain crystal faces, thus limiting crystal growth. The crystal faces concerned were identified by Jones et al. (2003).

Reeves and Mann (1991) studied the effect of organic phosphonate-based additives on the forced hydrolysis of ferric chloride solutions. Jones et al. (2003) investigated the potential for morphological control of iron oxide nanoparticles by employing various phosphonate-based molecules such as $\text{CH}_2(\text{PO}_3\text{H}_2)_2$, $\text{C}_2\text{H}_4(\text{P}_3\text{OH}_2)_2$, $\text{N}[\text{CH}_2\text{PO}(\text{OH}_2)]_3$ and $\text{C}_{12}\text{H}_{32}\text{N}_4\text{O}_{12}\text{P}_4$. The action of these additives appeared to be very specific, with the phosphonates binding only to one of the crystal faces. The particles were uniform single crystals of about 100 nm. The phosphonate additives were shown to be powerful growth modifiers; even at very low additive concentrations their effect on hematite crystallization was evident.

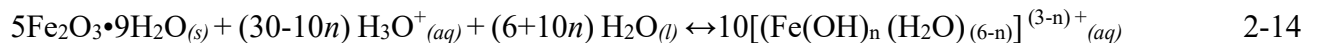
2.7 Transformation of ferrihydrite

Ferrihydrite is a metastable amorphous mineral and transforms into iron oxides such as goethite, hematite, and magnetite. The rate of transformation of ferrihydrite to hematite and goethite is a function of time, temperature, and pH (Cornell and Schwertmann, 1996). Hematite is formed by the initial rearrangement and dehydration within ferrihydrite aggregates while goethite formation occurs by re-precipitation of Fe(III) ions dissolved from ferrihydrite. A first long-term transformation assessment of ferrihydrite was performed by Schwertmann and Murad (1983). It was found that storing ferrihydrite in aqueous solution at 24°C for almost 3 years at different pH

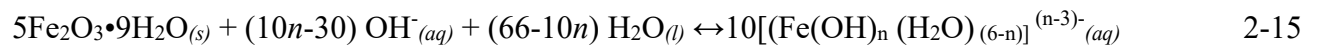
values resulted in the formation of goethite and/or hematite. Samples taken at different time intervals were subjected to oxalate treatment (the oxalate treatment procedure is reviewed in section 4.4). The proportion of oxalate-soluble Fe (Fe_o) with respect to total Fe (Fe_t) in these samples was used as an indicator of the degree of transformation of ferrihydrite to goethite and/or hematite i.e. the higher Fe_o , the lower the amount of transformation. The rate of transformation decreased with a decrease in pH as shown in Figure 2-20. For example, it took about 900 days to achieve 80% conversion of ferrihydrite at pH 2.5, whereas 98% conversion was achieved at pH 6 in the same timeframe. Hematite was favored in conditions where the Fe(III) equilibrium solubility with ferrihydrite was minimum, and goethite was favored in conditions when Fe(III) solubility was maximum.

Cudennec and Lecerf (2006) revised the mechanism of ferrihydrite transformation to hematite and goethite. Taking into consideration the work performed by Schwertmann and Murad (1983), they proposed the following scheme for ferrihydrite dissolution (Reactions 2-1 and 2-1):

Acidic solutions: $0 \leq n < 3$



Alkaline solutions: $3 < n \leq 6$



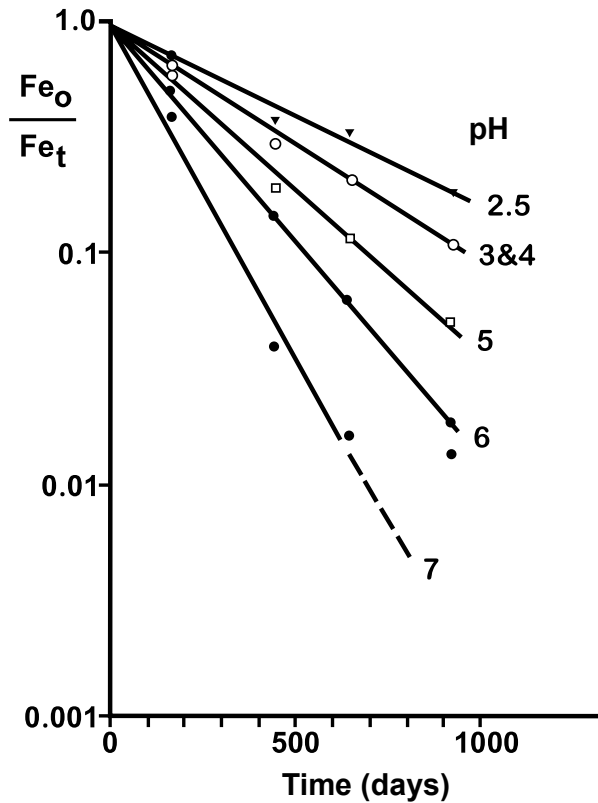
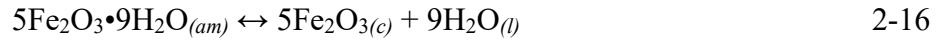


Figure 2-20: First-order reaction plot for the transformation of ferrihydrite at various pH values plotted for the ratio of Fe_o (oxalate soluble Fe) to Fe_t (total iron) versus time
(Schwertmann and Murad, 1983)

At pH higher than 7, iron is dissolved under the complex anions, $Fe(OH)_4(H_2O)_2^-$ ($n = 4$), $Fe(OH)_5(H_2O)^{2-}$ ($n = 5$) and eventually at very alkaline pH, under $Fe(OH)_6^{3-}$ ($n = 6$). In these conditions, the solubility of iron increases but is very low, and therefore goethite is obtained.

At pH around 7, H_3O^+ and OH^- concentrations are too weak for dissolving enough ferrihydrite for the formation of goethite through the solution. Therefore, the transformation takes place mainly in the solid-state, giving rise to hematite in solutions that present the minimum of solubility for ferrihydrite. At this stage, the main dissolved entity is the neutral complex $Fe(OH)_3(H_2O)_3$, but its

concentration is too weak, and therefore transformation in the solid-state is dominant, and hematite is obtained according to the scheme as shown in Reaction 2-16.



Cudennec and Lecerf (2006), also suggested that the dehydration of ferrihydrite $\text{Fe}_5\text{O}_7(\text{OH}) \cdot 4\text{H}_2\text{O}$ gives rise to $\text{Fe}_5\text{O}_{7.5}$ equivalent to Fe_2O_3 , hematite, and that the structure of ferrihydrite is contracted by 2% during its transformation. This fact is in favor of the formula chosen for ferrihydrite, $\text{Fe}_5\text{O}_7(\text{OH}) \cdot 4\text{H}_2\text{O}$, even if the O/OH rate is not necessarily fixed and can probably vary around a value near seven, and therefore, ferrihydrite is rather a hydrated oxide than a hydroxide.

Schwartzman and Murad (1983), were the first to suggest that high temperature favors the formation of hematite. Later Liu et al. (2010, 2007) carried out the transformation experiments of ferrihydrite in the presence of ferrous ion and with varying temperature (from 25°C to 100°C). They demonstrated that hematite is formed at higher temperatures (~100°C) while lower temperatures (40-60°C) are favorable to the dissolution and re-precipitation mechanism and the formation of goethite. There are several studies in the literature on complicated systems which contain other ions in solution or the iron oxyhydroxides structure. The results of the transformation reactions can be influenced by cations like Pb^{2+} (Vu et al., 2010), Cd^{2+} (Lin et al., 2003), Zn^{2+} (Jambor and Dutrizac, 1998), Mn^{2+} (Cornell and Giovanoli, 1987), Ni^{2+} (Punnoose et al., 2004), Al^{3+} (Jentsch and Penn, 2006) or anions like Cl^- (Liu et al., 2010), CO_3^{2-} (Hiemstra et al., 2009), SO_4^{2-} (Davidson et al., 2008) and PO_4^{3-} (Shaw et al., 2005). The substitution of these ions can lead to changes in the iron oxyhydroxide structure, and the presence of these ions in the structure

can catalyze or inhibit the transformation of ferrihydrite to a specific end-product under appropriate conditions.

Yee et al. (2006), studied the transformation of ferrihydrite using synchrotron-based diffraction technique with a Fe(II)/Fe(III) ratio that leads to pure goethite. They found that the activation energy for goethite formation was 56 ± 4 kJ/mol. Comparing this with the activation energy in the absence of ferrous ion indicates that Fe(II) acts as a catalyst and decreases the activation energy barrier by approximately 38 kJ/mol. It was also suggested that depending on Fe(II)/Fe(III) ratio and reaction time, the transformation product can be magnetite. Vu et al. (2010), showed that the presence of lead in the ferrihydrite structure at alkaline pH 13 enhanced the formation of hematite and reduced the induction time by 20-30%. It was also found that at this pH, goethite is an intermediate phase. Shaw et al. (2005), studied the effect of phosphate on ferrihydrite transformation to goethite and hematite under alkaline conditions using synchrotron diffraction. They found that the apparent activation energy of nucleation at pH 13.7 of the phosphate doped ferrihydrite system was three times higher than the activation energy without phosphate and that the phosphate slowed the ferrihydrite transformation to goethite.

Johnston and Lewis (1983), studied the transformation of ferrihydrite performed at pH (~1) and 92°C and found that ferrihydrite particles coalesced to form an extended ferrihydrite type structure which was similar to incompletely ordered hematite and acted as a nucleation site for hematite. The least stable phase nucleates first as explained by 'Ostwald' rule (Jaroslav, 2006). This also explains the higher solubility product of ferrihydrite compared to the more crystalline phases. The rates of formation of goethite and hematite are competitive and happen via solution transformation

of ferrihydrite (Schwertmann et al., 1999; Schwertmann and Cornell, 2000; Torrent and Guzman, 1982). Goethite is usually formed at high and low pH values, where the solubility of ferrihydrite is pronounced. The restricted solubility and aggregation results in hematite formation. The formation of goethite at high pH (pH:10-12) occurs upon dissolution of ferrihydrite and in the presence of favorable growth units ($\text{Fe}(\text{OH})_4^-$), (Cornell and Giovanoli, 1986; Knight and Sylva, 1974). Both goethite and hematite have also been demonstrated to nucleate through the dissolution of the ferrihydrite at $\text{pH} < 2$ (Atkinson et al., 1968; Van Der Woude et al., 1983). Hsu and Wang (1980) observed hematite to nucleate from low iron concentration solutions but at much lower pH and elevated temperatures.

2.8 Solubility of ferrihydrite, goethite, and hematite

The solubility of a solid is determined by the free energy of dissolution which is the opposite of crystallization. Except at extreme values of pH, ferrihydrite and goethite/hematite have a very low solubility in solution. The extent to which these phases dissolve is defined by the solubility product (K_{sp}). The solubility product represents the thermodynamic equilibrium between the solid and the concentration of its ions in a saturated solution. The solubility product of ferrihydrite represented using ferric hydroxide is around 10^{-37} and 10^{-44} for goethite and hematite (Cornell and Schwertmann, 1996). These K_{sp} values indicate that metastable ferrihydrite is more soluble than hematite and goethite but remains mostly insoluble. The precipitation of ferrihydrite follows crystallization kinetics, and this is reflected in precipitation mechanism dominated by nucleation. The low ferrihydrite equilibrium solubility results in the fast nucleation kinetics of ferrihydrite and is directly related to supersaturation. The supersaturation is the concentration of the ferric ion

relative to the equilibrium solubility of ferrihydrite at a given pH. The solubility of ferrihydrite is shown in Figure 2-21 (wherein ‘soil-Fe’ is naturally occurring crystalline $\text{Fe}(\text{OH})_3$). It depends on pH and is at the minimum at pH 6-10. The solubility is approximately 0.1 mg/L at 25°C (Baes and Mesmer, 1976; Biedermann and Schindler, 1957; Cornell and Schwertmann, 1996; Stumm and Morgan, 1996).

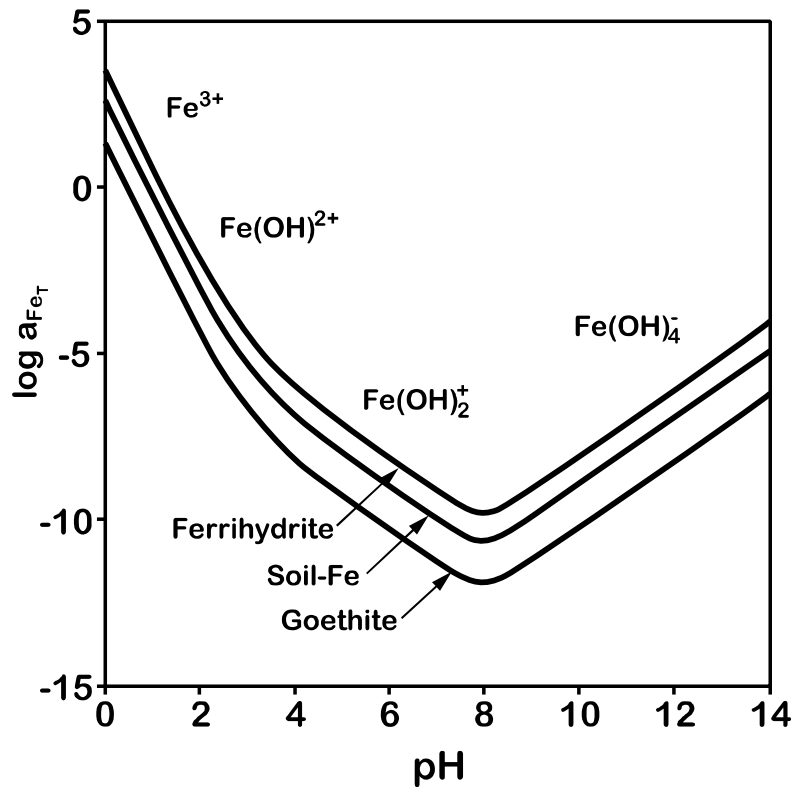
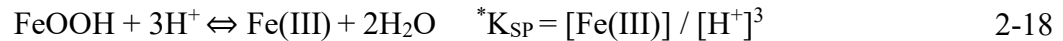
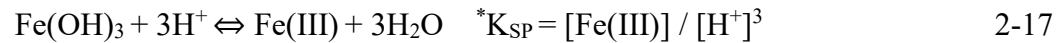


Figure 2-21: Solubility of ferrihydrite, goethite and ‘soil-Fe’ versus pH
(Cornell and Schwertmann, 1996; Lindsay, 1979)

The equilibrium solubility of ferrihydrite is dependent on pH at a constant temperature, pressure, and ionic strength. In acidic media, the solubility product can be expressed as shown in Reactions 2-17 and 2-18, representing ferric hydroxide or oxyhydroxides.



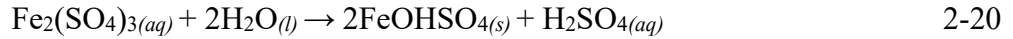
Jolivet et al. (2000) explained that the iron oxide and oxyhydroxides involve polycondensation and not ionic reaction. During polycondensation the iron oxides and iron oxyhydroxides are formed by the combination of initial nuclei comprising Fe^{3+} ions. This process is accompanied by dehydration, the release of water. Therefore, despite regarding precipitation as a reactive crystallization, it is difficult to relate this to an ionic process, and the theoretical calculation of solubility product may not be accurate. The ferric hydroxide in the reactions above does not describe ferrihydrite and may not be an accurate representation of its solubility product.

Measuring the equilibrium solubility of iron oxides has been attempted in the literature by two approaches: precipitation and dissolution. In a precipitation approach, the oxide is precipitated from a supersaturated solution of ions by addition of a base, and in a dissolution approach, the oxide is dissolved in an undersaturated solution. The pH is monitored, and total iron is measured until equilibrium is reached. In the solubility measurements, it is important that no phase transformation or recrystallization occurs during the experiment. Ferrihydrite transforms into less soluble phases hematite and/or goethite (Cornell and Schwertmann, 1996). To reach equilibrium in the case of iron oxides long periods are needed. Biedermann and Schindler (1957) found that the steady state in the precipitation method for ferrihydrite at 25°C was reached after 200 h. Solubility measurements for the less soluble oxides hematite and goethite take a much longer time to attain equilibrium. It took several years for the transformation of metastable schwertmannite into stable goethite at 25°C. The solubility of “ Fe(OH)_3 ” declines with aging and the solubility of

a solid mixture (ferrihydrite+hematite+goethite) is controlled by the least stable solid (Lemire et al., 2013). The difficulty in establishing the equilibrium may give rise to errors. The solubility product for an iron oxide measured by both the dissolution and precipitation methods must be in agreement (Cornell and Schwertmann, 1996). Schindler et al. (1963), measured solubility product for aged ferrihydrite by both precipitation and dissolution methods at 25°C in the pH range 1-2 and found that both methods gave the same value of $\log K_{sp} = 3.55 \pm 0.1$ for ferrihydrite. Diakonov et al. (1999), obtained $\log K_{sp} = 19.64 \pm 0.1$ for hematite from both dissolution and precipitation experiments at 60°C. Many researchers have studied hematite solubility under mildly acidic conditions relevant to geochemical processes, usually in concentrated chloride solutions of varying pH (Berner, 1969; Boctor et al., 1980; Sergeeva et al., 1999; Yishan et al., 1989).

Hematite solubility in sulfuric acid solutions under conditions relevant to hydrometallurgical processing has also been reported. Hematite solubility via both dissolution and precipitation from $\text{Fe}_2(\text{SO}_4)_3\text{-H}_2\text{SO}_4$ solutions at 150-200°C and under 980.7 kPa oxygen pressure was first performed by Umetsu et al. (1977). The experiments were conducted in a 1L stainless steel autoclave with a Teflon lining and agitation was provided by a magnetically driven titanium impeller. The autoclave was quickly cooled down, and the solution was externally filtered to remove solids. Their experimental set-up's shortcoming was a lack of in-situ filtration. Umetsu et al. (1977) showed that the hematite solubility demonstrates a linear relationship with the free acid concentration and hematite solubility was also found to decrease with increasing temperature. X-ray analysis revealed that hematite remained the stable solid phase during the experiments.

During the ferric hydrolysis precipitation experiments, it was demonstrated that hematite is stable up to 56 g/L and 65 g/L H₂SO₄ at 185 and 200°C, respectively (Reaction 2-19) but above these free acid concentrations, basic iron sulfate (FeOHSO₄) is stable at each temperature (Reaction 2-20).



The effects of Na₂SO₄, CuSO₄, and ZnSO₄ on hematite/jarosite precipitation were also investigated. Both ZnSO₄ and CuSO₄ pushed hematite conversion to jarosite to higher free acid levels. Na₂SO₄ addition decreased the iron solubility due to sodium jarosite precipitation which has a lower solubility than both hematite and potassium jarosite (Umetsu et al., 1977; Reaction 2-21).



Tozawa and Sasaki (1986) studied the hydrolytic precipitation of hematite and jarosite from Fe₂(SO₄)₃-H₂SO₄ solutions at 170-200°C under 980.7 kPa oxygen pressure in the presence of MgSO₄, ZnSO₄, Na₂SO₄, and CuSO₄. Their experimental set-up was an improvement over Umetsu et al. (1977) because samples could be taken at temperature. However, the set-up still did not provide in-situ filtration. Tozawa and Sasaki (1986) showed that hematite precipitated from Fe₂(SO₄)₃-H₂SO₄ solution up to a certain free H₂SO₄ concentration after which jarosite precipitates. It was demonstrated that MgSO₄, ZnSO₄, and CuSO₄ all shift the hematite/jarosite

transition to higher free H₂SO₄ with CuSO₄ having a much smaller effect than MgSO₄ and ZnSO₄ for comparable molar concentrations. The results were in agreement with Umetsu et al. (1977).

Tozawa and Sasaki (1986) calculated the H⁺ concentration using Meissener's activity coefficient method (Kusik and Meissner, 1978) and showed that the metal sulfates disassociated, the sulfate combined with H⁺ to form bisulfate ions, thereby reducing the H⁺ concentration (Reaction 2-22).



The bivalent metal sulfates reduced the H⁺ concentration and stabilized hematite precipitation relative to jarosite precipitation. Sasaki et al. (1993) also measured hematite solubility via hydrolytic precipitation from Fe₂(SO₄)₃-H₂SO₄ solutions at 150°C, 170°C, and 220°C. The researchers used an experimental set-up that was identical to that of Tozawa and Sasaki (1986). They found that hematite precipitation occurred up to a specific free H₂SO₄ concentration, after which basic ferric sulfate precipitated.

Papangelakis et al. (1994) studied the conditions relevant to the hematite process. They used speciation and thermodynamic data found in the scientific literature to build a hematite solubility model in H₂SO₄ solutions at elevated temperatures. The Vasil'ev approach was used to calculate mass-based equilibrium constants for the assumed speciation. The solubility of hematite from 50 to 100 g/L free H₂SO₄ at 200°C was experimentally measured to validate the model. The time required to reach equilibrium was not mentioned. A 2L titanium autoclave with a glass liner was used, and a magnetically driven titanium impeller provided agitation. The samples were drawn at temperature using a dip tube and heat exchanger arrangement. A 45µm graphite filter attached to

the sampling dip tube provided in-situ filtration. The experimental set-up had the advantage of the ability to sample at temperature with in-situ filtration. However, solids penetrated the filter due to its large porosity. The model required $\text{FeSO}_4\text{HSO}_4^0$ and FeHSO_4^{2+} complexes to produce the best fit to the experimental data. The $\text{FeSO}_4\text{HSO}_4^0$ and FeHSO_4^{2+} complexes were predicted to be the dominant species under conditions relevant to the hematite process. The speciation model yielded results that followed the experimental trends, but its predictions were not accurate when compared to the experimental data.

Liu et al. (2003) studied hematite solubility in H_2SO_4 solutions at 230-270°C. Their experimental setup consisted of a 600 mL titanium stirred autoclave with a dip tube for withdrawing samples at temperature. A 2 μm sintered titanium filter provided in-situ filtration. They identified Fe^{3+} , FeSO_4^+ , FeHSO_4^{2+} , $\text{Fe}_2(\text{SO}_4)_3^0$ and $\text{Fe}(\text{OH})_2\text{SO}_4^{2-}$ as the predominant species over the range of free H_2SO_4 (0 – 0.7 M) and temperature studied. Free H_2SO_4 was measured after the solubility test by chelating iron using Ca-CDTA followed by NaOH titration. Liu et al. (2003) also compared their calculated solubilities with experimental data from Umetsu et al. (1977), Tozawa and Sasaki (1986) and Papangelakis et al. (1994) and found that they were lower than the experimental data but on the same order of magnitude. They concluded that approaching equilibrium via precipitation yielded higher solubility values than approaching equilibrium via dissolution. However, as mentioned earlier the solubility product for an iron oxide measured by both the dissolution and precipitation methods should be in agreement provided the experimental difficulties involving filtration are overcome and sufficient time is allowed to reach equilibrium (Cornell and Schwertmann, 1996).

2.9 Sulfur and sulfur dispersing agents in leaching processes

Sulfur has complex behavior in the medium temperature oxygen pressure leaching of sulfide minerals. The recovery of elemental sulfur from sulfide concentrates is accomplished in four steps, which comprise the pressure leach itself, flotation, melting-filtration, and purification (Chalkley et al., 1993). Elemental sulfur formation becomes unfavorable with an increase in pH or temperature (Arauco and Doyle, 1986). Improvement in the leaching kinetics and a minimum viscosity of molten sulfur coincide at a leaching temperature near 150°C (Bolton, 1981). Temperature and oxygen partial pressure dictate the formation of sulfuric acid in oxygen pressure leaching. The rate of sulfur oxidation is extremely slow below its melting point, and above this temperature, it is appreciable and increases rapidly with increasing temperature (Corriou and Kikindai, 1981; Habashi and Bauer, 1966).

Sulfur, a yellow solid at room temperature is insoluble in water but soluble in carbon disulfide. Sulfur tends to form stable compounds with all elements except noble gases, and it has the largest number of allotropes (about thirty have been characterized). The main sulfur allotropes are S_λ , S_μ , and S_π . In the solid-state, S_λ is the only stable sulfur allotrope. It crystallizes either as orthorhombic α - S_8 , monoclinic β - S_8 or monoclinic γ - S_8 . At atmospheric pressures, α - S_8 is stable below 95.5°C; above this temperature it transforms to β - S_8 , which is stable up to 114.5°C (Steudel et al., 2003). Liquid sulfur is usually a combination of S_λ , S_μ , and S_π . The proportion of S_λ is more than 90% below 160°C. Above 160°C, the proportion of S_μ increases and at 180°C it is over 25%. The proportion of S_π is low at any temperature (Corriou and Kikindai, 1981). The dynamic viscosity of liquid sulfur exhibits a minimum of 0.007 Pa.s at 157°C but increases dramatically in the

temperature range 157-190°C, reaching a maximum of 93.2 Pa.s at 187°C. The viscosity begins to decrease above 190°C and reaches 0.1 Pa.s at the boiling point, 444.6°C (Matsushima, 1959; Meyer, 1964).

Sulfur dispersing agents used in hydrometallurgy are commonly referred to as surface active agents or surfactants. A sulfur dispersing agent may be described as any substance with the ability to disperse molten sulfur from sulfide mineral surfaces. Sulfur dispersing agents must have the ability to increase the contact angle between liquid sulfur and sulfide minerals under oxygen pressure leaching conditions. A surfactant is made up of a characteristic molecular structure which contains a hydrophobic group and a hydrophilic group. The surfactants can be categorized into four groups based on the nature of the hydrophilic group: anionic, cationic, zwitterionic, and non-ionic. The structures of the hydrophobic group can include (Rosen, 2004): straight/branched alkyl groups (C₈-C₂₀), alkylbenzene residues (C₈-C₁₅), alkylnaphthalene residues (\geq C₃), polyoxypropylene glycol derivatives, perfluoroalkyl and polysiloxane groups, rosin derivatives and lignin derivatives.

Sulfur dispersing agents (SDAs) used in the oxygen pressure leaching of sulfides should not introduce impurities into the slurry, they should not enter into any reactions that alter the essential chemical nature of the constituents in slurry, and they should not have any negative impact on downstream operations (Kawulka et al., 1975). Lignosulfonate (lignosol) and o-phenylenediamine (OPD) may be used in the Vale and Teck's CESL processes. In zinc pressure leaching, lignosol and quebracho are commonly used. However, low-rank coal was also found to be an inexpensive and effective additive with the potential to replace lignosol. It was found to be effective in

dispersing liquid sulfur in a pressure leaching experiment when more than 35% of the carbon in the coal was in the aliphatic form (Barta et al., 1998; Collins and Kofluk, 1998, 1997).

However, the addition of dispersant does not always result in increased metal extraction (Huang and Bernal, 1984). For example, a large amount of quebracho was found to hinder the reaction rate by creating a barrier to mass transfer across the mineral-solution interface (Arauco and Doyle, 1986). Sulfur dispersants may also have a negative impact on the flotation of elemental sulfur post-leaching. Lignosol and quebracho result in the formation of fine sulfur particles which are difficult to recover through flotation (Chalkley et al., 1993). While lignosol was detrimental to sulfur flotation due to its dispersing function (Xia et al., 1987), OPD had a negative impact on the power consumption of the subsequent zinc electro-winning process (Alfantazi and Dreisinger, 2003).

The use of SDAs for leaching chalcopyrite in the temperature range 125–155°C to solve the sulfur wetting problem and to enhance copper extraction was investigated (Hackl, 1995; Hackl et al., 1995b, 1995a). It was found that most of the SDAs decomposed quickly and the best results were obtained on a continuous addition of 50 kg/t OPD at 125°C. In the Dynatec process, low-rank coal was used as a sulfur dispersant instead of water-soluble SDAs. Recently some researchers have reported the use of polytetrafluoroethylene (PTFE) as a solid sorbent for sulfur removal (Guerra and Shepherd, 2011; Jin and Guerra, 2012; Mathew et al., 2010). The PTFE must be recovered from the residue and recycled for reuse.

While so much has been reported on SDAs, the literature is very scant on how these reagents affect iron precipitation in the leaching of sulfide ores. Most of the SDAs discussed in the literature

generate very fine sulfur particles which are mixed with iron oxide particles in the residue and must eventually be separated from each other for the recovery of precious metals.

2.9.1 O-Phenylenediamine and reaction products

Phenylenediamines are aromatic diamines. The amine is an organic compound derived from ammonia (NH_3) in which organic groups replace one or more hydrogen atoms. A 'diamine' is an organic compound with two amino groups, and an aromatic amine consists of an aromatic ring attached to an amine (Vogt and Gerulis, 2000). The three isomers of phenylenediamine are ortho-phenylenediamine (OPD), meta-phenylenediamine (MPD) and para-phenylenediamine (PPD), simply referred to as o-phenylenediamine, m-phenylenediamine, and p-phenylenediamine. The terms ortho, meta, and para are prefixes to indicate the position of the amine on the benzene ring. OPD is also known as 1, 2-diaminobenzene or 1, 2-phenylenediamine and these chemical structures are shown in Figure 2-22 and Figure 2-23.

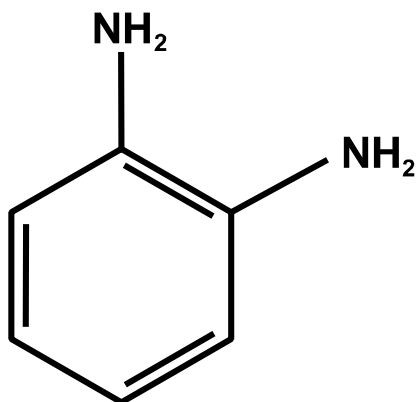


Figure 2-22: o-phenylenediamine (OPD)

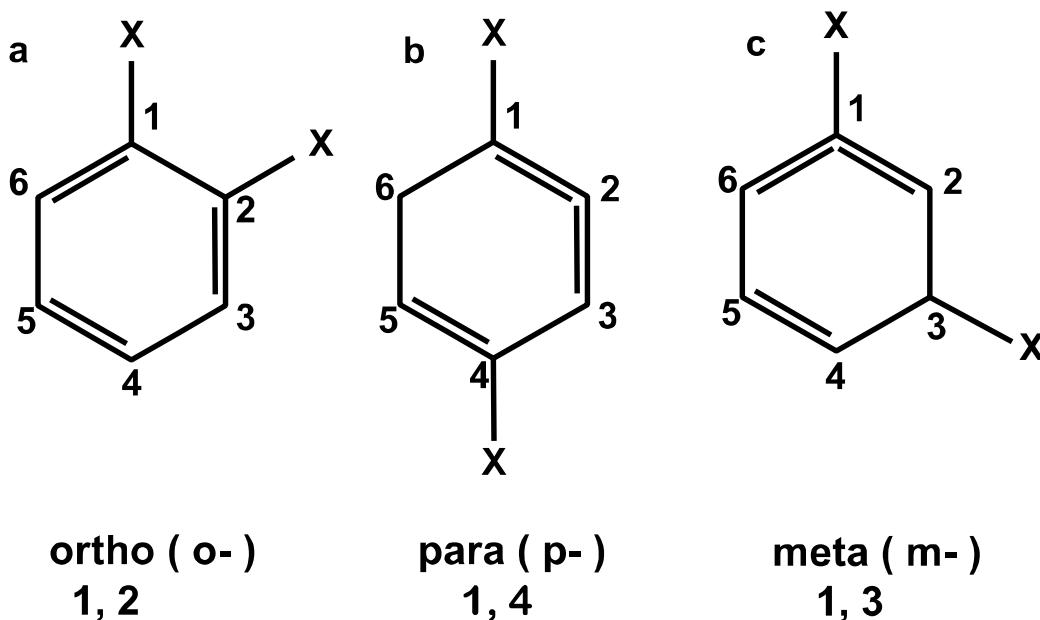


Figure 2-23: Positioning of the amine on the benzene ring

OPD is usually in the form of white to pale yellow leaf-like crystals or prism-like crystals. It changes color from white to yellow, brown, purple, and finally to black when exposed to air. It is readily soluble in hot water, ethanol, ether, chloroform and benzene (ChemicalBook, 2008). The melting and boiling points of the phenylenes are listed in Table 2-2.

Table 2-2: Melting and boiling points of phenylenediamines

(Smiley, 2000)

Compound	Melting point, °C	Boiling point, °C
<i>o</i> -Phenylenediamine	102-103	256-258
<i>m</i> -Phenylenediamine	62-63	284-287
<i>p</i> -Phenylenediamine	145-147	267

The phenylenediamines have similar chemical properties as aromatic amines. They form stable salts on reaction with acids. Their ease of oxidation to form complex colored compounds is the

basis for their use in dyes and hair colorants. The various isomers differ significantly in chemical reactivity due to the relative positions of the two amino groups. OPD readily form heterocyclic compounds, whereas the *m*- and *p*- isomers do not. Benzimidazole is formed by a ring-closure reaction of OPD with formic acid, and the oxidation of OPD with aqueous iron(III) chloride produces 2,3-diaminophenazine as shown in Figure 2-24 (Smiley, 2000).

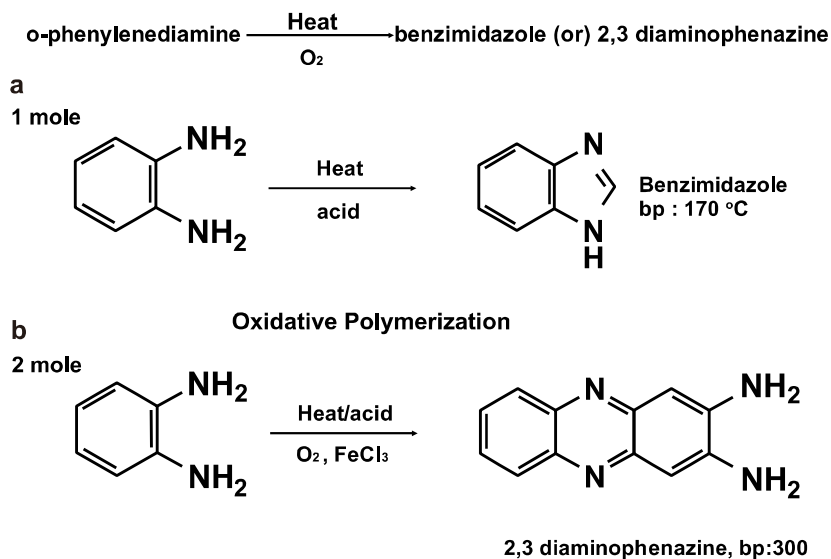


Figure 2-24: Reactions of *o*-phenylenediamine to form benzimidazole and 2,3-diaminophenazine
 (Smiley, 2000)

In subsequent reactions, oligomers and trimers can be formed from the dimeric diaminophenazine (Simándi et al., 1992; Smiley, 2000; Watanabe et al., 1989). Products of oxidative polymerization show remarkably high thermostability, perhaps this is one of the reasons why OPD works so well in pressure leaching of sulfides. The oxidation products formation mechanism is shown in Figure 2-25.

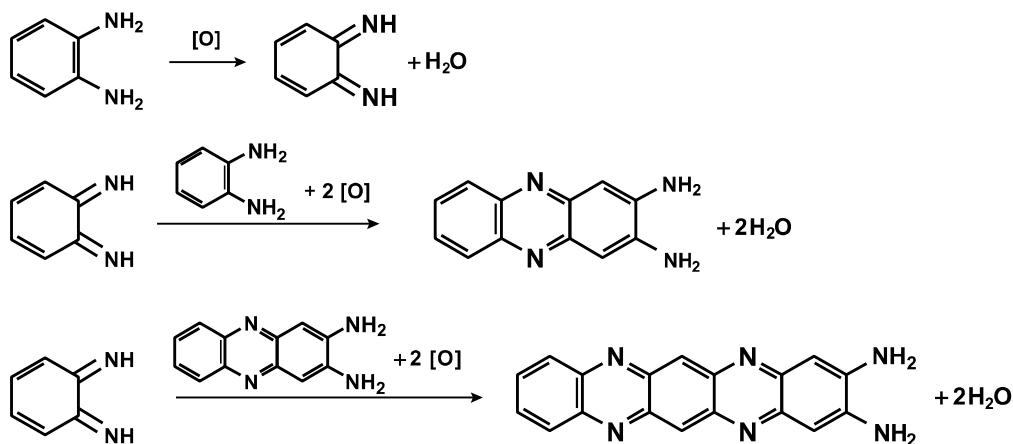


Figure 2-25: Oxidation of *o*-phenylenediamine

(Simándi et al., 1992; Smiley, 2000; Watanabe et al., 1989)

Phenylenediamines are prepared by aromatic nitration followed by reduction. The initial starting material in most cases is benzene. The principal method to synthesize OPD as shown in Figure 2-26, is by the reduction of 2-nitroaniline which is produced from 2-chloronitrobenzene with ammonia (Squire, 1975). OPD is also produced by several other methods which include the amination of 1,2-dichlorobenzene with ammonia (Andoh and Fujiwara, 1985), as shown in Figure 2-27 and the direct amination of aniline as shown in Figure 2-28 (Martin, 1939). A method involving cyclohexane, sulfur, and ammonia has also been reported (Weigert, 1981).

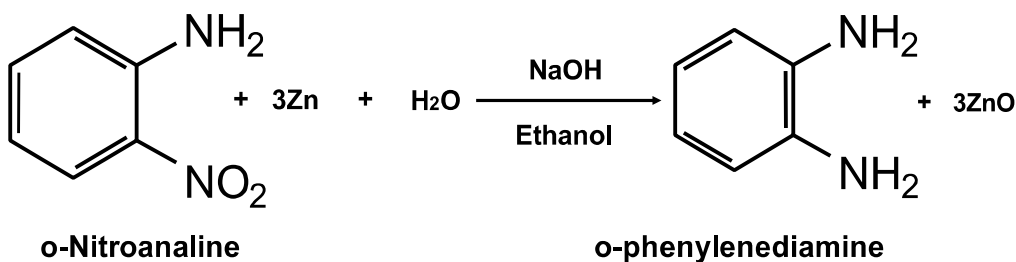


Figure 2-26: Synthesis *o*-phenylenediamine from *o*-nitroaniline

(Squire, 1975)

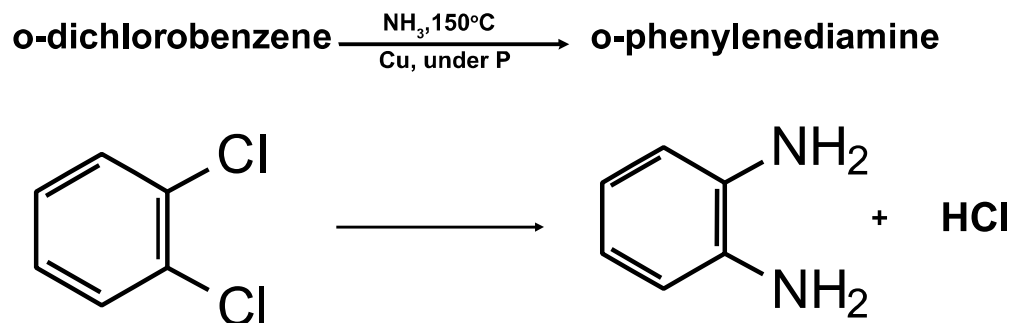


Figure 2-27: Synthesis *o*-phenylenediamine from *o*-dichlorobenzene
(Andoh and Fujiwara, 1985)

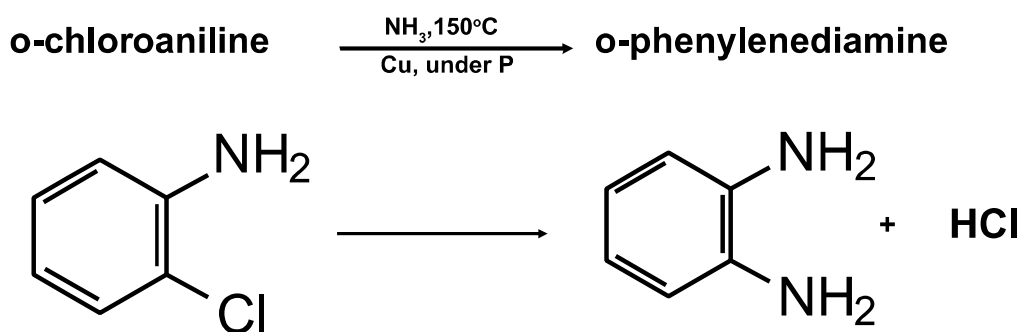


Figure 2-28: Synthesis *o*-phenylenediamine from *o*-chloroaniline
(Martin, 1939)

The discussion above explores the possibility of reactions OPD may be undergoing in an autoclave under CESL conditions. Aniline has been used as a surfactant for sulfur dispersion in CESL process (Salomon-de-Friedberg and Jang, 2015). The sulfonation of aniline as shown in Figure 2-29 also gives amino benzene sulfonic acid (Vogel and Furniss, 1989).

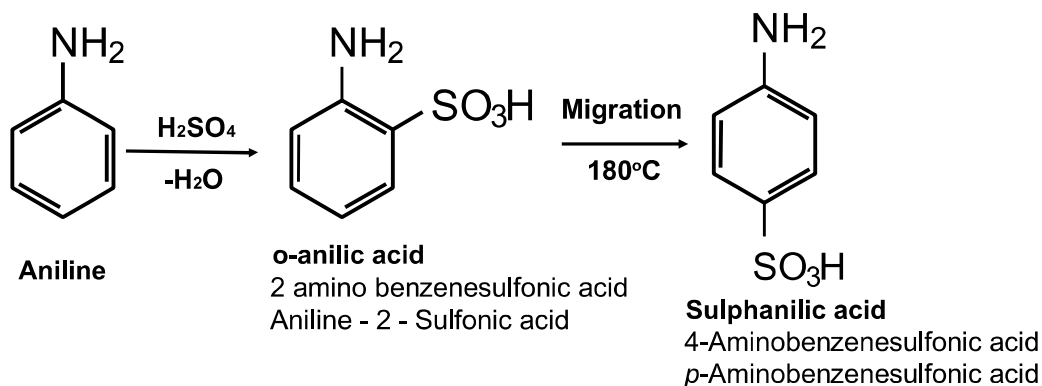


Figure 2-29: Sulfonation of aniline

(Vogel and Furniss, 1989)

2.9.2 Effect of organic reagents on the viscosity of sulfur

The temperature (159°C), where the viscosity of liquid sulfur is the lowest undergoes a change on the addition of various reagents to sulfur (Bacon and Fanelli, 1943; Doi, 1965; Fairbrother et al., 1955). Doi (1965), studied the effect of different types of reagents on the viscosity of sulfur in the temperature range of 120 to 200°C. The viscosity was measured with an Ostwald viscometer dipped in a glycerin bath. The reagents were then classified into three groups based on their effect on the viscosities of sulfur.

The halogen and dibenzothiazyl disulfide were classified as group 1. The temperature of the lowest viscosity decreased as the quantity of the reagent increased up to a certain point, and after that, the viscosity increased with the further addition of these reagents. Halogen was added as sulfur monochloride (S₂Cl₂), which on thermal cleavage of the S-S bond produce Cl-S· radicals and the bromine and iodine also produce Br- S· and I- S· radicals upon addition to liquid sulfur. Doi (1965), explained that these radicals react with sulfur and promote sulfur polymerization which

increases viscosities. Naphthalene, p-dichlorobenzene, diphenyl, and m-cresol were classified as group 2. The liquid sulfur viscosity-temperatures curves without any reagent and with naphthalene, p-dichlorobenzene or diphenyl are shown in Figure 2-30.

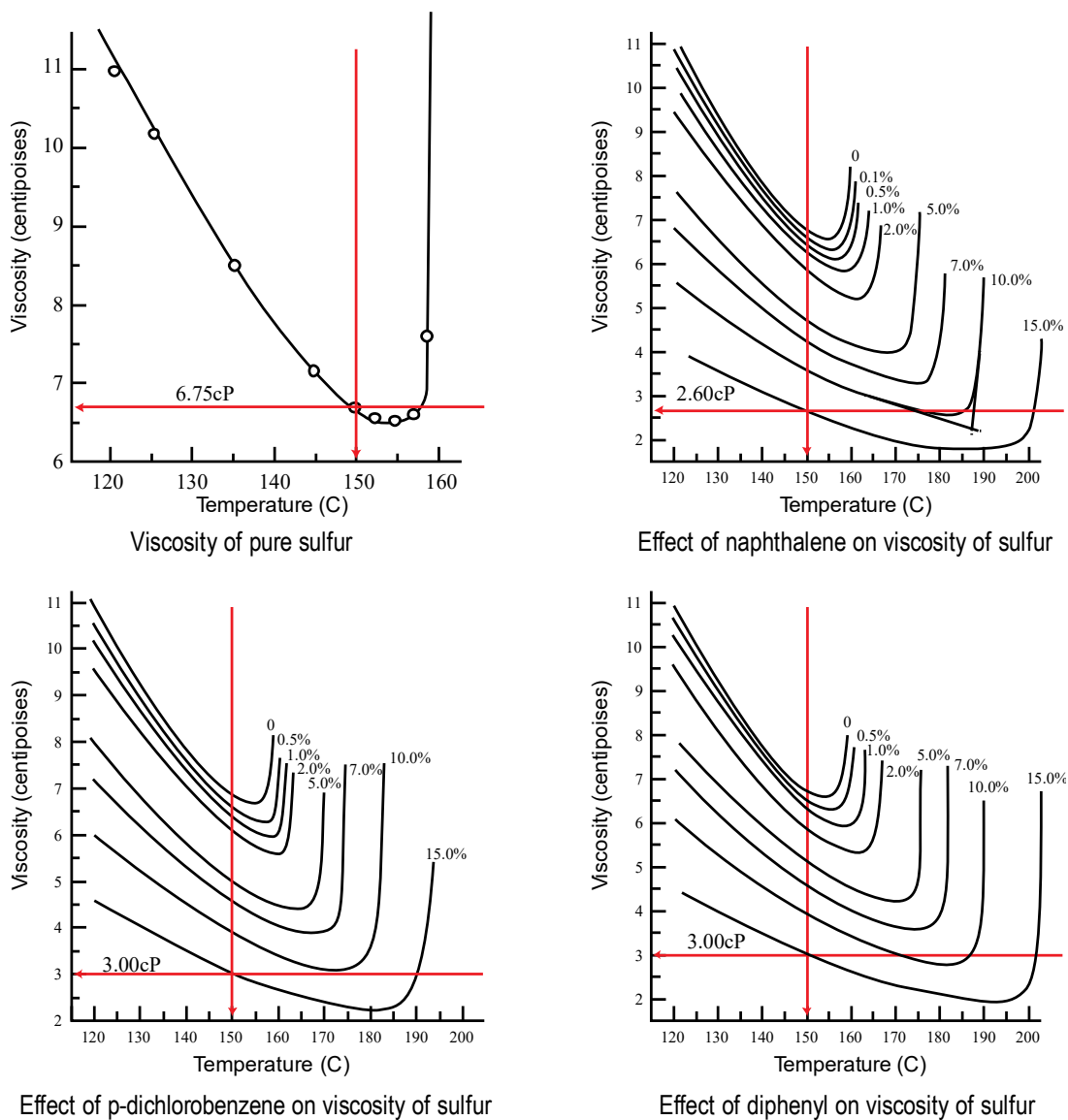


Figure 2-30: Effect of various reagents on the viscosity of sulfur

(Bacon and Fanelli, 1943; Doi, 1965)

These reagents raised the temperature at which sulfur viscosity is at its lowest, as their concentration was increased. The viscosity of sulfur at 150°C was decreased, which is of relevance to this work. These aromatic reagents do not react with sulfur but cause dilution of sulfur, thus decreasing the viscosity. A 0.5% addition resulted in a 5% reduction in viscosity through dilution as shown in Figure 2-30 . Hindrance of polymerization increases the temperature of the lowest viscosity point (Doi, 1965). The group 3 reagents consisted of pyrogallol, *p*-benzoquinone, α - naphthol, tetramethyl thiuram disulfide, 2 mercaptobenzothiazole, and diphenyl guanidine. These reagents were unstable against heat and changed considerably with time as did the viscosity of sulfur.

2.9.3 Effect of organic reagents on sulfur polymerization

The organic reagents result in the formation of sulfur agglomerates due to a polymerization process described in the literature as ‘inverse vulcanization’. Pyun et al. (2013, 2015), reported a novel process, which was termed “inverse vulcanization”, which is a creative reversal of the vulcanization process. Vulcanization has significant importance to the rubber industry. It is a chemical process for converting natural rubber into the more durable material by heating with sulfur. Sulfur modifies the polymer by forming cross-links (bridges) between individual polymer chains of carbon. In 1905, George Oenslager discovered that thiocarbanilide, accelerated the reaction of sulfur with rubber, leading to shorter cure times and reducing energy consumption (Oenslager, 1933). Thiocarbanilide (C_6H_5NH)₂CS is a derivative of thiourea, prepared by the reaction of aniline and carbon disulfide.

Later, in 1912, David Spence discovered *p*-aminodimethylaniline to be far superior accelerator, improving the tensile strength of the rubber (Geer and Bedford, 1925). *P*-aminodimethylaniline is also known as dimethyl-*p*-phenylenediamine (DMPD). Aniline, DMPD, and thiourea are used in the leaching of copper sulfides (Dixon et al., 2018; Salomon-de-Friedberg and Jang, 2015). Inverse vulcanization is a process where carbon atoms are introduced to cross-link the sulfur polymer chains. The inverse vulcanization method takes advantage of sulfur's ring-opening and chain-forming tendencies at elevated temperatures. The binding of C molecules, to the sulfur radicals, occurs when the sulfur's S₈ rings open as shown in Figure 2-31. The molten elemental sulfur itself serves as the solvent.

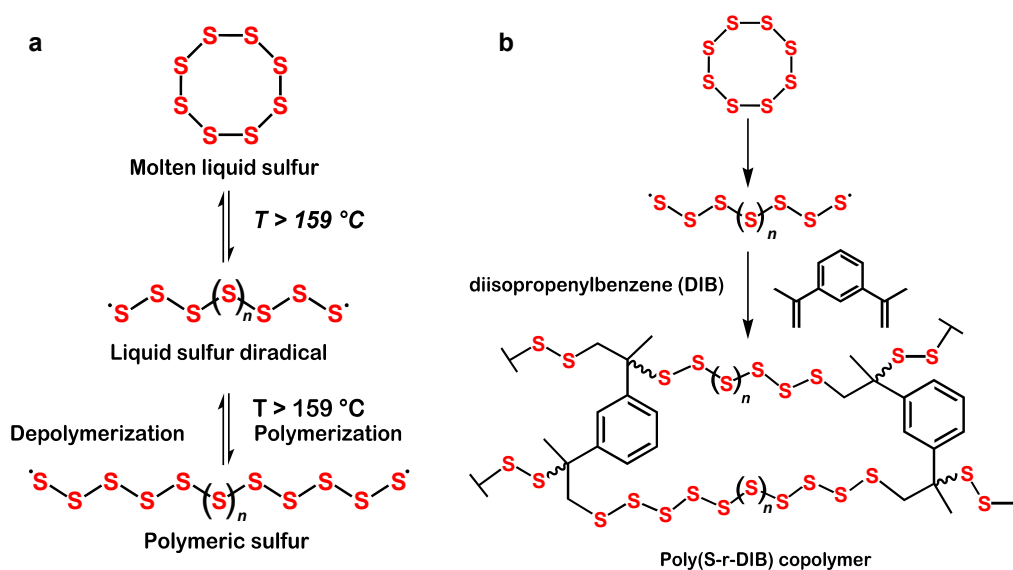


Figure 2-31: Schematic for (a) thermal ring opening of S₈ into polymeric sulfur diradical forms (b) copolymerization of S₈ with DIB to form chemically stable sulfur copolymers
(Pyun et al., 2013, 2015)

The synthesis of polysulfides by inverse vulcanization introduced a new class of materials which have been explored in a variety of contexts due to their interesting optical, electrochemical and

self-healing properties (Boyd, 2016). Crockett et al. (2016) introduced a polysulfide prepared by the inverse vulcanization of the renewable plant oil limonene as shown in Figure 2-32. The sulfur-limonene polysulfide was explored for use in coatings and devices that detect and remove palladium and mercury from water and soil. The polysulfide initially red in color turned yellow when exposed to mercury. Sulfur and unsaturated cooking oils from rapeseed, sunflower, and olive plants were also co-polymerized using inverse vulcanization to form a polysulfide that captured mercury from the air, water, and soil. This polysulfide was being considered for in situ remediations of mine tailings, soil, and agricultural wastewater (Worthington et al., 2017).

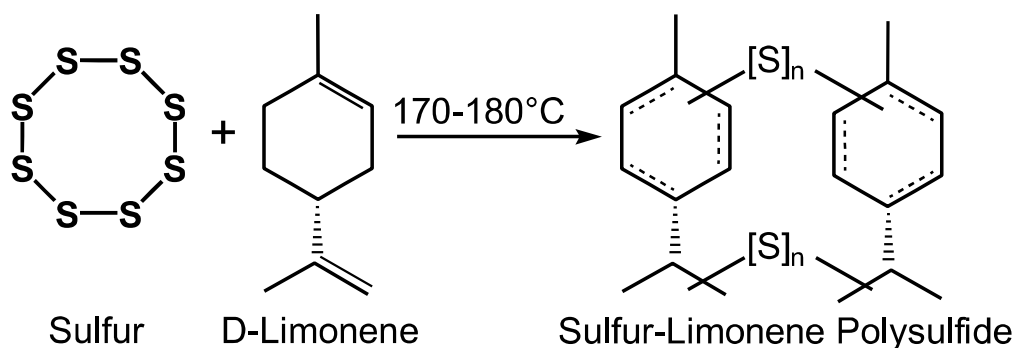


Figure 2-32: Schematic for copolymerization of S₈ with limonene to form chemically stable sulfur copolymers

(Crockett et al., 2016)

Reactions of sulfur with 1,3-dichlorobenzene and 1,4-dichlorobenzene have also been investigated to generate crosslinked or linear polysulfides, respectively (Boscato et al., 1981; Schmidt, 1970). They are shown in Figure 2-33.

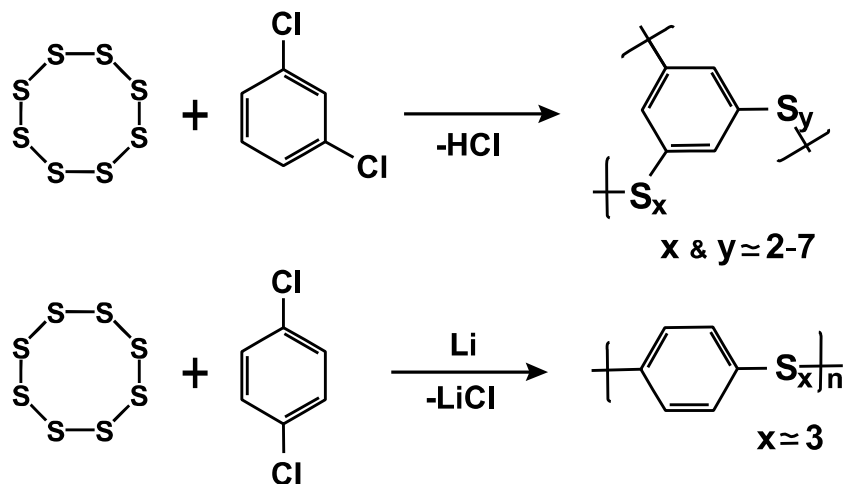


Figure 2-33: Thermally induced and the lithium-initiated reaction of dichlorobenzene and sulfur to generate polysulfides

(Boscato et al., 1981; Schmidt, 1970)

2.10 Summary

Iron control and removal is an important aspect of the hydrometallurgical leaching of sulfide concentrates. In the CESL and Vale medium temperature leaching processes for sulfide concentrates, iron is precipitated in the pressure oxidation step in the autoclave and reports to leach residue. These leach residues were found to contain valuable metals associated with amorphous iron oxide phases. The amorphous phases are metastable and transform to stable phases over time releasing the associated metals into the environment. More importantly, iron precipitates capture valuable metals and reduce overall process recoveries.

Therefore, these undesirable amorphous iron phases must be kept to a minimum to keep the loss of valuable metals to a minimum. In CESL and Vale processes, hematite is a preferred iron oxide as it is environmentally stable, compact and does not adsorb valuable metals comparatively.

Efficient control of process parameters and the addition of specific reagents can promote iron precipitation as hematite under the prevailing process conditions.

Iron precipitation as hematite involves several kinetic processes such as supersaturation, followed by primary nucleation and crystal growth. The secondary changes such as recrystallization, aging, aggregation, and secondary nucleation supersede crystal growth. Process conditions and faster reaction rates result in an undesirable amorphous metastable phase which transforms to a more stable phase on aging. The leach residue stability and metal intake are governed by the amount of this metastable phase in the residue. It is, therefore, important to investigate the factors influencing both amorphous Fe and hematite precipitation under the CESL and Vale processes. The quality of hematite precipitates in terms of purity, particle size, particle shape is also important, and a careful selection of seed and additives to achieve this goal also needs investigation. The metastable phase has been identified as ferrihydrite, and the solubility and transformation of ferrihydrite under CESL and Vale conditions also need investigation.

Sulfur control and removal is another important aspect of the hydrometallurgical process pertaining to the leaching of sulfide concentrates. During the pressure leaching process, which takes place at 150°C, sulfur is in its molten state and sulfur dispersants are used to prevent it from coating the unleached sulfur mineral particles. The effect of these dispersing agents on the iron precipitation also needs investigation. Furthermore, sulfur, in CESL and Vale's medium temperature leaching processes for sulfide concentrates reports to leach residue as elemental sulfur and is also often found associated with valuable metals such as gold and platinum group metals. Thus, the separation of the elemental sulfur product from the residues is an important process

consideration. Since surfactants can affect the size and nature of the sulfur product, they are also important from this perspective.

There remains a need to better understand the effect of various process parameters on the complex chemistry of iron precipitation and to explore the effect of various sulfur dispersing agents on sulfur and iron morphology for the conditions relevant to the CESL and Vale processes. The avenues that require further investigation are: characterization of the leach residue samples (particularly those generated from the Vale process) to reconfirm that amorphous iron oxide phases are indeed responsible for higher loss of associated metal in the leach residue as witnessed by Sahu and Asselin (2011); study of the process variables in sulfide concentrate leaching to elucidate the factors that have a pronounced effect on iron precipitation and associated metal loss; control the kinetics of the iron precipitation during leaching; study of the iron precipitation products; study the effect of various additives for sulfur control in the autoclave; and finally, the ferrihydrite solubility and its transformation kinetics. These aspects have been identified to better understand the CESL and Vale iron precipitation and sulfur behavior and ultimately will lead to rejection of iron and sulfur to the leach residue with the minimum associated metal loss, in a stable form and with improved (larger particles) sulfur morphology. This would then provide a more efficient iron and sulfur rejection process. Secondly, an improved understanding of the general aspects of iron precipitation, sulfur control, and additives can also be of benefit to a more general audience for iron and sulfur control in hydrometallurgy. The objectives of this work are discussed in Chapter 3 and are in accordance with the various aspects mentioned above.

CHAPTER 3: RESEARCH OBJECTIVES

The discussion in the previous sections indicates that ferrihydrite (or possibly schwertmannite) would form as a precursor to hematite even in an acidic sulfate medium at 150°C, although unequivocal evidence is lacking.

The exact nature of the “amorphous” phase is also unclear. However, regardless of the exact nature of the “amorphous” phase, reduced crystallinity is contributing to copper losses in the CESL process, and a similar phenomenon is likely at work in the Vale process. Furthermore, aside from the issue of “amorphous” phases, the conditions leading to the precipitation of jarosite have also not been clearly identified particularly with regards to precipitation during actual concentrate leaching (as opposed to reagent-based experiments). The main hypothesis presented in this thesis is that the nature and crystallinity of iron precipitates from the CESL and Vale processes can be beneficially controlled to make more hematite by altering the process conditions and chemistry.

Given the background presented above and the detailed literature review in Chapter 2, the objectives of the present research are:

1. Investigate and establish conditions to maximize the Fe to Cu (or Ni) ratio in the final process residues and minimize Cu (or Ni) losses to the Fe residue.
2. Establish the solubility of ferric in the sulfate-chloride system and identify the main mechanism contributing to ferrihydrite transformation so that it may be leveraged.

The objectives defined above are achieved through the following experimental studies:

- i. Residue characterization: Identifying the amorphous or poorly crystalline iron phases in the medium temperature sulfide concentrate leach residues by HaHC extractions, QXRPD, TEM, and Mössbauer spectroscopy. Ruling out the possibility that jarosite doped with copper is a poorly crystalline iron phase in the residues.
- ii. Optimizing process conditions: Investigating the effect of acid concentration, seed, seed recycle, residue recycle, retention time and grind size on HaHC soluble phase and copper recovery in pressure oxidation leaching of sulfide concentrates under CESL conditions.
- iii. Assessing the effect(s) of reagents: Examining the effect of sulfur dispersing agents on the HaHC soluble phase and copper recovery in pressure oxidation leaching of sulfide concentrates under CESL conditions.
- iv. Modifying reagent additions: Investigating the effect of hematite crystal growth modifiers, iron complexing agents and sulfur modifiers on the HaHC soluble phase and copper recovery in pressure oxidation leaching of copper sulfide concentrates under CESL conditions. Testing a novel reagent(s) for iron in pressure oxidation leaching of sulfide concentrates under CESL conditions.
- v. Transforming the residue: Studying synthetic ferrihydrite behavior including solubility and transformation in the presence of copper, nickel, and chloride ions under CESL conditions.

CHAPTER 4: EVALUATION OF CRYSTALLINITY IN CESL AND VALE LEACH RESIDUES

The leach residues produced from hydrometallurgical processing of sulfide ores at CESL's pilot plant and Vale's demonstration plant operating at medium temperature (150°C), were analyzed by various characterization techniques. The residues contain amorphous/poorly crystalline and metastable nanoscale iron oxides/oxyhydroxide phases which dictate the properties of these residues and contain a relatively high loading of the valuable (Cu, Ni) metals. The following characterization techniques were employed.

1. Quantitative X-ray powder diffraction QXRPD,
2. Sequential extraction,
3. Digestion & ICP-MS,
4. Transmission electron microscopy and
5. Mössbauer spectroscopy.

Digestion & ICP-MS was performed by dissolving the solids using a combination of HCl (hydrochloric acid), HNO₃ (nitric acid), HF (hydrofluoric acid) and HClO₄ (perchloric acid). The solutions thus obtained were analyzed by ICP-MS. The multi-acid digestion procedure is presented in Appendix A. The poor agreement between the total iron analysis by Digestion & ICP-MS and QXRPD indicated the presence of amorphous/poorly crystalline iron oxide phases. A two-stage sequential extraction process determined the distribution of copper and nickel in the amorphous and crystalline iron oxide phases. The QXRPD data combined with sequential extraction data was

used to quantify the amorphous iron phases. These amorphous iron oxides/oxyhydroxides were found to be the main source of copper and nickel losses to the residue. The amount of copper and nickel associated with the amorphous phases was found to be $\sim 2\text{--}4$ times higher than that associated with the crystalline iron oxide phases.

4.1 Introduction to iron phases in leach residues

The residues from the hydrometallurgical processes usually contain elemental sulfur and iron oxide phases along with associated gangue minerals. The chemistry of iron precipitation in hydrometallurgical circuits is quite complex, and it can precipitate in different oxide forms with variable crystallinity. Iron precipitates can be divided into three regimes to explain the different iron phases in the leach residues in the present study: (i) crystalline (ii) poorly crystalline and (iii) amorphous iron oxides. The regime (i) phases usually constitute hematite, goethite, and jarosite. The possible phases in regime (ii) can be hematite and goethite, as both phases have been shown to exhibit variable crystallinity (Johnston and Glasby, 1978; Machala et al., 2007; Schwertmann et al., 1985), and regime (iii) can contain phases such as ferrihydrite and schwertmannite. These regimes exist on a continuum.

Ferrihydrite, discussed in Section 2.4, although often labeled as amorphous is not strictly amorphous (Jambor and Dutrizac, 1998; Janney et al., 2001, 2000a, 2000b) and commonly refers to a range of poorly crystalline iron oxide phases of which 2-line ferrihydrite (exhibiting 2 broad XRD peaks) and 6-line ferrihydrite (exhibiting 6 broad XRD peaks) are more common. Several studies on hydrometallurgical residues have identified the presence of regime (iii) phases.

Loan (2002) identified approximately 40–50% 6-line ferrihydrite in the paragoethite process, which is used in zinc hydrometallurgy. Sahu and Asselin (2011), identified ferrihydrite in one of thirteen medium temperature sulfide leach residue samples. Steel et al. (2010), identified phases which were soluble in the reagents selective for amorphous iron oxides. However, true quantification of these phases, in hydrometallurgical residues, and associated valuable metal loss remains an issue in hydrometallurgy. In all the studies discussed above, the possible presence of regime (ii) phases was not addressed.

The amorphous/poorly crystalline phases do not respond to the X-ray diffraction as crystalline phases do. The regime (ii) and regime (iii) phases, if not considered carefully, result in inaccurate quantification of the crystalline phases determined by regular XRD. The leach residues have gangue minerals that can also contribute to the regime (ii) and regime (iii) phases. The focus of this study will be the iron oxide phases in the regime (ii) and (iii). The presence of regime (ii) and (iii) phases in CESL and Vale residues is determined by QXRPD combined with the elemental analysis from Digestion & ICP-MS and sequential extraction. TEM and Mössbauer studies complemented the results.

4.2 Samples and leaching conditions

Sulfide concentrate leach residue samples (labeled as S1, S2, and S3) were supplied from CESL (S1 and S2) and Vale (S3) operations. The Munsell color of sample S1 was 7.5YR 5/6 (strong brown dry), sample S2 was 10R 4/6 (red-dry), and sample S3 was 10R 3/6 (dark red-dry). The

mineralogy of the concentrates used to generate the three samples is given in Table 4-1. The general conditions under which samples were generated are given in Table 4-2.

Table 4-1: Mineralogy of concentrates pertaining to leach residues S1, S2, and S3

Phase name	Formula	R (wt %)		
		S1	S2	S3
Chalcopyrite	CuFeS ₂	38	35	7
Cubanite	CuFe ₂ S ₃	-	30	-
Enargite	Cu ₃ AsS ₄	20	1	-
Pyrite	FeS ₂	18	-	-
Bornite	Cu ₅ FeS ₄	7	-	-
Covellite	CuS	5	-	-
Tennantite	(Cu,Fe) ₁₂ As ₄ S ₁₃	2	-	-
Sphalerite	(Zn,Fe)S	2	-	-
Pentlandite	(Fe,Ni) ₉ S ₈	-	5	63
Pyrrhotite	Fe _{1-x} S	-	7	29
Others	Gangue	8	22	1

Table 4-2: Leaching conditions that generated leach residues S1, S2, and S3

^a Operating parameters	Unit	S1	S2	S3
Total pressure	kPa(g)	1298	1264	1030
Temperature	°C	150	150	150
Retention time	min	91	58	80
Free acid concentration	g/L	10.7	0.0	10-12
Solids loading	%	10.2	23.2	^b 5
[Cl ⁻]	g/L	11.2	10.4	5

^aThe horizontal Ti autoclave has four compartments, the first is larger and contains 2 agitators, the other three have only one agitator. It has a 2:1 ellipsoidal head with an inner diameter of 2.1m and a length of 10.7m (tangent-tangent);

^bThe Vale process operates at low solids loading due to restrictions on the tank house capacity. Feed slurry diluted with coolant and anolyte from electrowinning before entering the autoclave.

The leach residues, produced from the leaching of sulfide concentrates, were washed, sampled, and dried in an oven at 60°C overnight. Dried samples were lightly ground with an agate mortar and pestle and a portion completely digested using a combination of HCl (hydrochloric acid), HNO₃ (nitric acid), HF (hydrofluoric acid) and HClO₄ (perchloric acid) with the resulting solution analyzed by ICP-MS.

4.3 Quantitative X-ray powder diffraction (QXRPD)

Quantitative phase analysis was performed using the Rietveld method and X-ray powder diffraction data. For this purpose, each sample was reduced into a fine powder (~10 µm) to obtain an optimum grain-size range for X-ray analysis. A vibratory micronizing mill was used for this purpose. Corundum was employed as an internal standard for quantification of the relative amounts of crystalline and amorphous phases. Continuous-scan X-ray powder-diffraction data was collected over a range of 3–80° 2θ with CoKα radiation on a Bruker D8 Focus Bragg–Brentano diffractometer. The X-ray diffractograms were analyzed utilizing the International Centre for Diffraction Database PDF-4 and Search-Match software DiffracPlus Evaluation 19.0.0.0 before the Rietveld analysis.

The amorphous content was estimated by adding a weighed amount of a spike phase (NIST Standard Reference Material 676a) with known crystallinity of 99.02 wt%. In the presence of amorphous content, the amount of spike is overestimated, and the amorphous content can be determined. The illustration of the procedure is provided in Appendix B. This method enables the measurement of the amorphous content with an accuracy of close to 1% (De La Torre et al., 2001). The comparison of the phases using regular XRD and QXRPD is given in Table 4-3. The X-ray

amorphous content was varied between 30.5 and 52.7 wt% as shown in Table 4-3. The fraction of the amorphous phase resulting from the presence of regime (ii) and/or regime (iii) phases was determined by sequential extraction scheme as shown in Figure 4-1.

Table 4-3: Comparison of phases in samples S1, S2, and S3 as determined by XRD and QXRPD
X-ray amorphous content varies from 30.5 to 52.7 % (error ± 2 %)

Phase name	Ideal formula	Regular XRD			QXRPD		
		S1	S2	S3	S1	S2	S3
Albite low	NaAlSi ₃ O ₈	2.0	4.4	-	0.9	2.5	-
Chalcopyrite	CuFeS ₂	-	-	0.3	-	-	0.2
Goethite	α -Fe(III)O(OH)	-	6.3	11.5	-	3.5	8.0
Gypsum	CaSO ₄ .2H ₂ O	6.8	-	1.5	3.2	0.6	1.0
Hematite	α -Fe ₂ O ₃	-	37.1	50.4	-	20.6	35.0
Jarosite	KFe(III) ₃ (SO ₄) ₂ (OH) ₆	28.6	1.1	1.5	13.5	0.6	1.0
Lizardite 1T	Mg ₃ Si ₂ O ₅ (OH) ₄	2.8	-	-	1.3	-	-
Muscovite	KAl ₂ (Si ₃ Al)O ₁₀ (OH,F) ₂	8.3	4.0	-	3.9	2.2	-
Pyrite	FeS ₂	3.3	-	-	1.5	-	-
Quartz low	SiO ₂	9.0	-	-	4.2	-	-
Sulfur	S ₈	34.5	34.9	34.8	16.3	19.6	24.2
Talc 1A	Mg ₃ Si ₄ O ₁₀ (OH) ₂	3.8	12.1	-	1.8	6.7	-
Tennantite	(Cu, Fe) ₁₂ As ₄ S ₁₃	1.1	-	-	0.5	-	-
X-ray amorphous		-	-	-	52.7	44.5	30.5
Total		100	100	100	100	100	100

4.4 Iron phases by sequential extraction

In order to determine the amounts of amorphous and crystalline iron oxides/oxyhydroxides in leach residue samples and the distribution of copper/nickel in these phases, a two-stage sequential extraction was employed in this study. Hydroxylamine hydrochloride (HaHC) was the preferred reagent for selective extraction of the amorphous or poorly crystalline iron oxides/oxyhydroxides.

Studies of metal partitioning in soils and sediments have used selective dissolution of Fe and Mn oxides, to release the associated trace elements, with different types of acids and reducing reagents (Borggaard, 1982, 1981, 1976; Brook and Moore, 1988; Chao and Zhou, 1983; McCarty et al., 1998; Tessier et al., 1979). Such studies have not been able to directly demonstrate that the various extraction solutions specifically remove metals from only one component (e.g., ferric oxides only). It is not clear which crystalline phases (e.g., goethite or magnetite, etc.) are preferentially dissolved, even though claims are made as to species and crystallinity of the recovered compounds (Cornell and Schwertmann, 1996; Zelany et al., 1986).

A 0.2 M acid oxalate buffer (pH 3, with extraction over 4 h in the dark) has been considered a fairly specific solvent for ferrihydrite and other amorphous iron oxyhydroxides and has been widely used in the past for the selective dissolution of these phases. (Farmer et al., 1983; Parfitt and Childs, 1988). Borggaard (1982, 1979) concluded that ethylenediaminetetraacetic acid (EDTA) could selectively extract amorphous iron oxides from mixtures of crystalline iron oxides including goethite and hematite. A neutrally buffered citrate bicarbonate dithionite (CBD) system has been used for complete removal of free iron oxides (Mehra and Jackson, 1960). The most

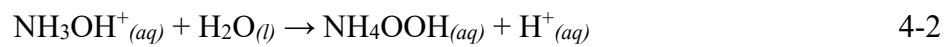
widely used chemical extractions for iron are those utilizing dithionite (Canfield, 1989; Mehra and Jackson, 1960), HaHC (Berger et al., 2008; Chester and Hughes, 1967) or ammonium oxalate (McKeague and Day, 1966; Phillips and Lovley, 1987).

The comparisons between these methods (Kostka and Luther, 1994; Poulton and Canfield, 2005; Raiswell et al., 1994) have clearly shown that HaHC is the most selective for iron oxyhydroxides, especially ferrihydrite. The use of HaHC for selective extraction of poorly crystalline/amorphous iron oxides was also preferred over other methods by Chao and Zhou (1983). It has the following advantages over the commonly used oxalate method: The oxalate method is complicated because it requires the extraction to be done in the dark over 4 h, it also recovers, in some cases, magnetite, and goethite (Brady et al., 1986; Golden et al., 1994; Rhoton et al., 1981), and Fe (II) catalyzes the reduction and dissolution of hematite in the presence of oxalate, and this same reaction has been shown to reductively recover magnetite (Luther et al., 1992; Sulzberger et al., 1989).

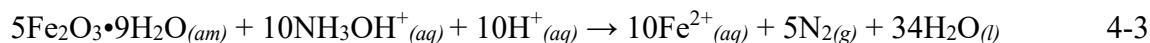
In comparison, HaHC is fast (30 min, does not require darkness), only attacks ferrihydrite and does not recover crystalline phases (<1 % of total iron) (Chao and Zhou, 1983). The dissolution of ferrihydrite by HaHC occurs by reduction of Fe(III) to Fe(II) like the dissolution mechanism of manganese oxide by reduction of Mn^{3+} to Mn^{2+} (Neaman et al., 2004) as shown in Reaction 4-1,



The hydrolysis of $NH_2OH-HCl$ in water produces protons consumed by the Reaction 4-2,



It can be assumed that HaHC dissolves ferrihydrite in the leach residues by the same theoretical mechanism as described above for manganese oxide as shown in Reaction 4-3,



The two-stage sequential extraction scheme is given in Figure 4-1. The regime (iii) phases, along with the water-soluble phases were recovered in the first stage. The regime (i) and (ii) phases were leached in the second stage.

In the first stage of extraction, ~ 5 g of the leach residue (R) was leached using 0.25 M HaHC and 0.25M hydrochloric acid at 50°C under atmospheric pressure for 30 min, keeping the solid to the liquid mass ratio at 1:50. The reaction mixture was filtered and analyzed for Cu, Fe, Ni, As, Si and Ca. The remaining residue (R1) was dried in an oven at 60°C, weighed and the percent weight loss was calculated. In the second stage, ~1.5 g of R1 was leached with 4 M hydrochloric acid at 95°C and atmospheric pressure for 30 min keeping the solid to the liquid mass ratio 1:50. The filtrates were analyzed for Fe, Cu, Ni, As, Si and Ca. The remaining unleached residue (R2) was dried in an oven at 60°C, weighed and the percent weight loss calculated. In some experiments where residue R2 was less than one gram, experiments were repeated several times to generate enough sample for characterization. After necessary correction for the water-soluble phases (crystalline gypsum) from the weight loss in the first stage extraction, the amount of regime (iii) phases was

determined. The weight loss in the second stage extraction gives the amount of regime (i) and (ii) iron oxide phases. Each sample was put through the two-stage sequential process eight times. Additionally, for each stage, two different solid to liquid ratios were utilized to check the reproducibility. The weight losses were within a standard deviation of 2%.

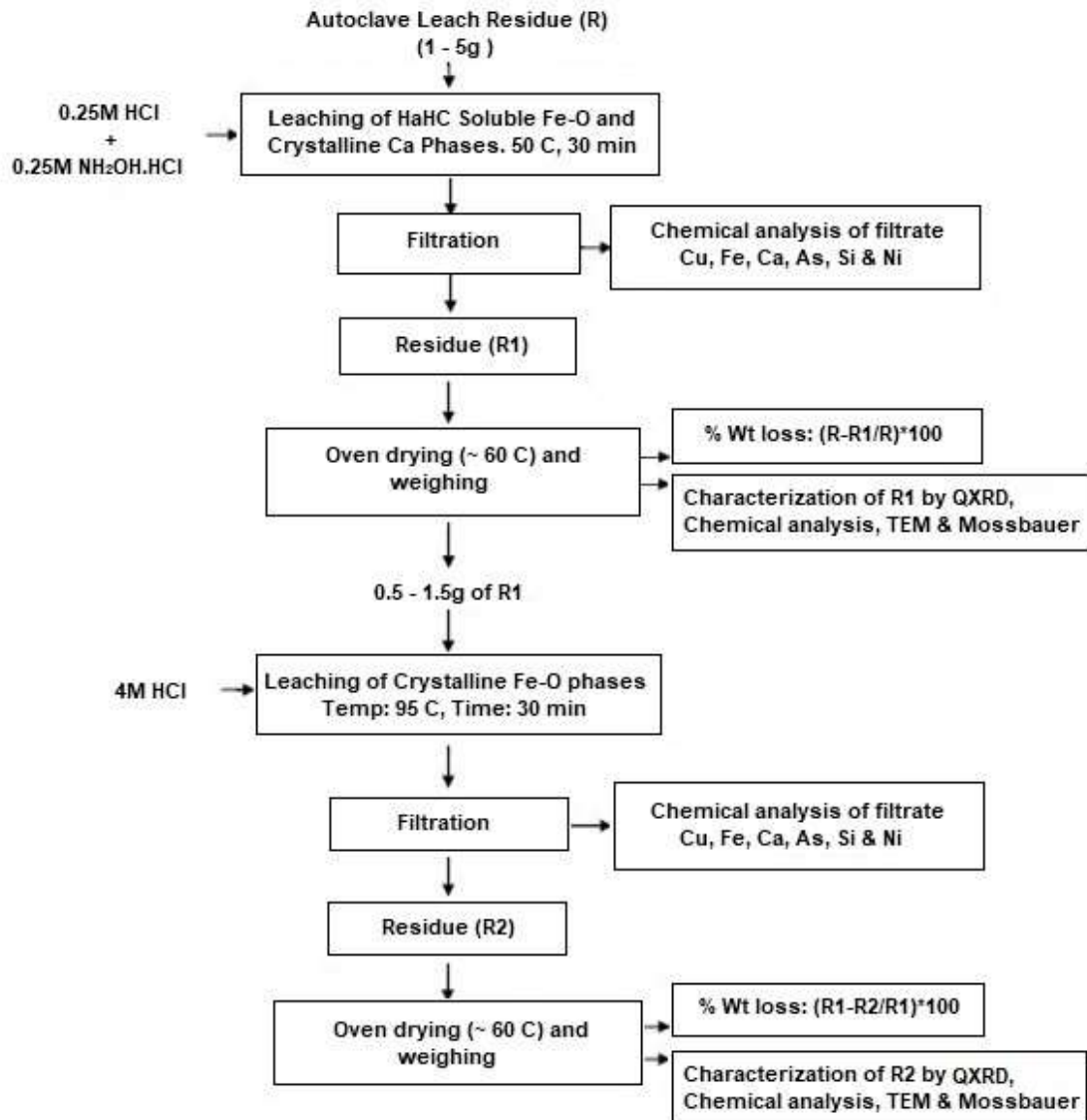


Figure 4-1: Sequential extraction scheme for the determination of HaHC soluble and crystalline iron oxides phases

The chemical analysis of the solid residue samples showed the presence of 1.1 and 1.4 wt% Cu, in samples S1 and S2, respectively, and approximately 1.0 wt% Ni in sample S3. The distribution of copper and nickel in different phases as determined by the two-stage sequential extraction technique are presented in Table 4-4.

Chemical analysis for Fe, Cu, As, Si, Ca and Ni was carried out on both the 1st stage and 2nd stage filtrates. Cu and Ni recovered during 1st stage extraction was attributed to regime (iii) phases, i.e., when these phases are recovered in 1st stage extraction, Cu and Ni associated with these phases are also solubilized. Regime (iii) phases are calculated after necessary correction for calcium, as 1st stage extraction results in calcium dissolution also.

The first stage extraction used in this study is considered selective for the dissolution of amorphous iron oxide phases and has been successfully used by many authors (Berger et al., 2008; Chao and Zhou, 1983; Chester and Hughes, 1967; Sahu and Asselin, 2011). As discussed earlier, this technique has several advantages over the conventional oxalate method (Raiswell et al., 1994). The Cu/Ni recovered during the 2nd stage extraction is thus associated with regime (i) and (ii) phases. All the elemental percentages are reported as a percentage of R. For example, “10% Fe” means that 10% of R was Fe. Total iron calculated from the two-stage extraction agrees well with the Digestion & ICP-MS analysis of solids in all three samples as shown in Table 4.3. The slight difference between sequential extraction iron data and the Digestion & ICP-MS iron data is attributed to the phases containing iron that remained un-recovered throughout the two-stage extraction as determined by QXRPD of residue (R2) (tennantite, pyrite, and chalcopyrite).

Table 4-4: Distributions of Fe, Cu, As, Ca and Ni in mass percent determined by the 1st and 2nd stages of sequential extraction and compared to Digestion & ICP-MS of the dried as-received solids

Sequential extraction	S1	S2	S3
Fe 1 st stage extraction (%)	12.1	4.5	1.1
Fe 2 nd stage extraction (%)	9.7	27.8	38.0
Total Fe (sequential extraction) (%)	21.8	32.3	39.1
Total Fe (Digestion & ICP-MS of R) (%)	22.6	32.8	40.0
% Fe recovered by sequential extraction	96.5	98.5	97.5
Cu 1 st stage extraction (%)	0.50	0.38	0.05
Cu 2 nd stage extraction (%)	0.23	0.94	0.46
Total Cu (Sequential extraction) (%)	0.73	1.32	0.51
Total Cu (Digestion & ICP-MS of R) (%)	1.1	1.38	0.57
% Cu recovered by Sequential extraction	66	96	89.5
Ni 1 st stage extraction (%)	-	-	0.05
Ni 2 nd stage extraction (%)	-	-	0.70
Total Ni (sequential extraction) (%)	-	-	0.75
Total Ni (Digestion & ICP-MS of R) (%)	-	-	0.90
% Ni recovered by sequential extraction	-	-	83.3
As 1 st stage extraction (%)	2.69	0.002	-
As 2 nd stage extraction (%)	2.64	0.320	-
Total As (Digestion & ICP-MS of R) (%)	6.10	0.340	-
Total Si (Digestion & ICP-MS of R) (%)	6.6	9.5	0.23
Ca 1 st stage extraction (%)	0.72	0.03	0.2
Ca 2 nd stage extraction (%)	0.061	0.37	0.03
Total Ca (%)	0.78	0.40	0.23

When ratios of Cu/Fe and Ni/Fe for the 1st and 2nd stage extractions were compared it was found that, in all cases, the ratios were higher for 1st stage extraction than for 2nd stage extraction as shown in Table 4-5. The copper and iron recovered during 1st stage extraction is compared in

Figure 4-2. It is clear from that a higher amount of amorphous iron leads to higher loss of Cu to the residue.

Table 4-5: Comparison of ratios of Cu/Fe and Ni/Fe during 1st and 2nd stage extractions

Sample	1 st stage	2 nd stage	1 st stage	2 nd stage
	Cu/Fe	Cu/Fe	Ni/Fe	Ni/Fe
S1	4.13	2.37	-	-
S2	8.44	3.38	-	-
S3	5.0	1.33	4.5	1.84

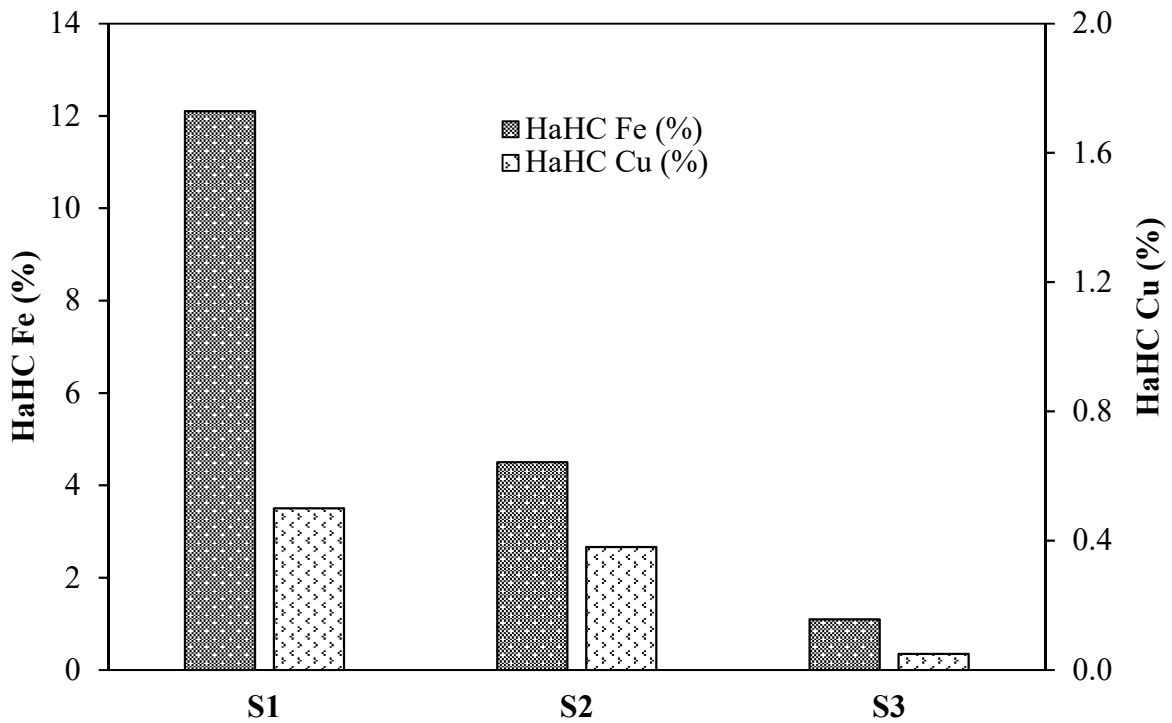


Figure 4-2: Fe and Cu dissolved by HaHC extraction for the samples S1, S2, and S3

4.5 Iron analysis comparison

Total iron determined from QXRPD and Digestion & ICP-MS analysis of the residues is compared in Table 4-6. All the elemental percentages are reported as a percentage of R as mentioned above. Only 5.3% iron in sample S1 is in the crystalline form, distributed among different minerals as determined by QXRPD (Table 4-3). The remaining iron (17.3%, Table 4-6) in S1, if present as a HaHC soluble phases, then the chemical analysis of 1st stage filtrate should have detected the remaining 17.3% as iron. However, only 12.1% of iron was recovered during the 1st stage of extraction, and the 2nd stage extraction recovered 9.7% iron. All iron oxides that remain unrecovered during 1st stage are recovered in the 2nd stage. Jarosite also is recovered during 2nd stage extraction, but other non-oxide (e.g., pyrite and tennantite) iron phases remain intact. After considering the iron from jarosite, it was found that approximately 5% of iron remained unaccounted for in unknown phases. This unaccounted iron was assigned to the regime (ii) phases. In a similar way, about 11.5% and 9.1% iron was found to be associated with regime (ii) phases in sample S2 and S3, respectively.

Table 4-6: Comparison of total Fe from Digestion & ICP-MS, QXRPD, 1st and 2nd stage extraction for S1, S2, S3

Sample	Total Fe %				
	Digestion & ICP	QXRPD	ICP-QXRPD	1 st stage	2 nd stage
S1	22.6	5.3	17.3	12.1	9.7
S2	32.8	16.8	16.0	4.5	27.8
S3	40.0	29.9	10.1	1.1	38.0

4.6 Determination of HaHC soluble amorphous phases

Based on the comparison of mass loss during 1st stage sequential extraction with the amount of amorphous content determined by QXRPD (Table 4-3), the amount of hydroxylamine hydrochloride (HaHC) soluble phase was determined. These phases are a subset of the X-ray amorphous phases and do not contribute to the diffraction patterns. These are recovered by a mild chemical attack by HaHC during sequential extraction. The amount of HaHC amorphous phase was calculated as Equation 4-4:

$$\text{HaHC (\%)} = \left(\frac{R - R1}{R} \right) * 100 - X \quad 4-4$$

Where R is the total mass of residue, R1 is the mass of the residue left after the first stage of extraction, and 'X' is the difference between the weight percent of phases in 'R' and 'R1' calculated from the QXRPD data as shown in Table 4-7. This difference was not considered when it was less than 1.0 wt%.

The difference between the amorphous phases calculated from sequential extraction and the QXRPD amorphous content of R and R1 were in good agreement (Table 4-7). These values also agree well with the mass balance of the Digestion & ICP-MS iron from first stage filtrates. For example, in the case of sample S1, the difference between QXRPD amorphous content of 'R' and 'R1' was 24.6 wt% while amorphous phase by sequential extraction was calculated to be 25.8 wt% (Table 4-7). In the case of S1 and S2, the difference between QXRPD amorphous content of R and R1 was 5.9 and 3.0 wt% while the amorphous phase by sequential extraction was calculated to be

7.2 and 2.2 wt%. Similarly, Digestion & ICP-MS analysis of the first stage filtrates showed the presence of ~12.1 wt% Fe.

Table 4-7: QXRPD analysis of samples S1, S2 and S3; as received (R), after 1st stage extraction (R1) and 2nd stage extraction (R2)

Weight loss during sequential extraction(SX), X-ray amorphous phase, and HaHC amorphous phases are compared. Weight losses for R1 and R2 are due to first and second stage extractions, respectively. Results are within 2 wt% error. R1 and R2 corrected for weight loss using Rietveld refinement

Phase name	Ideal formula	R (wt%)			R1 (wt%)			R2 (wt%)		
		S1	S2	S3	S1	S2	S3	S1	S2	S3
Albite low	NaAlSi ₃ O ₈	0.9	2.5	-	-	2.3	-	-	1.5	-
Alunite	KAl ₃ (SO ₄) ₂ (OH) ₆	-	-	-	-	-	-	0.2	0.2	-
Boehmite	AlO(OH)	-	-	-	-	-	-	0.4	0.2	-
Calcite	CaCO ₃	-	-	-	-	0.3	0.9	0.4	0.5	-
Chalcopyrite	CuFeS ₂	-	-	0.3	-	-	-	-	-	0.3
Goethite	α -Fe(III)O(OH)	-	3.5	8.0	-	3.9	10.1	-	-	-
Gypsum	CaSO ₄ .2H ₂ O	3.2	-	1.0	-	-	-	-	-	-
Hematite	α -Fe ₂ O ₃	-	20.6	35.0	-	17.9	33.6	-	-	-
Jarosite	NaFe(III) ₃ (SO ₄) ₂ (OH) ₆	13.5	0.6	1.0	8.2	-	-	-	-	-
Lizardite 1T	Mg ₃ Si ₂ O ₅ (OH) ₄	1.3	-	-	0.7	-	-	0.3	1.1	-
Magnetite	Fe ₃ O ₄	-	-	-	-	-	-	-	0.3	-
Muscovite	KAl ₂ (Si ₃ Al)O ₁₀ (OH,F) ₂	3.9	2.2	-	1.4	-	-	1.5	-	-
Pyrite	FeS ₂	1.5	-	-	1.0	-	-	1.1	0.3	0.1
Quartz low	SiO ₂	4.2	-	-	4.0	-	-	4.7	0.9	-
Sulfur	S ₈	16.3	19.6	24.2	17.2	20.4	23.4	20.7	21.6	22.9
Talc 1A	Mg ₃ Si ₄ O ₁₀ (OH) ₂	1.8	6.7	-	-	4.6	-	-	4.0	-
Tennantite	(Cu, Fe) ₁₂ As ₄ S ₁₃	0.5	-	-	0.5	-	-	0.7	-	-
X-ray amorphous		52.7	44.5	30.5	28.1	38.6	27.5	24.0	15.4	8.8
SX wt. loss		-	-	-	38.8	12.0	4.6	46.0	54.0	68.0
Total		100	100	100	100	100	100	100	100	100
HaHC amorphous		25.8	7.2	2.2	-	-	-	-	-	-

The stoichiometry of the iron compound dissolved in the first stage is not known. If it is assumed to be ferrihydrite with the generally accepted formula $5\text{Fe}_2\text{O}_3 \cdot 9\text{H}_2\text{O}$, the mass balance of the iron dissolved in the first stage indicates the presence of ~ 20 wt% ferrihydrite which is very close in comparison to the amorphous content calculated from QXRPD and sequential extraction. The amorphous/poorly crystalline iron oxyhydroxides identified in many soils (Schulze, 1981; Schwertmann et al., 1982; Taylor, 1959) and in hydrometallurgical residues (Claassen et al., 2002; Loan et al., 2002a, 2002b, 2006; Steel et al., 2010; Sahu and Asselin, 2011) were reported to be ferrihydrite. However, ferrihydrite could not be conclusively identified with sequential extraction and quantitative phase analysis.

4.7 Transmission electron microscope

The transmission electron microscope (TEM) is an important tool for the microstructural characterization of iron phases in leach residues. The basic principle in the case of the TEM is that the beam of electrons is transmitted from the sample, magnified, and then recorded using photographic film or digital imaging. Like X-ray diffraction technique, TEM can provide selected area electron diffraction crystallographic patterns by generating information about the arrangement of atoms, imaging of atomic scale defects, and the degree of crystalline order from the residues. In the XRD diffraction, the patterns measured are more quantitative than electron diffraction patterns measured by TEM. However, the electrons can be focused easily, and this is a significant advantage the electrons have over the X-rays. The diffraction patterns can be measured from microscopic regions by focusing the electron beam. It is often possible to select a single microcrystal for a diffraction measurement. The high-energy electrons in TEM cause electronic

excitations of the atoms in the specimen. TEM uses energy-dispersive X-ray spectrometry (EDS), to obtain chemical information from electronic excitations. The X-ray spectrum is acquired from small regions of the specimen illuminated with a focused electron beam. The characteristic X-rays from the chemical elements are used to determine the concentrations of the different elements in the sample. In scanning transmission electron microscope (STEM), a narrow ($\sim 1-10 \text{ \AA}$), a focused beam of electrons is moved in across the specimen. The emitted X-rays, secondary electrons, or backscattered electrons data is then acquired from the sample. The STEM mode of operation is beneficial for spectroscopy work, as it allows the acquisition of a “chemical map” of the sample. In a leach residue sample, we could make an image of the distribution of Fe in a sample if we were to measure the emission of Fe $K\alpha$ X-rays with the EDS spectrometer (Fultz and Howe, 2013).

In the case of nanocrystalline phases, the TEM is a versatile tool for obtaining information in real-space, i.e., directly from images and in reciprocal space, i.e., from diffraction (Bendersky and Gayle, 2001). Diffraction can be achieved by two common approaches, selected area diffraction (SAED) or convergent-beam electron diffraction (CBED), simply known as nano-diffraction. In SAED, a nearly parallel beam of electrons as small as $\sim 100 \text{ nm}$ in diameter is used to perform selected-area electron diffraction on particles. SAED is feasible on individual crystals, but it becomes problematic when the maximum particle dimensions are significantly less than the size of the beam (i.e., $\ll 100 \text{ nm}$) (Steeds and Morniroli, 1992). Therefore, in the case of nano-sized particles ($< 10 \text{ nm}$), SAED is instead performed by illuminating with the electron beam groups of particles aggregated with various orientations. The diffraction pattern resulting from scattering of many particles is characterized by rings instead of spots. Nano-diffraction involves diffraction on

extremely small individual crystals (Morniroli, 2006; Morniroli and Steeds, 1992). A convergent beam of electrons covering a range of incident angles can be focused to a spot size less than 1 nm in diameter. When directed at an individual particle the scattering generated results in a disc diffraction pattern and contained information of the structure. However, since it is not possible to tilt an individual crystal to any orientation, many diffraction patterns are obtained on many different particles, each with a different orientation. In both SAED and nano-diffraction, the resulting electron diffraction pattern (rings or discs) are ultimately treated in a manner synonymous with using standard XRD structure determination and analysis methods. The Bragg features are identified, and structural information is obtainable by matching it to known structure types.

In the direct measurement of crystal dimensions, crystal morphology and phase identification of iron oxides, TEM has proven to be a powerful technique. Schwertmann and Cornell (2000), reported that they could detect X-ray amorphous iron oxide phases with TEM. TEM was used to study the effect of the acid attack on akageneite, and it was found that the crystals became hollowed out in the [001] direction (Cornell and Giovanoli, 1988). Cornell et al. (1990) studied the effect of cysteine on goethite formation from ferrihydrite and were able to identify changes in the crystalline morphology. Cornell et al. (1987) used TEM to observe the effect of silicate species on the transformation of ferrihydrite to goethite and hematite crystals and found that silicate species retards the transformation. TEM was also used to study the transformation of ferrihydrite to manganian goethite or jacobsonite in the presence of manganese (Cornell and Giovanoli, 1987). The transformation of ferrihydrite in the presence of cobalt was studied, and it was found that goethite is suppressed in favor of hematite and magnetite (Cornell and Giovanoli, 1989). It was found that

the presence of copper slows the transformation of ferrihydrite ($5\text{Fe}_2\text{O}_3 \cdot 9\text{H}_2\text{O}$) into crystalline products (Cornell and Giovanoli, 1988). The extremely high magnification power of TEM has proven invaluable for the identification of crystal shapes, defect recognition and direct crystal measurements.

Loan et al. (2002), positively identified ferrihydrite in the hydrometallurgical residues using TEM. The broad reflections in an XRD pattern of ferrihydrite are the result of poor long-range structural order and very small primary particle size (1-7 nm). The number of these reflections seen as diffuse rings in electron diffraction (ED) patterns provides a basis for nomenclature and identification of ferrihydrites with different degrees of crystallinity, e.g., 2-line and 6-line ferrihydrite. TEM combined with SAED is an important ferrihydrite identification technique. It allows the poorly diffracting ferrihydrite to be discriminated from other phases. Morphology can be a good discriminator with conformation from SAED, as goethite generally precipitates with high aspect ratios, hematite as dense rhombs, plates, and prisms, and 2-line ferrihydrite as aggregates of 1-3 nm rounded crystals or 3-7 nm crystals with more hexagonal facets for 6-line ferrihydrite as listed in Table 4-8.

Two different TEM instruments were used for the analysis of the leach residue samples. TEM and SAED analyses were performed using an FEI Tecnai G2 instrument with a LaB_6 filament operated at 200 kV. The elemental mapping was carried out using FEI Tecnai Osiris™ scanning TEM (STEM) and EDX. This TEM is equipped with Super-X field emission gun and ChemiSTEM™ X-ray detection technology operating at 200 kV. EDX analyses were done in STEM High angle annular dark field (HAADF) imaging mode. The Esprit software was used for qualitative and

quantitative elemental mapping. A small amount of the dried leach residue sample (0.01) g was sonicated for 30 minutes in 5 mL of ice-cooled Milli-Q™ water. A few drops of this suspension were placed on a holey carbon TEM gold grid and allowed to dry in air. The grid of gold was chosen to prevent interference during the EDX mapping of copper associated with ferrihydrite phases.

Table 4-8: Summary of the morphology of naturally occurring iron oxides and oxyhydroxides

Solid phase	Morphology	Reference
Ferrihydrite	Irregular and Spherical	Cornell and Schwertmann, 1996; Jambor and Dutrizac, 1998; Kennedy et al., 2004; Konishi and Xu, 2012; Schwertmann and Cornell, 2000
Jarosite	Acicular	Cornell and Schwertmann, 1996; Jambor and Dutrizac, 1998; Silva et al., 2012
Goethite	Acicular	Cornell and Schwertmann, 1996; Jambor and Dutrizac, 1998
Hematite	Rounded, rhombohedral, platy	Jambor and Dutrizac, 1998; Silva et al., 2012
Schwertmannite	Hedgehog or pin cushion like	Jambor and Dutrizac, 1998; Loan et al., 2005; Marescotti et al., 2012; Paikaray and Peiffer, 2012

4.7.1 Phase identification

The TEM work aimed to obtain morphological, structural and elemental distribution information for iron oxide/oxyhydroxide phases in the leach residues. TEM images, SAED pattern and EDS results discussed here to serve as evidence for amorphous, poorly crystalline and nanoscale phase

of iron oxyhydroxides recovered in sequential extraction. The initial tests were primarily to collect standard TEM images of leach residue samples S1, S2, S3 and perform some preliminary electron diffraction, with the purpose of identifying nanocrystalline ferrihydrite. The images displayed randomly shaped aggregates made up of sub-micron particles that appeared to be ferrihydrite as shown in Figure 4-3. The diffraction pattern of the aggregates contained amorphous rings indicating 2-line ferrihydrite and Figure 4-4 resembles 6-line ferrihydrite, with sharper rings in the diffraction pattern and appearance of lattice fringes as reported by Janney et al. (2001, 2000). Each individual particle of ferrihydrite is nanocrystalline, and the structural strain, a high surface to volume ratio and very small scattering domains give amorphous responses to bulk techniques like XRD. The sample S2 contained much larger acicular crystals (rods), which are most likely goethite as shown in Figure 4-5. The rods were far more crystalline (Cornell and Schwertmann, 1996) and rounded hematite particles were observed in sample S3 as shown in Figure 4-6.

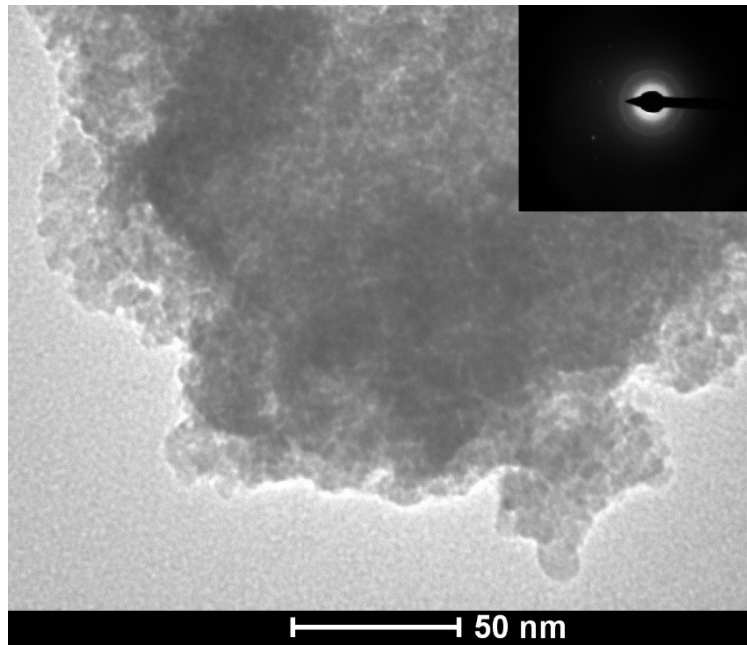


Figure 4-3: TEM image of 2-line ferrihydrite and diffraction pattern from sample S1

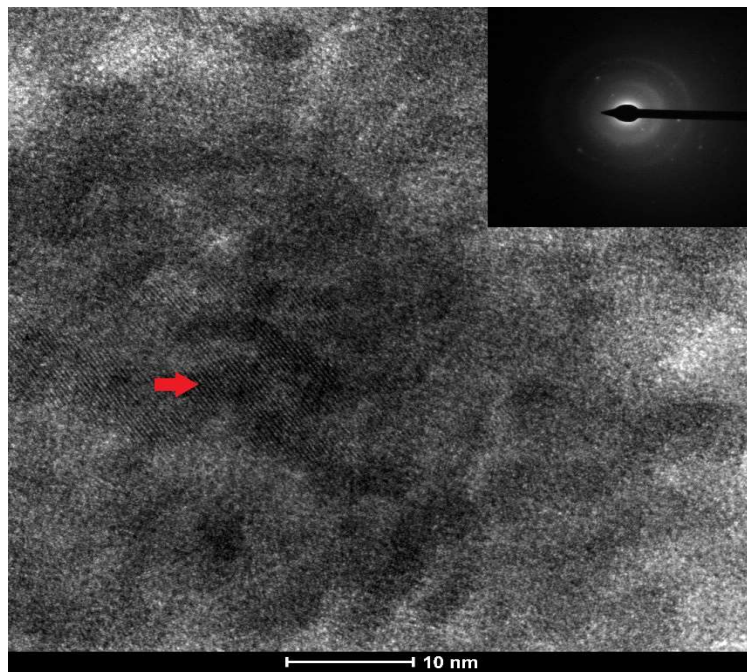


Figure 4-4: TEM image of 6-line ferrihydrite and diffraction pattern from sample S1
(lattice fringes marked with red arrow)

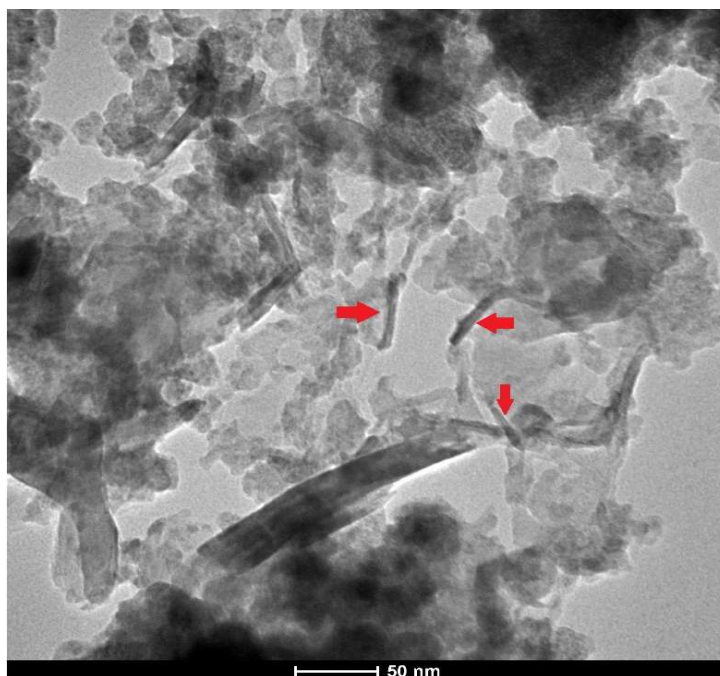


Figure 4-5: TEM image of acicular goethite nanorods from sample S2

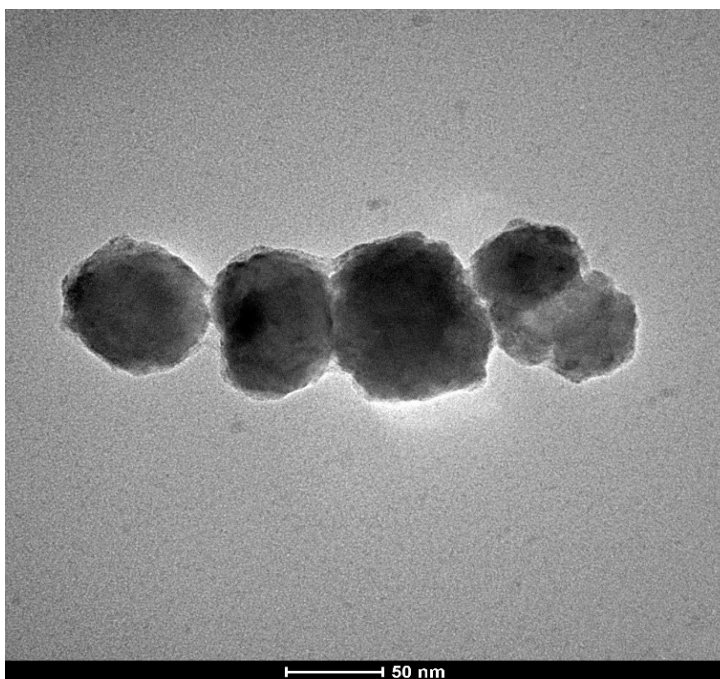


Figure 4-6: TEM image of rounded hematite particles from sample S3

There is no apparent presence of schwertmannite in either of the samples. As mentioned earlier, schwertmannite aggregates form as roughly spherical cores with fine needles radiating outward in all directions. This differs from ferrihydrite, which generally lacks such sharp features. Hockridge et al. (2009), showed that schwertmannite transforms into goethite and they also concluded that it is a ferrihydrite aggregate with goethite nanocrystals forming the radiating needles which are not seen in the residue samples analyzed for this work. CESL and Vale involve much greater hydrolysis rates because of higher iron concentrations and acidity. The effect of these conditions is to favor ferrihydrite formation, creating the mixture of phases observed in these samples. High hydrolysis rates will increase the number of nucleation events and this, in turn, will produce more particles which will experience a greater number of collisions and hence the agglomeration of nanocrystalline phases as observed in TEM images.

4.7.2 Elemental mapping

The EDS spectra were taken, and positions were selected to analyze the relative intensities of iron, sulfur, and copper in the samples. The STEM-HAADF image with overlaid EDS mapping is presented in Figure 4-7. The iron maps closely mimic the thickness maps throughout the aggregates, suggesting that the bulk of the material consisted of the iron-containing phase. Whereas, the copper map seemed to display a more iron map-oriented association. There is a region of greater intensity around the areas of iron intensity, which may indicate a greater association of copper with the iron. The copper maps of all the aggregates analyzed show the association of copper with the iron phase. There is also sulfur adjacent to the aggregate, but very

minimal or no copper was found associated with the sulfur when compared to that associated with the iron phase.

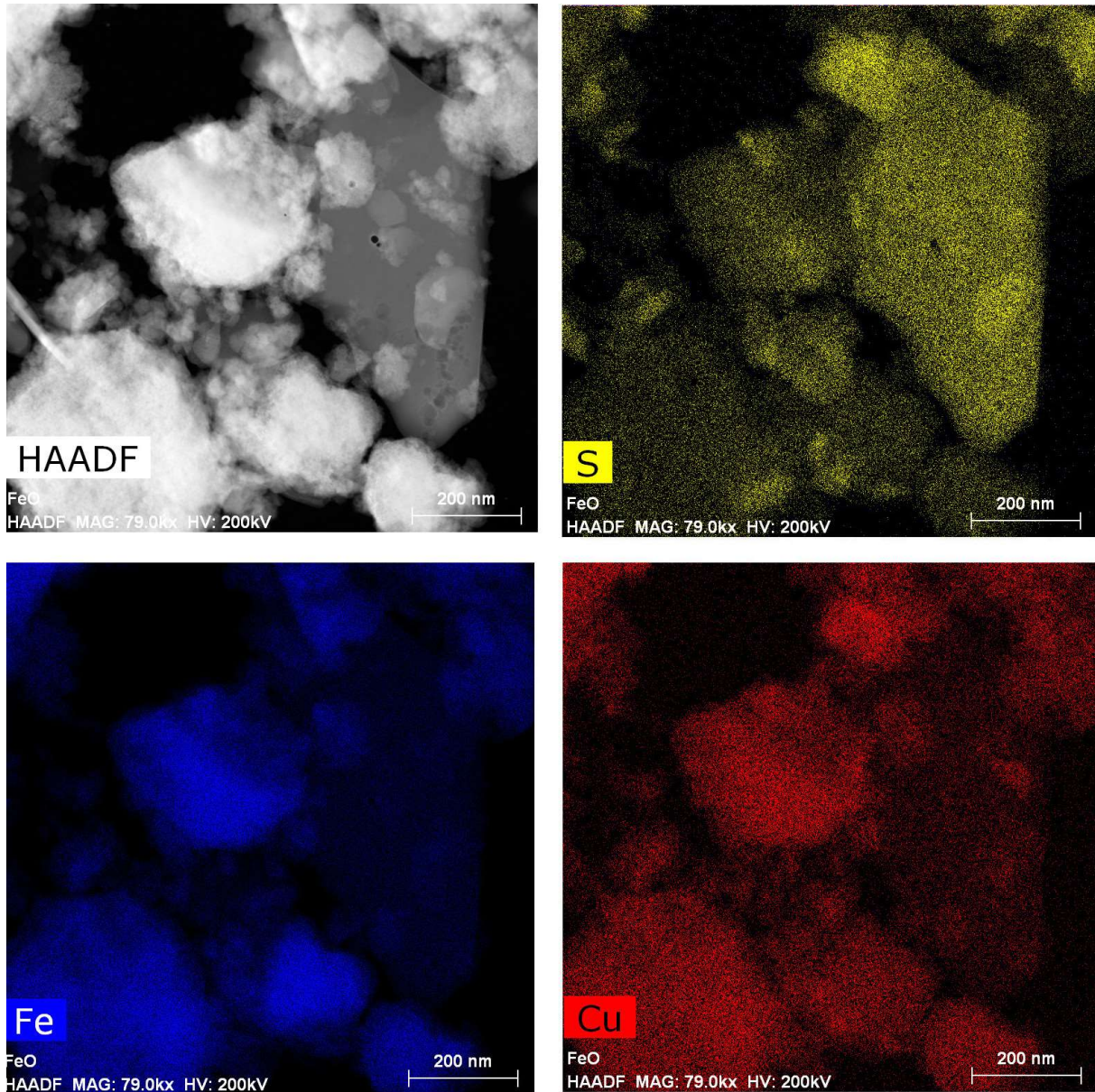


Figure 4-7: High-resolution TEM image of sample S1 with overlaid EDS mapping of S, Fe, and Cu
(scale bar 200nm)

There are strong iron, oxygen and copper peaks in the energy dispersive spectra (EDS) shown in Figure 4-8. Silica and arsenic are also found to be associated with ferrihydrite as reported by Dyer et al. (2012).

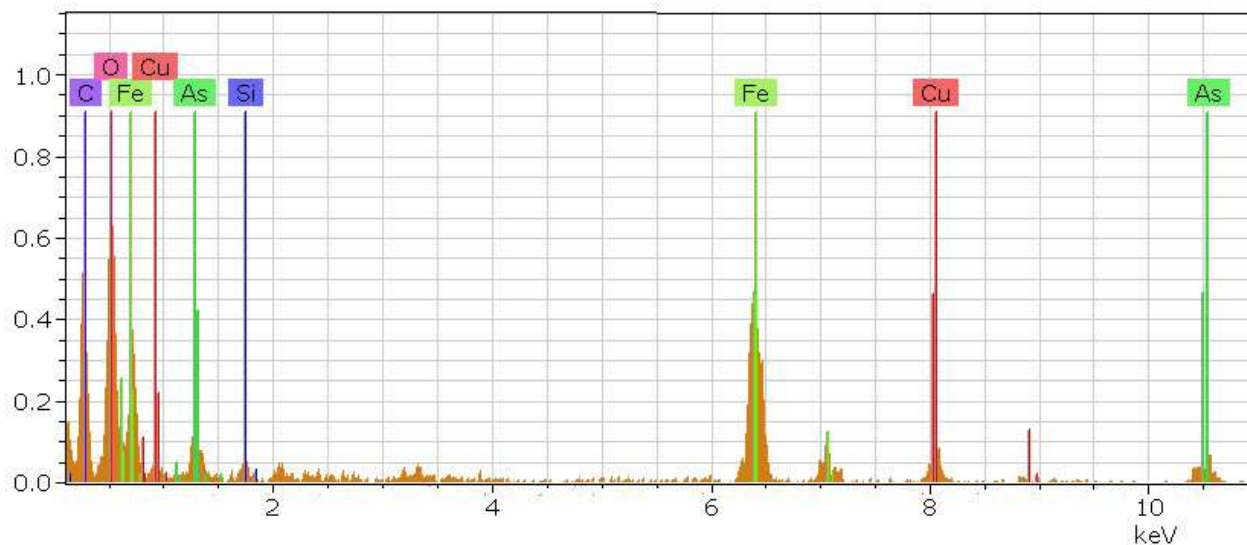


Figure 4-8: Spectrum from electron diffraction of sample S1

4.8 Mössbauer spectroscopy

Mössbauer spectroscopy is a bulk characterization technique that examines the nuclear excitation of an atom by gamma rays in the solid-state. The recoil-free technique of resonantly emitting and absorbing nuclear gamma rays is called the Mössbauer effect (Mössbauer, 2000, 1962). Mössbauer spectroscopy has the advantage of being impervious to all elements except that being examined, and therefore free from matrix effects which offer unique possibilities for studying the specific material characteristics or processes involving such an element. ^{57}Fe Mössbauer spectroscopy is among the most straightforward to operate and allows the characterization of iron speciation. ^{57}Fe Mössbauer spectroscopy provides information on the chemical and physical environments of Fe

within a solid material. A review of this technique and applications to iron oxides and oxyhydroxides is given in the text of Cornell and Schwertmann (1996). Distinct spectral signals can be obtained from both crystalline and non-crystalline forms of iron using Mössbauer spectroscopy, whereas XRD only provides information related to crystalline phases.

4.8.1 Mössbauer spectrometer and parameters

The basic elements of Mössbauer spectrometer are a γ ray source, an adsorber (sample), a detector, and a drive for the source or absorber as shown in Figure 4-9 (Dyar et al., 2006). The source is moved relative to the absorber, shifting the energy spectrum due to the Doppler effect. The spectra are usually graphed as percent transmission versus source velocity (energy). The interactions between the nucleus and its surrounding environment are known as hyperfine interactions. The hyperfine interactions depend strongly on the electronic, chemical, and magnetic state of the atom.

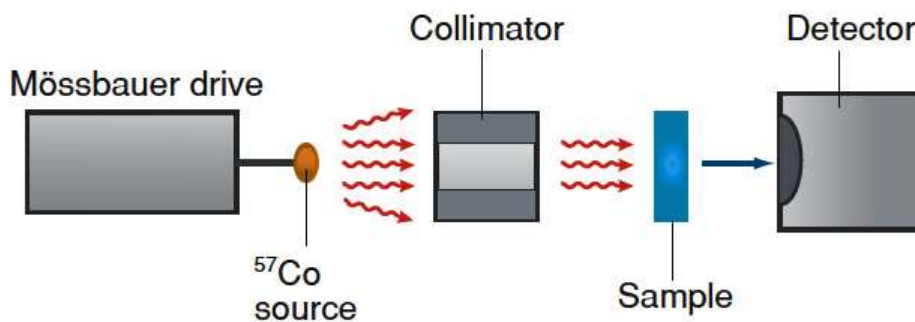


Figure 4-9: Basic elements of Mössbauer spectroscopy

(Dyar et al., 2006)

Information from these hyperfine interactions is provided by the hyperfine parameters such as isomer shift, quadrupole splitting and magnetic splitting as shown in Figure 4-10 and described in

Table 4-9. These parameters can be determined experimentally from the line positions in a Mössbauer spectrum. Several software packages are available to extract distributions of hyperfine parameters from Mössbauer spectra. Software for analysis of Mössbauer spectra uses a variety of physical models to generate model spectra to compare with the measured spectra, and different fitting algorithms to analyze the data. Lorentzian (Cauchy) line shapes are commonly employed in the modeling of Mössbauer spectra (Dyar et al., 2006; Hawthorne and Waychunas, 1988).

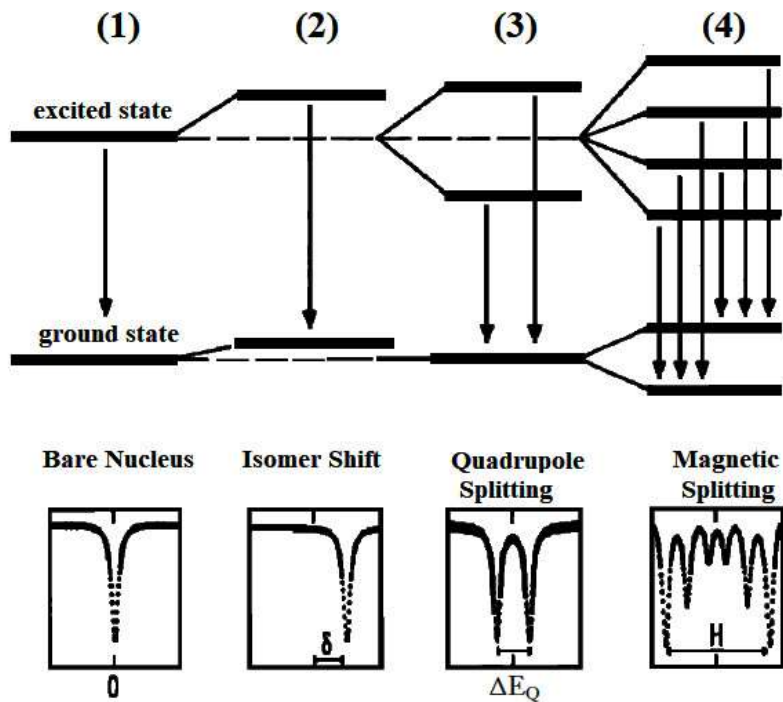


Figure 4-10: Hyperfine interactions for ^{57}Fe nuclei and resulting Mössbauer spectrum (McCammon, 1995)

Table 4-9: Description of Mössbauer parameters

(Adapted from McCammon, 1995)

Name	Units	Description
Electric monopole interaction (δ)	mm.s ⁻¹	It is a function of the electron density at the nucleus. Results in a displacement of the spectrum. Expressed as the velocity of the source. This isomer or chemical shift provides information about the coordination number, the valency and spin state of iron in the compound
Electric quadrupole interaction (ΔE_Q)	mm.s ⁻¹	It is generated when an electric field gradient acts on the nucleus. It provides information about site distortion, e.g., by specifically bound ligands. It increases with increasing distortion
Magnetic hyperfine field (B_{hf})	Tesla (T)	It provides information about the valence and magnetic properties of the compound. The spectra recorded at different temperatures as it depends on the temperature

4.8.2 Mössbauer spectra of leach residues

The samples for Mössbauer spectroscopy analysis were prepared by mixing ~40 mg of powdered leach residue sample with a powdered boron nitride. The ⁵⁷Fe Mössbauer spectra were acquired with a 50mCi ⁵⁷Co(Rh) source on a conventional spectrometer operating in constant-acceleration mode. Most spectra were obtained at room temperature, and some spectra were taken at lower temperatures using a vibration-isolated closed cycle helium refrigerator. The spectra were modeled using a conventional nonlinear least-squares minimization routine to the sum of Lorentzian lines with positions and intensities calculated utilizing a simple first-order perturbation model. Dr. Dominic Ryan performed Mössbauer analyses at the Physics Department, McGill University.

The Mössbauer spectra for samples S1, S2 and S3 are shown in Figure 4-11. Sample S1 presents a broadened, slightly asymmetric doublet with no trace of a magnetic component ($< 1\%$). A simple single-component fit yields an isomer shift (δ) of $0.38(1)$ mm/s and a quadrupole splitting (Δ) $0.92(1)$ mm/s, consistent with a paramagnetic ferric material. The sample, S2 and S3 exhibit a substantial (70–75%) magnetic component which is made up of two sub-components with hyperfine fields (B_{hf}) of $48.5(5)$ T and $43.7(5)$ T and area ratios of $\sim 3:1$. Both samples contain a paramagnetic component ($\delta=0.39(1)$ mm/s, $\Delta=0.67(1)$ mm/s) that is distinct from the one seen in sample S1. The sample S2 contains a small (3–4%) contribution from a ferrous compound. The severe misfit apparent in the spectrum of sample S3 is the result of a broad magnetic component that could not be fitted in a stable way due to severe overlap and cross-talk between adjustable parameters. Subtracting the best, highly constrained fit to most of the pattern left a residual pattern that could be fitted as a disordered magnetic material with an average B_{hf} of ~ 27 T and accounting for 15-20% of the total iron.

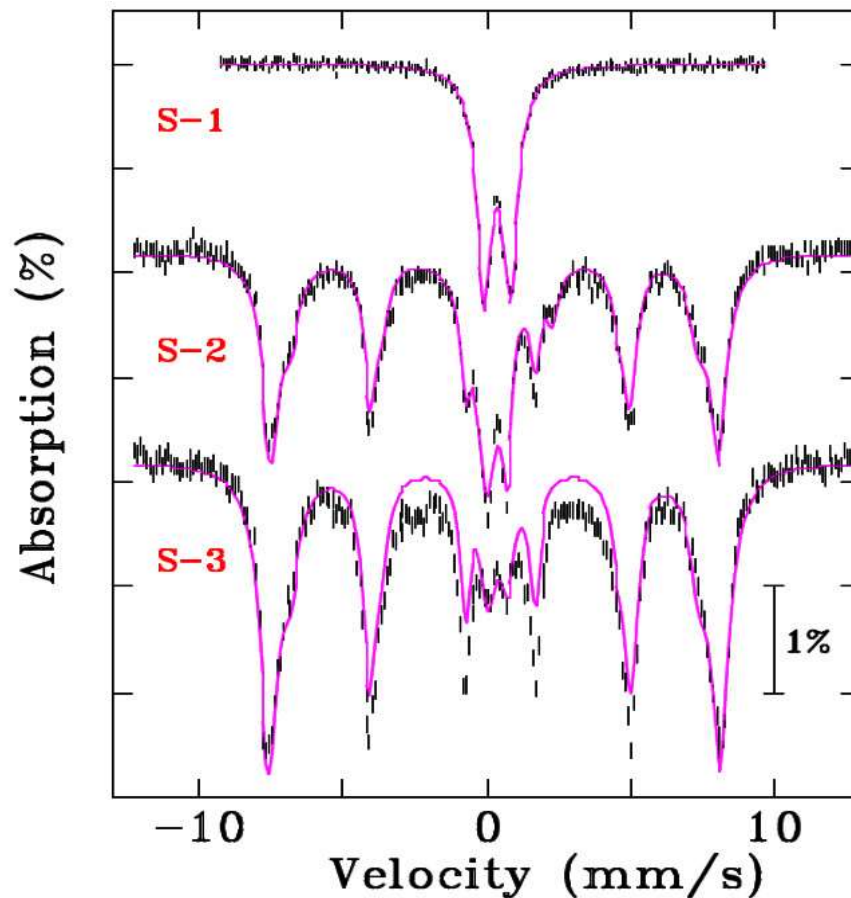


Figure 4-11: Room temperature Mössbauer spectra of the samples S1, S2, and S3
(In each case the magenta line is a fit described in the text)

4.8.3 Impact of HaHC treatment

All three samples were re-measured following the HaHC leaching described earlier (see Section 4.4). As shown in Figure 4-12, the leaching treatment leads to a much better-defined spectrum for Sample S1. The S1-R1 is spectra of S1 after leaching with HaHC. It can be fitted with two ferric doublets with a ~60:40 area ratio. Both have isomer shifts of 0.37(1) mm/s and quadrupole splitting of 1.10(1) mm/s (stronger component) and 0.62(1) mm/s. Using these parameters as constraints in

a fit to the original spectrum allows the form of the removed material to be determined. This is shown as the green doublet in Figure 4-12.

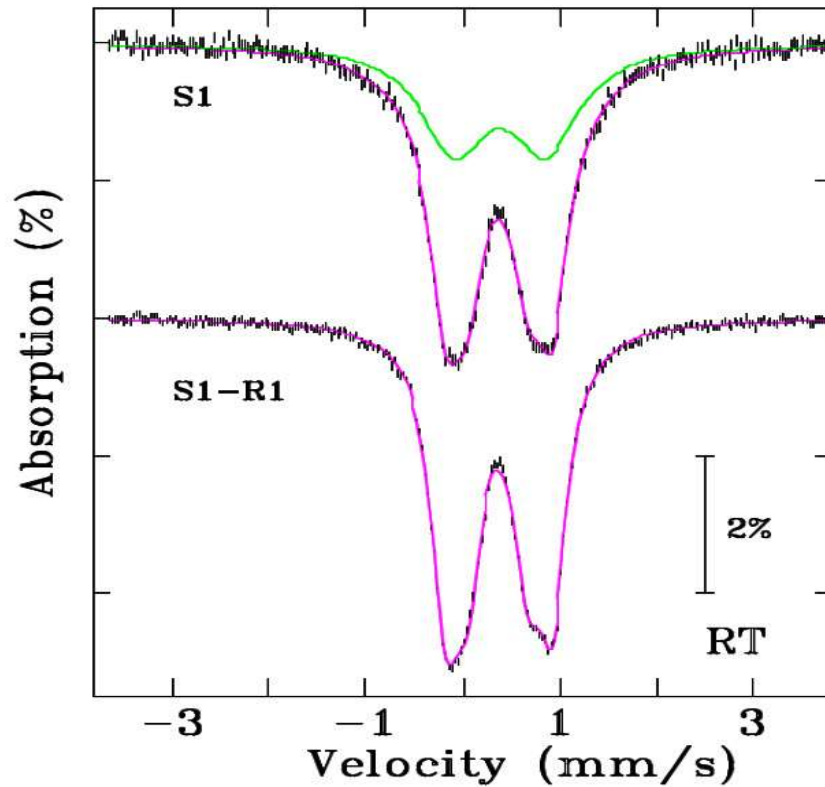


Figure 4-12: Room temperature Mössbauer spectra before (top, S1) and after (bottom, S1-R1) HaHC leaching

(The magenta line in each case is a fit described in the text. The doublet shown as a green line is the difference between the two spectra ‘S1’, ‘S1-R1’ and reflects the Mössbauer spectrum of material removed from S1 by HaHC leaching process)

This green doublet is quite broad, with $\delta=0.39(1)$ mm/s, $\Delta=0.95(1)$ mm/s and accounts for 45% of the spectral area. This value compares quite well with the amount of iron (36%) found to have been removed by the HaHC leaching. Leaching of sample S3 only removed 3% of the iron, and as can be seen in Figure 4-13 and Figure 4-14, this had almost no impact on the spectrum apart from

a slight reduction in the paramagnetic doublet. By contrast, the much stronger central doublet in sample S2 is greatly reduced in the leached sample. Subtracting the leached pattern from that of the untreated sample, as was done for sample S1, yields a well-defined doublet that accounts for ~15% of the spectral area, consistent with ~10% of the iron being removed by the HaHC leach. Its parameters are $\delta=0.37(1)$ mm/s, $\Delta=0.67(1)$ mm/s.

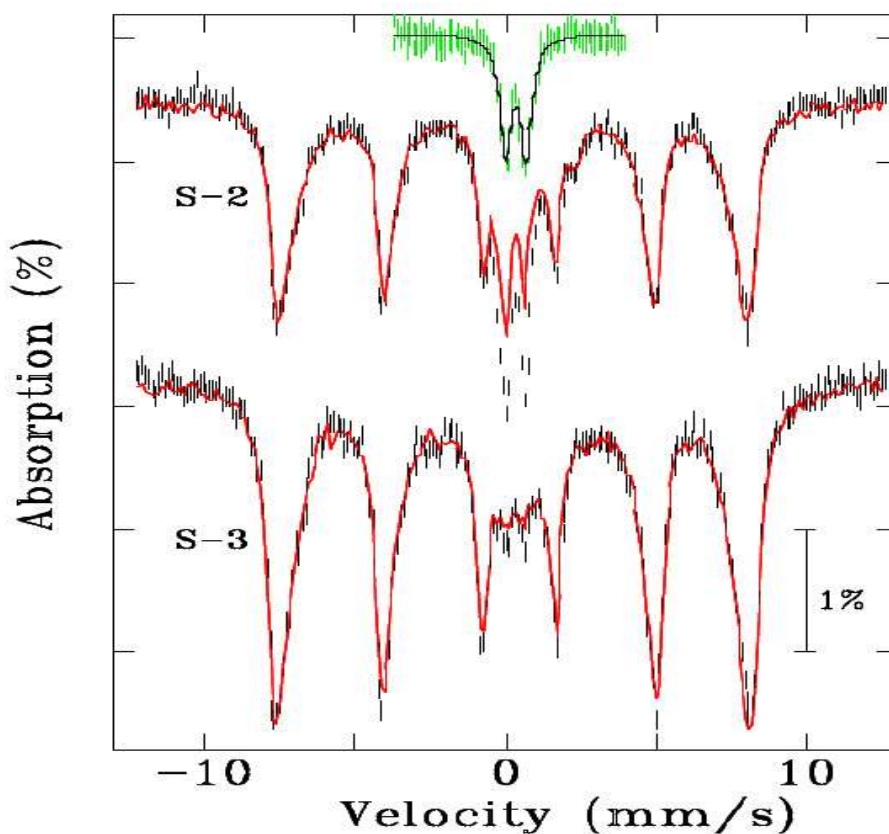


Figure 4-13: Room temperature Mössbauer spectra of samples S2 and S3 taken before (black bars) and after (solid red lines) HaHC leaching

(The doublet shown as green is the difference between the leached and untreated spectra and reflects the Mössbauer spectrum of material removed by HaHC leaching process)

4.8.4 Phase identification in leach residues

The isomer shift and quadrupole splitting indicate that the magnetic component in sample S2 and S3 is broadly consistent with hematite, although the hyperfine field is somewhat below the 51 T that would be expected for clean, well-crystallized hematite. Cooling S3-R1 to 11 K leads to a spectrum shown in Figure 4-14. Cooling from room temperature to 11K results in magnetic ordering and therefore eliminates the interference from magnetic dipole moments. The spectrum is sharper compared to the S3-R1 spectrum taken at room temperature (see Figure 4-13), with no hyperfine interactions of the central doublet confirming the assignment as a regime (ii) phase described in Section 4.1 or hematite as reported by Murad and Cashion (2011). The line broadening and the presence of an apparent paramagnetic component are likely the results of disorder and poor crystallinity. As the paramagnetic components in S2 and S3 have the same hyperfine parameters, and this component appears to be some form of hematite in the S3-R1 sample, we attribute the larger paramagnetic component observed in S2 to poorly crystallized hematite or a regime (ii) phase. It is clear from the comparison of the spectra taken for the untreated (S1) and HaHC leached material (S1-R1) of sample S1 in Figure 4-12, that S1 contains two distinct components. The spectral asymmetry and broad lines would appear to be consistent with iron phases from the ferrihydrite and schwertmannite family. However, while the fitted quadrupole splittings of two components (0.62(1)mm/s and 1.10(1) mm/s) are certainly within the range seen for ferrihydrites (Murad, 1988), the area ratios are reversed so a much larger average splitting (0.90mm/s) compared to values reported for ferrihydrite (0.72 mm/s) and/or schwertmannite (0.71 mm/s) is observed (Cashion and Murad, 2012). Mössbauer spectra post-cooling to 11 K should provide

some further discrimination. Room-temperature spectra of ferrihydrite is considered unspecific, and magnetic order is necessary to identify these minerals by Mössbauer spectroscopy. The poorer the crystallinity, the lower the magnetic ordering temperature. As shown in Figure 4-14, S1-R1 shows a magnetic pattern with relatively broad lines and a hyperfine field that is clearly smaller than that attributed to hematite in the S3-R1 sample. The hyperfine field is consistent with, but slightly higher than, that reported for both ferrihydrite and schwertmannite.

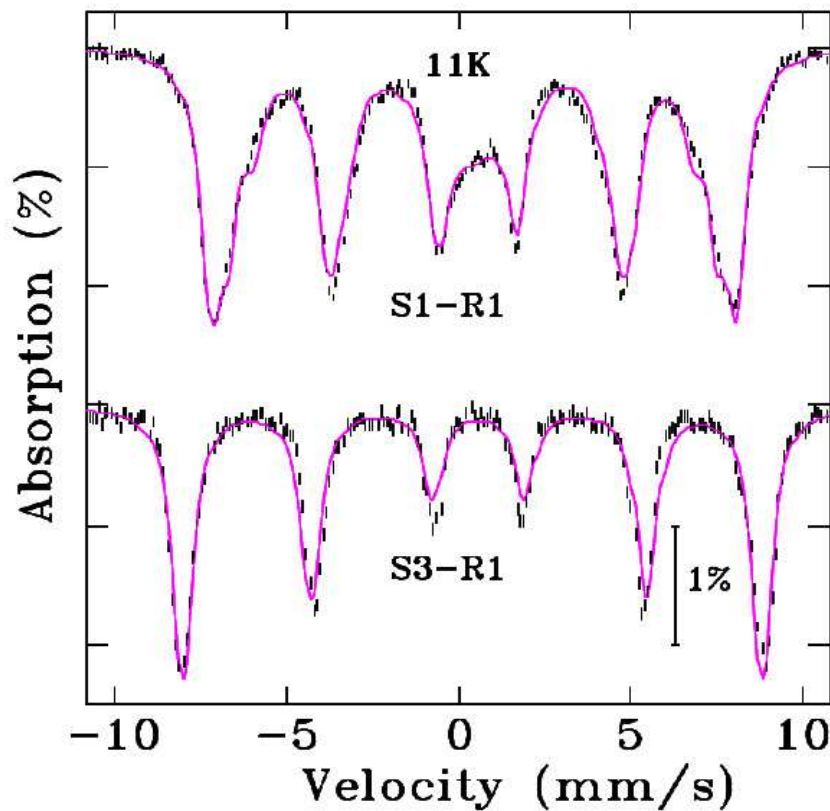


Figure 4-14: Mössbauer spectra of samples S1-R1 and S3-R3 (post- HaHC leaching) taken at 11K
(The magenta line in each case is a fit described in the text)

4.8.5 Indication of jarosite contributions

A significant amount of jarosite was detected in sample S1 by QXRPD (see Table 4-7), so this mineral should contribute to the Mössbauer spectrum. The jarosite group ($MFe_3(SO_4)_2(OH)_6$) can accommodate a wide variety of substitutional ions on the “M” site leading to a range of isomer shifts (0.375–0.394 mm/s) and quadrupole splittings (0.91–1.22 mm/s) (Leclerc, 1980), which certainly cover the higher range seen in the spectra of S1 and S1-R1, and the broad lines observed here would point to a range of substitutes being present. While the average hyperfine field seen at 11 K (45 T) is at the low end of the range reported (45–48 T) by Afanasev et al. (1974) and Townsend et al. (1986), it is not out of line. However, the observed ordering temperature seen here is far too high as, depending on the “M” ion, transition temperatures of 17 K–54 K have been reported (Afanasev et al., 1974). The iron atoms in the crystal structure of jarosite form a kagome lattice. Kagome is a traditional Japanese woven bamboo pattern and consists of the vertices and edges of the trihexagonal tiling (see Figure 4-15).

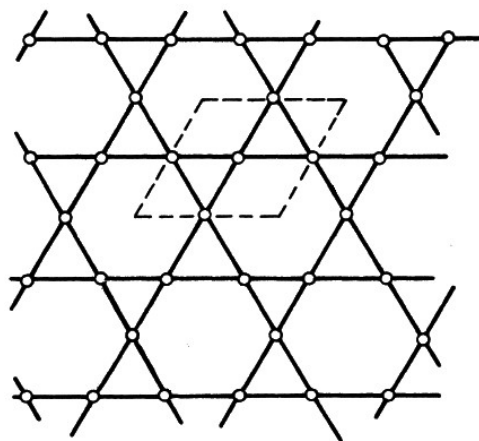


Figure 4-15: Iron atoms forming a kagome lattice in jarosites
(Townsend et al., 1986)

The electron spins of iron atoms in the kagome plane form triangular magnetic structures and fail to align into a stable magnetic order resulting in ‘frustrated’ magnetism behavior. The term ‘frustrated’ is to describe a magnet in which the electron spins fail to align into a stable magnetic order. This unique magnetism behavior is used to identify jarosites in Mössbauer spectra (Townsend et al., 1986). Therefore, one possibility that remains is that the ordering temperatures of jarosites are anomalously low because of the arrangement of iron in the kagome lattice. If this magnetic frustration due to kagome lattice were to be lifted, because of distortions caused by the M ions, or direct substitution for the iron, much higher ordering temperatures could occur. As elements can substitute on the M, Fe and SO₄ positions in jarosite, it is possible that some combination of substitutions is responsible for the higher ordering temperatures observed here. This means the sample (S1) contains doped jarosite (copper substituting for iron), which is not recovered by HaHC leaching and is also not detected by QXRPD, may be because of poor crystallinity and/or nanoparticles.

4.9 Conclusions

The residues from CESL and Vale, pilot and demonstration scale medium temperature sulfide leach processes were characterized via QXRPD, sequential extraction and Mössbauer spectroscopy. All three residues contain a significant amount of X-ray amorphous material. The X-ray amorphous and HaHC soluble phases were determined by a combination of QXRPD and sequential extraction techniques. Poor agreement between the quantification of total iron from QXRPD and sequential extraction indicated the presence of large amounts of iron (>30 wt%) in amorphous as well as poorly crystalline phases in the samples. Chemical analysis of solution from

sequential extraction revealed that HaHC soluble phases were the major source of copper and nickel loss in the residue. HaHC soluble phases were associated with 2–4 times more Cu/Ni than the crystalline iron oxide phases. A hydrometallurgical process for copper and nickel sulfide leaching which produces the minimum amount of HaHC soluble phases would lead to the minimum loss of copper/nickel to the residue. The process conditions described for sample S3 in Table 4-2 (10–12 g/L acid concentration with 5 g/L chloride concentration, 5% solids loading, 1030 kPa.g total O₂ pressure and 80 min retention time) generated a residue with the lowest amount of HaHC soluble phases. Ferrihydrite was identified by TEM and is likely responsible for a large portion of the HaHC soluble material. Mössbauer spectroscopy identified poorly crystalline hematite in the leach residue obtained after HaHC treatment of samples and also hinted at the doped jarosite contributions (based on ordering temperatures) in HaHC treated S1 sample referred to as S1-R1. Since the possible contribution of jarosite to Ni and Cu losses under CESL conditions has yet to be explored in the literature, the next chapter focusses on this possibility.

CHAPTER 5: EVALUATION OF CRYSTALLINITY IN SYNTHETIC JAROSITES

In the previous chapter, some portions of the Mössbauer spectrum of leach residue samples were speculated to be linked to jarosite but could not be positively identified as such. One sample, referred to as S1, resulted in substantial amorphous Fe phase formation. The amorphous phase was identified to be ferrihydrite by TEM. The residue sample obtained after recovering the ferrihydrite by HaHC referred to as S1-R1, still contained a poorly crystalline phase (refer to Section 4.5). However, there was a broad range of disorder present in the material and solely attributing it to jarosite proved difficult. Therefore, synthetic jarosites were precipitated with Cu substitutions for Mössbauer analysis to see if these products might match the poorly crystalline phases apparent in S1-R1. These were then characterized by X-ray Diffraction (XRD), Scanning Electron Microscopy (SEM), and complete sample digestion followed by Inductively Coupled Plasma Mass Spectroscopy (Digestion & ICP-MS). Ultimately the Mössbauer spectra of the synthetic jarosites is compared with that of the residues from the medium temperature (150°C) sulfide concentrate leaching.

5.1 Precipitation of synthetic jarosites

Jarosite synthesis was performed using reagent grade chemicals using the procedure described in the literature (Dutrizac, 1984; Dutrizac and Kaiman, 1976). Sodium jarosite (Na-Jarosite) was prepared by dissolving 64 g of Na_2SO_4 in one liter of solution containing 10 g of Fe(III) as ferric sulfate and 0.01 M H_2SO_4 . The solution was heated in air to 95°C and was stirred at this

temperature for 3 hr. The precipitate was allowed to settle and then filtered followed by washing with water. The precipitate was dried overnight at 110°C to remove any loosely bound water. The Munsell color of the product formed was 5Y 6/4 (pale yellow-dry). Potassium jarosite (K-Jarosite) was prepared in a similar way by dissolving 30 g of KNO₃ in one liter of solution containing 8 g of Fe(III) as ferric sulfate and 0.01 M H₂SO₄. Potassium nitrate was used instead of potassium sulfate as it has been reported in the literature that potassium nitrate produces a product richer in alkali (Dutrizac and Kaiman, 1976). The precipitate thus formed was treated in the same manner as the sodium jarosite. Sodium jarosite and potassium jarosite were also doped with copper by precipitating them in the presence of 10 g/L of Cu as copper sulfate. Dried samples were ground with the help of mortar and pestle, and a small portion was analyzed by Digestion & ICP-MS for iron, potassium, and sodium after complete multi-acid digestion. The total sulfur content was determined using the LECO method.

5.2 Chemical characterization of synthetic jarosites

The chemical composition of the synthetic jarosites is given in Table 5-1. The synthesis of jarosite and the incorporation of divalent base metals into the jarosite lattice is well established (Dutrizac and Kaiman, 1976; Dutrizac, 1984). The conditions affecting the formation of jarosites are known to be temperature, pH, and concentration of M⁺ (Na⁺ or K⁺) ions, reaction time and concentration of Fe(III) ions. The issue of the incorporation of divalent base metals into the jarosite lattice during the formation of alkali (Na, K) jarosites is of paramount importance to the metallurgical industry since such alkali jarosites are commonly precipitated from iron solutions rich in Zn²⁺, Cu²⁺, Ni²⁺, etc. (Dutrizac, 1983). The extent of incorporation of copper into sodium jarosite depends on the

iron concentration and the initial acidity. Approximately 0.75 wt% and 0.31 wt% Cu in sodium and potassium jarosite were achieved respectively. The jarosites precipitated were thoroughly washed with distilled water to eliminate entrained liquor. Rewashing of the dried jarosite with dilute sulfuric acid and extraction by HaHC did not remove any significant amount of copper from the jarosite.

Table 5-1: Chemical composition of synthetic jarosite samples

Elements	Na-Jarosite (wt%)	Na-Jarosite with Cu (wt%)	K-Jarosite (wt%)	K-Jarosite with Cu (wt%)
Fe	29.5	26.5	25.9	25.8
Na	3.5	3.3	–	–
K	–	–	5.77	5.76
S	13.4	13.0	12.8	12.3
Cu	–	0.57	–	0.31
Approximate formula	(Na _{0.73} H ₃ O _{0.27}) Fe _{2.52} (SO ₄) ₂ (OH) ₆	(Na _{0.71} H ₃ O _{0.29}) Cu _{0.04} Fe _{2.33} (SO ₄) ₂ (OH) ₆	(K _{0.73} H ₃ O _{0.27}) Fe _{2.31} (SO ₄) ₂ (OH) ₆	(K _{0.77} H ₃ O _{0.23}) Cu _{0.03} Fe _{2.40} (SO ₄) ₂ (OH) ₆

Microscopy of the products by SEM, shown in Figure 5-1 did not reveal any anomalous phases. It would appear from these studies that the copper was incorporated into the jarosite lattice.

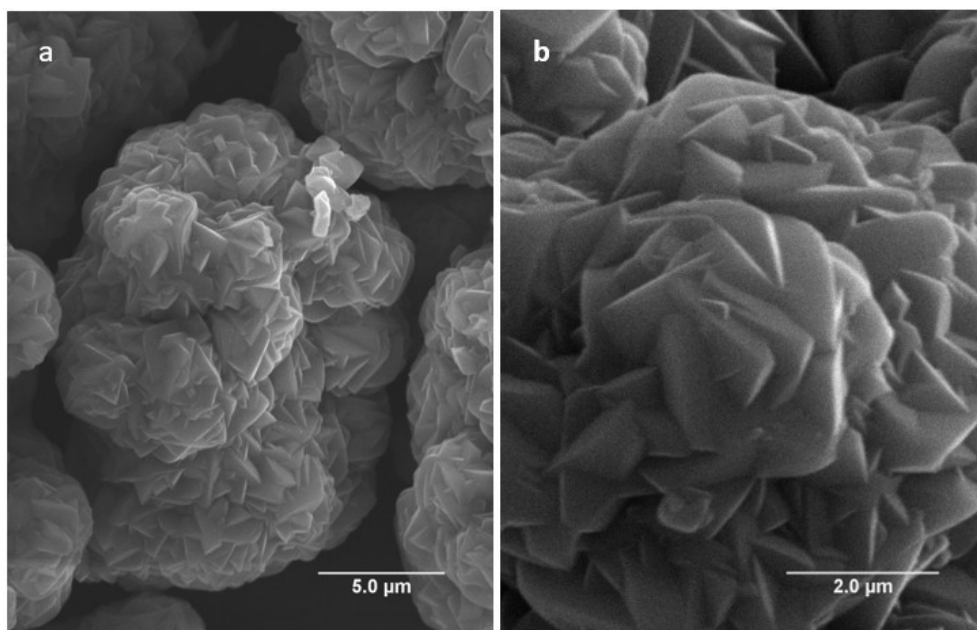


Figure 5-1: SEM micrographs of Na-Jarosite doped with Cu

5.3 Powder X-ray diffraction (PXRD) of synthetic jarosites

Powder X-ray diffraction (PXRD) patterns were recorded on a Siemens D5000 X-ray Diffractometer, θ - θ Bragg-Brentano geometry, using $\text{CuK}\alpha$ radiation ($\lambda = 1.54184 \text{ \AA}$). Powder patterns were recorded at room temperature in the interval of 7° – 70° 2θ , with a step size of $\Delta 2\theta = 0.02$ and a total counting time of about 35 min was used for each sample. The patterns were analyzed with the software X'Pert HighScore Plus. The cell parameters of the unit cells were determined with Rietveld refinements, using a sample displacement correction. The diffraction profiles were modeled by using the pseudo-Voigt function, the Cagliotti function for the peak broadening and the Thomson-Cox-Hastings correction for low angle asymmetry.

The X-ray diffraction patterns for jarosites are well established (Dutrizac and Kaiman, 1976; Kato, 1977; Kubisz, 1964, 1969; May, Sjoberg, and Baglin, 1973). The data obtained in the present study on these compounds agree closely with the previous values concerning both d -spacing's, and the derived a and c parameters. The basic structure of the jarosite group consists of SO_4 tetrahedra and Fe-cation octahedra, where the octahedra corner-share to form sheets perpendicular to the c axis. The SO_4 tetrahedra have two orientations within a layer; one set of SO_4 points towards $+c$, which alternate with another set pointing toward $-c$. Twelve anions, consisting of six oxygen atoms (O_2) and six OH groups (O_3) form an icosahedron, in which the alkali cation (K^+ , Na^+ , etc.) is located. The diffraction peaks of PXRD patterns for four synthetics samples, Na-Jarosite, Na-Jarosite doped with Cu, K-Jarosite and K-Jarosite doped with Cu are presented in Figure 5-2. The diffraction peaks of the X-ray powder patterns correspond to a rhombohedral K-Jarosite structure with $R\bar{3}m$ symmetry similar to inorganic crystal structure database (ICSD) structure 34344, PDF 76-629 (Kato, 1977) for the sample containing potassium. The samples containing sodium are well represented by a modified ICSD 34344 structure in which all the original potassium atoms have been substituted with sodium atoms.

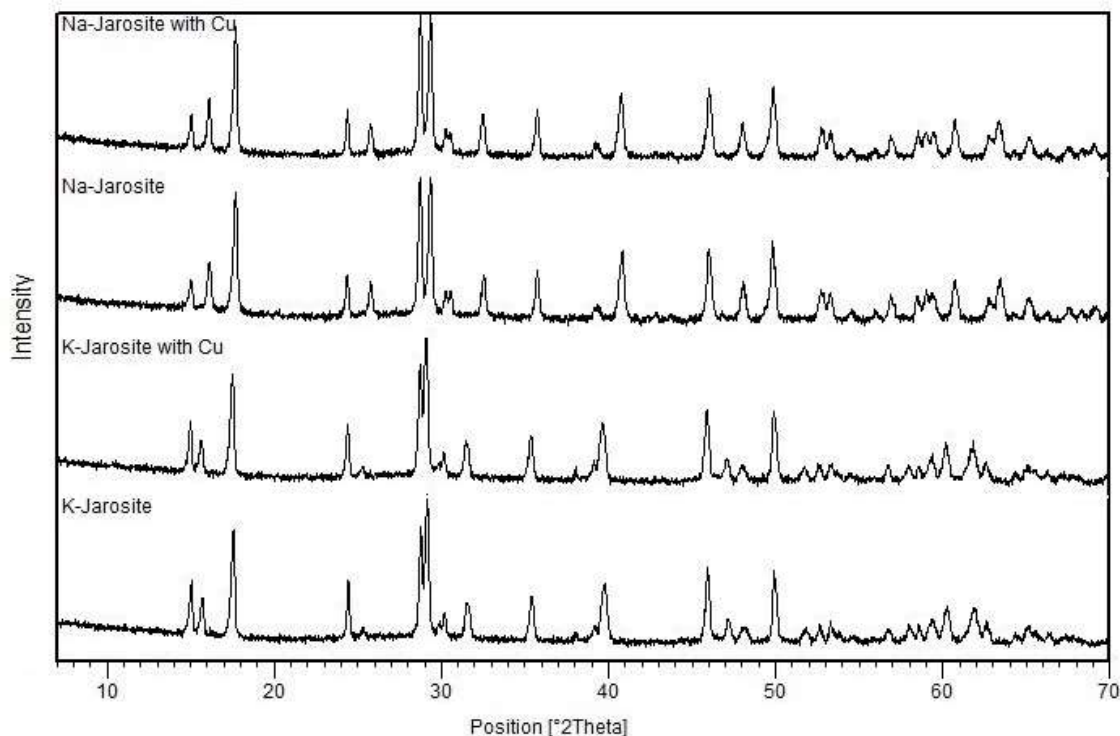


Figure 5-2: Experimental X-ray powder diffraction patterns for the four jarosite samples

The unit cell parameters obtained by Rietveld refinement are presented in Table 5-2. The sodium jarosite has a much smaller unit cell volume than potassium jarosite as a result of the smaller diameter of Na^+ : 1.39Å, than K^+ : 1.64Å (Dutrizac and Jambor, 2000; Shannon, 1976). Substitution of sodium into potassium jarosite decreases unit cell parameter ‘*c*’ significantly (0.617 Å) and increases ‘*a*’ to a minor degree (0.012 Å). The diffraction peaks of the sodium jarosite are shifted at higher 2θ angles accordingly with the larger unit cell parameters. The ‘*a*’ cell parameter remains virtually unchanged between the pure jarosite and the jarosite doped with Cu. In contrast, the ‘*c*’ cell parameter increases very slightly from 16.55 Å to 16.57 Å for the sodium jarosite doped with Cu. Such modest variations in the ‘*a*’ and ‘*c*’ cell parameters are not unexpected given the minor Cu contents of the jarosites, but the variations imply the structural incorporation of Cu in the

sodium jarosite. Amorphous content in Table 5-2 was estimated by adding a weighed amount of a spike phase (NIST Standard Reference Material 676a) with known crystallinity (99.02 wt%). In the presence of amorphous content, the amount of spike will be overestimated, and the amorphous content can be determined (De La Torre, 2001). The amount of X-ray amorphous phase increases very slightly from 15 wt% to 17 wt% for the sodium jarosite doped with copper; the variation again implies the structural incorporation of Cu in the sodium jarosite.

Table 5-2: Unit cell parameters and amorphous content obtained by Rietveld refinement
(standard deviations given by Rietveld algorithm are indicated in parentheses)

Cell Parameters	Na-Jarosite	Na-Jarosite with Cu	K-Jarosite	K-Jarosite with Cu
a (Å) = b (Å)	7.3264±0.0004	7.3236±0.0004	7.3141±0.0005	7.3160±0.0005
c (Å)	16.554±0.001	16.577±0.001	17.074±0.001	17.054±0.001
*X-ray amorphous (wt%)	15	17	20	20

*X-ray amorphous (wt%) was determined by the internal standard method, using corundum as a doping material

5.4 Mössbauer spectroscopy of synthetic jarosites

The synthetic jarosite samples for Mössbauer spectroscopy were prepared in a similar manner as described in Section 4.8.2 and were also performed by Dr. Dominic Ryan at the Physics Department, of McGill University.

The Mössbauer spectra obtained for Na-jarosite doped with Cu, K-jarosite doped with Cu and S1-R1 (refer to Sections 4.3 – 4.6) are shown in Figure 5-3.

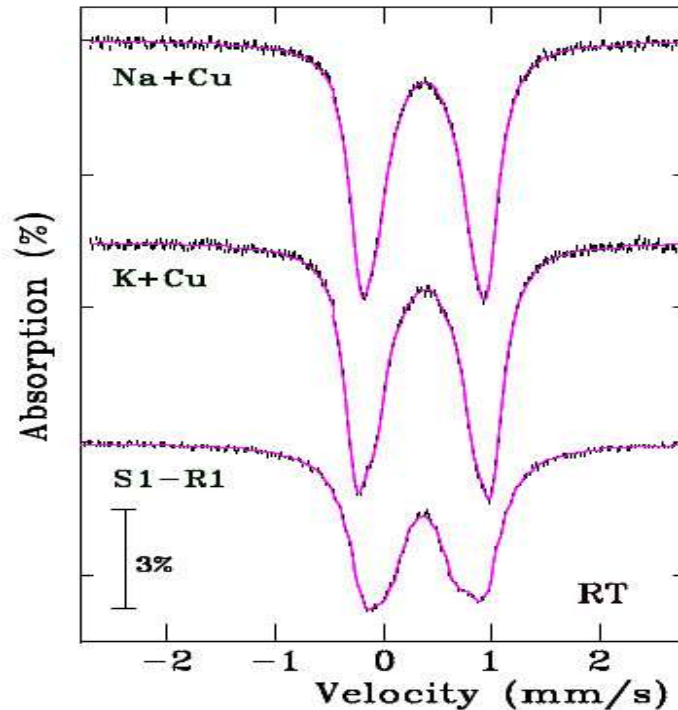


Figure 5-3: Room temperature Mössbauer spectra of the jarosite doped with Cu and HaHC leached residue sample

(In each case the magenta line is a fit described in the text)

Accurately fitting the spectra of the two synthetic samples required three doublets even though the jarosite structure only contains a single iron site. This may be the result of the disorder and has been noted before (Rothstein, 2006). The three doublets had the same isomer shift (0.38 mm/s) but different quadrupole splittings (1.24 mm/s, 0.90 mm/s and 0.43 mm/s in order of decreasing intensity). In Mössbauer spectra, the area under the absorption line(s) is proportional to the amount of iron in that phase. If the sample has several phases, the relative areas of the subspectra belonging to each phase are calculated to estimate the amount of each phase (Vandenberghe and De Grave, 2013). An attempt to fit the S1-R1 spectrum to a combination of synthetic jarosite and an additional doublet yields a good fit, and suggests a 70:30 (jarosite : “unknown”) breakdown, but the

parameters of the unknown doublet (isomer shift 0.37(1) mm/s, quadrupole splitting 0.52(1) mm/s) while consistent with many ferric sulfate minerals, are not diagnostic (Dyar et al., 2013).

Further insight was gained by looking at the low-temperature spectra. The spectra for the Cu-doped sodium jarosite shown in Figure 5-4 reveal a progressive broadening of the magnetic pattern on warming (Kovács et al., 2008), likely due to the highly frustrated nature of the kagome lattice occupied by the iron in this mineral (see Section 4.8.5, Chapter 4).

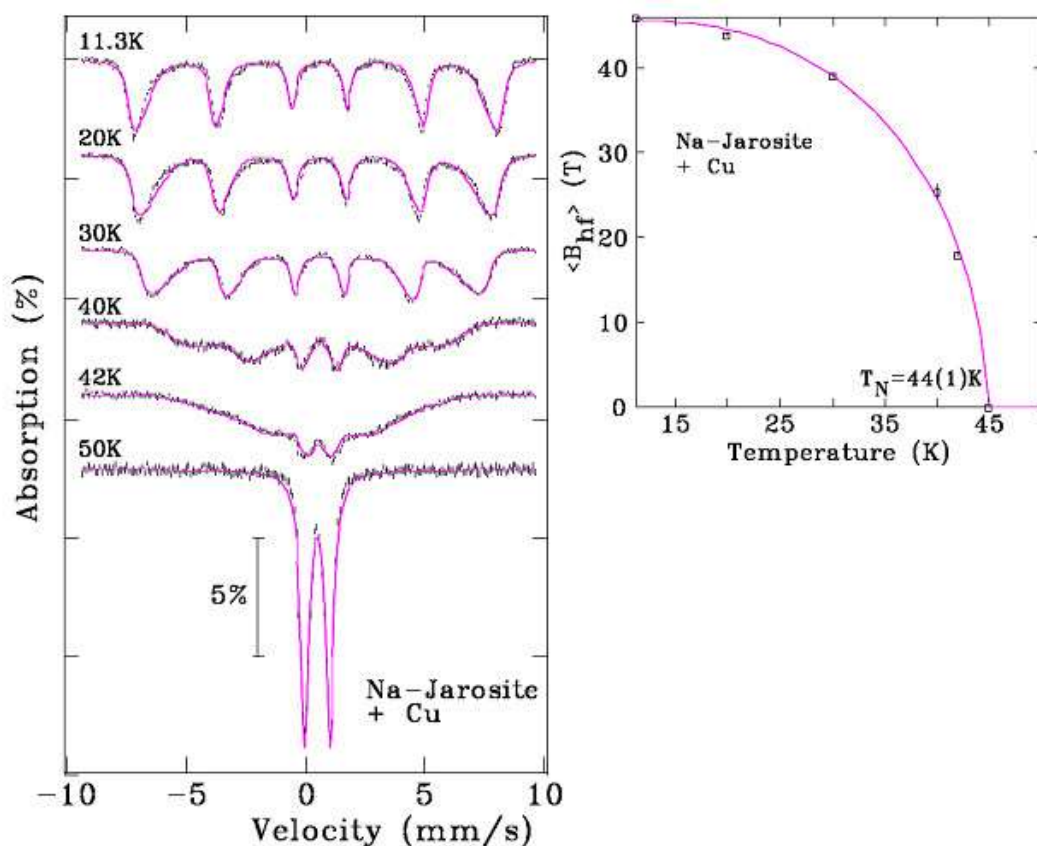


Figure 5-4: Mössbauer spectra of the Cu-doped sodium Jarosite taken at 50 K and below
 (The broadening of the magnetic component on warming from 11 K and the eventual loss by 50 K is shown. Fitting the temperature dependence of the average hyperfine field to a Brillouin function yields an ordering temperature of 44(1) K)

This is comparable to that reported for similar materials (Wills et al., 2000) with ~90% coverage of the iron sub-lattice, but somewhat lower than the 65 K seen for stoichiometrically pure jarosites (Grohol et al., 2003).

The behavior of the S1- R1 sample shown in Figure 5-5 is not as simple as that of the synthetic sample. Warming from 11 K initially leads to the same progressive broadening and collapse of the magnetic component that was seen in the synthetic sample; however, this does not continue beyond 50 K. Instead, a magnetic component persists as far as 150 K, getting weaker but with a roughly constant hyperfine field. Tracking the average hyperfine field ($\langle B_{\text{hf}} \rangle$) and the area of the magnetic component reveals a clear break around 40 K and the hyperfine parameters of the doublet that dominates the center of the spectrum is consistent with that of jarosite. The combination of parameters at 50 K and the clear ordering just above 40 K strongly suggests that about 40% of the iron in the S1-R1 sample is associated with some form of jarosite. Further heating leads to a progressive loss of the magnetic component and a steady reduction of the average quadrupole splitting associated with the paramagnetic component as it grows in the area. This clearly reflects the presence of one or more ferric minerals with much smaller quadrupole splittings as noted in the discussion of the fits to the room temperature spectra in Figure 5-5. However, the analysis of the low-temperature spectra suggests a significantly lower jarosite content (40% rather than the 70% found above). Unique identification of the secondary mineral(s) is not possible. There is clearly, a very broad range of ordering temperatures (50 K – 150 K) which likely reflects a comparable range of stoichiometries, and the strong line overlap makes a clean deconvolution

impractical. Based on the low-temperature Mössbauer studies on synthetic jarosites, it can be deduced that about half of the iron in the S1-R1 sample is associated with jarosite.

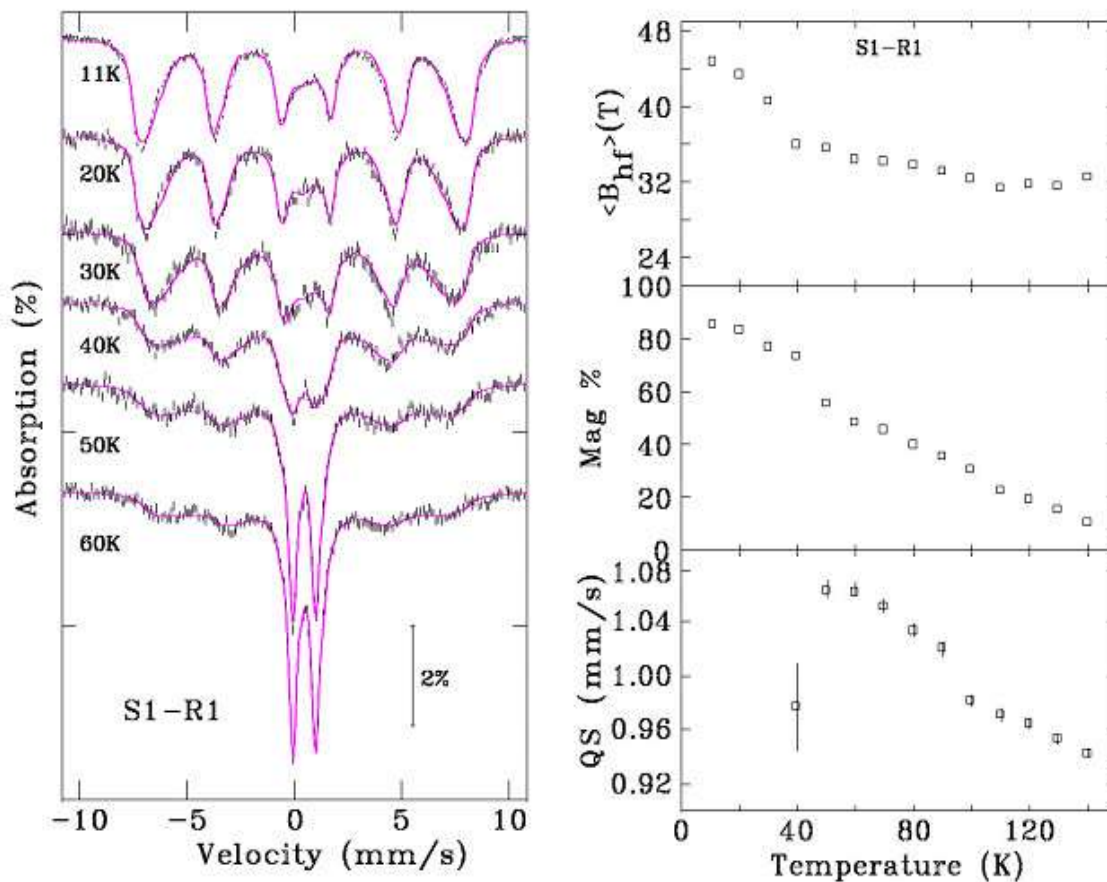


Figure 5-5: Mössbauer spectra of the S1-R1 sample taken at 60 K and below

(The broadening of the magnetic component on warming from 11 K and the growth of a paramagnetic doublet is shown, the magnetic component persists well beyond 60 K (right panel). Temperature dependence of the average hyperfine field ($\langle B_{hf} \rangle$), the area of the magnetic component and the quadrupole splitting (QS) of the paramagnetic doublet is shown. Note the marked break in $\langle B_{hf} \rangle$ and the magnetic area near 40 K)

5.5 Conclusions

The sample S1 was found to contain a significant amount of HaHC soluble, amorphous iron phase (see Section 4.3) and no hematite as confirmed by X-ray diffraction studies. The sample S1-R1, which is the residue from HaHC treatment of sample S1 was studied using Mössbauer spectroscopy in Section 4.8. Mössbauer study of S1-R1 indicated the presence of an iron phase that is similar to jarosite but not well-formed jarosite which could be the result of some metal cation substitutions. To further understand this jarosite-like iron phase, a synthesis of jarosite doped with either Cu or Ni was attempted which was then studied using Mössbauer spectroscopy to compare it with the spectra of S1-R1.

Jarosite synthesis was successfully performed using reagent grade chemicals. This was confirmed by powder X-ray diffraction data. Synthetic Na-jarosite and K-jarosite were doped with copper. This was confirmed by the chemical analysis by Digestion & ICP-MS. The PXRD data did not show any impurity phases. The copper ions were incorporated to a minor extent (0.4 wt%), and these appear to substitute for iron in $\text{NaFe}_3(\text{SO}_4)_2(\text{OH})_6$ and $\text{KFe}_3(\text{SO}_4)_2(\text{OH})_6$. This could result in loss of copper to jarosite residue in hydrometallurgical processes. SEM images revealed typical jarosite crystals without any anomalous phases. Mössbauer study of HaHC treated CESL residue samples (S1-R1), and the synthetic Cu doped jarosite performed at room temperature indicated that jarosite with Cu substitutional ions may not be present in the residue. However, further Mössbauer studies at lower temperatures provided some insight into the effect of Cu substitutions into pure jarosite. The Cu doped jarosites have lower ordering temperatures compared to the pure jarosites; which means less crystallinity and a higher tendency to be associated with Cu losses.

However, the behavior of S1-R1 spectra is not as simple as that of the Cu-doped synthetic jarosite sample and reflects the presence of one or more additional ferric minerals. A unique identification of these additional secondary mineral(s) was not possible. Based on the relative areas of the subspectra it can be said with some confidence that about half of S1-R1 is some form of poorly crystalline jarosite similar to the Cu-doped synthetic jarosite sample.

CHAPTER 6: PRESSURE LEACHING OF SULFIDE CONCENTRATES

6.1 Introduction

As discussed in previous chapters, leaching of sulfide concentrates of copper and nickel at medium temperature (150°C) produces residues that contain sulfur and iron-bearing minerals. During the leaching process depending on various process parameters, iron may be precipitated as hematite, goethite, jarosite or other oxyhydroxides, which may exhibit a very wide range of crystallinity. Hematite is the favored iron precipitate because it is stable and does not adsorb as much copper, nickel or other solution constituents during precipitation. However, the low solubility of iron during the medium temperature processing of sulfide ores can favor the formation of poorly crystalline, nano-scale iron oxide/oxyhydroxide phases. In some cases, these phases have been positively identified as the metastable ferrihydrite, which transforms into stable iron oxides such as goethite, hematite, and magnetite over time. A better understanding of what helps in driving this transformation during leaching would ultimately result in lower valuable metal losses and more stable leach residues.

The autoclave pressure leaching experiments of sulfide concentrate followed by hydroxylamine hydrochloride (HaHC) treatment of the residues was performed. In this chapter, the amount of copper extracted during pressure leaching and the amount of HaHC soluble, amorphous phase in the residue is presented. The effect of acid concentration and the effect of some new surfactants on iron and sulfur in the leach residue is presented. Specifically, it was possible to influence the

morphology and crystallinity of the iron precipitates, and the size and morphology of the residue sulfur.

6.2 Experimental

6.2.1 Materials and sample preparation

The copper, copper-arsenic and copper-nickel sulfide concentrate samples were supplied by Teck. They consisted of flotation concentrates with P_{80} of 50-100 μm . The concentrates were ground in a ceramic ball mill to a size of $P_{80} \sim 20 \mu\text{m}$. Dried samples were lightly ground, and a portion was analyzed by Digestion & ICP-MS after complete multi-acid digestion as described in Section 4.2. Quantitative X-ray diffraction was performed as described in Section 4.3. The chemical assay of the copper concentrate used in the leaching experiments is given in Table 6-1. The leach residues, produced from the leaching of the sulfide concentrate, were dried in an oven at 60°C overnight. Dried samples were analyzed by Digestion & ICP-MS, QXRPD, and sequential extraction.

Table 6-1: Chemical analysis of copper sulfide concentrate

Element	Units	CESL Con.	Element	Units	CESL Con.
Al	ppm	9606	Mn	ppm	386
As	ppm	4380	Mo	ppm	839
Bi	ppm	<100	Na	%	0.077
Ca	ppm	4490	Ni	%	<0.01
Cd	ppm	<100	Pb	ppm	997
Co	ppm	<100	Sb	ppm	675
Cu	%	22.1	Se	ppm	<100
Fe	%	22.4	Zn	ppm	16200
K	ppm	3250	S	%	29.6
Mg	%	1.74			

6.2.2 Quantitative phase analysis

Quantitative phase analysis of all the residue samples was performed using the Rietveld method and X-ray powder diffraction data as described in Section 4.3. The concentrate quantitative mineralogical analysis is given in Table 6-2.

Table 6-2: QXRPD phase analysis of copper concentrate

Mineral	Ideal formula	CESL concentrate (phase %)
Brochantite	$\text{Cu}_4(\text{SO}_4)(\text{OH})_6$	1.4
Chalcopyrite	CuFeS_2	37.3
Covellite	CuS	11.6
Enargite	Cu_3AsS_4	1.4
Tennantite	$(\text{Cu,Ag,Fe,Zn})_{12}\text{As}_4\text{S}_{13}$	1.9
Pyrite	FeS_2	24.7
Sphalerite	$(\text{Zn,Fe})\text{S}$	2.5
Molybdenite	MoS_2	0.4
Gypsum	$\text{CaSO}_4 \cdot 2\text{H}_2\text{O}$	2.1
Quartz	SiO_2	2.9
Clinochlore	$(\text{Mg, Fe})_5\text{Al}(\text{Si}_3\text{Al})\text{O}_{10}(\text{OH})_8$	2.1
Talc	$\text{Mg}_3\text{Si}_4\text{O}_{10}(\text{OH})_2$	5.5
Muscovite	$\text{KAl}_2\text{AlSi}_3\text{O}_{10}(\text{OH})_2$	2.3
Plagioclase	$\text{NaAlSi}_3\text{O}_8 - \text{CaAl}_2\text{Si}_2\text{O}_8$	2.7
Actinolite	$\text{Ca}_2(\text{Mg,Fe})_5\text{Si}_8\text{O}_{22}(\text{OH})_2$	1.2
Total		100

6.2.3 HaHC extraction

Hydroxylamine hydrochloride (HaHC) was the preferred reagent for selective extraction of the amorphous or poorly crystalline iron oxides/oxyhydroxides in the present study. The HaHC extraction was performed as described in Section 4.4. The leach residue (R) was leached using 0.25 M HaHC and 0.25 M hydrochloric acid at 50°C and atmospheric pressure for 30 minutes. The remaining residue (R1) was dried in an oven at 60°C, weighed and the percent weight loss was calculated. The amount lost is referred to as a HaHC soluble phase. Residue samples were put through the HaHC extraction at least eight times to check for reproducibility. The average result is presented (sample calculation shown in Appendix C). The standard deviation (SD) for the HaHC soluble fraction was 0.4 – 0.5 wt%.

6.2.4 Pressure leaching autoclave

Pressure leaching experiments were performed using an autoclave. A one-liter (1 L) Parr autoclave with titanium internals was used. Temperature is controlled in this autoclave via an external heater and internal cooling coils. The external heater is a completely closed heating jacket with a power relay and switches. The cooling coil is fed by tap-pressurized water. Water flow is controlled by a fine needle valve in line with a solenoid, which is controlled by a digital temperature controller device. The thermocouple for temperature control is inserted into the thermo-well of the reactor. Temperature fluctuations with this system are limited to a $\pm 2^\circ\text{C}$. A 1/8 HP motor is used to turn the magnetic drive, which in turn rotates the two, four-bladed, 2" diameter 45° angled impellers. A multi-drive DC motor speed controller controls the agitation rate. Oxygen was supplied by a 40-

kg capacity cylinder (roughly 98% O₂ and 2% N₂), which is regulated by a double-stage regulator. The oxygen supplied directly into the autoclave is controlled by a needle valve at the inlet line to the autoclave. Oxygen bleed gas from the autoclave can be manually controlled by a fine needle valve on the bleed line to a predetermined flow meter setting and is measured by a rotameter.

6.2.5 Pressure leaching procedure

Feed slurry of 500 mL containing the concentrate solids, the source of Cl⁻(CuCl₂), surfactant, copper sulfate, and sulfuric acid was transferred to the bomb at room temperature. The temperature was raised to 150°C over a period of 20 min, and the agitation was maintained at 700 rpm (agitation at 1000 rpm did not result in any differences in recovery). At 145°C and steam pressure of approximately 414 kPa, oxygen is injected, and the pressure is raised to 1034 or 1379 kPa. This is time 'zero'. After 60 or 90 min of leaching, the oxygen supply is cut off, the pressure is brought down to 414 kPa, and the autoclave is cooled down to 25°C in 8 min. The autoclave is disassembled, and the residue is immediately pressure filtered and washed. The concentrate samples were put through the pressure leach at least three times to check for reproducibility. The experimental leaching plan is shown in Table 6-3.

6.2.6 Atmospheric leaching procedure

The CESL laboratory in Richmond, BC utilizes an EAL process to account for removable Cu lost to the residue as basic copper sulfate. EAL is used by CESL to assess the efficiency of the pressure leaching process. It closely resembles the atmospheric leach stage that they practice at larger scales. In this process, residues are stirred at 70°C for 2 h residence time in a 5 g/L KCl synthetic

solution, at a set pH (~1.4) which is maintained with acid additions. An alternative EAL was also carried out on pressure leach residues obtained from the autoclave in this study. In this process, residues were stirred at 60°C for a two-hour residence time in a 10 g/L H₂SO₄ solution. The solids content was 10% w/w for these experiments. The EAL was conducted in glass jacketed reactors connected to a water bath and was maintained at 60°C. If sulfur pellets were present in the residue obtained from the autoclave, the pellets were separated from the residue by using a 325 Mesh (44 µm) sieve, and reground (pulverized) and added back to the residue. The residues were then stirred at 60°C for two-hour residence time in a 10 g/L H₂SO₄ solution. Residue samples were put through the EAL at least three times to check for reproducibility.

The redox potential of the solution was measured by a saturated Ag/AgCl electrode. All measured potentials were converted from Ag/AgCl to the standard hydrogen electrode (SHE). All further potentials in this study are quoted with respect to the SHE at 25°C unless otherwise stated.

Table 6-3: Pressure leaching experimental matrix

Process parameter	Typical industry standards^a	Concentrate leaching batch experiments
Temperature (°C)	150	150
Total pressure (kPa)	1000-1300	1000-1300
Retention time (min) ^b	60-90	90
Feed conditions – solids		
P ₈₀ (µm)	20-25	21.5
Concentrate solids (mass % of total feed)	5-25	10
Hematite or residue seed (mass % of total feed)	NA ^c	0-60
Hematite seed P ₈₀ (µm)	NA ^c	5
Feed conditions – solutions		
Lignosol /OPD ^d (kg /t)	3-5	3
Sulfuric acid (g/L)	NA ^c	5-30
Cl ⁻ as CuCl ₂ (g/L)	5-12	12
Cu ²⁺ as CuSO ₄ (g/L)	5-15	12
Novel surfactants(kg/t)	NA ^c	3

^a Industry standard is in reference to a continuous multi-chamber autoclave industrial process; ^b Retention time in minutes from the time the batch system reaches 150°C to the time cooling is started; ^c NA refers to no addition;

^d Lignin sulfonate is normally used, and OPD has been found to work well for refractory ores.

6.3 Results and discussion

6.3.1 Acid concentration

Concentrate pressure leaching tests were performed at varying initial acid concentrations; leach residues were treated with hydroxylamine hydrochloride (HaHC) to determine the amount of HaHC soluble mass and the Cu associated with it. The results for the leaching of copper concentrate at various acid concentration are presented in Table 6-4. Final acid versus pH data provided by Teck is depicted in Figure 6-1.

Table 6-4: Effect of acid on HaHC soluble phase (Cu SD: 0.02% and HaHC SD: 0.5%)

Initial acid (g/L)	Final pH	^aFinal Acid (g/L)	ORP (mV)	Cu extn. (%)	^bHaHC sol. (%)
5	1.64	1.0	704	97.5	16.6
10	1.30	6.5	707	98.1	16.0
15	1.20	9.0	710	98.2	15.5
20	1.00	13.5	707	98.4	14.8
25	0.89	16.0	708	98.5	14.6
30	0.80	18.5	714	98.5	13.4

^aFinal acid determined from the FA - pH plot provided by Teck (see Figure 6-1); ^bHaHC was performed on leach residues after EAL(calculations in Appendix C)

The initial acid condition of 5–30 g/L was chosen because the experiments could not be performed at acid concentrations higher than 30 g/L due to surfactant deterioration apparent from a resultant agglomeration of concentrate particles during leaching. The acid concentration used in these

particular leaching experiments is limited by the surfactant's ability to withstand aggressive acid. The surfactant in these experiments was OPD.

As shown in Table 6-4, increasing initial acid concentration results in improved copper extractions. The copper extraction increased from 97.5% for a 5 g/L of initial acid concentration to 98.5% for a 30 g/L initial acid concentration. The amount of HaHC soluble phase also decreased from 16.6% for a 5 g/L acid concentration to 13.4% for a 30 g/L.

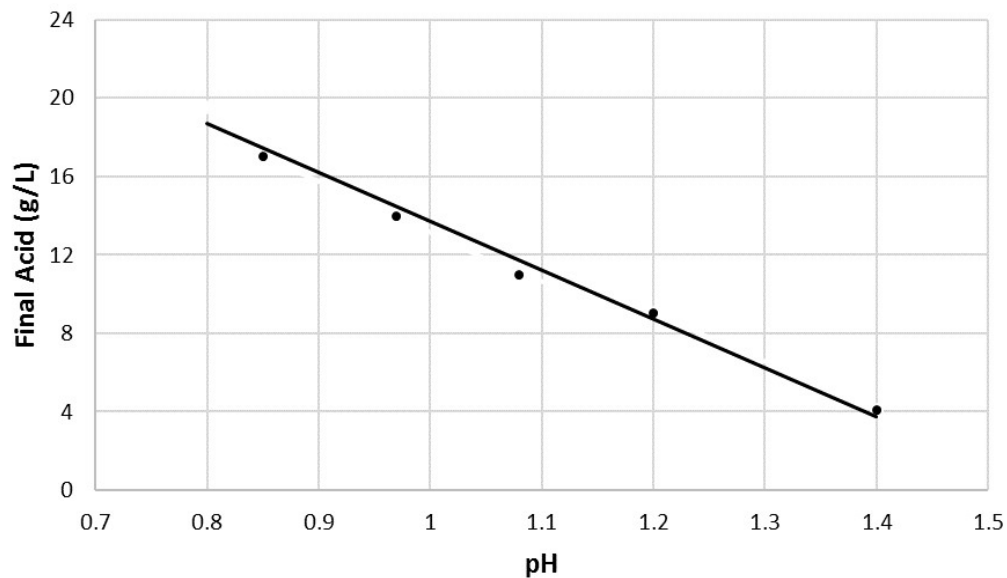


Figure 6-1: Final acid (g/L) versus pH
(reproduced from data provided by Teck)

The copper and iron in the leach residue are presented in Table 6-5. The amount of copper decreased from 1.89% at 5 g/L of initial acid to 1.12% at 30 g/L. The amount of iron decreased from 27.7% to 25.5%. The standard deviation was 0.02%. The effect of acid concentration on the HaHC soluble phase is shown in Figure 6-2.

Table 6-5: Cu and Fe in leach residue at varying free acid concentration (Cu and Fe SD: 0.02%)

Initial acid (g/L)	The residue (mass fraction)	
	Cu (%)	Fe (%)
5	1.89	27.7
10	1.66	27.2
15	1.41	26.8
20	1.35	26.9
25	1.14	26.5
30	1.12	25.5

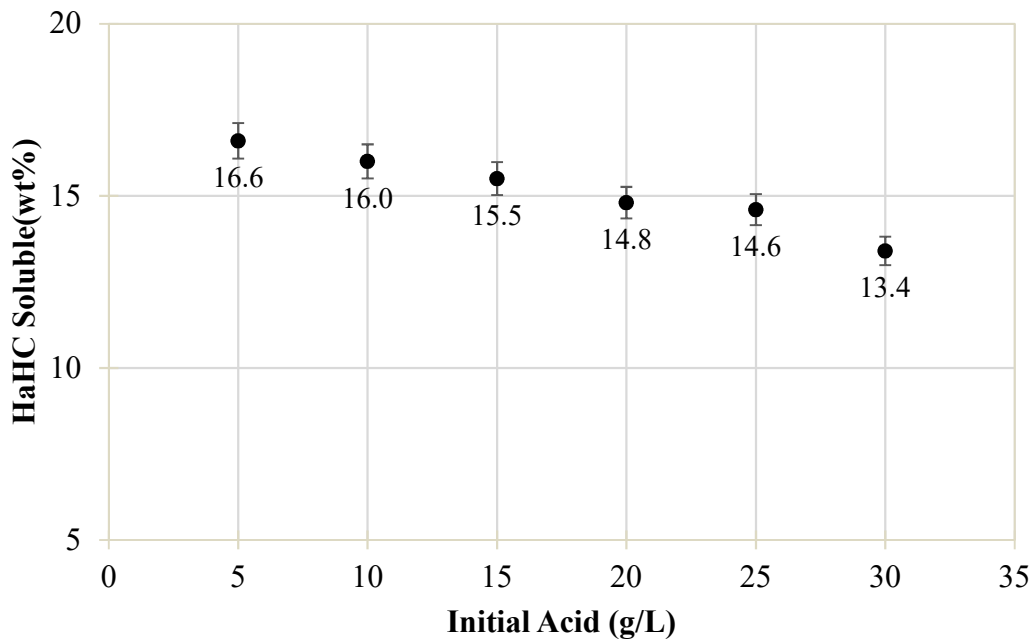


Figure 6-2: HaHC soluble mass (wt%) versus free acid (g/L)

The amount of copper and iron dissolved by HaHC treatment of the residue is shown in Table 6-6.

A 5 g sample from the leach residue was taken and treated with HaHC at 50°C for 30 min.

The 5 g sample contains 0.06–0.09 g of copper and 1.28 to 1.39 g of iron for varying acid concentrations. The HaHC dissolved copper decreases from 44.0% to 33.0% for residues generated with an initial acid concentration of 5 g/L to 30 g/L, respectively. The iron recovered also decreases, which agrees with the HaHC soluble numbers in Table 6-4. The HaHC soluble copper versus iron ratio was calculated. The Cu/Fe ratio remained the same at an average value of 0.08 and a standard deviation of 0.02. With the increase in acid concentrations, the amount of the HaHC soluble phase is reduced, which is consistent with the reduced supersaturation of ferric ions.

Table 6-6: Amount of Cu and Fe recovered by HaHC treatment of the residue at varying acid concentrations (Cu and Fe SD: 0.02%)

Initial acid (g/L)	Dissolved in HaHC		Cu/Fe ratio
	Cu (%)	Fe (%)	
5	44.0	25.2	0.11
10	37.5	27.2	0.08
15	42.0	27.6	0.08
20	42.0	23.0	0.10
25	33.0	27.0	0.06
30	33.0	22.7	0.07

The two important factors determining Fe(III) precipitation are temperature, and hydrogen ion or acid concentration as illustrated in Figure 6-3. The Fe(III) hydrolysis process generates acid and affects the acidity of the precipitate environment. The free H₂SO₄, that is released or present in the initial solution, reduces the degree of hydrolysis. The solid-phase composition is therefore affected

by the free acid concentrations as a lower degree of supersaturation slows the iron(III) precipitation kinetics (Vračar and Cerović, 1997).

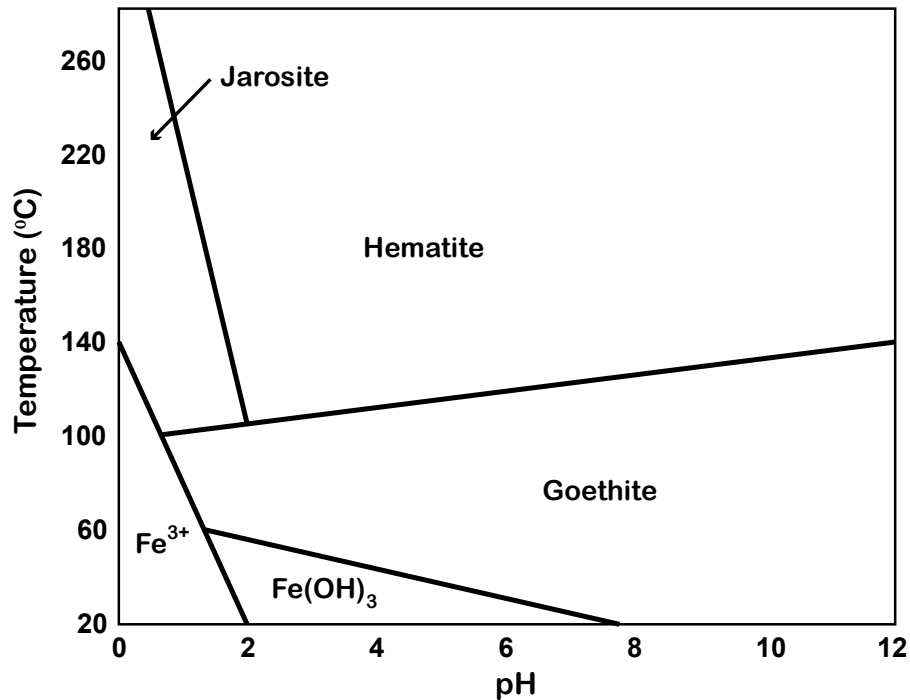


Figure 6-3: Effect of temperature and pH on the stability of the Fe compounds
(Babcan, 1971)

The production of well-grown crystals, which is of relevance to CESL and Vale processes, can be achieved by maintaining low supersaturation (Figure 2-17, Section 2.5) or the use of seed (residue recycle). The seed recycle is often practiced in an industrial process. The maintenance of low supersaturation, however, has been often neglected in aqueous precipitation process research and development (Demopoulos, 2009). It is clear, from the discussion in Section 2.5, that supersaturation control is important if the quality of the iron precipitates is to be improved. The

supersaturation can be controlled in practice by pH control, metal complexation, dilution, a redox reaction or a dissolution reaction. Precipitation of Fe(III) (oxy)hydroxides is a hydrolytic precipitation phenomenon. The formation of the hydroxide solid is preceded by the partial hydrolysis of metals ions and formation of soluble hydrolyzed species. These hydrolyzed species under high supersaturation undergo polymerization to form precipitates that are mostly amorphous. Meticulous control of supersaturation at very low values is necessary to overcome this tendency of metal ion hydrolytic polymerization (Demopoulos, 2009).

A critical value of the free acid concentration of sulfuric acid ($[H_2SO_4]_{cr}$), defines the stability region of hematite. Hematite is stable below this value, and above this value basic ferric sulfate is stable. At a temperature of 150°C, hydrolysis and precipitation of hematite occurred up to the sulfuric acid concentration of 53.4 g/L (Sasaki et al., 1993). The stability region was found to be enlarged in the presence of metal sulfate salts such as $ZnSO_4$, $CuSO_4$, $MgSO_4$, and Na_2SO_4 . The free H^+ concentration governs the solubility of hematite, and the addition of sulfate salts decreases the free H^+ concentration resulting in the enlargement of the hematite stability region (Umetsu et al., 1977).

Rubisov and Papangelakis (1999) characterized the precipitates obtained by acid leaching of limonite laterite at 270°C using SEM/EDX and laser particle analysis and found that the shape of hematite particles gradually changes from thin flakes at lower acidity to spherical structures at higher acidity. As shown in Figure 6-4, taken from the same paper, low acidity of 0.158 mol/L (15 g/L) produced very thin platelet flakes of hematite precipitate. As the acidity increased, the flakes became smaller and thicker and finally at 0.342 mol/L (42 g/L) of free sulfuric acid, the particles

developed a spherical or slightly elliptical shape. This change in morphology was explained using the hydrogen ion concentration at 270°C, calculated from speciation analysis.

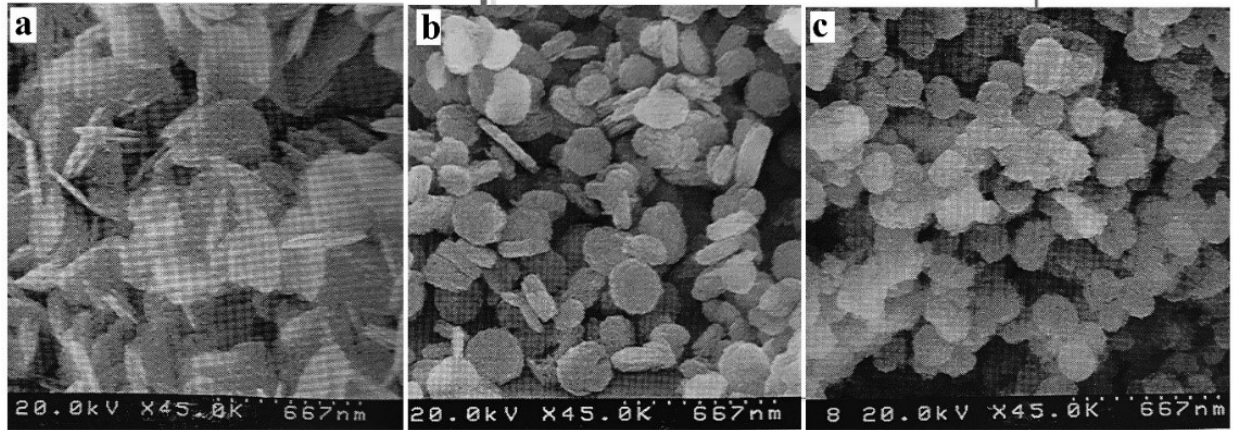


Figure 6-4: Effect of acid concentration on the morphology of hematite precipitate
a) at 0.158 mol/L b) at 0.220 mol/L c) 0.342 mol/L (Rubisov and Papangelakis, 1999)

According to the surface adsorption theory, if the solution pH is above the point of zero charge (PZC), the surface concentration of OH^- on that oxide dominates (Stumm, 1992). The PZC of hematite at 70°C is at a pH of 7.75 (Stumm, 1992) and therefore platelet hematite can be formed above pH 7.75. The shape transition of the hematite precipitates formed at 270°C by Rubisov and Papangelakis (1999) was shown to occur at the point of zero charge (PZC) of the hematite (~ 0.16 mol/L H^+ , at 270°C) and was also attributed to the preferential adsorption of specific ions on the surface. It was concluded that the hematite platelets were also precipitating under the influence of OH^- on the surface and therefore, the acidity ($[\text{H}^+]_T = 0.16$ mol/L) at which the transition from platelets to spheres takes place was close to the PZC of hematite at 270°C. The PZC of many oxides decreases as the temperature increases, and in the case of hematite, the PZC is at pH=8.7 at 20°C and decreases to pH=7.65 at 80°C (Stumm, 1992). Rubisov and Papangelakis (1999) used

the hydrogen ion activity coefficient calculation performed by Baghalha and Papangelakis (1998) at 250°C, to estimate the PZC for hematite at 270°C and determined the PZC of hematite at 270°C to be $-\log(0.4 \cdot 0.16)$ which is equal to pH 1.2.

Sugimoto and Muramatsu (1996), prepared monodispersed hematite by a gel-sol method at 70°C and have shown that growing hematite platelet particles requires a highly basic solution (at least 2.5 mL/L NaOH). Whereas, Sugimoto and Wang (1998) prepared elliptical or peanut type particles under more acidic conditions and in the presence of sulfates. They explained this difference in the shape was due to adsorption of hydroxyl complexes on the hematite surface. OH^- adsorbs on the $\{001\}$ face of hematite retarding its growth. In acidic conditions, the adsorption of SO_4^{2-} controls the particle shape. Ruiz et al. (2007) also reported that the initial concentration of sulfuric acid has a significant influence on the particle size of the precipitate. They have found that the hematite particles produced at 200°C, in the presence of 10 g/L H_2SO_4 , were significantly larger than the particles produced at 1 g/L H_2SO_4 . The particle size d_{50} values were 31.4 μm for 10 g/L H_2SO_4 and 2.5 μm for 1 g/L H_2SO_4 . They ascribed the smaller average size at the lower acid concentration to a higher supersaturation and particle growth inhibition. They stated that the supersaturation of ferric ions would increase at lower acid concentrations and therefore, the nucleation rate increases leading to the production of finer hematite particles. Moreover, the rapid formation of these small particles may inhibit the agglomeration and growth mechanism leaching small particles at low acid concentrations.

Dutrillac and Chen (2009) found the precipitate crystallinity to increase with the increasing acid concentration. They produced hematite particles from a mixed sulfate-chloride solution at 150°C.

The precipitate consisted of ~ 10 μm agglomerates resembling tiny cauliflowers. At a lower initial acid concentration of less than 0.125 mol/kg (~ 12 g/L) H_2SO_4 , varying amounts of poorly crystalline goethite were detected. At higher initial acid levels hematite of typically 60% Fe and 5 to 7% SO_4 precipitated and the goethite was suppressed.

Therefore, pH is an important factor for controlling particle size, especially in the formation of iron oxides and iron oxyhydroxide. The pH or excessive concentration of ferric ions in the nucleation stage dictates the final size of the hematite particles prepared in the gel-sol system (Sugimoto et al., 1993; Sugimoto and Muramatsu, 1996). Owing to the constant solubility product of the $\text{Fe}(\text{OH})_3$ gel in this case, the control of pH and the control of the excess concentration of ferric ion was equivalent. In the nucleation stage of the hematite, the solute in the solution phase was in equilibrium with the $\text{Fe}(\text{OH})_3$ gel (Sugimoto et al., 1993). In terms of solubility product, the supersaturation for this nucleation was kept constant with the change of pH. The increase in pH resulted in enhanced nucleation, and this was because of an increase in the concentration of some specific hydroxide precursor complex of ferric ions with pH and the nucleation of hematite ceased when the pH was lowered below a certain level such as $\text{pH}=1$ by the formation of $\beta\text{-FeOOH}$. It was, therefore, possible by varying pH or the excess concentration of ferric ions to control the final size of the hematite. The forced hydrolysis of a dilute homogeneous solution of a ferric salt, such as FeCl_3 , $\text{Fe}(\text{Cl}_4)_3$, or $\text{Fe}(\text{NO}_3)_3$ at a relatively high pH above 3 produces nanosized hematite less than 10 nm in very small amounts and at the lower pH, more particles with larger sizes are formed. These trends are observed in general synthetic systems of metal oxides and metal hydroxides.

6.3.2 Seeding and residue recycle

Leaching experiments on the concentrates were performed in the presence of the following seed materials:

- i. Synthetic hematite seed (*pure hematite Fe_2O_3*)
- ii. Synthetic hematite seed residue recycles (*residue generated using pure hematite seed*)
- iii. Residue recycle (*residue generated in the absence of any seed*)

When a seed is used, the HaHC calculation has to take into account the crystalline part of the seed, and this amount has to be subtracted from the HaHC mass loss of the residue to give a calculated (actual) amount of the HaHC soluble phase. The schematic for the calculation of HaHC phase for seeding experiments is presented in Figure 6-5.

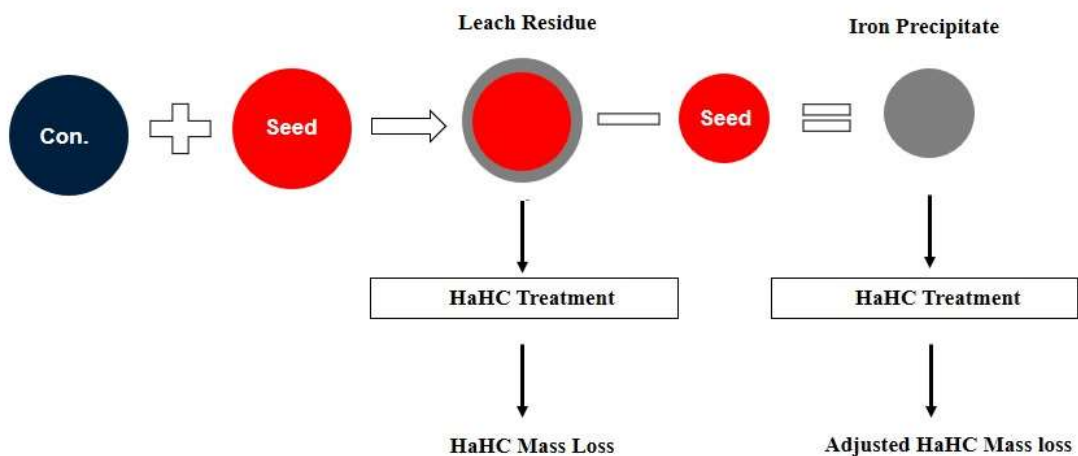


Figure 6-5: Schematic representation of calculating HaHC soluble phase

The effect of synthetic hematite seed (i), synthetic hematite seed residue recycle (ii) and residue recycle (iii) for copper concentrate is presented in Table 6-7 to Table 6-9 and Figure 6-6.

Table 6-7: Effect of synthetic hematite seed (Cu extn SD: 0.02%)

Seed (g)	Seed (wt% of feed solids)	HaHC (wt%)	Initial acid (g/L)	Final pH	Free acid (~g/L)	ORP (Eh) (mV)	Cu extn. (%)
5	10	10.8	15	1.10	10	703	97.50
10	20	8.8	15	1.05	10	695	97.84
15	30	7.2	15	1.08	10	688	97.75
20	40	4.8	15	1.04	10	688	97.42
25	50	4.6	15	1.09	10	694	97.69
30	60	4.8	15	1.05	10	691	97.68

The HaHC soluble phase decreases from 10.8% to 4.8% for a seed of 5-30 wt% of feed solids respectively. The seed may help in reducing the HaHC soluble phase by improved hematite nucleation, but the copper extractions are not greatly influenced. The lower extractions can be attributed to the dilution factor. The addition of seed increased the wt% solids in the reactor. Seed may have also adsorbed some of the surfactant making it less effective. The recycled seed also introduces some amorphous iron oxides into the reactor (see Figure 6-5), therefore, increasing the loss of copper to the residue and lowering the extractions. The effect of synthetic hematite seed on the calculated HaHC soluble phase is shown in Table 6-8. The HaHC soluble phase decreases from 12.6% to 8.2% for a varying amount of seed addition.

Table 6-8: Effect of synthetic hematite seed on calculated HaHC soluble phase (HaHC SD: 0.5%)

Seed (wt% of feed solids) Seed(g)/50(g)*100	HaHC mass loss (wt%)	*Calculated HaHC soluble (wt%)
10	11.2	12.6
20	8.8	11.0
30	7.2	10.0
40	4.8	7.3
50	4.6	7.6
60	4.8	8.2

*The calculated HaHC numbers were generated using the method presented in Figure 6-5.

The effect of seed recycle on the amount of HaHC soluble phase is presented in Table 6-9. The ‘seed recycle’ is the term used to describe a seed that is the residue resulting from the use of the synthetic seed. The seed recycle is not pure hematite and has other phases associated with it, and its HaHC soluble content is 10%. As seen in Table 6-9, it is not as effective in decreasing the HaHC soluble phase as pure hematite seed.

Table 6-9: Effect of seed recycle on HaHC soluble phase (HaHC SD: 0.5%)

Seed (wt% of feed solids)	HaHC mass loss (wt%)	Calculated HaHC soluble (wt%)
10	13.6	15.3
20	8.6	11.7
30	6.6	10.5

The effect of residue recycle on the HaHC soluble phase is presented in Table 6-10. The ‘residue recycle’ is the term used to describe a seed that is the residue resulting from an un-seeded leaching experiment. The residue recycle has other phases associated with it, and its HaHC soluble content is 15%. As seen in Table 6-10, the seed does not affect the HaHC soluble phase in the amounts tested here. Perhaps, for the residue recycle to work, we may have to use recycle in amounts much higher than 30 wt% of feed solids. The resultant disadvantage of this is a requirement to heat up all that residue recycle material. Sulfur is also put back into the autoclave, which is undesirable, as it interferes with copper extraction and/or requires more surfactant. Residue recycling also introduces amorphous iron oxides into the reactor, therefore, possibly increasing the loss of copper to the residue and lowering ultimate extractions.

Table 6-10: Effect of residue recycle on HaHC soluble phase (HaHC SD: 0.5%)

Seed (wt% of feed solids)	HaHC mass loss (wt%)	Calculated HaHC soluble (wt%)
10	15.4	17.1
20	11.8	15.6
30	10.0	15.2

The comparison of the effect of synthetic seed, seed recycle, and residue recycle on the amount of HaHC soluble phase is presented in Figure 6-6. The amount of HaHC soluble phase is significantly reduced from 16% to 7% upon the addition of synthetic hematite seed whereas the residue recycles does not seem to affect the HaHC soluble phase. This may be due to the lack of fresh hematite surface for the new nuclei to grow on. However, seeding did not improve the copper extractions.

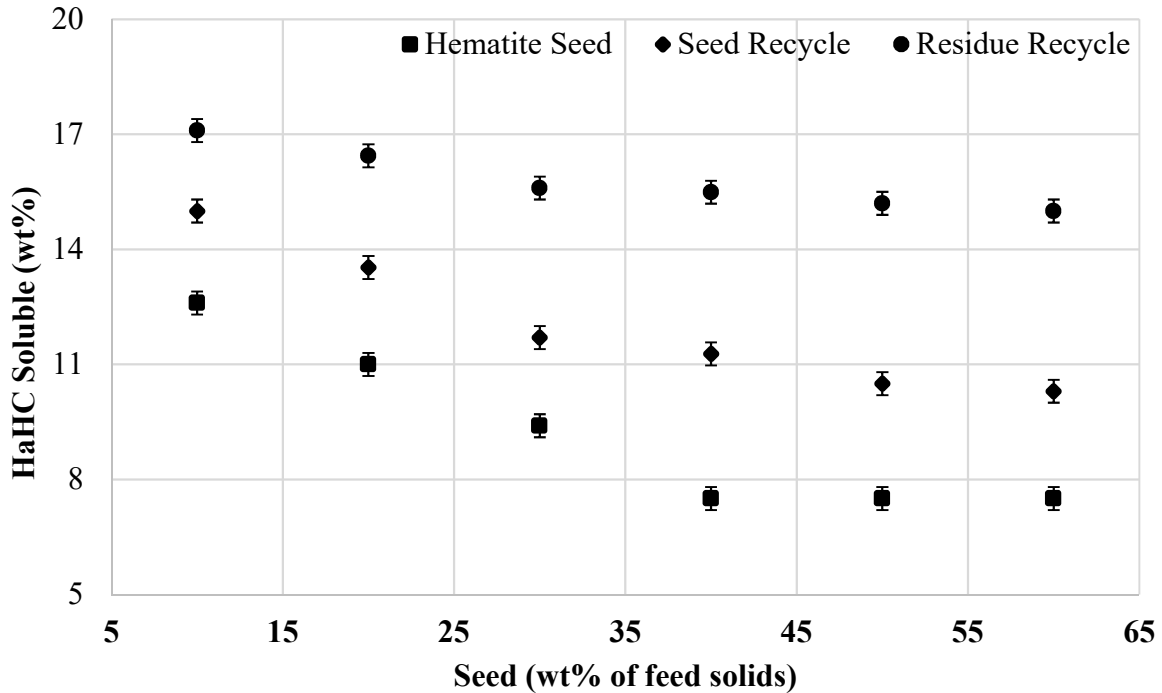


Figure 6-6: Effect of hematite seed, seed recycle and residue recycle on HaHC soluble phase

Seeding is a useful technique, and the addition of the seeds lowers the supersaturation. The separation between nucleation and growth can be achieved readily by seeding. Furthermore, if the added seeds work at maximum efficiency, the final particle number will be equal to the number of the seeds. Even if the efficiency is not 100%, the final particle number is at least proportional to the number of the added seeds, and thus quantitative size control of a high reproducibility is readily realized. The final sizes of monodispersed hematite particles in a dilute homogeneous system (Sugimoto and Muramatsu, 1996) and in condensed gel-sol systems (Sugimoto et al., 1998; Sugimoto et al., 1993b) were controlled by using seeds of hematite.

Riveros and Dutrizac (1997) studied the precipitation of hematite from ferric chloride media at 150°C. They found that in the absence of seed the hematite particles were very small spheres of 1

μm in size which coalesced into loose aggregates of 10 – 20 μm . However, in the presence of hematite seed (20 g/L), the hematite particles were larger, several microns in size and resulted in larger aggregates with extensive particle agglomeration. Seeding with hematite was found to promote hematite formation and resulted in the improved filterability of the precipitate. Seeding also enhanced the kinetics of precipitation resulting in complete precipitation during the ‘heat-up’ time, i.e., by the time the contents of the autoclave were heated to temperature. In another study, Dutrizac and Riveros (1999) confirmed hematite seed promoted direct precipitation of hematite instead of metastable akageneite. The seed particles provided an initial surface area for the secondary nucleation mechanism to take place and resulted in hematite precipitation and growth.

Chen and Dutrizac (2009) studied the factors affecting the precipitation of hematite rather than jarosite in nickel sulfide concentrates leached under autoclave conditions at 150°C and again found the presence of hematite seed promoted hematite formation while suppressing jarosite precipitation. Dutrizac and Sunyer (2012) studied the hydrothermal conversion of jarosite type compounds to hematite and found that, in the presence of hematite seed (20-50 g/L), the conversion was complete within 2 hr at 225°C. The presence of hematite seed promoted the hydrothermal conversion of ‘in situ’ formed jarosite compounds significantly and the hematite formed was found to consist of spheroidal or sub spheroidal agglomerates 10–100 μm in size.

Marsden et al. (2010) patented the use of seeding material in their pressure oxidation process. A seed was added to the pressure leaching autoclave to provide a nucleation site for the crystallization and growth of hematite residue. They indicated that a seeding agent might be generated either by recycling of the residue or by the introduction of foreign substances and in some cases, more than

one or a combination of seed agents may be used during pressure leaching. They found that residue that precipitates from solution passivates the reactive process by encapsulating a metal that is being recovered. In the presence of a seeding agent, the precipitates form at or in proximity to the seed, instead of the metal value, thus leaving the metal value exposed and amenable to leaching recovery. The hematite precipitated during leaching or the recycled hematite-containing residue from the previous pressure leaching cycle was found to act as the precipitate nucleation sites. In the absence of which, unreactive particles precipitated on the surface of the metal values, rendering the metal values unrecoverable by occluding the desired metal values. Therefore, a seed prevented such occlusion and assisted in better metal recovery.

Kubota et al. (2001), mentioned that seeding is carried out as more of an art than a science and according to Heffels and Kind (1999) the amount of seed added is based on trial and error experience. However, to cause the deposition of the precipitate on the seed, in most cases, a seed concentration of $C_s=1.0$ was found to be sufficient. Where C_s is the ratio of the seed added to the theoretical yield calculated from solubility data (Doki et al., 2001). According to Heffels and Kind (1999), the particle size of the seed is determined by the stirrer speed that would be used in the experiments based on considerations of secondary nucleation. A very fine seed would result in small particles with narrow size distribution and therefore not recommended.

Hove et al. (2009), studied the ferrous iron oxidation and precipitation process in the presence of seed and found that seed showed a catalytic effect on the rate of oxidation of Fe(II) and formed stable iron precipitates at the expense of less stable phases which are kinetically favored. They found that seeding suppressed homogeneous nucleation by providing a large surface area that

lowered or reduced the degree of supersaturation and this resulted in enhanced growth of the precipitated particles. The surface area provided by the seeds was found to depend on the amount of seed added and the particle size of the seed. Tamura et al. (1976) and Sung and Morgan (1980) also found that hematite seed had a catalytic effect on the rates of ferrous oxidation. The heterogeneous oxidation of ferrous iron was proportional to the amount of ferrous iron adsorbed on the oxide surface (Park and Dempsey, 2005). Jeon et al. (2001) also demonstrated that a hematite seed is a good absorbent for ferrous iron and resulted in heterogeneous oxidation of the ferrous iron in the presence of oxygen. It has also been reported in that ferrous iron adsorbed on metastable ferrihydrite catalyzed the transformation of ferrihydrite into more stable phases (Jolivet et al., 1992; Park and Dempsey, 2005; Tronc et al., 1992).

6.3.3 Novel reagent for iron and sulfur control

During the leaching experiments, a novel additive (commercially available “WD40[®]”) that seems to aid in the formation of hematite was accidentally discovered. Following this discovery, a series of other reagents were tested. The reagents were added to the feed slurry before leaching as described in Section 6.2.5. These reagents may displace the water from the ferrihydrite structure and expedite its transformation to hematite. They may also help in binding the sulfur particles together into clusters or agglomerates that can be more easily separated from the residue.

The effect of WD40[®], nonane and cyclohexane is presented in Table 6-11. For a concentrate with a particle size of P₈₀:21.5 μm in combination with OPD, WD40[®] is shown to improve the copper extraction to 98.8% as compared to 98.0% in the absence of WD40[®] with a standard deviation of

0.02%. Further, WD40[®] in combination with OPD will effectively leach a concentrate with particle size P₈₀:75 µm. This may eliminate the need for upfront grinding of the feed material. When a P₈₀:75 µm concentrate is leached with OPD in the absence of WD40[®], the copper extraction is only 90.3%. Table 6-11 also presents the effect of nonane, which functions in the absence of OPD and which has the potential to replace OPD.

Table 6-11: Effect of WD40[®], nonane and cyclohexane (Cu extraction SD: 0.02%)

Feed solids P ₈₀ (µm)	Reagent (3 kg/t)	OPD (kg/t)	Conc. (g/L)	Acid in (g/L)	Cu extn (%) pressure leach	Cu extn (%) after EAL*
20	WD40 [®]	3	100	15	96.5	98.8
75	WD40 [®]	3	100	15	95.4	98.4
20	Nonane	3	100	15	96.6	98.7
20	Nonane	None	100	15	95.9	98.5
20	Cyclohexane	3	100	15	96.6	98.9
Base case						
20	None	3	100	15	96.6	98.0
75	None	3	100	15	86.9	90.3

*EAL for residue containing sulfur pellets was performed as described in Section 6.2.6

The effects of decane, mineral oil, and carbon disulfide is presented in Table 6-12. The effect of decane for a concentrate with a particle size of P₈₀:21.5 µm, and in combination with OPD, is to improve the copper extraction to 99.4% as compared to 98.0% in the absence of decane. Further, decane in combination with OPD leaches a concentrate with particle size P₈₀:75 µm, but with the resultant copper extraction of 99.1, an improvement compared to WD40[®]. Decane was tested in

the absence of OPD, and it appears to have the potential to replace OPD. WD40[®] does not work in the absence of OPD. Mineral oil offers similar copper extractions to decane and has the potential to leach P₈₀:75 µm feed concentrates.

Table 6-12: Effect of decane and mineral oil (Cu extraction SD: 0.02%)

Feed solids P₈₀ (µm)	Reagent (3 kg/t)	OPD (kg/t)	Conc. (g/L)	Acid in (g/L)	Cu extn (%) pressure leach	Cu extn (%) after EAL
20	Decane	3	100	15	96.8	99.4
75	Decane	3	100	15	95.6	99.1
20	Mineral oil	3	100	15	96.9	99.2
75	Mineral oil	3	100	15	95.7	98.9
20	Carbon disulfide	None	100	15	96.6	99.3
----- Base case -----						
20	None	3	100	15	96.6	98.0
75	None	3	100	15	86.9	90.3

The effects of benzene sulfonic acid (BS), nonane sulfonic acid (NS), methane sulfonic acid (MS) and phenyl phosphonic acid (PP) are presented in Table 6-13. These are another class of reagents that are iron complexing and result in similar effects as the others, and they have the potential to replace OPD as they function in the absence of OPD and give excellent copper extractions. One such candidate, benzene sulfonic acid, for example, is plentiful and relatively inexpensive as compared to OPD.

Table 6-13: Effect of NS, BS, MS, and PP (Cu extraction SD: 0.02%)

Feed solids P₈₀ (μm)	Reagent (3 kg/t)	OPD (kg/t)	Conc. (g/L)	Acid in (g/L)	Cu extn (%) pressure leach	Cu extn (%) after EAL
20	Nonane sulfonic acid	None	100	15	96.5	98.8
20	Benzene sulfonic acid	None	100	15	95.4	99.3
20	Methane sulfonic acid	None	100	15	96.6	98.5
75	Methane sulfonic acid	3	100	15	95.9	99.2
20	Phenyl Phosphonic acid	None	100	15	96.5	99.1
20	Phenyl Phosphonic acid	3	100	15	95.8	99.2
Base case						
20	None	3	100	15	96.6	98.0
75	None	3	100	15	86.9	90.3

All the reagents: WD40[®], nonane, cyclohexane, decane, mineral oil, carbon disulfide, nonane sulfonic acid, benzene sulfonic acid, methane sulfonic acid, and phenyl phosphonic acid result in sulfur “prills” (0.5-1.5 mm) rather than small particles (20-35 μ m). OPD is the only surfactant that does not result in visible sulfur prills, as shown in Figure 6-7. The sulfur prills obtained with different reagents are presented in Figure 6-8 to Figure 6-11. These sulfur prills come in different shapes and sizes, and they contain impurity phases such as pyrite and unleached sulfides. Irrespective of this fact, the copper extractions from the feed concentrate remain high. However, there are two issues to consider regarding large sulfur prills. First, excessive pooling or accumulation of sulfur at the bottom of the vessel could lead to localized reducing conditions, an

incomplete reaction and catastrophic outcomes for the autoclave. Second, downstream "sanding out" in tanks and additional wear on equipment (these particles will erode metal if agitated sufficiently) may occur. So, it is a matter of finding the conditions that result in the largest sulfur particles that do not cause operational issues. The ideal range appears to be 0.1 to 1 mm for easy separation from the balance of the iron-rich residue (Salomon-De-Friedberg, 2017).

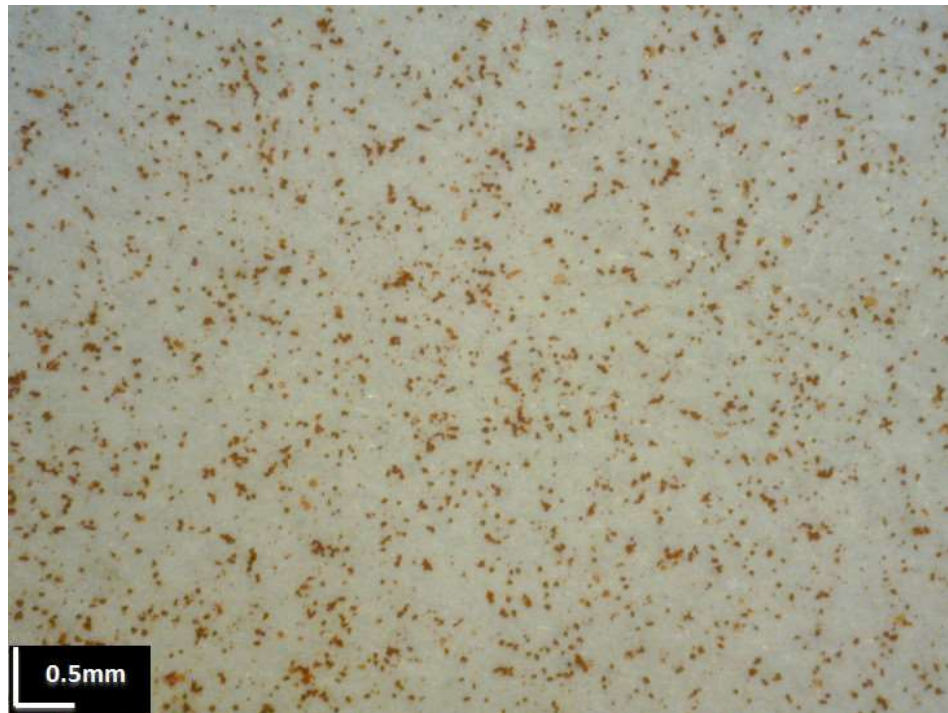


Figure 6-7: Effect of OPD on sulfur in the leach residue (no visible sulfur prills)



Figure 6-8: Effect of WD40[®]+OPD on sulfur in the leach residue



Figure 6-9: Effect of benzene sulfonic acid on sulfur in the leach residue

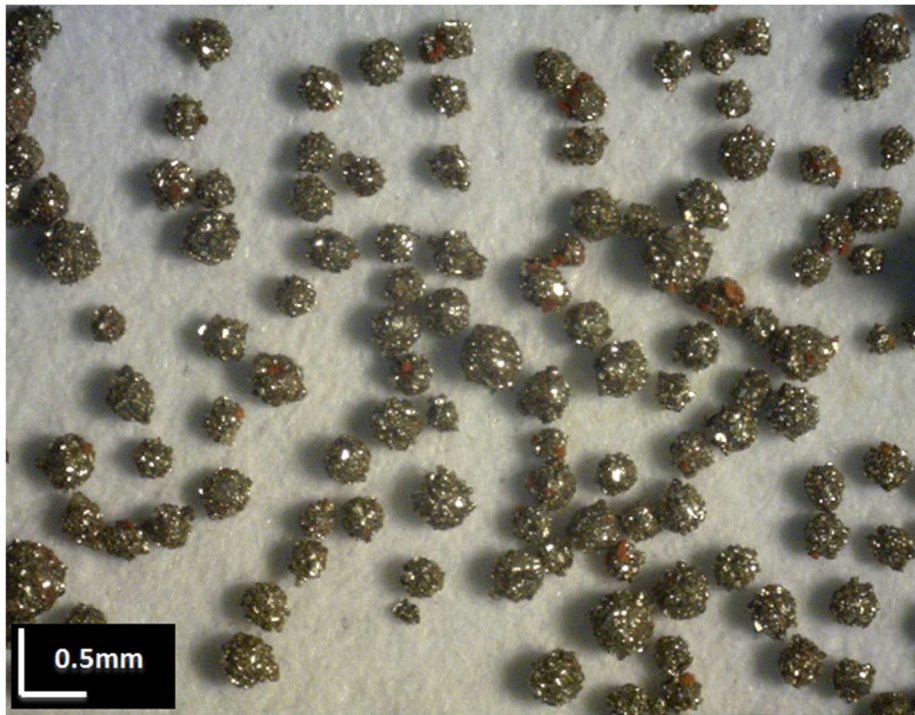


Figure 6-10: Effect of phenyl phosphonic acid on sulfur in the leach residue



Figure 6-11: Effect of phenyl phosphonic acid on sulfur (crushed) in the leach residue

The amount of pyrite recovery in the leach residue, calculated from the mass balance of pyrite in the feed concentrate and pyrite in the leach residue, is presented in Figure 6-12 and the quantitative mineralogical phase analysis of the residue generated with different reagents is presented in Table 6-14. There is no chalcopyrite remaining in the residue indicating complete copper extraction. There is a minor amount (0.1 – 0.5%) of tennantite that remains unleached, which accounts for the minor amounts of copper (0.02 – 0.05%) in the residue. The copper concentrations in the quantitative mineralogical phase analysis match well with the copper extractions calculated from chemical analysis. WD40[®] yields the maximum amount of hematite (32.3%). Another phase of interest here is pyrite. Some reagents, such as benzene sulfonic acid and phenyl phosphonic acid seem to reduce pyrite oxidation and increase the concentration of pyrite in the leach residue (Figure 6-12), which may be beneficial for process economics (due to the need for less acid neutralization and/or less elemental S yield).

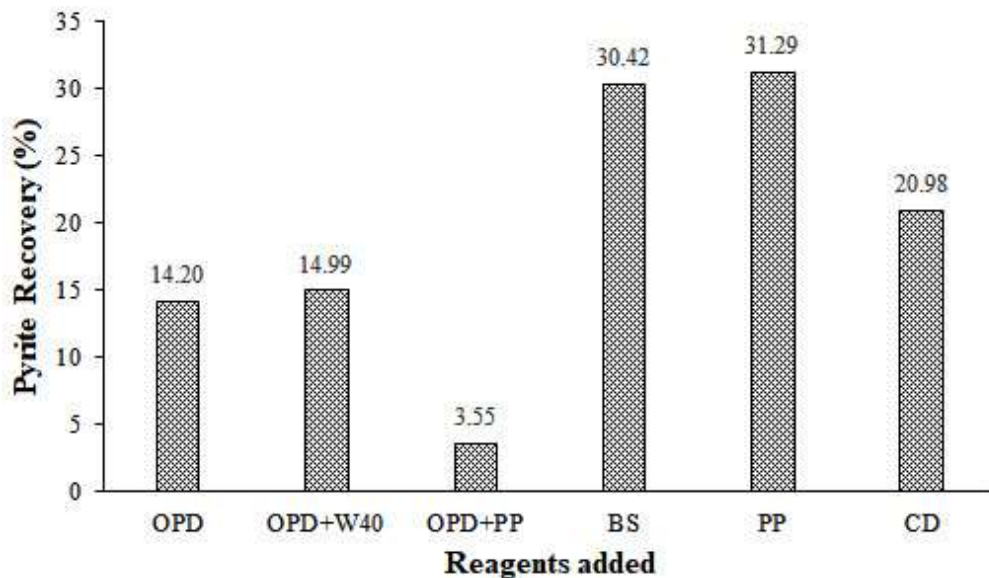


Figure 6-12: Effect of various reagents on the pyrite recovery in the leach residue

Table 6-14: Effect of reagents on QXRPD of the residue from the standard copper concentrate leaching experiments

Crystalline phases	Base case	OPD+ WD40[®]	OPD+ PP	Benzene sulfonic	Phenyl phosphonic	Carbon disulfide
Actinolite	1.0	0.8	1.4	1.0	1.5	1.2
Albite low	4.0	3.1	3.8	4.0	4.5	4.1
Clinchlore	2.6	2.0	2.6	2.6	3.7	2.1
Hematite	29.6	32.3	31.1	26.4	23.7	31.3
Muscovite	4.3	3.9	4.3	4.2	4.3	4.1
Jarosite	2.1	1.9	2.0	2.7	2.9	3.8
Molybdenite	0.3	0.5	0.4	0.2	0.3	0.2
Pyrite	4.9	5.1	1.3	10.1	10.5	7.1
Quartz low	5.8	5.7	5.7	6.2	5.9	6.2
Sulfur	32.4	32.1	33.7	29.6	30.2	27.5
Talc 1A	12.5	12.1	13.3	12.5	12.4	12.0
Tennantite	0.5	0.6	0.4	0.5	0.1	0.5

As seen via comparison of Table 6-14 with Table 4-3, both the batch experiments in this work and the continuous plant operations generate remarkably similar residues (see Section 4.3, Chapter 4). The effect of reagents on the HaHC soluble phase is presented in Table 6-15. The HaHC soluble phase is clearly affected by the reagents. For example, the HaHC soluble phase for WD40[®] decreased to 7%. The HaHC soluble phase in the absence of WD40[®] was 15%. The lowered amount of HaHC implies lowered amounts of amorphous Fe residue formed, which would explain a lessened amount of Cu lost to this phase resulting in higher overall Cu extraction.

Table 6-15: Effect of reagents on HaHC soluble phase (HaHC SD: 0.5%)

Feed solids P₈₀ (μm)	VOCs (3 kg/t)	OPD (kg/t)	HaHC soluble phase (%)
20	WD40 [®]	3	6
75	WD40 [®]	3	6
20	Decane	3	7
75	Decane	3	7
20	Mineral oil	3	7
75	Mineral oil	None	7
20	Benzene sulfonic	None	7
20	Carbon disulfide	None	7
20	Phenyl phosphonic	None	7
----- Base case -----			
20	None	3	15
75	None	3	15

To illustrate the effect of WD40[®] on hematite particles, synthetic hematite was precipitated in a separate set of experiments in the presence of and in the absence of WD40[®] in sulfate-chloride solutions at 150°C. The hematite particles were then studied under a scanning electron microscope (SEM). The SEM micrographs are shown in Figure 6-13 and Figure 6-14.

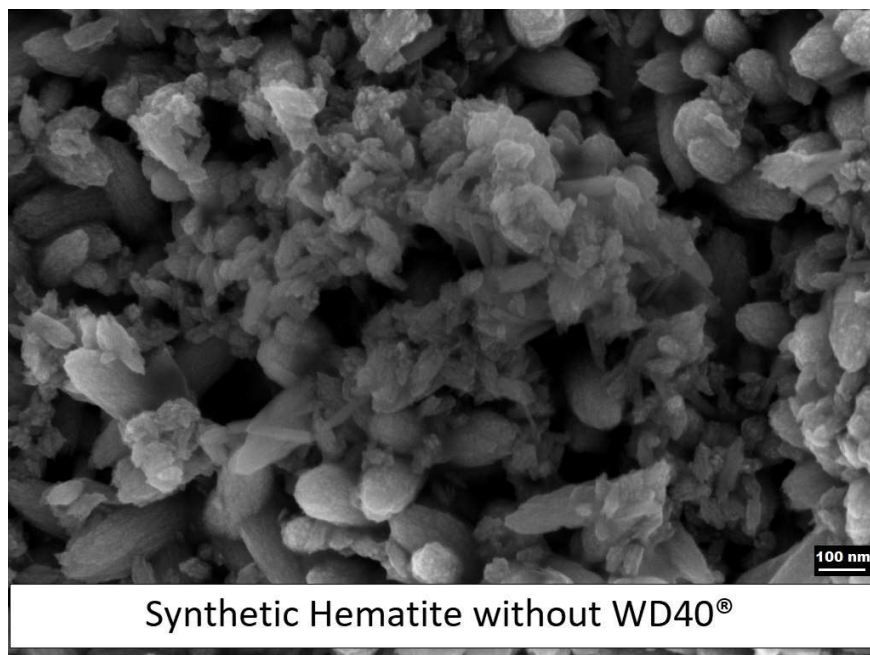


Figure 6-13: Synthetic hematite in the absence of WD40®
(The scale bar is 100 nm)



Figure 6-14: Synthetic hematite in the presence of WD40®
(The scale bar is 100 nm)

In the presence of WD40[®] the hematite particles precipitated as peanut-shaped spindle particles. It appears that adsorption and surface interactions of WD40[®] with the nuclei influence the subsequent growth mechanism of hematite particles resulting in the peanut shaped-spindle type morphology. Ozaki et al. (1984) demonstrated that the presence of small amounts of phosphate and hypophosphite ions during the forced hydrolysis of ferric chloride solutions also result in this spindle-type hematite. The adsorption of phosphate ions on hematite and surface interactions of phosphate ions with the nuclei influencing the subsequent growth mechanism was resulting in the change in morphology. The hematite prepared in the presence of WD40[®] is very similar in morphology to the hematite prepared by Ozaki et al. (1984).

6.3.3.1 Water displacement formula WD40[®]

The term "WD-40[®]" is abbreviated from Water Displacement, 40th formula, as the product was the result of the 40th attempt. The formula was never patented and remains a trade secret. The WD40[®] company website states that the main ingredient is a non-volatile viscous oil which gives protection from moisture and provides lubrication. This non-volatile oil is diluted with a volatile hydrocarbon to help penetrate crevices, which eventually evaporates leaving behind the oil ("WD40[®]"). However, the main ingredients according to the WD40[®] U.S. Material Safety Data Sheet information are 50% aliphatic hydrocarbons, 25% petroleum-based oil, 12–18% low vapor pressure aliphatic hydrocarbons, 2–3% carbon dioxide (propellant) and less than 10% inert ingredients. While the German version of the mandatory EU safety sheet lists the following safety-relevant ingredient(s) 60–80% hydrogen-treated heavy naphtha, Di Justo (2009), published the

results of gas chromatography and mass spectroscopy tests on WD-40[®]. The principal components were mostly alkanes (nonane, decane, tridecane, tetradecane) and mineral oil.

The complexation of Fe by WD40[®] during pressure leaching is a possibility. This could occur similarly to the complexation of Fe with organic compounds as described in Sections 2.6 and 6.3.3.2. The pressure leaching experiment involving WD40[®] also contained an equal amount of sulfur dispersing agent OPD (0.15 g, 3 kg/t). OPD is adsorbed chemically through the interaction of C-N functional groups with the metal ions forming a metal-amine complex (Owusu, 1993). This chemisorption is a monolayer phenomenon, and a small amount of 0.15 g OPD is therefore sufficient to influence the 50 g of chalcopyrite concentrate used in the present study. Similarly, WD40[®] may be adsorbed chemically through interactions of the R-COOH functional groups with ferric ions forming a metal-WD40[®] complex resulting in monolayer chemisorption. The reaction of OPD with WD40[®] (comprising alkanes) may be giving rise to these carboxyl (R-COOH) functional groups (Section 2.9.1). WD40[®], when tested in the absence of OPD, resulted in agglomerates of unleached concentrate, suggesting it does not assist in sulfur dispersion.

While complexation may play a small role in controlling supersaturation, it is most likely that WD40[®] acts as a crystal nucleation-controller. A proposed mechanism for the effect of WD40[®] on nucleation and growth of hematite particles is schematized in Figure 6-15. The preferential attachment of WD40[®] on planes of hematite nuclei results in the growth of anisometric primary particles similar to the phosphate adsorption mechanism on hematite nuclei reported by Ocaña et al. (1995), which then aggregate producing final ellipsoidal particles (refer to the SEM image in Figure 6-14). The WD40[®] is detached during the aggregation process, and the chemical Fe-O-Fe

bonds are formed at the interphase of the primary particles, resulting in interparticle aggregation at temperatures of 150°C. The detachment of WD40® could be a consequence of the pH decrease which originates as the hydrolysis reaction proceeds and would cause a change in the surface nature of the hematite particles (Ocaña et al., 1995).

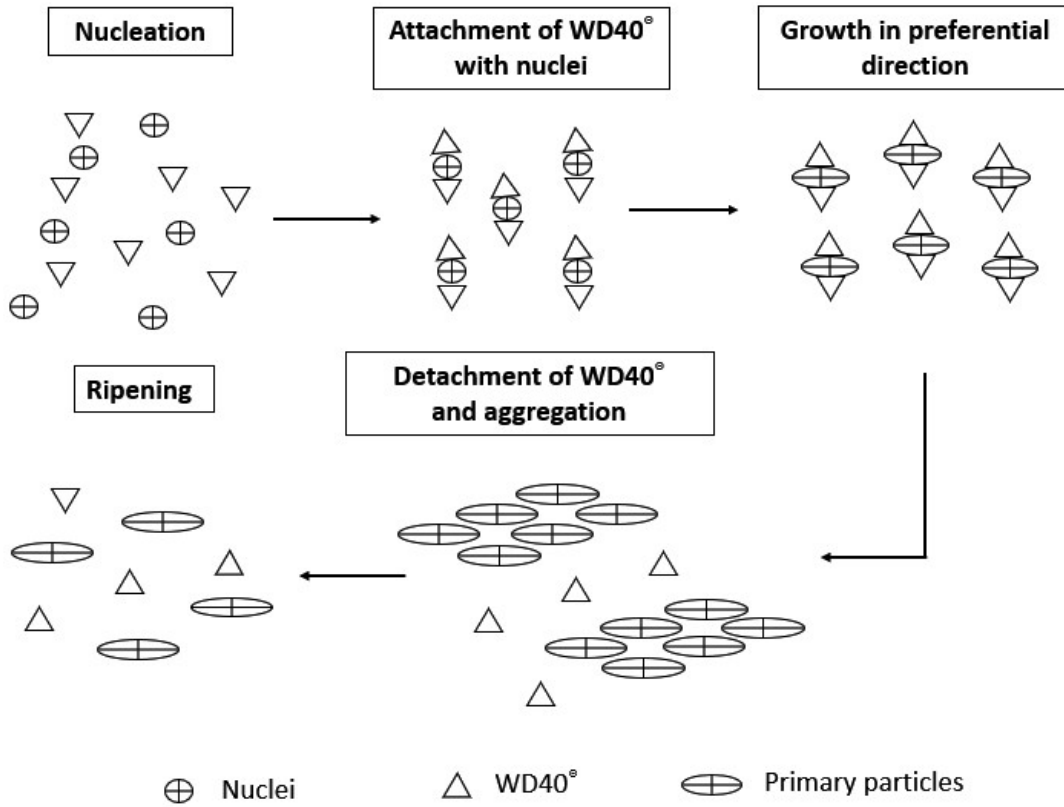


Figure 6-15: Schematic diagram of the proposed mechanism for the formation of hematite particles from sulfate-chloride solutions in the presence of WD40® at 150°C
(modified from Ocaña et al., 1995)

6.3.3.2 Effect of organic additives on hematite

Sapieszko and Matijevic (1980), prepared disk-like hematite particles by using triethanolamine. A basic solution of ferric triethanolamine complexes was heated to ~ 250 °C. In a basic media, usually hexagonal platelet particles of hematite are obtained. The intra-particle recrystallization may have resulted in the dissolution of the side corners when the total concentration of the solute fell below the solubility of the side corners in the last stage of precipitation producing circular disks of hematite. The triethanolamine seems to have played the role of a solvent of hematite to enhance the recrystallization at the high temperature. Hamada et al. (1986), used glycine to prepare uniform double spheres of hematite by forced hydrolysis of FeCl_3 in a dilute acidic medium. The true mechanism was not explained, but it may be similar to the growth process of the peanut-type particles in the gel-sol system since the shape is close to that of the peanut-type particles prepared with phosphate (Sugimoto et al., 1993a). Matsumoto (1980), used organic phosphonic acids to prepare ellipsoidal hematite particles of $0.5 - 0.8$ μm in length with fairly narrow size distributions. It is also possible to form ellipsoidal and rod-like hematite particles with oxalate (Fischer and Schwertmann, 1975) and citrate (Matsumoto et al., 1983). Moreover, dihydroxybenzenes, benzoquinones, dihydroxynaphthalene, NTA, EDTA have been used to control the aspect ratio of monodispersed ellipsoidal hematite particles in gel-sol systems with acidic media around pH 1-2 in the presence of a high concentration of chloride ions at 100°C (Sugimoto et al., 1998)

Daichuan et al. (1995), used *urea* in the forced hydrolysis process of FeCl_3 in an acidic range and observed a morphological change of hematite from monocrystalline spheroidal shape to rhombohedral. The specific adsorption effect of urea may have caused this change. Hamada et al.

(1989) prepared uniform polycrystalline spheroidal particles of hematite (0.35 μm) by forced hydrolysis of 2,2'-bipyridine-iron(II) complex in the presence of KNO_3 as an oxidizing agent of Fe(II) in an acidic medium. Sugimoto et al. (1998), used nitrilotriacetic acid (NTA) to prepare spherical polycrystalline hematite particles from a suspension containing $\alpha\text{-Fe}_2\text{O}_3$ seeds at 100 $^\circ\text{C}$ for 48 h through phase transformation from $\beta\text{-FeOOH}$. Anionic surfactants such as sodium dodecyl sulfate, sodium dodecanoate, sodium alkyl (C-12) benzenesulfonate, sodium alkyl (C-4) naphthalenesulfonate, polyacrylic acid, polymaleic acid, copolymers of maleic acid, and the formalin condensate of p-naphthalene sulfonic acid, are known as good stabilizers of hematite particles in aqueous media. The reagents used in the present work may also act as stabilizers of hematite in pressure leaching (see Section 2.6).

6.3.3.3 Iron complexation by benzene sulfonic and phenyl phosphonic acids

Sulfonic and phosphonic acids are known for their iron chelating properties and have been extensively used in the ion exchange process for the removal of iron from electrolytes before electrowinning. Ion exchange is a process of removal of specific ions from solution by attaching them with an ionic bond onto a resin surface. To selectively remove only iron from the electrolyte, a chelating ion exchange resin is generally used. In chelating ion exchange resins, the reactive portion of the resin binds ions through the formation of complexes as opposed to just ionic bonds that are formed in standard ion exchange resins. A specific ion exchange resin is used to remove a specific ionic species such as a ferric ion while other ionic species such as cupric etc., remain unaffected. Dorfner (1991) has published a detailed explanation of the different types of ion exchange resins.

Shaw et al. (2006) reviewed chelating resins available for iron ion exchange and identified five main resin types and they are iminodiacetic, picolylamine, aminophosphonic, sulphonated phosphonic and sulphonated diphosphonic. The ingredients of commercially available ion exchange resins Purolite S975, Eichrom Diphonix, Lanxess Lewatit TP 20 are shown in Table 6-16. Sodium alkylbenzene sulfonate has been reported as a sulfur dispersing agent in pressure leaching of sulfide concentrates by Marsden et al. (2010). Sulfonic and phosphonic acids, when used in leaching of sulfide concentrates under CESL conditions result in leach residues which have a lower proportion of HaHC soluble phase.

Table 6-16: Ion exchange resins

Manufacture	Resin name	Resin type
Eichrom	Diphonix	Sulphonated Diphosphonic
Purolite	S957	Sulphonated Monophosphonic
Lanxess	Lewatit Monoplus TP 2	Aminophosphonic
Generic	D416	Sulphonated Monophosphonic
Eichrom	Monophosphonic	Sulphonated Monophosphonic

6.4 Conclusions

The existing CESL and Vale processes for the extraction of Cu and Ni from sulfide concentrates by aqueous acidic leaching operate at 150°C, above the melting point of sulfur (119°C) but below (159°C) where sulfur becomes highly viscous. One of the biggest challenges of this process is to effectively disperse the molten sulfur from concentrate particles, thus exposing the particles to the

solution. Without dispersants, the concentrates do not leach effectively because molten sulfur coats the concentrate particles and prevents leaching. The sulfur dispersants currently used in industry are lignosol and/or OPD. Under otherwise normal process conditions, these surfactants typically result in Cu and Ni extractions of about 97%. The sulfur in the residue is usually fine (5-10 μm) and difficult to separate from the residue. The iron in the residue can be in the form of hematite, jarosite, goethite and less crystalline ferric oxy-hydroxides such as ferrihydrite. Crystalline hematite is preferred as it is stable and captures a minimum amount of valuable metal from the solution. Ferrihydrite (amorphous) is always associated with valuable metal losses. Hence the amount of ferrihydrite in the residue should be minimized. The concentrate fed to the CESL and Vale processes typically must be ground to 80% passing 20 – 45 μm . Grinding requires energy and is thus expensive.

Novel additives or a class of additives that outperform the conventional OPD and lignosol surfactants that are currently used in the CESL and Vale processes were discovered. The additives disperse sulfur (in that they allow for leaching to progress even in the absence of OPD) and assist in iron control by reducing the amount of poorly crystalline matter in the iron residues (HaHC soluble phase reduction from 15 ± 0.5 to 7 ± 0.5 wt%). These additives result in the preferential formation of hematite. It is thought that the additives work by acting as iron complexing agents. For example, phenyl phosphonic acid was used in the present study (see Table 6-13) and phosphonic acid-containing resins are regularly used in ion exchange due to their iron complexing properties. They may be reducing supersaturation by lowering the effective Fe concentration in pressure leaching under CESL conditions. Further, these new surfactants appear to have a role in

precipitating or coagulating sulfur in the form of sulfur chunks or prills of size $\sim 0.5 - 1.0$ mm, which makes them more readily separable from the iron residues. The additives result in enhanced recovery of copper metal from sulfide concentrates: the extractions are on the order of 98.5 – 99.1% (vs. about 97% under traditional CESL conditions with OPD). The additives eliminate the need for upfront fine grinding of the feed solids by being able to leach the concentrates at $P_{80}:75$ μm (Teck's CESL process generally uses feed solids of $P_{80}:20$ μm). The residues have better settling and dewatering characteristics. The slurry from post leaching containing the pregnant leach liquor and leach residue settle faster, has a clear over-flow solution and lacks any visible colloids. The filtering time is reduced by half and the filter cake is drier retaining 5% moisture compared to 10% moisture in absence of additives. The additives act as crystal growth modifiers for hematite as evidenced from SEM images, that reveal well grown and larger particles. The pyrite in the leach residue is increased from 4.9 ± 2 % to 10.5 ± 2 %, this suggests that the additives may reduce the oxidation of pyrite.

CHAPTER 7: SOLUBILITY OF METASTABLE FERRIHYDRITE IN SULFATE-CHLORIDE SOLUTIONS AT 150°C

In the previous chapters, ferrihydrite, goethite, jarosite, and hematite were found to precipitate in the CESL process. It was postulated that goethite formed via dissolution of ferrihydrite and reprecipitation as goethite, and that hematite formed by the transformation of ferrihydrite. Furthermore, a reduction in supersaturation was important to mitigate against the formation or retention of a ferrihydrite phase (Section 2.7). However, the solubility of ferrihydrite in the CESL process is not known nor are the formation or transformation rates of ferrihydrite to goethite and hematite.

The approach adopted in this chapter was to synthesize ferrihydrite and perform solubility experiments in sulfate-chloride solutions at 150°C, rather than precipitation experiments involving ferrous/ferric sulfate (Section 2.8). These experiments would help understand the dissolution of ferrihydrite and its re-precipitation as hematite and/or goethite, its solid-state transformation to hematite and the solubility of hematite in sulfate-chloride solutions at various levels of acid concentration (0-25 g/L). This may help elucidate the pathway of iron precipitation in the CESL process, including insight into the transformation of ferrihydrite. Furthermore, there are no public reports of ferrihydrite and transformed hematite solubility in chloride-sulfate solutions, so this chapter adds to the literature in this area.

The batch solubility of synthetic ferrihydrite and the transformed hematite was measured under CESL process conditions. Experiments were performed in sulfate-chloride solutions at 150°C,

with and without copper sulfate or nickel sulfate at different acid concentrations, to create a final hematite product with increased crystallinity. The effect of initial acid concentration on the final transformed hematite product was correlated with previously analyzed precipitates from the CESL process (Chapter 4). As noted above, the solubility of ferrihydrite, and the hematite formed from ferrihydrite, in an autoclave (at CESL conditions) has not previously been attempted.

7.1 Experimental

7.1.1 Ferrihydrite synthesis

The ferrihydrite synthesis was performed using the solvent deficient method recently reported for the synthesis of metal oxide nanoparticles (Smith et al., 2012; Woodfield et al., 2007). Smith et al. (2012) demonstrated that the solvent-deficient synthetic method produces chemically pure ferrihydrite crystallites (2-6 nm) suitable for adsorption applications due to their high surface areas, high porosity, and low water content. The ferrihydrite produced by the solvent deficient method was identical in structure to that produced by other synthetic methods (Michel et al., 2007).

The ferrihydrite synthesis was performed in four simple steps: mixing, drying, washing, and re-drying. Iron(III) nitrate nonahydrate ($\text{Fe}(\text{NO}_3)_3 \cdot 9\text{H}_2\text{O}$) and ammonium bicarbonate (NH_4HCO_3) were mixed at a 1:3 mole ratio in a glass mortar and pestle (to avoid contamination). The water of hydration from the metal salt is released due to the mixing action, and the reagents begin to dissociate. The metal cations impart acidity to the slurry, and the bicarbonate decomposes into CO_2 gas and H_2O . This additional H_2O from the decomposition of bicarbonate results in a chain reaction of dissociation and decomposition producing bubbles. The mixing is continued until the

bubbling ceases and a dark brown product is formed. The so-obtained product was dried in an oven at 80°C. Drying resulted in the formation of white ammonium nitrate (NH_4NO_3), which was washed away using distilled water and a vacuum filter. The washed precipitate was re-dried in an oven, again at 80°C, and the resulting precipitate was characterized and used in the solubility experiments.

Microscopy (SEM) revealed large aggregates of ferrihydrite particles measuring up to 25 μm . However, these easily disintegrated and dissolved in HaHC, as demonstrated in Section 7.1.3. The SEM micrographs are shown in Figure 7-1. The micrographs are similar to those reported by Das et al. (2011).

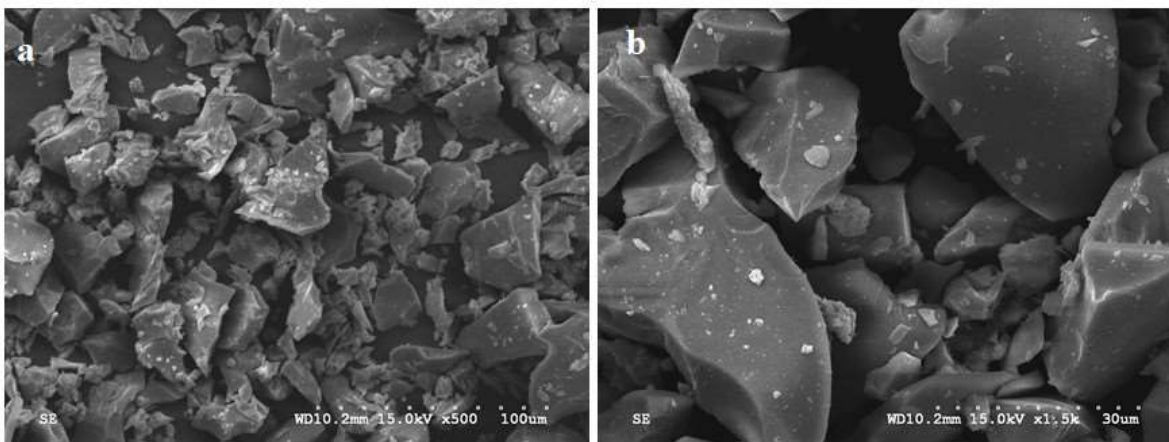


Figure 7-1: SEM micrographs of synthetic ferrihydrite aggregates

Scale bar a) 100 μm and b) 30 μm

7.1.2 Quantitative X-ray powder diffraction (QXRPD)

The quantitative phase analysis was performed using the Rietveld method and X-ray powder diffraction data (refer to Section 4.4).

The QXRPD found the synthetic ferrihydrite to be 100% amorphous. The X-ray spectrum of the as-synthesized ferrihydrite is presented in Figure 7-2. The X-ray spectrum matches the X-ray patterns of “2-line” ferrihydrite and the structural scheme proposed by Eggleton and Fitzpatrick (1988) and Drits et al. (1993). According to Loan et al. (2002), ferrihydrite shows low-intensity broad reflections in an XRD pattern due to short-range structural order and very small particle size (1–7 nm). Thus the aggregates in Figure 7-1, are composed of nanoscale particles. Ferrihydrite’s structure was reviewed in Section 2.4.

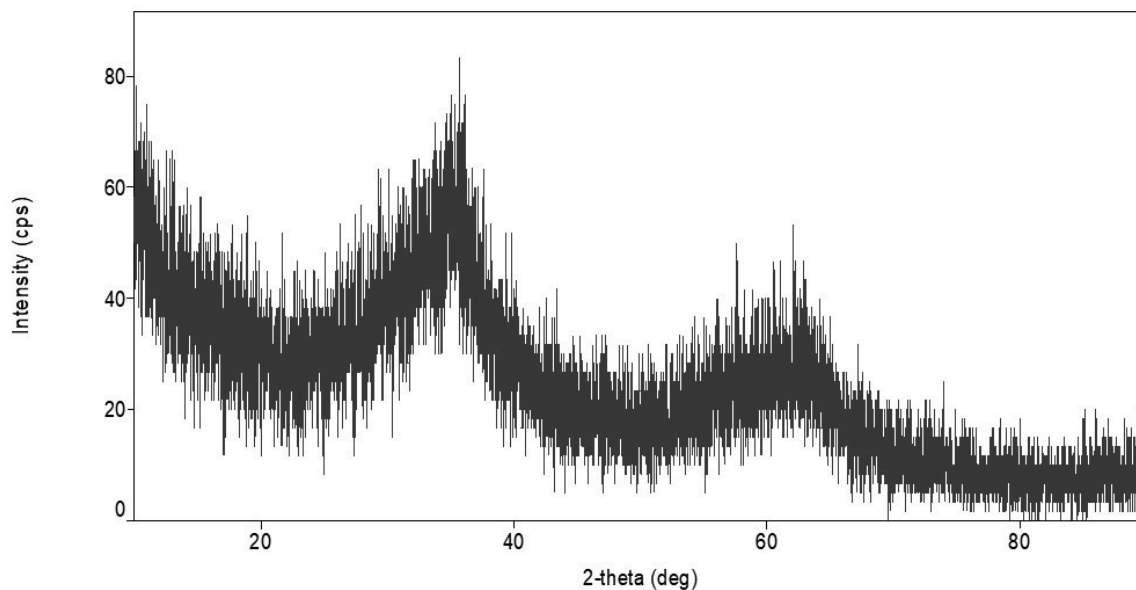


Figure 7-2: X-Ray diffraction pattern of the as-synthesized ferrihydrite via the solvent deficient method

7.1.3 HaHC extraction

Hydroxylamine hydrochloride (HaHC) was used for the selective extraction of the amorphous or poorly crystalline iron oxides/oxyhydroxides (as described in Section 4.4). The synthetic

ferrihydrite, as expected, completely dissolved into the solution and no residue (R1) was left as shown in Figure 7-3. This implies that the synthetic ferrihydrite was free of crystalline ferric oxyhydroxides such as hematite or goethite (please see Section 4.4 for further information).

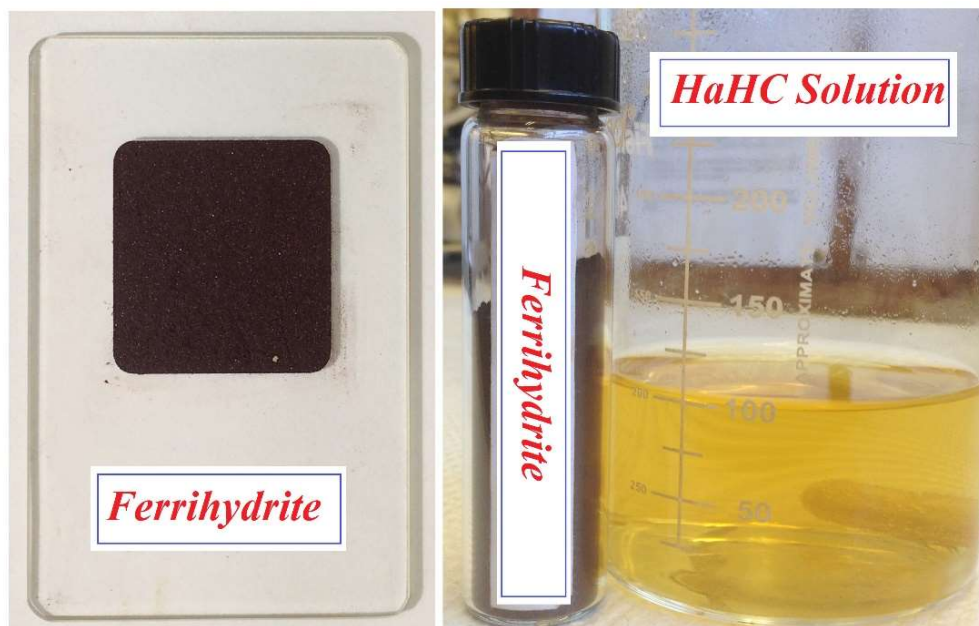


Figure 7-3: Synthetic ferrihydrite solubility in HaHC at 50°C

7.1.4 Electrolyte preparation for ORP tests

Oxidation-reduction potential (ORP) is a measure of the tendency of solution species to either gain or lose electrons and thereby be reduced or oxidized, respectively. The ORP of the solubility test solutions was measured to gather information on the speciation of iron (Yue et al. 2014, 2015). To verify that the ORP-speciation model used herein remained valid for high-chloride CESL-type solutions, control solutions with known ferrous and ferric concentrations were prepared. These solutions were prepared according to the procedure described by Yue (2015). Deionized water, sulfuric acid (H_2SO_4 , 95.0-98.0%, Fisher Scientific Canada), iron(III) sulfate pentahydrate

($\text{Fe}_2(\text{SO}_4)_3 \cdot 5\text{H}_2\text{O}$, 97%, Acros), iron(II) sulfate heptahydrate ($\text{FeSO}_4 \cdot 7\text{H}_2\text{O}$, 99+% for analysis ACS, Acros), copper(II) sulfate pentahydrate ($\text{CuSO}_4 \cdot 5\text{H}_2\text{O}$) and nickel(II) sulfate hexahydrate ($\text{NiSO}_4 \cdot 6\text{H}_2\text{O}$) were used to prepare the desired electrolyte. Before each test, a fresh background solution was prepared, with 10 g/L H_2SO_4 . The ferrous ion concentration was determined by the various nominal Fe(III) to Fe(II) molar ratios of (1:1, 10:1, 100:1). The solution was prepared by dissolving 22.73 g of $\text{Fe}_2(\text{SO}_4)_3 \cdot 5\text{H}_2\text{O}$, and the corresponding amount of $\text{FeSO}_4 \cdot 7\text{H}_2\text{O}$ was balanced and dissolved in the H_2SO_4 . Solutions containing copper and nickel were prepared in a similar way, where copper was added as $\text{CuSO}_4 \cdot 5\text{H}_2\text{O}$ and nickel as $\text{NiSO}_4 \cdot 6\text{H}_2\text{O}$.

7.1.5 Experimental procedure for solubility measurements

The solubility experiments were performed using a 1.0 L titanium autoclave from the Parr instrument company. The impellers were driven at 300 rpm to mix the slurry thoroughly, and to promote thermal equilibrium within the vessel. It is important to note that the impellers and impeller shaft were made from titanium as this will become significant in the discussion below. Sampling was performed using a titanium dip tube that extended into the solution. The dip tube was fitted with a sintered 2 μm titanium filter. A 0.5 μm titanium frit enclosed inside a titanium union fitting was connected in series with the 2 μm titanium filter to provide finer in-situ filtration. There was no visual evidence that solids passed through the filter during sampling. Solution samples were cooled in the sampling tube outside the autoclave before being collected into polystyrene test tubes. The sample cooling was performed by passing cold water through a copper coil that was wrapped around the titanium sampling tube. A titanium needle valve was used to control the sampling.

Feed slurry of 500 mL containing the synthetic ferrihydrite, sulfuric acid, the source of Cl^- (LiCl), copper sulfate, and nickel sulfate was transferred to the autoclave vessel at room temperature. The slurry was held in a glass liner to limit the exposure of the titanium vessel to the acidic solutions to prevent contamination and corrosion. The temperature was raised to 150°C over a period of 20 min, and the agitation was maintained at 300 rpm (higher agitation was avoided to prevent splashing of the solution over the wall of the glass liner). Time 'zero' was the point at which the system attained 150°C . The samples were collected every 30 min for up to 120 min and every 60 min after that. Sampling was performed in a clean titanium sampling line to prevent contamination and re-dissolution of the precipitate/colloidal iron particles due to cooling. Before the start of each experiment, the dip tube and sampling line were thoroughly washed with 10 g/L sulfuric acid followed by deionized water and pressurized air was used to drive off any remaining liquid. Samples were collected by opening the needle valve on the sampling line. The first 5 mL of solution withdrawn was discarded before another 5 mL was withdrawn and analyzed. This ensured that stagnant liquid in the sampling line was removed before the well-mixed solution from inside the autoclave was collected. After 360 min of operation, the autoclave was cooled down to 25°C in 8 min. The autoclave was disassembled, and the residue was immediately filtered, washed, dried and analyzed.

The redox potential of the final solution was measured with a saturated Ag/AgCl electrode. All measured potentials were converted from Ag/AgCl to the standard hydrogen electrode (SHE). All potentials in this study are quoted with respect to the SHE at 25°C unless otherwise stated. Final acid concentration of the solutions was determined by titration with 0.1 N NaOH. A solution of

Mg-EDTA (0.2 M MgSO_4 + 0.1 M EDTA) was used to complex with hydrolyzable metal ions which contribute protons by reaction with hydroxide ions in the water (Rolia and Dutrizac, 1984).

The Mg-EDTA stock solution was prepared by dissolving 0.1 moles (29.225 g) of EDTA in 600 mL of H_2O and 0.2 moles (40.66 g) of $\text{MgCl}_2 \cdot 6\text{H}_2\text{O}$ in 150 mL of H_2O . The stock solutions were combined with slow addition of 10% NaOH solution to raise the pH of the solution to 9 – 10 while mixing with a magnetic stirrer until a clear solution was obtained. Using 0.01 mol/L of the sulfuric acid solution, the pH of the Mg-EDTA solute was lowered to 7. The final volume was brought to 1 L with distilled water. Free acid was determined using Mg-EDTA titration with the fixed pH endpoint method (Rolia and Dutrizac, 1984; Zhu et al., 2009). A 50 mL Mg-EDTA stock solution was transferred to a 150 mL beaker. The pH of the stock solution was measured, and if required, it was adjusted to 7 with 0.01 mol/L H_2SO_4 and 0.01 mol/L NaOH solutions. 1 mL of the sample solution was added to the beaker, and the pH of the system dropped due to the free acid contained in the added sample. The system was stirred with a magnetic stirrer and titrated with a standard 0.01 mol/L NaOH solution until the pH returned to the original set value of 7. Free acid in the sample was calculated using the volume of the NaOH solution used for titration. All titrations were repeated three times, and the average values are reported.

The chemical speciation of the system was calculated using the thermochemical modeling software PHREEQC (Parkhurst and Appelo, 1999). There are a variety of similar programs available for speciation studies. These programs are classified into two categories depending on their theoretical basis: the law of mass action (e.g. PHREEQC, MIN3P, and Geochemist's workbench) or the Gibbs energy minimization theories (e.g. GEMS, ChemApp). However, international benchmark

activities have established that they are equivalent if the thermodynamic database provides equal parameters (Steeffel et al., 2015). Therefore, accurate predictions mostly rely on a thermodynamic database that is valid for the conditions studied. For the present calculations, the database 'sit.dat' in combination with 'lnl.dat' was employed. Sit.dat was derived from databases that use thermodynamic data compiled by the Lawrence Livermore National Laboratory such as of EQ3/6 and geochemist's workbench (Parkhurst and Appelo, 2013).

7.2 Results and discussion

The synthetic ferrihydrite was expected to completely transform into crystalline hematite in the autoclave at 150°C as discussed in Sections 2.7 and 2.8 (Reactions 2-16, 2-17 and 2-19). The percent of iron dissolved at various initial acid concentrations ranging from 0 g/L to 25 g/L is presented in Figure 7-4. The amount of iron dissolved was higher for higher sulfuric acid concentrations, but it slowly decreased with time and reached a near-asymptote after about 120 min. For a low acid concentration, between 0 g/L and 5 g/L, there was a lower level of dissolved iron in the solution indicating low solubility for ferrihydrite and transformed hematite at low acid concentrations.

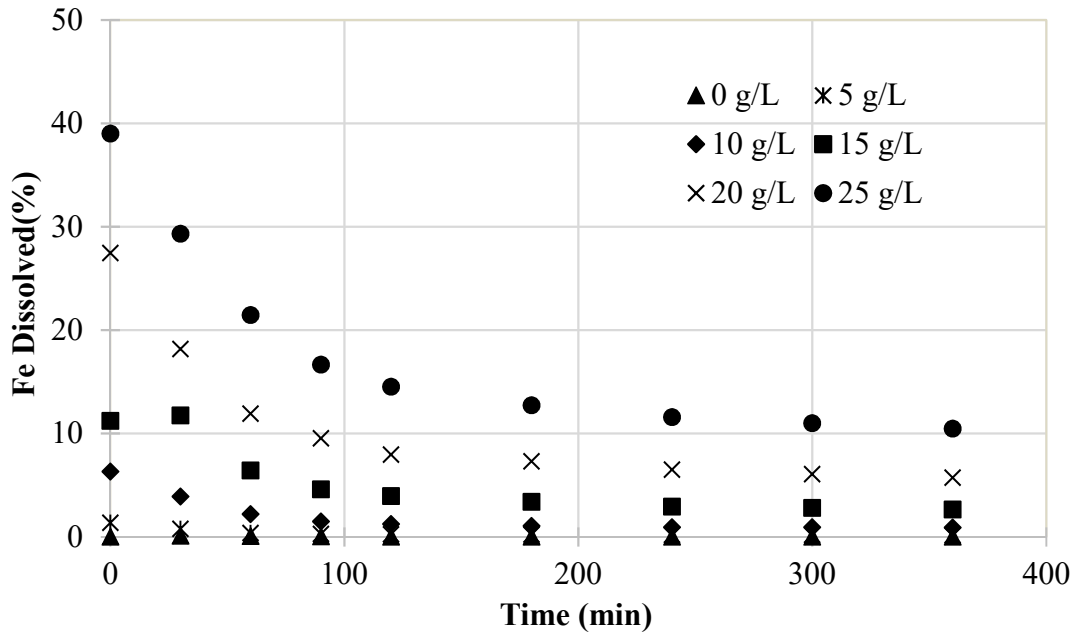


Figure 7-4: Percent of Fe dissolved from the total initial Fe put into the system as synthetic ferrihydrite (20 g/L) at various initial sulfuric acid concentrations (inset legend) in sulfate-chloride (12 g/L) solutions at 150°C

To interpret these results, it is essential to understand the mechanism of ferrihydrite dissolution, its reprecipitation as hematite and its solvent-mediated solid-state transformation to hematite in the autoclave at 150°C. Many solid-solid transformations are capable, given enough time, of converting from one form to another. These conversions occur much more rapidly in the presence of a solvent. These are referred to as solvent-mediated transformations (Aucamp et al., 2015). The hematite with the lowest solubility is the most stable at a given temperature. Ferrihydrite, with a higher solubility than hematite, would eventually dissolve and recrystallize as hematite as the system tends to equilibrium. Ferrihydrite also undergoes a simultaneous solvent-mediated solid-state transformation to hematite (Cornell and Schwertmann, 1996). In any hydrometallurgical

process it is generally advisable to precipitate iron as the most stable hematite to avoid any subsequent transformations that may impact on the process or on long term storage of the residues (see Section 2.3).

The solvent-mediated transformation may prevent accurate solubility measurements of metastable ferrihydrite. The situation is similar to the solubility of metastable polymorphs described in the solubility studies of certain polymorphic pharmaceutical drugs and reviewed by Nicoud et al. (2018). The solvent-mediated metastable polymorphs also prevent accurate solubility measurements and solubility obtained for such substances has been described by the expression “kinetic solubility” (Brittain, 2014). However, Nicoud et al. (2018) argue that solubility is not a kinetic property, and its real value would not be affected by the time course of a polymorphic transformation.

Experimental determination of the solubility of metastable polymorphs is challenging due to the solvent-mediated transformation toward a more stable form. The transformation occurs due to the difference in solubility between the metastable form and the stable form. The supersaturation of the stable polymorph is still positive when the solute concentration is equal to the solubility of the metastable polymorph, and therefore the stable form will start crystallizing. This results in a decrease in the solute concentration and takes it to below the solubility limit of the metastable form, triggering the dissolution of the metastable form (Nicoud et al., 2018).

During this transformation, if the metastable form dissolves faster than the precipitation of the stable form, the solute concentration remains equal to the solubility of the metastable form. On the

other hand, if the metastable form dissolves more slowly than the precipitation of the stable form, the solute concentration falls below the solubility of the metastable form. When all the crystals of the metastable form have transformed, the stable form continues to precipitate until reaching equilibrium. The solvent-mediated transformation of several polymorphs during solubility measurement has been studied experimentally, and it is reported that the crystallization of the stable form often starts on the surface of the metastable crystals, a phenomenon referred to as cross-nucleation (Cashell et al., 2003; Nicoud et al., 2018).

In the current study, the solubility of metastable ferrihydrite proceeds via the following five steps.

1. Dissolution of ferrihydrite to Fe(III) (Reaction 2-17)
2. Re-precipitation of Fe(III) as hematite due to cross nucleation (Reaction 2-19)
3. Solid-state transformation of the remaining ferrihydrite to hematite (Reaction 2-16)
4. Dissolution of transformed hematite to Fe(III) (Reaction 2-19)
5. Growth of the remaining hematite particles (Section 2.5)

As described in the experimental procedure above, ferrihydrite is introduced into the autoclave at room temperature and heated to 150°C. The time ($t = 0$) marks the system's attainment of 150°C. In order to see if the ferrihydrite is completely dissolved and reprecipitated as hematite (steps 1, 2, 4 and 5), some preliminary experiments were performed at various temperatures with varying acid concentrations in sulfate-chloride solutions. At 0 to 25 g/L H_2SO_4 and 12 g/L Cl^- and temperatures of 25, 60 and 95°C, complete dissolution of ferrihydrite did not occur even after 48 h. However, at an acid concentration of 50 g/L H_2SO_4 and 12 g/L Cl^- at 60°C, complete dissolution of

ferrihydrite was observed within the first 5 min. This suggests that, during the heat-up, complete dissolution of ferrihydrite only occurs at acid concentrations higher than those employed in the current study.

To further validate this, experiments were performed wherein ferrihydrite was introduced into the autoclave in 10 g/L H₂SO₄ and 12 g/L Cl⁻ and heated to 150°C, whereupon the reactor was immediately cooled down to 25°C at t = 0 min and then, separately, at t = 60 min. The residues were then analyzed by QXRPD and via HaHC leaching to determine the amount of ferrihydrite and transformed hematite. In another set of experiments Fe(III) was introduced into the autoclave as Fe₂(SO₄)₃•5H₂O, while keeping the amount of Fe(III) as Fe₂(SO₄)₃•5H₂O equal to the amount of Fe(III) present as ferrihydrite in the previous experiments. The acid concentration studied was 10 g/L H₂SO₄ and 12 g/L Cl⁻ at 150°C and time t = 0 and t = 60 min.

The experiments with Fe₂(SO₄)₃•5H₂O did not result in the precipitation of iron oxides at either t = 0 or t = 60 min. This agrees with the precipitation studies involving Fe₂(SO₄)₃•5H₂O performed by Javed and Asselin (2018). It was reported that precipitation only occurred in the presence of 30 g/L Cu and/or the presence of hematite seed. Therefore, if all the ferrihydrite in the current study dissolved during the heat-up stage, no precipitation of ferrihydrite or hematite would be anticipated, and there would be no iron oxide residue found in the autoclave. However, in the experiments involving ferrihydrite at t = 0 and t = 60 min in 10 g/L H₂SO₄ and 12 g/L Cl⁻ at 150°C, significant amounts of ferrihydrite and hematite were present. This indicates that ferrihydrite does indeed undergo some dissolution and reprecipitation as hematite due to cross nucleation and, perhaps, a solid-state transformation.

The QXRPD analysis of the residue from the ferrihydrite feed experiment at $t = 0$ (150°C) determined that $\sim 99\%$ of the residue remained as ferrihydrite (diffractogram shown in Appendix D) while the HaHC treatment indicated the presence of 43.2 ± 0.5 wt% HaHC soluble phase (56.8 ± 0.5 wt% remained undissolved). The difference between QXRPD and HaHC soluble phase is due to the presence of poorly crystalline hematite (as discussed in Chapter 4). QXRPD cannot detect poorly crystalline hematite and therefore shows it as an amorphous X-ray phase while HaHC is very selective towards ferrihydrite (see Chapter 4, Section 4.4). The QXRPD analysis of the residue from time $t = 60$ min at 150°C (the CESL process retention time is normally close to 60 min) was 66.5 ± 2.0 % hematite while 82.8 ± 0.5 wt% was undissolved by HaHC (i.e., likely hematite of various particle sizes). This finding is important for the CESL process: the ferrihydrite that forms during the leaching of sulfide concentrates at the usual free acid concentration of 10 g/L H_2SO_4 and at 12 g/L Cl^- , 150°C , never fully transforms to hematite. This agrees with residue analysis performed for CESL conditions (see Chapter 4 and 6). The QXRPD and HaHC analysis at $t = 6$ h are presented later in Table 7.4.

The percent of iron dissolved at 10 g/L initial acid concentration in the presence of Cu and Ni ions is shown in Figure 7-5. The initial amount of iron dissolved from hematite was 6% in the presence of Cu and 4% in the presence of Ni compared to 6.5 % for the blank test that did not contain any Cu or Ni. At room temperature, Cornell's group found that nickel slowed the transformation of amorphous iron(III) hydroxides to goethite by stabilizing it against dissolution. It also affected the transformation to hematite by suppressing the internal rearrangement process (Cornell et al., 1992). Copper was also found to slow the transformation of ferrihydrite by suppressing goethite formation

through the hindrance of the dissolution of ferrihydrite (Cornell and Giovanoli, 1988). However, the decrease in the amount of iron dissolved and shown in Figure 7-5 may be due to an increase in hematite precipitation in the presence of CuSO_4 or NiSO_4 . This is probably due to the formation of bisulfate (HSO_4^-) from the extra sulfate added to the system. Sulfate acts as a sponge for protons, and Ni or Cu addition as sulfate should, therefore, increase pH at temperature, which results in a decrease in the activity of the hydrogen ion (Tozawa and Sasaki, 1986). It has been demonstrated that NiSO_4 and MgSO_4 at high temperatures buffered the 'at temperature' acidity (Baghalha and Papangelakis, 2000, 1998; Jankovic et al., 2009; Rubisov and Papangelakis, 2000). The percent of initial Fe dissolved for all three cases in Figure 7-5 decreased with time and stabilized after 120 min. At the end of 6 h, the difference between the amount of iron dissolved from hematite in the presence of Cu or Ni is insignificant but both are lower than the blank test that did not contain any Cu or Ni. This is consistent with the lower solubility of hematite in the presence of zinc as reported by (Tozawa and Sasaki, 1986). At the end of 6 h in the current study, most of the dissolved iron has precipitated as hematite, and most of the remaining ferrihydrite transformed to hematite, and one could infer that the iron concentration at this point represents the solubility of hematite for this condition (see Table 7-4).

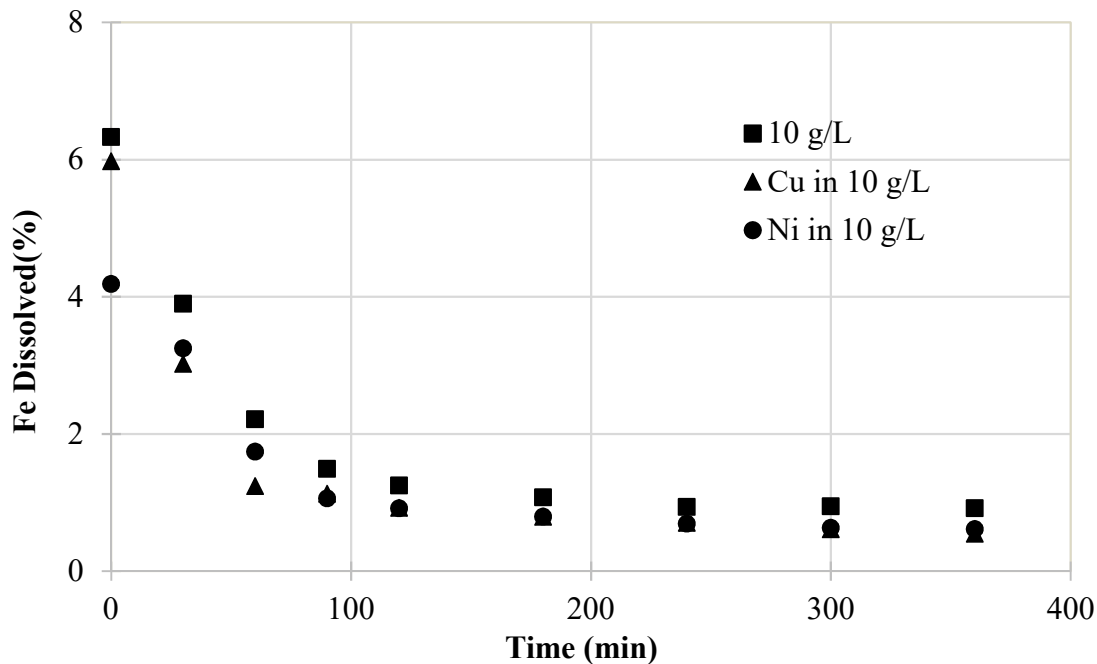


Figure 7-5: Percent of Fe dissolved in the presence of Cu and Ni from the total initial Fe put into the system as synthetic ferrihydrite at 10 g/L initial sulfuric acid, 12 g/L chloride solutions at 150°C

Hematite solubility data has been experimentally determined by Umetsu et al. (1977), Sasaki et al. (1993) and Reid and Papangelakis (2006), as discussed in Section 2.8. Sasaki et al. (1993) measured solubilities via hydrolytic precipitation of hematite from ferric sulfate solutions while Umetsu et al. (1977), and Reid and Papangelakis (2006) measured solubility via the dissolution of hematite.

Umetsu et al. (1977) and Sasaki et al. (1993), developed equations for different temperatures relating the equilibrium iron concentration to the equilibrium free acid concentration. The concentration of iron decreased with time and attained a constant value. It was assumed that hematite was at equilibrium when the iron concentration became constant after *ca.* 16 h. When

equilibrium was reached in various concentrations of sulfuric acid at 150°C, the relationship between the concentrations of iron and free sulfuric acid at equilibrium resulted in a straight line on a log-log graph. These relationships were based on a least-squares fit of the data and were expressed as an equation. Similar equations were developed here from the data presented by Reid and Papangelakis (2005, 2006) and for the current work after 6 h of solubility measurement for various acid concentrations. The concentrations in Equations 7-1 to 7-4 are in g/L, and the temperature is 150°C.

Umetsu et al. 1977(sulfate solutions)

$$\log[\text{Fe}^{3+}] = 3.80 \log[\text{H}_2\text{SO}_4] - 6.05 \quad 7-1$$

Sasaki et al. 1987 (sulfate solutions)

$$\log[\text{Fe}^{3+}] = 3.24 \log[\text{H}_2\text{SO}_4] - 4.44 \quad 7-2$$

Reid, 2005; Reid and Papangelakis, 2006 (sulfate solutions)

$$\log[\text{Fe}^{3+}] = 3.26 \log[\text{H}_2\text{SO}_4] - 5.29 \quad 7-3$$

Current work (sulfate-chloride solutions)

$$\log[\text{Fe}^{3+}] = 1.92 \log[\text{H}_2\text{SO}_4] - 2.90 \quad 7-4$$

The end-point solubility data generated by the current work is different as it originates from the solubility of ferrihydrite and its transformation product (“transformed hematite”) in mixed sulfate-chloride solutions. Nevertheless, the data gathered here is compared to the previous experimental work on hematite in Figure 7-6.

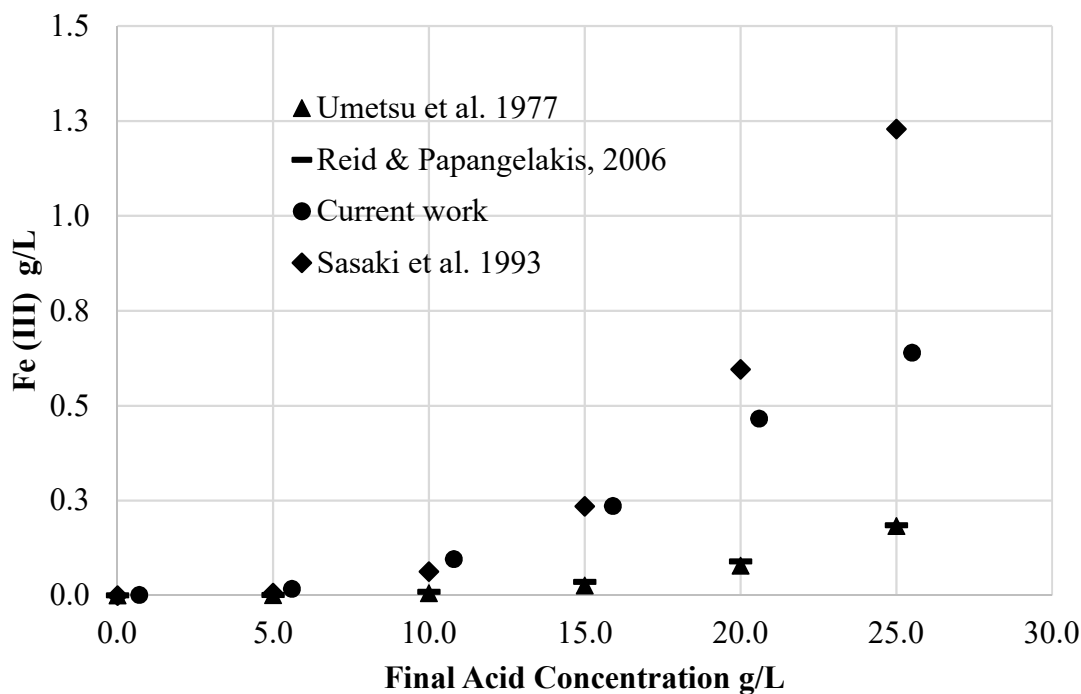


Figure 7-6: Comparison of solubility data from sulfate-chloride solutions with Umetsu et al. (1977), Sasaki et al. (1993) and Reid and Papangelakis (2006)

The current work produces lower solubilities versus final acid concentrations than those predicted by the previous work of Sasaki et al. (1993). This discrepancy is due to the approach to equilibrium via precipitation and due to the lack of in-situ sample filtration in the Sasaki work. Hematite solubility results are affected by the route taken to reach equilibrium, which, as discussed above, includes hydrolytic precipitation of hematite or hematite dissolution. Hematite precipitation occurs when the solution becomes supersaturated in iron. Supersaturated solutions generate metastable ferrihydrite in colloidal-sized particles that are eventually transformed to hematite. These ferrihydrite colloidal particles have been shown to readily dissolve at low temperatures by Reid and Papangelakis (2006) at higher acid concentrations of up to 70 g/L H₂SO₄. Approaching

equilibrium via the precipitation route is expected to generate more colloids versus the hematite dissolution route. This is because precipitation requires solution supersaturation that is a prerequisite for colloidal formation. Whereas, hematite dissolution does not produce solution supersaturation because hematite dissolution is driven by the fact that the solution is not saturated. Dissolution ceases once the solution is saturated in iron and the equilibrium has been attained. In-situ sampling was not employed by Sasaki et al. (1993) and, therefore, both the hematite and the colloidal particles were exposed to low temperatures as the samples were cooled. As temperature decreases, the solubility of hematite increases, and colloidal particles would have dissolved into the solution during sampling, thus inflating the measured solubility.

On the other hand, the current work produces higher solubilities versus final acid concentrations than those predicted by the previous studies of Umetsu et al. (1977) and Reid and Papangelakis (2006). It is important to reiterate that the data presented here is for solubility of ferrihydrite and the transformed hematite in a *mixed chloride-sulfate background* whereas that from previous studies is of hematite-only in a sulfate-only background. The possibility of the presence of Cl^- in the current system forming complexes with ferric and increasing its solubility is explored in the following paragraphs.

The $\text{Fe}^{3+}/\text{Fe}^{2+}$ redox potentials are higher in chloride solution compared to sulfate solutions. Fe^{3+} forms strong complexes with the sulfate and bisulfate anions, lowering the activity of the oxidant. In chloride solution, the complexation of Fe^{3+} is not as strong, and the oxidant has higher activity. Riveros and Dutrizac (1997) attributed the reduction of the yield of hematite from chloride solutions to the effect of chloride ions on the activity of the hydrogen ions in solution. Higher

acidity (i.e., increasing hydrogen ion activity) sharply decreased the amount of hematite precipitated. Majima and Awakura (1981) have shown that increasing concentrations of 'free' chloride ion significantly increases the activity of the hydrogen ions, that, in turn, causes a decrease in the amount of hematite precipitated.

Majima et al. (1985) studied the leaching of hematite in hydrochloric acid and sulfuric acid solutions at 55°C. The experimental rate data showed that a chemical reaction process controlled the overall leaching reaction. The leaching rate of hematite was found to be of first order with respect to proton activity (a_{H^+}) in hydrochloric acid while it was of half order in sulfuric acid solutions. Majima et al. (1985) also found that hematite leaching was enhanced by the addition of sodium chloride to sulfuric acid. The addition of sodium chloride increased proton activity in the sulfuric acid solution, and this increased the leaching rate, which then approached that of the hydrochloric acid solutions. If the dissolution reaction of hematite in an acid solution is controlled merely by the action of hydrogen ions, the same leaching rate should be obtained when different acid solutions, which have the same level proton activity, are compared. However, the leaching rate in sulfuric acid solution was different from that in hydrochloric acid.

Majima et al. (1985), hypothesized that adsorption of anions onto the mineral surface also directly determined the leaching rate. Since the hematite surface is positively charged, the ions adsorbed next to the surface would be anions from the solution. The anions present in the solutions in their study were hydroxyl ions, anions dissociated from the acids and salts added, and complex anions of Fe(III). The main anions are bisulfate and sulfate ions in the sulfuric acid system and chloride ions in hydrochloride acid systems. According to Majima et al. (1985), the fact that the leaching

rates of hematite were quite different in various acids having the same a_{H^+} indicated the importance of anion adsorption. The higher hematite solubilities in a mixed chloride-sulfate background compared to previous studies performed only in a sulfate background (see Figure 7-6), may be attributed to the combined effect of proton activity and anion adsorption.

A speciation analysis was performed to verify the effect of Cl^- . The speciation of Fe(III) at various pHs in the sulfate-chloride system at 150°C is shown in Figure 7-7. The sulfate-only system is shown in Figure 7-8. At $pH > 0.4$, Fe in the aqueous phase is below 1.68 g/L (see Figures 7-9, 7-11 to 7-15). Therefore, the molar fractions for aqueous species, in %, are plotted as the molality of each species divided by the total molality of dissolved Fe. However, for the Fe in solid phases: it is calculated, in %, as the moles of hematite divided by the moles of hematite plus the total molality of dissolved Fe. Total Fe in the system is a sum of Fe as free ferric, Fe as complexes and Fe as hematite as illustrated as follows:

$$[Fe^{3+}]_{Tot} = [Fe^{3+}]_{Free} + \sum [Fe^{3+}]_{Complexes} + [Fe^{3+}]_{Hematite}$$

The pH of the solution was measured at 25°C after 6 h for initial acid concentrations from 0 to 25 g/L used in the current study and found to vary between pH 0.4 and 0.9, which would increase at 150°C to ‘at temperature acidity’. At pH 0.5, corresponding to the acid concentration of 15 g/L, the amount of Fe as hematite at 150°C is ~96% according to the speciation analysis (see Figure 7.7). This agrees with the chemical analyses of Fe performed on the solution samples drawn from the autoclave at 150°C. The soluble Fe was 0.43 g/L at 15 g/L acid concentration and pH 0.5 (see Figure 7-13), which is about 3.9% of 11 g/L total Fe introduced as ferrihydrite and therefore the remaining 96.1% Fe should be present as hematite (same is shown in Figure 7.7). The soluble Fe

at 0.43 g/L is made up of ~50% free ferric ($[\text{Fe}^{3+}]_{\text{Free}}$), and the rest of the soluble Fe exists as Fe complexes ($[\text{Fe}^{3+}]_{\text{Complexes}}$). The presence of Cl^- results in the ferric chloride complexes FeCl^{2+} and FeCl_2^+ and decreases the amount of ferric sulfate complexes FeSO_4^+ and FeHSO_4^{2+} and seems to be of significance below pH 0.4, i.e. at higher concentrations of acid than those studied here (see Figure 7.7). However, between the pH values of 0.4 – 0.9 or higher, which are relevant to the current study, the hematite is always present in the system and is approximately 96 %, in both sulfate-chloride and sulfate-only systems at pH 0.5 (15 g/L acid concentration). Therefore, in the current study, the presence of Cl^- does not appear to be contributing to the measured solubility, as shown in Figure 7-6. The higher solubilities seen in Figure 7-6 are likely a result, then, of the higher ferrihydrite solubility and solvent-mediated transformation of metastable ferrihydrite to stable hematite as discussed earlier. These transformations are ongoing and require a higher supersaturation, and perhaps the poorly crystalline hematite formed in the current study is more readily soluble than the well-formed synthetic hematite employed in previous studies. Lastly, there remains the possibility of colloidal hematite particles passing through the sampling filter. This is deemed unlikely, however, as no colloids were observed in sample solutions. Sampling was performed by opening the valve for about 2-3 seconds and letting out ~5 mL of solution. Therefore, if colloidal hematite did pass through the filter, it was likely not a significant amount but this source of error cannot be ruled out.

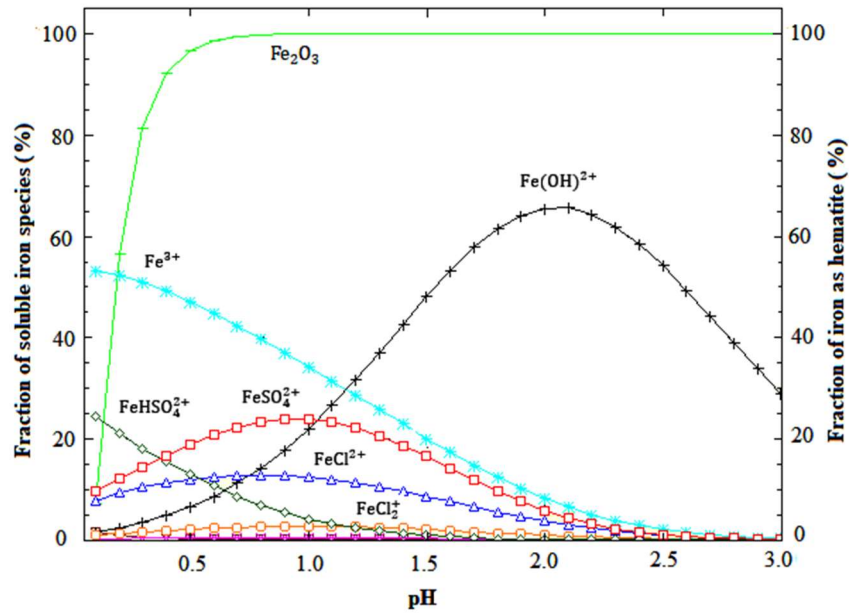


Figure 7-7: PHREEQC calculated equilibrium Fe(III) species of the solution at 150°C in the presence of 11 g/L Fe(III) and 12 g/L Cl^- added as LiCl

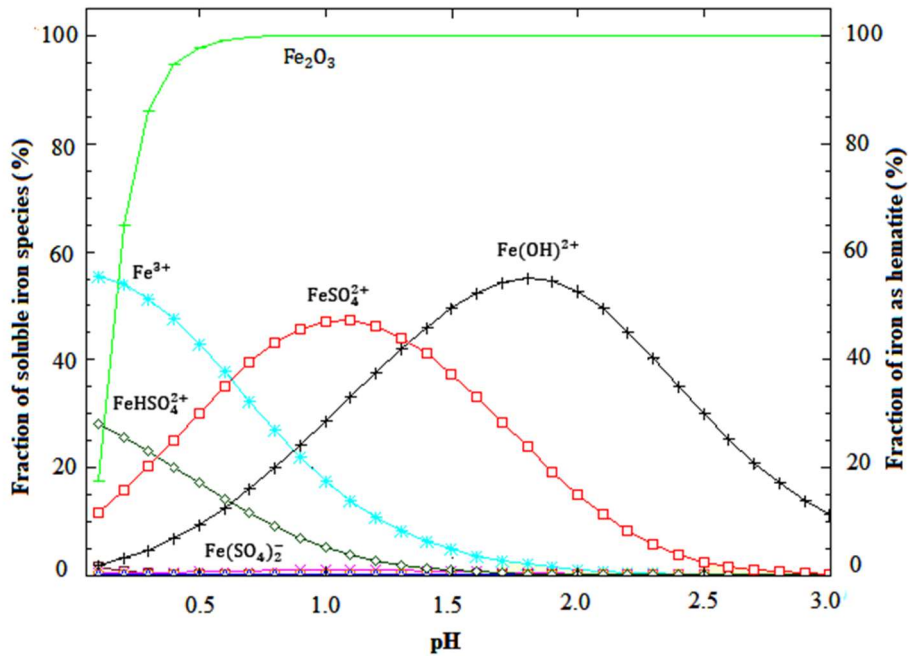


Figure 7-8: PHREEQC calculated equilibrium Fe(III) species of the solution at 150°C in the presence of 11 g/L Fe(III) and in the absence of added Cl^-

Further insight into the solubility of ferrihydrite can be gained from relative amounts of Fe(III) and Fe(II) that were present (more on the presence of Fe(II) later). Yue et al. (2014), developed a thermodynamic model for predicting the oxidation-reduction potential (ORP) of the $\text{H}_2\text{SO}_4\text{-Fe}_2(\text{SO}_4)_3\text{-FeSO}_4\text{-H}_2\text{O}$ system through a wide range of solution compositions and temperatures up to 150°C . In H_2SO_4 solutions, free Fe(III) ions, Fe^{3+} , were found to account for only a small percentage of total Fe(III), as most of the Fe(III) was distributed as sulfate complexes or as hematite. However, a significant amount of Fe(II) was found to exist as free Fe(II) ions, Fe^{2+} . Yue et al. (2016) demonstrated that the model predicts the change in redox potential for all Fe(III) to Fe(II) ratios at various temperatures. An expression was developed to predict the redox potential of the Fe(III)/Fe(II) couple, which also predicts ORP since the Fe(III)/Fe(II) couple is potential determinant in such systems (Equation 7-5). The redox potential can accurately be determined based only on the variables of temperature and the nominal Fe(III) to Fe(II) ratio (Yue et al., 2016) using Equation 7-5.

$$E(\text{mV}) = -1 \times 10^{-3} \times [T(\text{K})]^2 + 0.91 \times T(\text{K}) + \frac{2.303R}{nF} \times T(\text{K}) \times 10^3 \times \log \frac{C_{\text{ferric,nominal}}}{C_{\text{ferrous,nominal}}} + 492 \quad 7-5$$

Equation 7-5 was verified for this work for chloride, Cu and Ni-containing solutions. Synthetic solutions containing Cu, Ni, Fe(II) and Fe(III) at known ratios were prepared as described in Section 7.1.4. The chloride concentration was maintained at 12 g/L. The ORP measurement was performed on these solutions, and the measured ORP values were used in Equation 7-5 to obtain

the nominal Fe(III) to Fe(II) ratio. The nominal Fe(III) to Fe(II) ratios calculated using Equation 7-5 were found to be in good agreement with the actual Fe(III) to Fe(II) ratio used to generate the synthetic solutions, as shown in Table 7-1. The average error between the actual ratio in the synthetic solution and the calculated Fe(III) to Fe(II) ratio was less than 3%. This is not surprising given the wide range of applicability of this equation as pointed out by Yue et al. (2016), where metals such as Cu, Ni, Zn, and Pb were present (Cu: 5 g/L, Ni: 55 mg/L, Zn: 142 mg/L and Pb: 17.35 mg/L).

Table 7-1: Ferric to ferrous ratio of synthetic solutions containing chloride, copper and nickel in 10g/L H₂SO₄ at 25°C

Synthetic solution composition (10 g/L H₂SO₄)	Actual Fe(III) to Fe(II) ratio in synthetic soln.	Measured ORP values at 25°C (SHE)	Calculated Fe(III) to Fe(II) ratio using Eqn 7-5	% error
	1:1	675.0	1.0:1	1.0
12 g/L Cl	10:1	734.0	10.2:1	1.6
	100:1	792.8	100.1:1	0.1
12 g/L Cl	1:1	676.0	1.1:1	5.7
+ 12 g/L Cu	10:1	735.0	10.6:1	5.3
	100:1	793.0	100.9:1	0.9
12 g/L Cl	1:1	676.0	1.1:1	5.7
+ 12 g/L Ni	10:1	734.8	10.5:1	4.6
	100:1	792.8	100.1:1	0.1

Equation 7-5 was used to calculate the nominal Fe (III) to Fe (II) ratio from the ORP measurements taken from the solution samples obtained from the ferrihydrite solubility experiments. The ORP values were measured at 25°C, and they are shown in Table 7-2.

Table 7-2: The oxidation-reduction potential of solutions from the hematite solubility experiments

Time (min)	Measured ORP values at 25°C (SHE)							
	0 g/L	5 g/L	10 g/L	10g/L+Cu	10g/L+Ni	15 g/L	20 g/L	25 g/L
0	690	796	771	725	806	748	806	742
30	709	778	756	755	909	735	740	732
60	717	770	745	870	905	734	734	728
90	730	765	744	885	903	733	733	725
120	742	765	744	885	895	732	727	721
180	771	765	744	885	892	732	727	718
240	810	760	744	885	892	731	728	714
300	820	753	744	885	892	731	726	710
360	820	743	744	885	892	731	725	710

The calculated ferric to ferrous ratio using Equation 7-5 is shown in Table 7-3. The total iron concentrations obtained from the chemical analysis of solution samples and the calculation method are shown in Appendix E.

Table 7-3: Ferric to ferrous ratio in hematite solubility solutions at 25°C at varying acid concentrations (12 g/L Cu and 12 g/L Ni added only at 10 g/L H₂SO₄)

Time (min)	Calculated Ferric to ferrous ratio at 25°C (using Equation 7-5)							
	0 g/L	5 g/L	10 g/L	10g/L+Cu	10g/L+Ni	15 g/L	20 g/L	25 g/L
0	0.3	8.3	4.1	1.0	10.9	2.1	10.9	1.7
30	0.6	5.0	2.6	2.6	186.8	1.4	1.6	1.3
60	0.8	4.0	1.9	64.0	167.4	1.4	1.4	1.1
90	1.2	3.4	1.8	96.7	158.5	1.3	1.3	1.0
120	1.7	3.4	1.8	96.7	127.2	1.3	1.1	0.9
180	4.1	3.4	1.8	96.7	117.2	1.3	1.1	0.8
240	12.2	3.0	1.8	96.7	117.2	1.2	1.1	0.7
300	16.1	2.4	1.8	96.7	117.2	1.2	1.1	0.6
360	16.1	1.8	1.8	96.7	117.2	1.2	1.0	0.6

The amount of iron dissolved, which is present as Fe(III) and Fe(II), along with total iron at various initial acid concentrations ranging from 0 g/L to 25 g/L is presented in Figure 7-9 and Figure 7-11 to Figure 7-15. The amount of total iron dissolved increases as the acid concentration increases for all cases ranging from 0 g/L to 25 g/L. However, the behavior of Fe(III) and Fe(II) ions varies for different acid concentrations and over time.

At 0 g/L initial acid containing 12 g/L chloride (initial pH 4.0, final pH 1.65) and over the first 120 min, there is more Fe(II) than Fe(III) (as shown in Figure 7-9), however, after 120 min, the Fe(II) decreases and the Fe(III) increases. The presence of these Fe(II) ions may be due to the residual

ferrous (~0.1%) that is present in the synthetic ferrihydrite feed sample and which may leach rapidly.

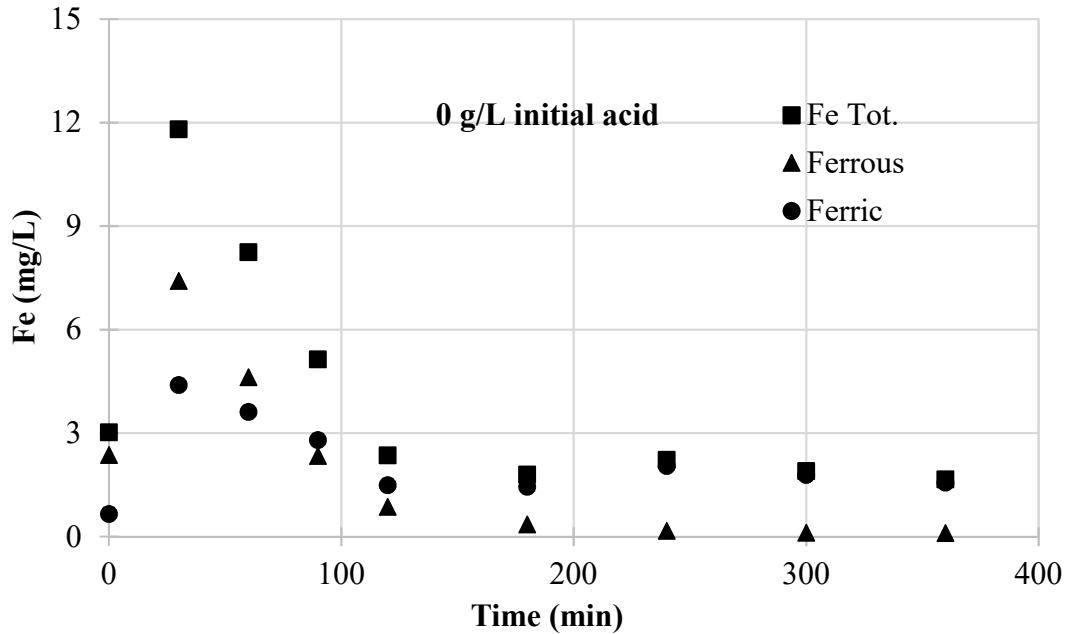


Figure 7-9: Concentration of total iron, ferric and ferrous iron dissolved from hematite in sulfate-chloride solutions at 150°C for 0 g/L initial acid. Chloride ion added as LiCl.

The corresponding Fe-Cl speciation diagram at 25°C for the conditions related to Figure 7-9, is shown in Figure 7-10. The speciation diagram shows that Fe is soluble in the solution up to pH 2.0. The chloride complexes with Fe and keeps it dissolved in the solution for the conditions relevant to the experiments in this work.

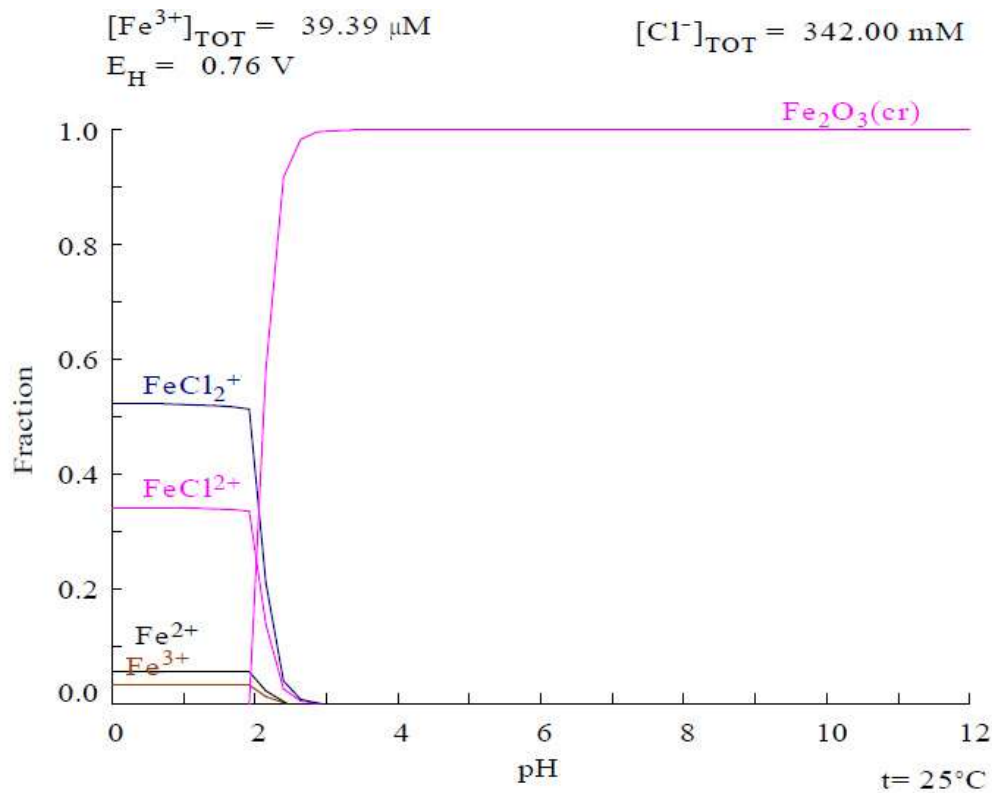


Figure 7-10: Fe-Cl speciation diagram for 0 g/L initial acid concentration, pH 1.68 at the end of 6 h and the measured ORP of 0.76 V at 25°C (SHE)
 (software used:Medusa)

At initial acid concentrations of 5 g/L, 10 g/L and 15 g/L, the amount of Fe(III) and Fe(II), as well as the total dissolved iron, shows a similar trend, as seen in Figure 7-11, Figure 7-12 and Figure 7-13. In all three cases, the amount of dissolved Fe(III) is higher than Fe(II). However, as the initial acid concentration increased from 5 g/L towards 15 g/L, the ferric concentration decreased, and ferrous concentration increased. The gap between the ferric line and ferrous line decreased, indicating that the Fe(III) to Fe(II) ratio approached 1.0 (as can also be seen in Table 7-3).

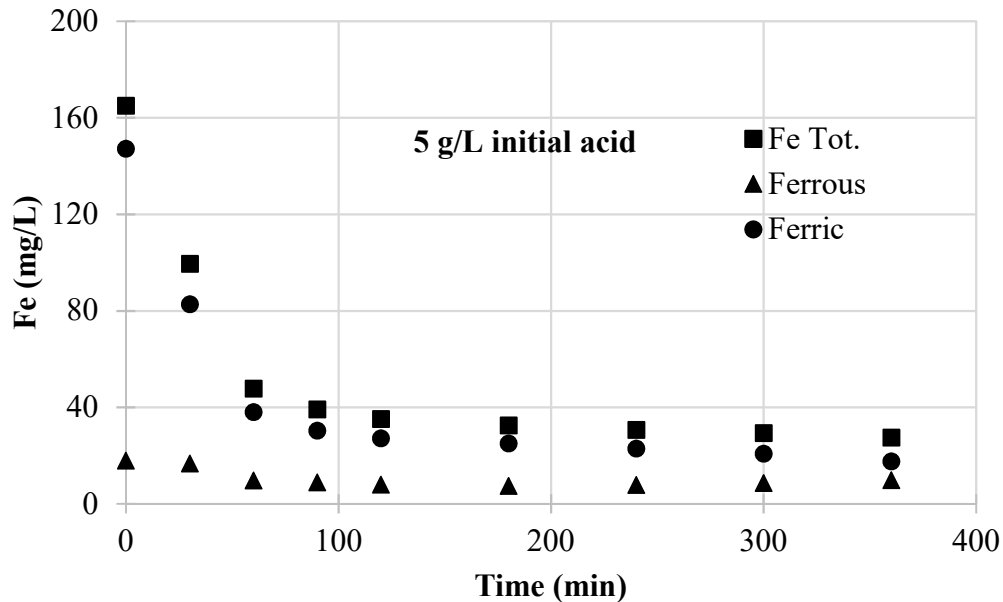


Figure 7-11: Concentration of total iron, ferric and ferrous iron dissolved from hematite in sulfate-chloride solutions at 150°C for 5 g/L initial acid

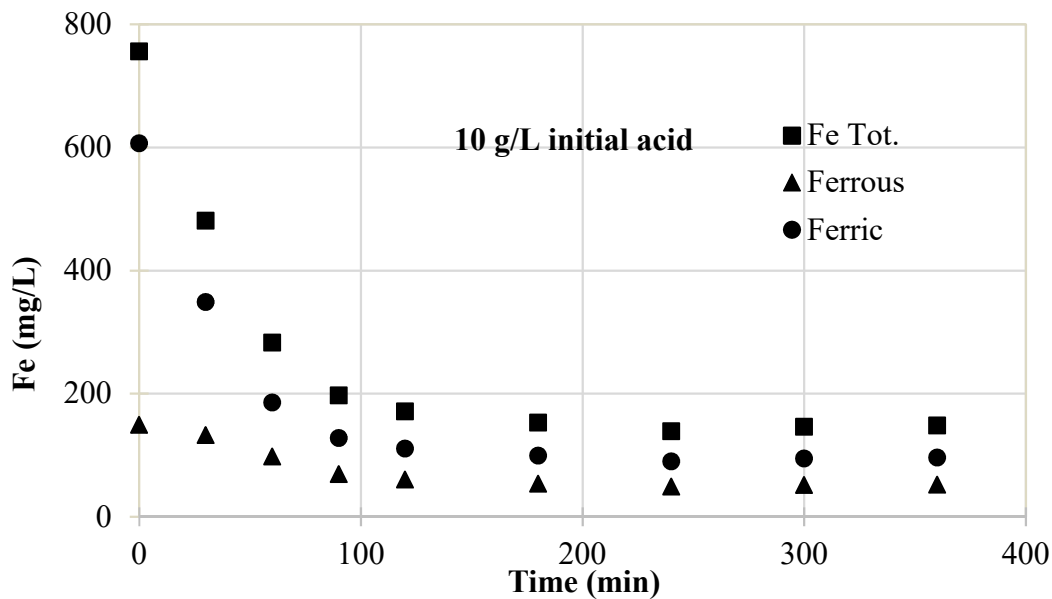


Figure 7-12: Concentration of total iron, ferric and ferrous iron dissolved from hematite in sulfate-chloride solutions at 150°C for 10 g/L initial acid

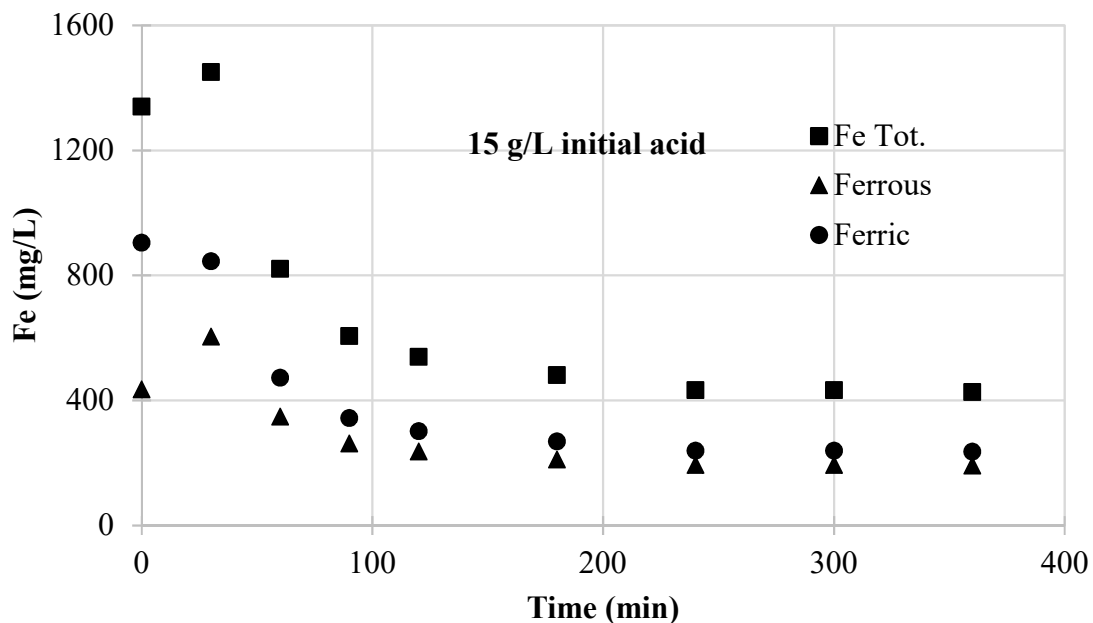


Figure 7-13: Concentration of total iron, ferric and ferrous iron dissolved from hematite in sulfate-chloride solutions at 150°C for 15 g/L initial acid

At an initial acid concentration of 20 g/L, as shown in Figure 7-14, the amount of Fe(III) and Fe(II) is similar after the initial 120 min. The ratio of Fe(III) to Fe(II) approaches 1:1. The results presented in Table 7-4 show that most of the ferric precipitated as stable hematite under these conditions. Yue (2015) also found that a large amount of Fe(III) precipitated as Fe_2O_3 when the nominal Fe(III) to Fe(II) ratio was 1:1 and attributed this to FeSO_4 . The Fe(III) to Fe(II) ratio of 1:1 means there is a lot of FeSO_4 which increases pH at high temperature resulting in so-called “at temperature acidity” (Rubisov and Papangelakis, 1999).

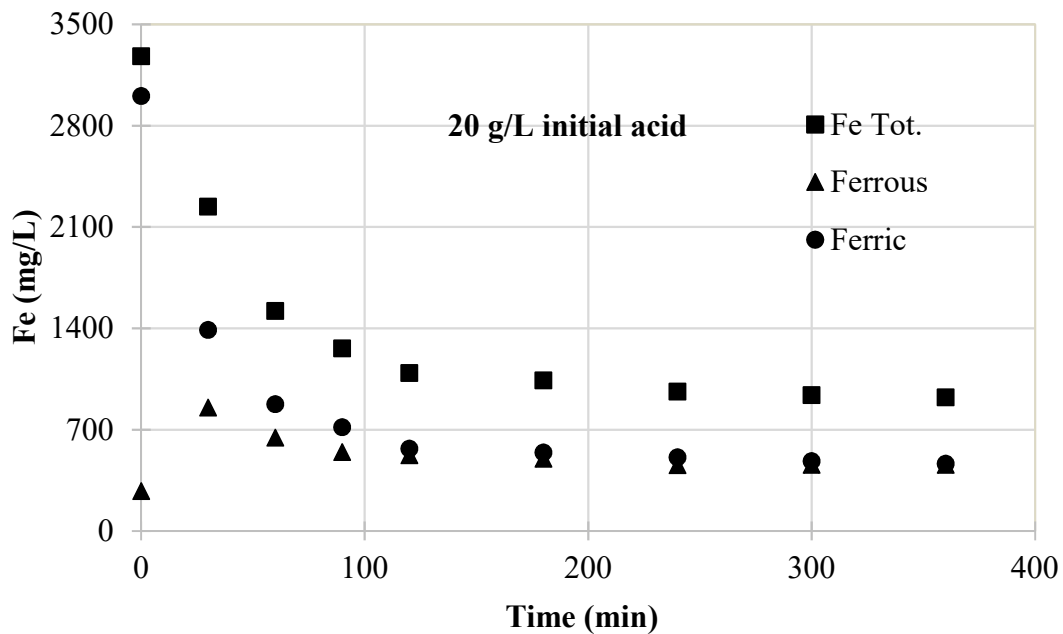


Figure 7-14: Concentration of total iron, ferric and ferrous iron dissolved from hematite in sulfate-chloride solutions at 150°C for 20 g/L initial acid

The Fe(III)-Fe(II) relationship changed at 25 g/L acid, as shown in Figure 7-15. The solubility of hematite proceeded in a similar manner to that seen for low acid concentrations up to about 100 min, after which time the amount of ferrous increased. The total amount of iron dissolved for the 25 g/L acid condition was the highest among all the acid concentrations tested here. The Fe(III) to Fe(II) ratio was less than 1.0 at 25 g/L acid. Since Fe(II) promotes the stability of goethite (Section 2.7), this phase was expected in the final product.

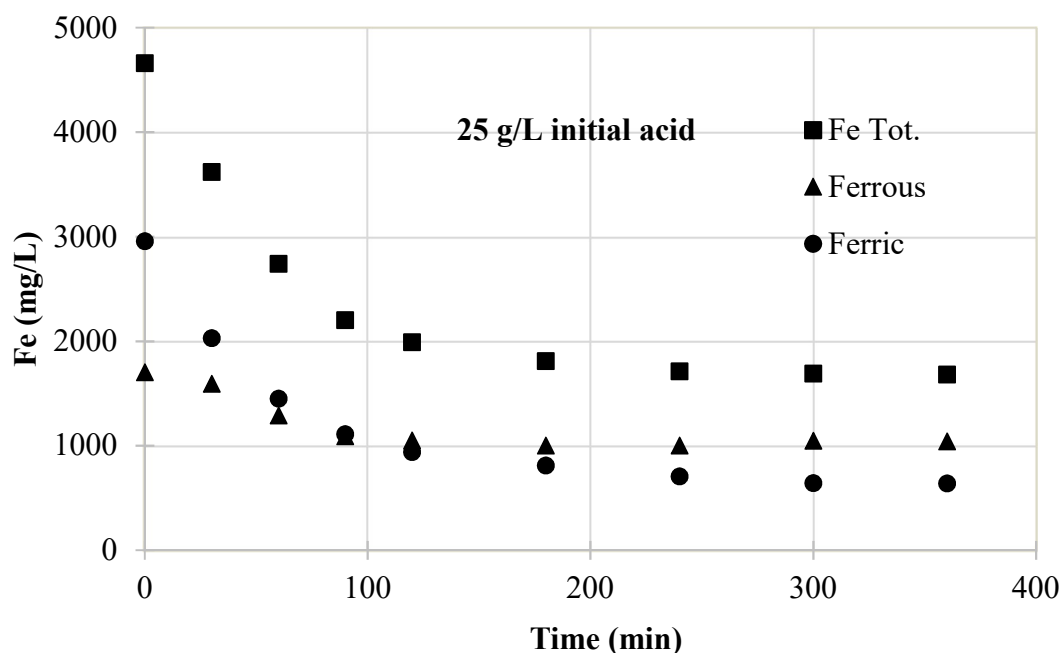


Figure 7-15: Concentration of total iron, ferric and ferrous iron dissolved from hematite in sulfate-chloride solutions at 150°C for 25 g/L initial acid

The concentrations of Fe(III) and Fe(II) in the presence of dissolved Cu and Ni are compared in Figure 7-16 and Figure 7-17. The effect of Cu and Ni during the solubility of hematite was discussed earlier (see Figure 7.5). The amount of Fe(II) in the presence of dissolved Cu and Ni, after 120 min at 10 g/L acid was negligible and stayed the same throughout the rest of the experiment. The amount of Fe(III) and the amount of total iron remained the same, indicating that Fe(III) was the predominant soluble oxidation state in the presence of dissolved Cu or Ni. This is an important finding given the corrosion discussion that follows.

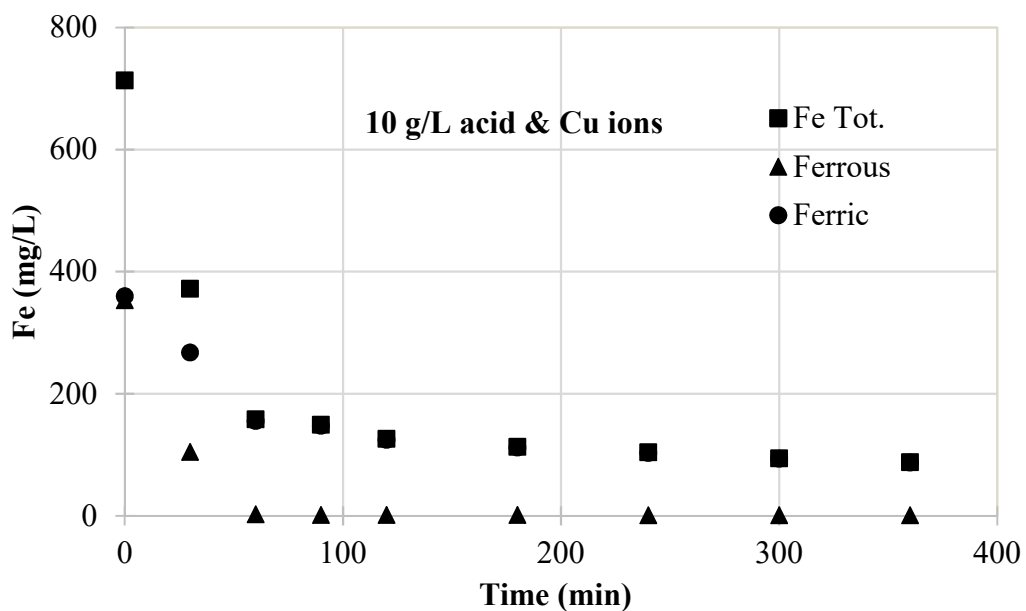


Figure 7-16: Concentration of total iron, ferric and ferrous iron dissolved from hematite in sulfate-chloride solutions at 150°C for 10 g/L initial acid in presence of 12 g/L Cu ions

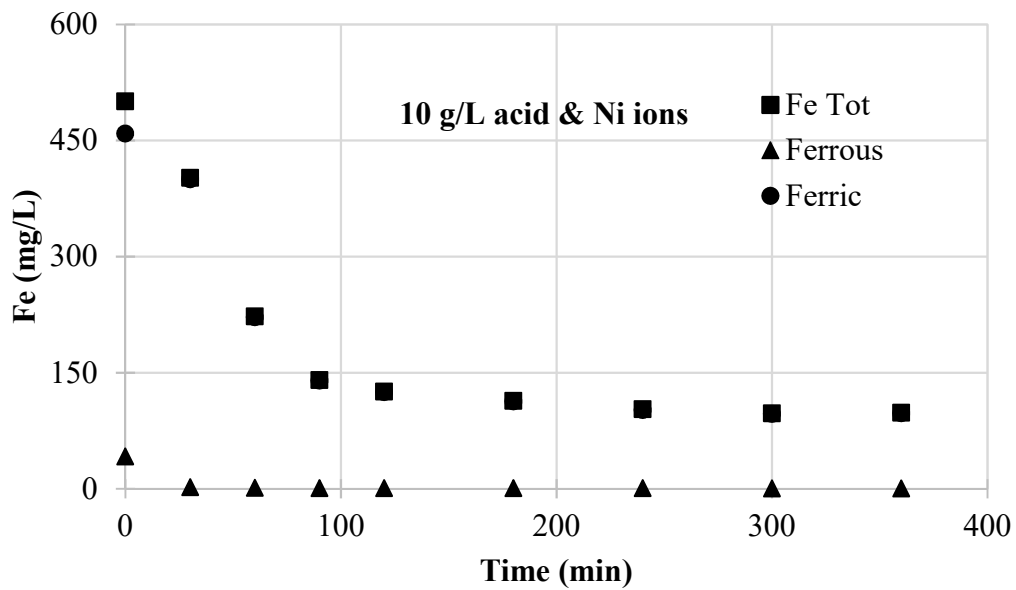


Figure 7-17: Concentration of total iron, ferric and ferrous iron dissolved from hematite in sulfate-chloride solutions at 150°C for 10 g/L initial acid in the presence of 12 g/L Ni ions

7.2.1 Titanium corrosion

Ferric iron reduction in the present work (and in the absence of soluble Cu or Ni) was almost certainly caused by passive titanium corrosion (corrosion at a low rate and through the passive film). While steps were taken here to limit this phenomenon (the use of a glass liner, for example, and the presence of Fe(III)), the extent to which this corrosion would change the solution chemistry was unanticipated. Ti corrosion while measuring hematite solubility in sulfuric acid has been previously described by Reid and Papangelakis (2006).

As noted above, it was initially thought that the ferrihydrite dissolution would yield sufficient ferric ions to strongly passivate the exposed internal titanium surfaces of the autoclave (which consisted only of the agitator shaft, impeller, and sampling frit). Liu (2015) studied titanium corrosion in sulfate-chloride solutions at 150°C and reported that corrosion rates in such solutions can be extremely high in the absence of inhibitors such as Fe(III) or Cu(II). For example, after one-week of immersion in 30 g/L H₂SO₄ and 12 g/L Cl⁻ at 150°C, Ti coupons were completely corroded. It was assumed that the Ti coupons dissolved over a period of 7 days (although this could have occurred faster) and the corrosion rate of Ti was conservatively estimated to be at least 62 mm per year in sulfate-chloride solution at 150°C. The corrosion conditions, in fact, became so reducing that sulfate was reduced to hydrogen sulfide during the exposure period (Liu, 2015). Such a scenario of rapid impeller and shaft corrosion could only have occurred in the very early stages of the solubility experiments before a significant concentration of ferric was attained. Liu (2018) found that the critical concentration of Fe(III) required to passivate Ti in 30 g/L H₂SO₄ and 12 g/L Cl⁻ solutions, at temperature 30 – 80°C, was 1.0 – 6.0 mM, in the absence of Fe(II). If Fe(II)

was present at a higher concentration than Fe(III), it might not matter how much Fe(III) is in the system and the ORP might be low simply due to high ferrous to ferric ratio. Using the corrosion rate of 62 mm/yr at an initial H₂SO₄ concentration of 25 g/L (cf. Figure 7-4 and 7-15 for conditions), one could expect about 0.01 g (0.0002 mol) of Ti to have corroded over a period of 15 min for an impeller blade surface area of 12 cm². The soluble titanium concentration for this condition was measured post-experiment, and it was found to be 8.85 mg/L (or approximately 0.01 g in 360 mL solution), which agrees with the expected corrosion rate in uninhibited sulfuric acid solutions. Referring again to the 25 g/L H₂SO₄ condition (Figure 7-15) the terminal Fe(III) concentration was approximately 0.6 g/L and the Fe(II) concentration approximately 1 g/L or about 0.5 g (0.009 mol) of total Fe(II) in the 0.36 L volume. This yields a Fe(II) to Ti mol ratio of approximately 44, which is not consistent with Fe(III) being reduced by the oxidation of Ti to Ti(II), as discussed below.

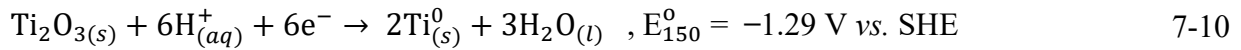
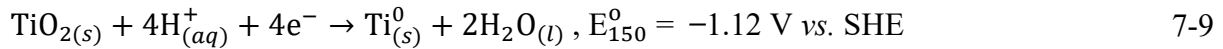
Ma and Peres (1951) presumed that sulfuric acid attacks titanium by forming Ti[(SO₄)_{2+x}]^{-2x} ions when solutions are 40 wt% or less in acid. Electrochemically, this would require titanium to be oxidized to Ti(IV). However, this was not based on any experimental evidence, and work by Armstrong et al. (1970) indicated that titanium is in the 3+ oxidation state when corroding in sulfuric acid. It was demonstrated that the titanium corrosion products in the sulfuric acid solution could be oxidized. This indicated that the corrosion product was in either the 2+ or 3+ oxidation state. Furthermore, Armstrong et al. (1970) indicated that Ti(II) could be oxidized by water, leaving 3+ as the only possible titanium oxidation state. As ferric iron is reduced to ferrous, one electron is consumed, and as titanium is oxidized from the metallic state to Ti(III), three electrons

are liberated. Hence, if all the ferric reduction was associated with the soluble titanium found in solution, then the [Fe(II)]:[Ti] ratio should be equal to 3. The significance of the [Fe(II)]:[Ti] ratio exceeding 3 is that all the ferrous iron that was generated could not solely be due to Ti^0 being oxidized to Ti(III). There must be another oxidation reaction causing the ferric reduction reaction.

This second oxidation reaction is likely the formation of the oxide surface layer. The titanium is initially oxidized to the 3+ state before being further oxidized and bound into the oxide layer. However, titanium oxide surface characterization in sulfuric acid has shown that titanium exists in a mixture of oxidation states within the oxide layer. Thomas and Nobe (1969) determined that the passive oxide layer was a mixture of TiO_2 and Ti_2O_3 . Asami et al. (1993) concluded that Ti(II), Ti(III), and Ti(IV) were all present in the oxide layer using X-ray photoelectron spectroscopy (XPS). Taking this into account, the likely ferric iron reduction mechanism involves the oxidation of metallic titanium to soluble Ti(III) sulfate complexes and Ti(III) and Ti(IV) oxides (See Reactions 7-6 to Reaction 7-11). The standard equilibrium potentials, E_{150}^0 , of Reactions 7-7 to 7-10 at 150°C were calculated and are presented. The required standard Gibb's free energies at 150°C are available in the literature (Lee, 1981; Murray & Cubicciotti, 1983).

An [Fe(II)]:[Ti] ratio > 3 requires that the current that cannot be accounted for by the soluble Ti(III) must be carried by the formation of either TiO_2 and/or Ti_2O_3 (Reactions 7-9 and 7-10). The combination of Reactions 7-7 (ferric reduction) and 7-8 (titanium oxidation) results in Reaction 7-11. The ΔG_{150}^0 of Reaction 7-11 is negative (-649.84 kJ) and therefore it is spontaneous. Similarly, for a combined reaction of ferric reduction (Reaction 7-7) and titanium oxidation to a solid phase (Reactions 7-9 and/or 7-10), the ΔG_{150}^0 values are also negative (-817.17 kJ and/or -1324.36 kJ)

making these reactions thermodynamically feasible. The required standard Gibb's free energies at 150°C are available in the literature (Lee, 1981; Biernat and Robins, 1972)



Ferric iron reduction clearly impacts the hematite solubility experiments presented here, and as discussed below, especially at elevated initial acid concentrations (25 g/L). Therefore, this a scientific limitation of the work presented here, in that solution chemistry was altered by the apparatus. It is clear that due to Ti oxidation, this study combines results from the hydrolysis of ferrihydrite and its dissolution induced by the catalytic action of aqueous Fe(II) discussed below (see Section 7.2.2). However, it should be noted that the chemistry in medium-temperature leaching is highly complex due to the presence of elemental sulfur, titanium surfaces, gangue minerals, and sulfides. Thus, ferrous species are generated during CESL leaching in both batch and continuous reactors. For example, CESL reports that the mean Fe(III):Fe(II) ratio in output solutions from 77 batch leaching tests of enargite concentrates is 14.6 ± 9.1 with terminal ORP values measured at 40°C of 744 ± 23.3 mV(SHE). Further, the standard ratio of Fe(III) to Fe(II)

in the output solutions from demonstration plant campaigns of enargite or chalcopyrite concentrates is 80:20. Thus, the transformation of ferrihydrite formed under CESL conditions also occurs in the presence of ferrous. As such, the data here is industrially relevant as it links the oxidative condition prevailing during transformation to the nature of the precipitate, as discussed further below.

The quantitative phase analysis of the transformed residue generated from the hematite solubility experiments is presented in Table 7-4. All the residues were bright red indicating a transformation from the original blackish-brown ferrihydrite. The phase analyses of the residues from the 5 – 15 g/L acid experiments show that, on average, 81% of the residues is crystalline hematite and about 19% is X-ray amorphous. The X-ray amorphous phase may be ferrihydrite or poorly crystalline hematite. The HaHC soluble fraction was about 11%, therefore the remaining 8% (19–11 = 8) could be poorly crystalline hematite. It appears that for the test conditions studied, 100% hematite formation was not achieved. Javed and Asselin (2018) precipitated hematite using ferric sulfate ($\text{Fe}_2(\text{SO}_4)_3$) in sulfate-chloride solutions at 150°C in the presence of 0 – 60 g/L Cu (there was no precipitation at 0 g/L Cu). They found that for 30 g/L Cu at the end of 1 hour the product contained about 86.6% hematite, 1.0% volaschioite ($\text{Fe}_4(\text{SO}_4)\text{O}_2(\text{OH})_6 \cdot 2\text{H}_2\text{O}$) and ~12.4% X-ray amorphous phase. Although it was reported that after 4 h the product was 100% hematite, this is likely a simplification as most crystalline solids are not, in fact, 100% crystalline under X-ray analysis. There is always some X-ray amorphous phase present. Therefore, the product formed in the study of Javed and Asselin (2008), would almost certainly contain minor amounts of ferrihydrite.

The residue from the 25 g/L acid concentration in the current study contained about 11% goethite at the end of 6 h. This was expected, as ferrous promotes goethite formation and the ORP measurements showed more ferrous than ferric in the total dissolved iron at the 25 g/L initial acid condition (Figure 7-15). The residue generated in the presence of Cu and Ni had a similar amount of hematite.

Table 7-4: QXRPD of the residues from the ferrihydrite solubility experiments after 6 h in sulfate-chloride solutions at 150°C (HaHC SD: 0.5%)

Phase	Initial acid concentration						
	0 g/L	5 g/L	10 g/L	10 g/L+Cu	10 g/L+Ni	15 g/L	*25 g/L
Hematite	80.3	82.9	81.9	80.1	79.0	81.9	70.8
Goethite	-	-	-	-	-	-	11.1
Quartz low	0.1	0.2	0.2	0.1	0.0	0.3	0.3
X- Ray Amorphous	19.6	16.9	17.9	19.8	20.9	17.9	17.8
Total	100.0	100.0	100.0	100.0	100.0	100.0	100.0
HaHC Treatment							
HaHC Sol(wt%) (ferrihydrite)	13.8	11.0	10.8	10.7	10.6	10.4	10.0
HaHC Insol(wt%) (hematite)	86.2	89.0	89.2	89.3	89.4	89.6	*90.0

*HaHC insoluble at 25 g/L is mixture of hematite and goethite

The phase analysis of the residue from 0 g/L acid in Table 7-4, shows that it is 80.3% hematite (X-ray) and 86.2% (HaHC hematite), the difference being the poorly crystalline hematite. The amount of Fe dissolved at 0 g/L acid was 0.03% or 3.02 mg/L from a total of 11.6 g/L Fe introduced as

ferrihydrate, which is almost negligible (see Table 7-5). This is a compelling evidence that the solid-state transformation mentioned above on Page 184 and in Section 2.7 does occur. The Fe distribution present in transformed hematite was determined as follows: residue mass (8.35 g) and crystalline hematite from QXRPD analysis of residue (80.3% from Table 7-4) was used to calculate the amount of hematite in the residue (6 g Fe₂O₃). The stoichiometry of Fe in Fe₂O₃ (69.94%) was then used to calculate the amount of Fe in transformed hematite (4.41 g Fe). The amount of Fe thus determined was termed ‘Fe_{Solid-State Hematite}’ in reference to its transformation to hematite via solid-state transformation and was found to be 80.99% of the total Fe put in the system (see Table 7-5).

The Fe in the ferrihydrate feed that remained untransformed, at 0 g/L acid, and carried on ‘as is’ to the final residue, termed ‘Fe_{Ferrihydrate}’ was found to be 11.52% (calculated from the HaHC soluble amount). The poorly crystalline phase, that is not detected by X-ray analysis was calculated from the difference between the HaHC insoluble phase and X-ray crystalline hematite (Table 7-4). The Fe in this poorly crystalline phase is labelled as ‘Fe_[Solid-State Hematite + precipitate]’ and was found to be 5.96% (see Table 7-5). Poorly crystalline phases result from both solid-state transformation and dissolution-reprecipitation mechanisms for hematite formation. Poorly crystalline phases arising from solid-state transformation are evident from the QXRPD analysis of the residue collected at t = 0 (150°C) and 10 g/L acid. This residue was comprised of ~99.9% X-ray amorphous phase or ferrihydrate (see Appendix D) while the HaHC treatment indicated the presence of 56.8 ± 0.5 wt% of HaHC insoluble phase. This 56.8 ± 0.5 wt% of HaHC insoluble phase is the poorly crystalline hematite (see Page 187), therefore it remained undetected by X-ray analysis. Poorly crystalline

phases also result from dissolution-reprecipitation mechanisms. This is evident from the increase in ‘ $\text{Fe}_{[\text{Solid-State Hematite} + \text{precipitate}]}$ ’ (see Table 7-5). As the acid concentration increases, ‘ $\text{Fe}_{\text{MaxDissolved}}$ ’ and ‘ $\text{Fe}_{\text{Precipitated}}$ ’ increases and contributes to ‘ $\text{Fe}_{[\text{Solid-State Hematite} + \text{precipitate}]}$ ’ of the poorly crystalline fraction.

For all the acid concentrations studied here (0 – 25 g/L), solid-state transformation appears to have been the most important mechanism. The literature is, however, scant with regards to this transformation in acidic solutions at $T > 100^\circ\text{C}$, but the existing studies indicate that solid-state transformation is a slow process (see Section 2.7). Therefore, the complete solid-state transformation of ferrihydrite to hematite may not be achieved in industrial time frames (CESL: 60 min). Since, this transformation may not complete, industrial leach residues are very likely to contain ferrihydrite and poorly crystalline hematite (refer to Section 2.4; HaHC soluble phase in Section 4.4). Reduction in the HaHC soluble phase can be achieved by employing higher acid concentrations (see Section 6.3.1, Chapter 6). The higher acid concentrations result in dissolution and reprecipitation of Fe as hematite. However, due to high supersaturation and insufficient time for crystal growth in industrial processes dissolution and reprecipitation also contain poorly crystalline hematite. Poorly crystalline hematite, although undesirable, does not result in as much Cu loss compared to ferrihydrite, therefore high acid concentrations are recommended to achieve a good compromise between poorly crystalline hematite and ferrihydrite in industrial processes.

Table 7-5: Solid-state transformation of ferrihydrite (where percentages are with respect to the total amount of Fe put into the system as ferrihydrite)

Fe (%)	Initial acid concentration (g/L)					
	0	5	10	15	^h 20	25
^a Fe _{MaxDissolved}	0.03	1.38	6.33	11.22	27.48	39.02
^b Fe _{Equilibrium}	0.01	0.16	0.92	2.66	5.74	10.48
^c Fe _{Precipitated}	0.02	1.22	5.41	8.56	21.74	28.54
^d Fe _{Undissolved}	99.97	98.62	93.67	88.78	72.52	60.98
Distribution of Fe in various phases (%)						
^e Fe _{Solid-State Hematite (crystalline)}	80.99	79.89	75.89	71.92	-	62.69
^f Fe _{Ferrihydrite}	11.52	9.43	9.17	8.63	-	0.08
^g Fe _{[Solid-State Hematite + precipitate] (poorly crystalline)}	5.95	6.31	7.49	7.72	-	*7.17

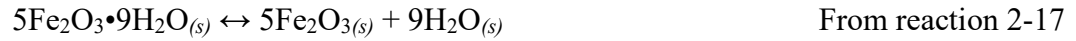
^aMaximum amount of Fe dissolved; ^bmaximum amount of dissolved Fe at t = 6 h; ^ccalculated by difference between Fe_{Dissolved} and Fe_{Equilibrium}; ^dcalculated from the difference between total Fe put into the system as ferrihydrite and Fe_{MaxDissolved}; ^ecalculated using mass balance, hematite stoichiometry and hematite percent in Table 7-4; ^fcalculated from the difference between HaHC insoluble and hematite percent in Table 7-4 (*Fe in goethite was accounted for at 25 g/L acid); ^gcalculated from HaHC soluble phase. ^hdistribution of Fe in various phases was not calculated for 20 g/L, as QXRPD information for this residue was not available.

The final acid concentrations were determined by titration with sodium hydroxide using the Mg-EDTA method described above, and the initial and final acids are compared in Table 7-6.

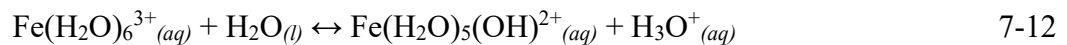
Table 7-6: Comparison of initial and final molar acid equivalents for ferrihydrite solubility solutions (error: ~ 2.0%)

Initial H⁺ (mol/L)	0.00	0.05	0.10	0.15	0.20	0.25
Final H⁺ (mol/L)	0.01	0.06	0.11	0.16	0.21	0.26

As shown in Table 7-6, only a small amount of acid was generated. According to Reaction 2-17 (see Section 2.7), no acid should be generated through solid-state transformation.



At room temperature, when 5 g ferrihydrite was added to DI water and a 12 g/L solution of Cl^- ions, the pH dropped right away from around pH 6 to pH 4. After 6 h of mixing the pH was stable and remained at pH 4. The acidity of these solutions cannot be attributed to the Cl^- ions because these ions are weak bases. The acidity of these solutions must, therefore, result from the behavior of the Fe^{3+} , Cu^{2+} , Ni^{2+} ions. However, the Fe^{3+} , Cu^{2+} , Ni^{2+} ions cannot be Bronsted acids by themselves. They act as proton donors by influencing the ability of the neighboring water molecules to release H^+ ions. They do this by forming coordinate bonds with six water molecules to form a complex ion. Water molecules bound to one of these metal ions are more acidic than normal. Thus, reactions such as the following occur.



Reaction 7-12 gives rise to a net increase in the H_3O^+ ion concentration in these solutions, thereby making the solutions more acidic.

7.2.2 Fe(II) catalyzed transformation

The percentage of total dissolved iron that is in the form of ferric and ferrous ions was calculated from ORP measurements and was plotted against acid concentration as shown in Figure 7-18. The proportion of ferric decreases as the final acid concentration increases from 0 g/L to 20 g/L, where the amount of ferrous iron in the solution increases. The ferric and ferrous curves intersect at the acid concentration of ~20 g/L indicating that there is more ferrous in the system after this point. The residue obtained at this condition has goethite as seen in the phase analysis by quantitative X-ray diffraction (Table 7-4). The presence of ferrous ions in sampling solutions was confirmed by titrations performed at CESL (as opposed to the ORP measurements used herein). However, the time lapse between solution collection and the titration experiments (4 months) yielded different results from the ORP calculations done here, which are based on ORP measurements on fresh solutions. Nonetheless, the corrosion of the titanium internals is very plausible and is certainly a limitation of this work in that the solubility results were clearly impacted.

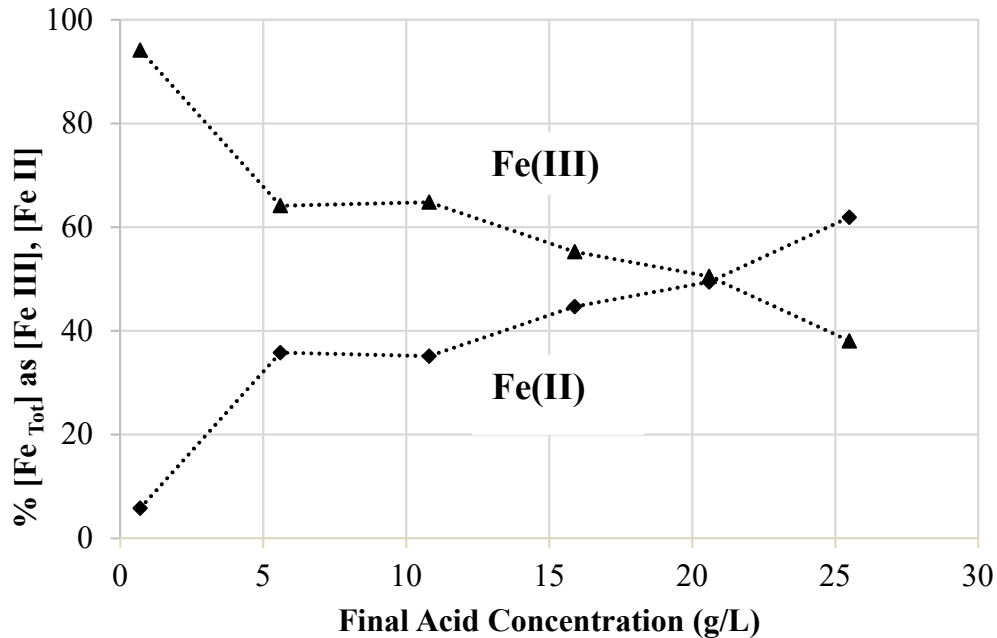


Figure 7-18: Percentage of ferric and ferrous iron relative to the total iron concentration at various final acid concentration for hematite in sulfate-chloride solutions at 150°C

Goethite (FeOOH) precipitates instead of hematite if the ferric concentration has been minimized by reduction to ferrous. In an environment low in ferric iron, goethite can precipitate directly from ferrous iron. Goethite has been found to be present in CESL residues alongside hematite (see Table 4-3, Chapter 4). Industrially, goethite precipitation occurs from ferrous iron according to Reaction 7-13.



Schwertmann (1991), noted that Fe(II) catalyzes the dissolution of ferrihydrite. Bruyère and Blesa (1985) also noticed that the dissolution rate of magnetite was enhanced with the similar accelerating effect of added Fe(II). The transformation of various iron oxides in the presence of Fe(II) has been reported by several authors (Hansel et al., 2003; Jeon et al., 2001; Jeon et al., 2003;

Jolivet et al., 1992; Tamaura et al., 1983; Tronc et al., 1992). Hansel et al. (2003) found that in the presence of Fe(II), ferrihydrite transformed into goethite, lepidocrocite, and magnetite. Tronc et al. (1992) and Jolivet et al. (1992) studied the transformation of ferrihydrite at varying Fe(II)/Fe(III) ratios of 0.0 – 0.5 and 0.10 – 0.50 in distilled water (pH 8) at 25°C and found that for low Fe(II) concentrations, ferrihydrite transformed into goethite whereas at higher Fe(II) concentrations magnetite was formed. Lepidocrocite was found to transform into magnetite in the presence of Fe(II) (Tamaura et al., 1983; Jeon et al., 2001). Pedersen et al. (2015), studied the transformation of iron oxides submerged in Fe(II) solutions (prepared by adding 0.0 – 1.0 mM FeCl₂ added to deionized water and pH adjusted to 6.5 with sodium bicarbonate) at 25°C and found that ferrihydrite transformed completely into goethite, even at the lowest Fe(II) concentration. The transformation was attributed to the catalytic action of Fe(II). This mechanism involves electron exchange between the Fe(III) in the solid phase and an inner-sphere bound Fe(II) ion across the edge of the outermost octahedron of the ferrihydrite surface through metal-metal bonding by overlapping d-orbitals (Sherman, 1987). Another possible mechanism is the exchange of Fe(II) for Fe(III) in the terminal octahedral positions similar to Fe(III) isotopic exchange described by Rea et al. (1994). The electron from Fe(II) migrates through the crystal lattice of the ferrihydrite according to spectroscopic evidence provided by Williams and Scherer (2004). The Fe(II)-O bond is more labile (weaker) than the Fe(III)-O bond, and therefore, the presence of the extra electrons in the crystal lattice decreases its stability. Ferrihydrite crystal lattice is broken down, and goethite is precipitated. This explains the presence of goethite in the ferrihydrite solubility residues at acid conditions where more iron was found dissolved as ferrous compared to ferric.

7.3 Conclusions

The solubility of metastable ferrihydrite was measured in sulfate-chloride solutions in an autoclave with an in-situ filtration system via solid-state transformation of ferrihydrite by internal rearrangement, partial dissolution of ferrihydrite, and its subsequent re-precipitation as hematite. The solid-state transformation of ferrihydrite to hematite was found to be the major mechanism at all acid concentrations. As the acid concentration increased partial dissolution of ferrihydrite, and its subsequent re-precipitation as hematite occurred. The dissolution of ferrihydrite increased with increasing acid concentration or decreasing pH. It was also found that the addition of Cu and Ni both reduce the solubility of ferrihydrite; this is attributed to lower 'at temperature' acidity. The total iron was found by chemical analysis, and the ferric-ferrous ratio was calculated by a novel equation developed at UBC. The ferrous concentrations were likely the result of titanium corrosion, which would have been higher at higher initial acid concentrations. Thus, it was found that the ferric concentration was greater than ferrous for all cases but at the highest acid concentration (25 g/L). The quantitative phase analysis of the residues showed that the presence of more ferrous iron compared to ferric ion results in precipitation of goethite along with hematite. Approximately 89.5% of the residue was hematite when the final dissolved ferric concentration was higher than the ferrous concentration (see Table 7-4). These results indicate that if ferrihydrite is formed in the CESL process, operating at 60 min retention time, most, but not all, of this ferrihydrite (about 82.5%, see Page 186) will eventually transform to hematite or dissolve and re-precipitate as hematite or goethite. However, the prevailing oxidative condition, probably dictated by the extent of sulfide oxidation, and measured via the ferric to ferrous ratio, plays an important

role in the formation of the final precipitates. This accounts for the variability in precipitates and the remaining amorphous phases found in Chapters 4 and 6.

CHAPTER 8: CONCLUSIONS AND RECOMMENDATIONS

8.1 Conclusions

A detailed conclusion is presented at the end of each chapter. In this chapter, extended conclusions of the thesis research on iron and sulfur control in the leaching of sulfide concentrates are summarized, and suggestions are made for future work.

The work in this thesis can be summarized in four general areas as follows:

- Analysis of the leach residue from CESL and Vale processes. Evaluation of the crystallinity of iron phases in leach residue and quantification of the loss of metals associated with the iron phases.
- Leaching of sulfide concentrates targeting the precipitation of crystalline hematite in the leach residue by supersaturation control
- Novel reagent(s) for iron and sulfur control in the leaching of sulfide concentrates.
- The solubility of metastable ferrihydrite under CESL conditions at 150°C.

8.1.1 Analysis of the leach residue from CESL and Vale processes

- Chemical analysis of the filtrates from sequential extraction revealed that HaHC soluble phases were the major source of copper and nickel loss to the residue. HaHC soluble phases contained 2–4 times more Cu/Ni than the crystalline iron oxide phases.
- The HaHC soluble phases were positively identified to be ferrihydrite by transmission electron microscopy. Mössbauer spectroscopy identified poorly crystalline hematite and some form of

poorly crystalline jarosite resembling the copper doped synthetic jarosite in the leach residue samples.

- A hydrometallurgical process for copper and nickel sulfide leaching which produces the minimum amount of HaHC soluble phases would lead to the minimum loss of copper/nickel to the residue.
- In a continuous industrial process setting, HaHC treatment of residues may be practiced as a standard to determine the quality of iron phases in leach residue on a regular basis.

8.1.2 Leaching of sulfide concentrates

- The degree of crystallinity in iron residues generated during the leaching of sulfide concentrates under CESL conditions at 150°C with chloride catalyst, and sulfuric acid lixiviant was achieved by optimum acid concentration and the addition of various seed.
- Higher acid concentration (~35 g/L) produced residues with lower HaHC numbers and reduced the loss of Cu and Ni to the residue, thereby improving the extractions. The final acid concentration was found to be an important factor in the precipitation of hematite.
- The addition of various types of seed also reduced the HaHC numbers. Seeding is useful because it reduces the degree of supersaturation. The best results were achieved with the addition of synthetic hematite seed.
- In a continuous industrial operation, optimum control of acid concentration and the addition of seed should be practiced for generating better residues and reducing loss metals to the residue.

8.1.3 Novel reagent(s) for iron and sulfur control

- A class of novel additives that outperform the conventional OPD and lignosol surfactants were discovered. These additives have iron complexation, sulfur dispersion, and sulfur modification properties.
- The iron complexing properties of the new additives (benzene sulfonic acid, phenyl phosphonic acid) also achieve the preferential formation of hematite and better residues with lower HaHC numbers.
- These additives assist in sulfur dispersion and coagulate sulfur in the form of chunks or prills which are then easy to separate from the iron residues.
- The additives result in enhanced recovery of copper from sulfide concentrates. The additives are able to leach the concentrates of P₈₀:75 μm (Teck's CESL process generally use feed solids of P₈₀:20 μm). The additives may reduce the oxidation of pyrite, which could offer the ability to tune the reaction process for one mineral over another.

8.1.4 Solubility of metastable ferrihydrite under CESL conditions at 150°C

- The ferrihydrite formed in the CESL process will eventually transform to hematite by a mix of solid-state transformation, dissolution and reprecipitation.
- The solid-state transformation of ferrihydrite to hematite was found to be the major mechanism at all acid concentrations, but it is reduced at high acid concentrations (> 25 g/L).

- This transformation was not complete within the time (60 min) that is normally used in CESL conditions. This means that if ferrihydrite phases are formed, they will persist in CESL residues and will result in associated metal loss (Chapter 4).
- To avoid goethite formation care should be taken to keep the conditions sufficiently oxidizing to avoid the formation of ferrous iron. Sufficiently oxidizing conditions are not typically achieved in CESL leaching.
- An expedited way of determining the ratio of ferric and ferrous in an industrial setting is to employ the equation developed by a co-worker in the Asselin group and used in this study to infer the ferrous to ferric ratio using the measured ORP values.

8.2 Recommendations for future work

- Characterization of iron phases in leach residues using QXRPD is relatively straightforward: patterns can be easily matched, indexed and attributed to appropriate phases quantitatively using Rietveld refinement. X-ray amorphous and poorly crystalline iron phases in admixtures can also be quantified using the sequential extraction procedure. However sequential extraction is time consuming and obtaining reproducibility during repeats requires a lot of practice. Characterization of leach residues can be further extended to include X-ray absorption fine spectroscopy (EXAFS), X-ray absorption near edge structure (XANES) and synchrotron-based radiation techniques such as X-ray absorption spectroscopy (XAS). Analysis by synchrotron diffraction increases the speed of data collection significantly. The higher energies provided by the synchrotron beam make in-situ studies of solids in solution and phase transformation at temperature possible. Examples of these include: characterization

of the colloidal iron phase documented to occur in the Bayer process (Basu et al., 1986), investigations of chalcopryrite dissolution (Majuste et al., 2013) and dissolution mechanisms involving hematite (McBriarty et al., 2019).

- The temperature (159°C), where the viscosity of liquid sulfur is the lowest changes upon addition of various reagents to sulfur. Doi (1965), studied the effect of different types of reagents on the viscosity of sulfur in the temperature range of 120 to 200°C. The viscosity was measured using an Ostwald viscometer dipped in a glycerin bath. The impact of the new reagents, used in this study, on the viscosity of sulfur should be examined. Commercially available Anton-Paar modular rheometers that measure the viscosity of aqueous system and slurries and operate at high temperatures and pressures may be used. An example of this is determination of rheometric properties of pure liquid elemental sulfur by Sofekun et al. (2018).
- The use of novel reagents should be extended to study copper-arsenic concentrates or enargite concentrates. Enargite is refractory and very difficult to leach as compared to chalcopryrite. It is known that arsenic increases the viscosity of sulfur. The effect of novel reagents used in this study on the viscosity of sulfur in the presence of arsenic needs to be investigated, and efforts should continue to develop a unique combination of reagents to achieve this goal.
- The use of novel reagents used in this study should be investigated in the absence of chloride. It is known that chloride is corrosive and increases the cost of materials of construction for the autoclave. Chloride complexes with iron and helps form hematite, it also affects sulfur viscosity (Defreyne and Cabral, 2009; Riveros and Dutrizac, 1997). The novel reagents in this

study also exhibit similar effects on both iron and sulfur, therefore, it may be possible to eliminate or reduce the amount of chloride used in the process and this should be examined. However, the effect of chloride concentration reduction on the kinetics of the process, vis-à-vis its role in the Cu(II)/Cu(I) couple may limit the usefulness of this approach.

- The use of novel reagents should be extended to study a wider range of temperatures. As some reagents delay the rise in sulfur viscosity to higher temperatures, leaching at more elevated temperatures may become possible. Perhaps by leaching at higher temperatures, while keeping the viscosity at a minimum in the presence of these novel reagents, better extractions may be achieved with refractory concentrates containing arsenic.
- Although there was an industrial relevance to the ferrihydrite solubility experiments performed here in that ferrous is always present in the CESL process, these experiments should be duplicated using an agitator shaft, impeller, and filter made of materials such as PTFE to prevent ferric reduction to ferrous.
- The solid-state transformation of ferrihydrite to hematite was found to be the major mechanism in ferrihydrite solubility experiments. This is an important new finding and must be extended to include detailed kinetic studies in sulfate-only, chloride-only and sulfate-chloride systems. A wide range of temperatures (25-225°C) and longer time frames must be studied. In situ synchrotron analysis as mentioned earlier in this sub-section should be employed.

REFERENCES

- Afanasev, A.M., Gorobchenko, V.D., Kulgawczuk, D.S., Lukashevich, I.I., 1974. Nuclear γ -resonance in iron sulphates of the jarosite group. *Phys. Status Solidi* 26, 697–701.
- Alfantazi, A.M., Dreisinger, D.B., 2003. An investigation on the effects of orthophenylene diamine and sodium lignin sulfonate on zinc electrowinning from the industrial electrolyte. *Hydrometallurgy* 69, 99–107.
- Anderson, C.G., 2003. Treatment of copper ores and concentrates with industrial nitrogen species catalyzed pressure leaching and non-cyanide precious metals recovery. *JOM* 55, 32–36.
- Andoh, N., Fujiwara, S., 1985. Process for producing aromatic amine. US4521622A.
- Arauco, H., Doyle, F.M., 1986. Hydrolysis and precipitation of iron during first stage pressure leaching of zinc sulphide concentrates, in: Dutrizac, J.E., Monhemius, A.J. (Eds.), *Proceedings of International Symposium on Iron Control in Hydrometallurgy*. Toronto, pp. 409–430.
- Armstrong, R.D., Harrison, J.A., Thirsk, H.R., Whitfield, R., 1970. Anodic dissolution of titanium in sulfuric acid. *J. Electrochem. Soc.*, 117, 1003–1006.
- Asami, K., Chen, S.C., Habazaki, H., Hashimoto, K., 1993. The surface characterization of titanium and titanium-nickel alloys in sulfuric acid. *Corros. Sci.* 35, 43–49.
- Atkinson, R.J., Posner, A.M., Quirk, J.P., 1968. Crystal nucleation in Fe(III) solutions and hydroxide gels. *J. Inorg. Nucl. Chem.* 30, 2371–2381.
- Aucamp, M.E., Liebenberg, W., Stieger, N., 2015. Solvent-interactive transformations of pharmaceutical compounds, in: *Advanced topics in crystallization*. InTech, London, pp. 2–26.
- Babcan, J., 1971. Synthesis of jarosite $\text{KFe}_3(\text{SO}_4)_2(\text{OH})$. *Geol. Zb* 22, 299–304.

- Bacon, R.F., Fanelli, R., 1943. The viscosity of sulfur. *J. Am. Chem. Soc.* 65, 639–648.
- Baes, C.F., Mesmer, R., 1976. *The hydrolysis of cations*. J. Wiley and Sons, New Jersey.
- Baghalha, M., Papangelakis, V.G., 1998. Pressure acid leaching of laterites at 250°C: A Solution chemical model and its applications. *Metall. Mater. Trans. B* 29, 945–952.
- Baghalha, M., Papangelakis, V.G., 2000. Ion-association-interaction approach at high temperature: Application to aqueous $\text{H}_2\text{SO}_4\text{-Al}_2(\text{SO}_4)_3\text{-MgSO}_4$ solutions in hydrometallurgy, in: *Proceedings of the International Conference on Properties of Water and Steam*. Toronto, pp. 700–710.
- Bailey, J.K., Brinker, C.J., Mecartney, M.L., 1993. Growth mechanisms of iron oxide particles of differing morphologies from the forced hydrolysis of ferric chloride solutions. *J. Colloid Interface Sci.* 157, 1–13.
- Barta, L.A., Collins, M.J., Masters, I.M., 1998. Use of coal as an additive in the Dynatec zinc pressure leach process in zinc and lead Processing, in: Dutrizac, J.E. (Ed.), *Proceedings of an International Symposium on Zinc and Lead Processing*. Calgary, pp. 749–764.
- Basu, P., Nitowski, G.A., The, P.J., 1986. Chemical interactions of iron minerals during Bayer digest and clarification, in: Dutrizac, J.E., Monhemius, A.J. (Eds.), *Proceedings of International Symposium on Iron Control in Hydrometallurgy*. Toronto, pp. 223-244.
- Batty, J.D., Rorke, G.V., 2006. Development and commercial demonstration of the BioCOP™ thermophile process. *Hydrometallurgy* 83, 83–89.
- Bendersky, L.A., Gayle, F.W., 2001. Electron diffraction using transmission electron microscopy. *J. Res. Natl. Inst. Stand. Technol.* 106, 997–1012.
- Berezowsky, R., Trytten, L., 2002. Commercialization of the acid pressure leaching of chalcopyrite, in: *Proceedings of ALTA Conference*. Melbourne, pp. 227–267.

- Berger, C.J.M., Lippiatt, S.M., Lawrence, M.G., Bruland, K.W., 2008. Application of a chemical leach technique for estimating labile particulate aluminum, iron, and manganese in the Columbia River plume and coastal waters off Oregon and Washington. *J. Geophys. Res.* 113, 1–16.
- Berner, R.A., 1969. Goethite stability and the origin of red beds. *Geochim. Cosmochim. Acta* 267–273.
- Beverkog, B., Puigdomenech, I., 1995. Revised Pourbaix diagrams for Copper at 5-150 C. SKI Report 95:73. Swedish Nuclear Power Inspectorate, Stockholm.
- Biedermann, G., Schindler, P., 1957. On the solubility product of precipitated iron(III) hydroxide. *Acta Chem. Scand.* 11, 731–740.
- Biernat, R.J., Robins, R.G., 1972. High-temperature potential/pH diagrams for the iron-water and iron-water-sulphur systems. *Electrochim. Acta* 17, 1261–1283.
- Biernat, R.J., Robins, R.G., 1969. High temperature potential/ph diagrams for the sulphur-water system. *Electrochim. Acta* 14, 809–820.
- Blesa, M., Matijević, E., 1989. Phase transformations of iron oxides, oxyhydroxides, and hydrous oxides in aqueous media. *Adv. Colloid Interface Sci.* 29, 173–221.
- Boctor, N.Z., Popp, R.K., Frantz, J.D., 1980. Mineral-solution equilibria - IV. Solubilities and the thermodynamic properties of FeCl_2^0 in the system $\text{Fe}_2\text{O}_3\text{-H}_2\text{-H}_2\text{O-HCl}$. *Geochim. Cosmochim. Acta* 44, 1509–1518.
- Boldt, J.R., 1967. *The winning of nickel: It's geology, mining, and extractive metallurgy*. Van Nostrand Company, New Jersey.
- Bolton, G.L., 1981. Sulphur production by pressure leaching of metal sulphides, in: *Proceedings of Sulphur-81: An International Conference*. Calgary, pp. 277–286.

- Borggaard, O.K., 1982. Selective extraction of amorphous iron oxides by EDTA from selected silicates and mixtures of amorphous and crystalline iron oxides. *Clay Miner.* 17, 365–368.
- Borggaard, O.K., 1981. Selective extraction of amorphous iron oxides by EDTA from soils from Denmark and Tanzania. *J. Soil Sci.* 32, 427–432.
- Borggaard, O.K., 1979. Selective extraction of amorphous iron oxides by EDTA from a Danish sandy loam. *J. Soil Sci.* 30, 727–734.
- Borggaard, O.K., 1976. Selective extraction of amorphous iron oxides by EDTA from a mixture of amorphous iron oxide, goethite, and hematite. *J. Soil Sci.* 27, 478–486.
- Boscato, J.F., Catala, J.M., Clouet, F., Brossas, J., 1981. Synthesis of polyphenylene polysulfur. *Polym. Bull.* 4, 357–359.
- Boyd, D., 2016. Sulfur and its role in modern materials science, *Angew. Chem. Int. Ed.* 55, 15486 - 15502.
- Brady, K.S., Bigham, J.M., Jaynes, W.F., Logan, T.J., 1986. Influence of sulfate on Fe-oxide formation: Comparisons with a stream receiving acid mine drainage. *Clays Clay Miner.* 34, 266–274.
- Brewer, R.E., 2004. Copper concentrate pressure leaching - plant scale-up from continuous laboratory testing. *Miner. Metall. Process.* 21, 202–208.
- Brittain, H.G., 2014. Thermodynamic vs. kinetic solubility: Knowing which is which. *Am. Pharm. Rev.* 17, 10–15.
- Brook, E.J., Moore, J.N., 1988. Particle-size and chemical control of As, Cd, Cu, Fe, Mn, Ni, Pb, and Zn in bed sediment from the Clark Fork River, Montana (U.S.A.). *Sci. Total Environ.* 76, 247–266.
- Brown, J., Papangelakis, V., 2005. Interfacial studies of liquid sulphur during aqueous pressure

- oxidation of nickel sulphide. *Miner. Eng.* 18, 1378–1385.
- Bruyère, V.I.E., Blesa, M.A., 1985. Acidic and reductive dissolution of magnetite in aqueous sulfuric acid: Site-binding model and experimental results. *J. Electroanal. Chem. Interfacial Electrochem.* 182, 141–156.
- Burkin, A.R., 1966. *The chemistry of hydrometallurgical processes.* E. and F.N. Spon, London.
- Canfield, D.E., 1989. Reactive iron in marine sediments. *Geochim. Cosmochim. Acta* 53, 619–632.
- Cashell, C., Sutton, D., Corcoran, D., Hodnett, B.K., 2003. Inclusion of the stable form of a polymorph within crystals of its metastable form. *Cryst. Growth Des.* 3, 869–872.
- Cashion, J., Murad, E., 2012. Mössbauer spectra of the acid mine drainage mineral Schwertmannite from the Sokolov basin, Czech Republic, in: *Proceedings of 36th Annual Condensed Matter and Materials Meeting, 2012.* Wagga Wagga, pp. TP30–TP34.
- Chalkley, M.E., Collins, M.J., Ozberk, E., 1993. The Behaviour of sulphur in the Sherritt zinc pressure leach process, in: *Proceedings of International Symposium on Zinc- World Zinc '93.* Hobart, pp. 325–331.
- Chao, T.T., Zhou, L., 1983. Extraction techniques for selective dissolution of amorphous iron oxides from soils and sediments. *Soil Sci. Soc. Am. J.* 47, 225-232.
- ChemicalBook, 2008. ChemicalBook---Chemical Search Engine. Retrieved from <http://www.chemicalbook.com/>
- Chen, T.T., Dutrizac, J.E., Poirier, G., Kerfoot, D.G., Singhal, A., 2006. Characterization of the iron-rich residues generated during the pressure oxidative leaching of Voisey's Bay nickel sulphide concentrate, in: *Proceedings of International Symposium on Iron Control in Hydrometallurgy.* Montreal, pp. 429–444.

- Chester, R., Hughes, M.J., 1967. A chemical technique for the separation of ferromanganese minerals, carbonate minerals and adsorbed trace elements from pelagic sediments. *Chem. Geol.* 2, 249–262.
- Chung, W.J., Griebel, J.J., Kim, E.T., Yoon, H., Simmonds, A.G., Ji, H.J., Dirlam, P.T., Glass, R.S., Wie, J.J., Nguyen, N. A., Guralnick, B.W., Park, J., Somogyi, A., Theato, P., Mackay, M.E., Sung, Y., Char, K., Pyun, J., Somogyi, Á., Theato, P., Mackay, M.E., Sung, Y., Char, K., Pyun, J., Somogyi, A., Theato, P., Mackay, M.E., Sung, Y., Char, K., Pyun, J., Somogyi, Á., Theato, P., Mackay, M.E., Sung, Y., Char, K., Pyun, J., 2013. The use of elemental sulfur as an alternative feedstock for polymeric materials. *Nat. Chem.* 5, 518–524.
- Ciobanu, C.L., Wade, B.P., Cook, N.J., Schmidt Mumm, A., Giles, D., 2013. Uranium-bearing hematite from the Olympic Dam Cu-U-Au deposit, South Australia: A geochemical tracer and reconnaissance Pb-Pb geochronometer. *Precambrian Res.* 238, 129–147.
- Collins, M.J., Kofluk, D.K., 1998. Hydrometallurgical process for the extraction of copper from sulphidic concentrations. US5730776A.
- Collins, M.J., Kofluk, D.K., 1997. Recovery of zinc from sulphidic concentrates. US5651947.
- Cornell, R.M., Giovanoli, R., 1989. Effect of cobalt on the formation of crystalline iron oxides from ferrihydrite in alkaline media. *Clays Clay Miner.* 37, 65–70.
- Cornell, R.M., Giovanoli, R., 1988. The influence of copper on the transformation of ferrihydrite ($5\text{Fe}_2\text{O}_3 \cdot 9\text{H}_2\text{O}$) into crystalline products in alkaline media. *Polyhedron* 7, 385–391.
- Cornell, R.M., Giovanoli, R., 1987. Effect of manganese on the transformation of ferrihydrite into goethite and jacobsonite in alkaline media. *Clays Clay Miner.* 35, 11–20.
- Cornell, R.M., Giovanoli, R., 1986. Factors that govern the formation of multi-domainic goethites. *Clays Clay Miner.* 34, 557–564.

- Cornell, R.M., Giovanoli, R., Schindler, P.W., 1987. Effect of silicate species on the transformation of ferrihydrite into goethite and hematite in alkaline media. *Clays Clay Miner.* 35, 21–28.
- Cornell, R.M., Giovanoli, R., Schneider, W., 1992. The effect of nickel on the conversion of amorphous iron(III) hydroxide into more crystalline iron oxides in alkaline media. *J. Chem. Technol. Biotechnol.* 53, 73–79.
- Cornell, R.M., Giovanoli, R., Schneider, W., 1990. Effect of cysteine and manganese on the crystallization of noncrystalline iron(III) hydroxide at pH 8. *Clays Clay Miner.* 38, 21–28.
- Cornell, R.M., Schwertmann, U., 1996. *The iron oxides: structure, properties, reactions, occurrence and uses.* VCH, Weinheim.
- Corrans, I.J., Johnson, G.D., Angove, J.E., 1993. The recovery of nickel and gold from sulfide concentrates, in: *Proceedings of 18th International Mineral Processing Congress.* Sydney, pp. 1227–1238.
- Corriou, J.P., Kikindai, T., 1981. The aqueous oxidation of elemental sulfur and different chemical properties of the allotropic forms S_λ and S_μ . *J. Inorg. Nucl. Chem.* 43, 9–15.
- Crockett, M.P., Evans, A.M., Worthington, M.J.H., Albuquerque, I.S., Slattery, A.D., Gibson, C.T., Campbell, J.A., Lewis, D.A., Bernardes, G.J.L., Chalker, J.M., 2016. Sulfur-limonene polysulfide: A material synthesized entirely from industrial by-products and its use in removing toxic metals from water and soil. *Angew. Chem. Int. Ed.* 55, 1714–1718.
- Cudennec, Y., Lecerf, A., 2006. The transformation of ferrihydrite into goethite or hematite revisited. *J. Solid State Chem.* 179, 716–722.
- Daichuan, D., Pinjie, H., Shushan, D., 1995. Preparation of uniform α - Fe_2O_3 particles by microwave-induced hydrolysis of ferric salts. *Mater. Res. Bull.* 30, 531–535.

- Dalton, R.F., Diaz, G., Price, R., Zunkel, A.D., 1991. The cuprex metal extraction process: Recovering copper from sulfide ores. *JOM* 43, 51–56.
- Dalvi, A.D., Bacon, W.G., Osborne, R., 2004. The past and the future of nickel laterites, in: *Proceedings of PDAC International Convention*. Toronto, pp.1–27
- Das, S., Hendry, M.J., Essilfie-Dughan, J., 2011. Transformation of two-line ferrihydrite to goethite and hematite as a function of pH and temperature. *Environ. Sci. Technol.* 45, 268–275.
- Davidson, L.E., Shaw, S., Benning, L.G., 2008. The kinetics and mechanisms of schwertmannite transformation to goethite and hematite under alkaline conditions. *Am. Mineral.* 93, 1326–1337.
- Defreyne, J., Barr, G., McCunn, G., de Souza Costa, R., Lage Goncalves, L.R., 2004. CESL copper process - moving from pilot plant to production scale operation. Retrieved from <https://www.cesl.com>
- Defreyne, J., Brace, T., Miller, C., Omena, A., Matos, M., Cobral, T., 2008. Commissioning UHC: a Vale copper refinery based on CESL technology, in: Young, C.A., Taylor, P.R., Anderson, C.G. (Eds.), *Proceedings of the 6th International Symposium on Hydrometallurgy*, Phoenix, pp. 357–366.
- Defreyne, J., Cabral, T., 2009. Early copper production results from Vale's hydrometallurgical CESL refinery, in: *Proceedings of ALTA Copper Conference*. Perth, pp. 298–309.
- Defreyne, J., Grieve, W., Jones, D.L., Mayhew, K., 2006. The role of iron in the CESL process, in: *Proceedings of 3rd International Symposium on Iron Control in Hydrometallurgy*, Montreal, pp. 205–220.
- Demopoulos, G., 1993. Precipitation in aqueous processing of inorganic materials: A unified colloid-crystallization approach to the production of powders with controlled properties, in:

- Henein, H., Oki, T. (Eds.), 1st Conference on Processing Materials for Properties, Warrendale, pp. 537–540.
- Demopoulos, G.P., 2009. Aqueous precipitation and crystallization for the production of particulate solids with desired properties. *Hydrometallurgy* 96, 199–214.
- Dempsey, P., Dreisinger, D.B., 2003. Process for the extraction of copper. US6503293.
- Di Justo, P., 2009. What's Inside WD-40? Superlube's Secret Sauce. Retrieved from <https://www.wired.com/2009/04/st-whatsinside-6/>
- Diakonov, I.I., Schott, J., Martin, F., Harrichourry, J.C., Escalier, J., 1999. Iron(III) solubility and speciation in aqueous solutions. Experimental study and modeling: Part 1. Hematite solubility from 60 to 300°C in NaOH-NaCl solutions and thermodynamic properties of Fe(OH)₄-(aq). *Geochim. Cosmochim. Acta* 63, 2247–2261.
- Dirksen, J.A., Ring, T.A., 1991. Fundamentals of crystallization: Kinetic effects on particle size distributions and morphology. *Chem. Eng. Sci.* 46, 2389–2427.
- Dixon, D., Asselin, E., Ren, Z., Mora, N., 2018. Process for leaching metal sulfides with reagents having thiocarbonyl functional groups. WO2018072029A1.
- Dixon, D.G., Mayne, D.D., Baxter, K.G., 2008. Galvanox™ - A novel galvanically assisted atmospheric leaching technology for copper concentrates. *Can. Metall. Q.* 47, 327–336.
- Doi, T., 1965. Physicochemical properties of sulfur. II. Effects of different types of reagents on viscosities of liquid sulfur. *Rev. Phys. Chem. Japan* 35, 1–10.
- Doki, N., Kubota, N., Sato, A., Yokota, M., 2001. Effect of cooling mode on product crystal size in seeded batch crystallization of potassium alum. *Chem. Eng. J.* 81, 313–316.
- Dorfner, K., 1991. Ion Exchangers. Walter de Gruyter and Co., New York.

- Dreisinger, D., Marsh, J., Dempsey, P., 2002. The Anglo American Corporation and University of British Columbia (AAC - UBC) chalcopryrite copper hydrometallurgical process, in: Proceedings of ALTA Copper Conference. Melbourne, pp. 330–354.
- Dreisinger, D., 2006. Copper leaching from primary sulfides: Options for biological and chemical extraction of copper. *Hydrometallurgy* 83, 10–20.
- Dreisinger, D., 2003. New developments in the leaching of base and precious metal ores and concentrates, in: Lorenzen, L., Bradshaw, D.J. (Eds.), Proceedings of the 22nd International Mineral Processing Congress. Johannesburg, pp. 70–80.
- Drits, V., 1993. Structural model for ferrihydrite. *Clay Miner.* 28, 185–207.
- Drits, V.A., Sakharov, B.A., Manceau, A., 1993. Structure of ferrihydrite as determined by simulation of X-ray diffraction curves. *Clay Miner.* 28, 209–222.
- Drits, V.A., Sakharov, B.A., Salyn, A.L., Manceau, A., 1993. Structural model for ferrihydrite. *Clay Miner.* 28, 185–207.
- Duncan, I.J., 1994. Olympic Dam. A review of the discovery, resource, development, metallurgy, and environment. *Erzmetall* 47, 464–469.
- Dutrizac, J.E., 1987. An overview of iron precipitation in hydrometallurgy, in: Strathdee, G.L., Klein, M.O., Melis, L.A. (Eds.), Proceedings of the International Symposium on Crystallization and Precipitation. Saskatoon, pp. 259–283.
- Dutrizac, J.E., 1984. The behavior of impurities during jarosite precipitation, in: Bautista R.G. (Eds.), *Hydrometallurgical Process Fundamentals*. NATO Conf. Ser. VI Mater. Sci. 10, 125–169.
- Dutrizac, J.E., 1983. Factors affecting alkali jarosite precipitation. *Metall. Trans. B Process Metall.* 14B, 531–539.

- Dutrizac, J.E., 1979. The physical chemistry of iron precipitation in the zinc industry, in: Cigan, J.M., Mackey, T.S., O'Keefe, T.J. (Eds.), Proceedings of a World Symposium on Metallurgy and Environmental Control : Lead-Zinc-Tin '80. Las Vegas, pp. 532–564.
- Dutrizac, J.E., Chen, T.T., 2009. Factors affecting the precipitation of hematite rather than jarosite in nickel sulphate-chloride solutions, in: Budac, J., Fraser, R., Mihaylov, I., Papangelakis, V.G., Robinson, D.J. (Eds.), Proceedings of 39th Annual Hydrometallurgy Meeting. Sudbury, pp. 295–320.
- Dutrizac, J.E., Jambor, J.L., 2000. Jarosites and their application in hydrometallurgy. *Rev. Mineral. Geochemistry* 40, 405–452.
- Dutrizac, J.E., Kaiman, S., 1976. Synthesis and properties of jarosite-type compounds. *Can. Mineral.* 14 (2), 151–158.
- Dutrizac, J.E., Riveros, P.A., 1999. The precipitation of hematite from ferric chloride media at atmospheric pressure. *Metall. Mater. Trans. B* 30, 993–1001.
- Dutrizac, J.E., Sunyer, A., 2012. Hematite formation from jarosite type compounds by hydrothermal conversion. *Can. Metall. Q.* 51, 11–23.
- Duyvesteyn, W.P.C., 1995. The development of the Escondida leach process and its implementation in the Escondida copper cathode plant, in: Proceedings of ALTA conference, Brisbane, pp. 58–72.
- Dyar, D.M., Agresti, D.G., Schaefer, M.W., Grant, C.A., Sklute, E.C., 2006. Mössbauer spectroscopy of earth and planetary materials. *Annu. Rev. Earth Planet. Sci.* 34, 83–125.
- Dyar, M.D., Breves, E., Jawin, E., Marchand, G., Nelms, M., O'Connor, V., Peel, S., Rothstein, Y., Sklute, E.C., Lane, M.D., Bishop, J.L., Mertzman, S.A., 2013. Mössbauer parameters of iron in sulfate minerals. *Am. Mineral.* 98, 1943–1965.

- Dyer, L.G., Chapman, K.W., English, P., Saunders, M., Richmond, W.R., 2012. Insights into the crystal and aggregate structure of Fe³⁺ oxide/silica co-precipitates. *Am. Mineral.* 97, 63–69.
- Dzombak, D., Morel, F., 1990. *Surface complexation modeling: Hydrous ferric oxide*. J. Wiley and Sons, New York.
- Eggleton, R.A., Fitzpatrick, R.W., 1988. New data and a revised structural model for ferrihydrite. *Clays Clay Miner.* 36, 111–124.
- Fairbrother, F., Gee, G., Merrall, G.T., 1955. The polymerization of sulfur. *J. Polym. Sci.* 16, 459–469.
- Farmer, V.C., Russell, J.D., Smith, B.F.L., 1983. Extraction of inorganic forms of translocated Al, Fe and Si from a Podzol Bs horizon. *J. Soil Sci.* 34, 571–576.
- Ferron, C.F., Fleming, C.A., Dreisinger, D.B., 2001. PLATSOL Treatment of the northmet copper nickel PGM bulk concentrate - pilot plant results, in: ALTA nickel cobalt conference. Melbourne, pp. 425–458
- Fischer, W.R., Schwertmann, U., 1975. The formation of hematite from amorphous iron(III) hydroxide. *Clays Clay Miner.* 23.
- Forward, F.A., 1951. Extracting of nickel from nickeliferous sulfide material. US2576314.
- Forward, F.A., Warren, I.H., 1960. Extraction of metals from sulphide ores by wet methods. *Metall. Rev.* 5, 137–164.
- Fountain, C., 2008. When does further processing at the mine site make sense?, in: *Proceedings of Metallurgical Plant Design and Operating Strategies*. Perth, pp. 157–173.
- Fountain, C., 2013. The whys and wherefores of penalty elements in copper concentrates, in: *Proceedings of Metallurgical Plant Design and Operating Strategies*. Perth, pp. 502–518.

- Fultz, B., Howe, J.M., 2013. Transmission electron microscopy and diffractometry of materials. Springer-Verlag, Berlin.
- Geer, W.C., Bedford, C.W., 1925. The history of organic accelerators in the rubber industry. *Ind. Eng. Chem.* 17, 393–396.
- George, L.L., Cook, N.J., Crowe, B.B.P., Ciobanu, C.L., 2018. Trace elements in hydrothermal chalcopyrite. *Mineral. Mag.* 82, 59–88.
- Golden, D.C., Ming, D.W., Bowen, L.H., Morris, R. V., Lauer, H. V., 1994. Acidified oxalate and dithionite solubility and color of synthetic, partially oxidized Al-magnetites and their thermal oxidation products. *Clays Clay Miner.* 42, 53–62.
- Granata, G., Miura, A., Liu, W., Pagnanelli, F., Tokoro, C., 2019. Iodide-assisted leaching of chalcopyrite in acidic ferric sulfate media. *Hydrometallurgy* 186, 244–251.
- Grohol, D., Nocera, D., Papoutsakis, D., 2003. Magnetism of pure iron jarosites. *Phys. Rev. B* 67, 1–13.
- Guerra, E., Shepherd, J.L., 2011. The effect of polytetrafluoroethylene on pressure oxidation of nickeliferous pyrrhotite. *Hydrometallurgy* 106, 179–182.
- Gusenius, E.M., 1969. Beginnings of greatness in Swedish chemistry (II): Axel Fredrick Cronstedt (1722-1765). *Trans. Kansas Acad. Sci.* 72, 476–485.
- Habashi, F., Bauer, E.L., 1966. Aqueous oxidation of elemental sulfur. *Ind. Eng. Chem. Fundam.* 5, 469–471.
- Habashi, F., 1997. *Handbook of Extractive Metallurgy II*. Wiley-VCH, New York.
- Hackl, R.P., 1995. The leaching and passivation of chalcopyrite in acid sulfate media. The University of British Columbia.

- Hackl, R.P., Dreisinger, D.B., King, J.A., 1995a. Effect of sulfur dispersing surfactants on the oxygen pressure leaching of chalcopyrite, in: Cooper, W.C., Dreisinger, D.B., Dutrizac, J.E., Hein, H., Ugarte, G. (Eds.), *Proceeding of Copper 95-Cobre 95 International Conference*. Montreal, pp. 559–577.
- Hackl, R.P., Dreisinger, D.B., Peters, E., King, J.A., 1995b. Passivation of chalcopyrite during oxidative leaching in sulfate media. *Hydrometallurgy* 39, 25–48.
- Hamada, S., Kudo, Y., Matsumoto, T., 1989. The Preparation of monodispersed α -iron(III) oxide particles from 2,2'-Bipyridineiron(II) Complex. *Bull. Chem. Soc. Jpn.* 62, 1017–1022.
- Hamada, S., Niizeki, S., Kudo, Y., 1986. The precipitation of monodispersed α -iron(III) oxide particles from iron(III) chloride–glycine system in aqueous and 2-propanol/water media. *Bull. Chem. Soc. Jpn.* 59, 3443–3450.
- Hansel, C.M., Benner, S.G., Neiss, J., Dohnalkova, A., Kukkadapu, R.K., Fendorf, S., 2003. Secondary mineralization pathways induced by dissimilatory iron reduction of ferrihydrite under advective flow. *Geochim. Cosmochim. Acta* 67, 2977–2992.
- Hawthorne, F.C., Waychunas, G.A., 1988. Spectrum-fitting methods. *Rev. Mineral.* 18, 63–98.
- Heffels, S.K., Kind, M., 1999. Seeding technology: An underestimated critical success factor for crystallization, in: *Proceedings of 14th International Symposium of Industrial Crystallization*. Rugby, pp. 1990–2003.
- Hiemstra, T., Van Riemsdijk, W.H., Rossberg, A., Ulrich, K.U., 2009. A surface structural model for ferrihydrite II: Adsorption of uranyl and carbonate. *Geochim. Cosmochim. Acta* 73, 4437–4451.
- Hockridge, J.G., Jones, F., Loan, M., Richmond, W.R., 2009. An electron microscopy study of the crystal growth of schwertmannite needles through oriented aggregation of goethite nanocrystals. *J. Cryst. Growth* 311, 3876–3882.

- Honey, D.J., Muir, D.M., Hunt, P.R., 1997. Hydrometallurgical processing options for nickel sulfide concentrates, in: Cooper, W.C., Mihaylov, I. (Eds.), Proceedings of Nickel Cobalt 97, Vol. II: Hydrometallurgy and Refining. Sudbury, pp. 15–29.
- Hourn, M., Turner, D., Holzberger, I., 1996. Atmospheric mineral leaching process. US5993635A.
- Hove, M., Van Hille, R.P., Lewis, A.E., 2009. The effect of different types of seeds on the oxidation and precipitation of iron. *Hydrometallurgy* 97, 180-184.
- Howard-White, F.B., 1963. Nickel, an historical review. Van Nostrand Company, New Jersey.
- Howard, J.W., 1929. The story of copper. *J. Chem. Educ.* 6, 413–431.
- HSC Chemistry Computer Software, 2002.
- Hsu, P.H., Wang, M.K., 1980. Crystallization of goethite and hematite at 70°C. *Soil Sci. Soc. Am. J.* 44, 143.
- Huang, H.H., Bernal, J., 1984. Kinetic study on direct leaching of sphalerite in sulfuric acid solution using ferrous sulfate as the catalyst, in: Proceedings of the International Symposium on Electrochemistry in Mineral and Metal Processing. New Jersey, pp. 469–485.
- Huay, R.J., 1801. *Traite De Mineralogie*. Paris.
- Hyvärinen, O., Hämäläinen, M., 2005. HydroCopper™ - a new technology producing copper directly from concentrate. *Hydrometallurgy* 77, 61–65.
- ICSG, 2019. Copper market forecast for 2019-2020 by International Copper Study Group. Retrieved from <http://www.icsg.org/>
- INSG, 2019. Nickel market observations for 2018-2019 by International nickel study group. Retrieved from <http://www.insg.org/>
- Jambor, J.L., Dutrizac, J.E., 1998. Occurrence and constitution of natural and synthetic

- ferrihydrate, a widespread iron oxyhydroxide. *Chem. Rev.* 98, 2549–2586.
- Jankovic, Z., Papangelakis, V.G., Lvov, S.N., 2009. Effect of nickel sulphate and magnesium sulphate on pH of sulphuric acid solutions at elevated temperatures. *J. Appl. Electrochem.* 39, 751–759.
- Janney, D.E., Cowley, J.M., Buseck, P.R., 2001. Structure of synthetic 6-line ferrihydrate by electron nanodiffraction. *Am. Mineral.* 86, 327–335.
- Janney, D.E., Cowley, J.M., Buseck, P.R., 2000a. Transmission electron microscopy of synthetic 2- and 6-line ferrihydrate. *Clays Clay Miner.* 48, 111–119.
- Janney, D.E., Cowley, J.M., Buseck, P.R., 2000b. Structure of synthetic 2-line ferrihydrate by electron nanodiffraction. *Am. Mineral.* 85, 1180–1187.
- Jansen, E., Kyek, A., Schäfer, W., Schwertmann, U., 2002. The structure of six-line ferrihydrate. *Appl. Phys. A Mater. Sci. Process.* 74, 1004–1006.
- Jaroslav, N., 2006. The Ostwald Rule of Stages. *Cryst. Res. Technol.* 30, 443–449.
- Javed, T., Asselin, E., 2015. Hematite precipitation from sulphate chloride solutions at 150°C, in: *Proceedings of the Conference of Metallurgists. Toronto*, pp. 1–13.
- Jentzsch, T.L., Penn, R.L., 2006. Influence of aluminum doping on ferrihydrate nanoparticle reactivity. *J. Phys. Chem. B* 110, 11746–11750.
- Jeon, B.H., Dempsey, B.A., Burgos, W.D., 2003. Kinetics and mechanisms for reactions of Fe(II) with Iron(III) oxides. *Environ. Sci. Technol.* 37, 3309–3315.
- Jeon, B.H., Dempsey, B.A., Burgos, W.D., Royer, R.A., 2001. Reactions of ferrous iron with hematite. *Colloids Surfaces Physicochem. Eng. Asp.* 191, 41–55.
- Jin, N., Guerra, E., 2012. The effect of polytetrafluoroethylene on pressure oxidation of

- chalcopyrite, in: Shijie Wang, S., Dutrizac, J.E., Free, M.L., Hwang, J.Y., Kim, D. (Eds.), Proceedings of T.T. Chen Honorary Symposium on Hydrometallurgy. Orlando, pp. 207-215.
- Johnston, J.H., Glasby, G.P., 1978. The secondary iron oxide hydroxide mineralogy of some deep-sea and fossil manganese nodules : A Mössbauer and X-ray study. *Geochem. J.* 12, 153–164.
- Johnston, J.H., Lewis, D.G., 1983. A detailed study of the transformation of ferrihydrite to hematite in an aqueous medium at 92°C. *Geochim. Cosmochim. Acta* 47, 1823–1831.
- Jolivet, J.P., Belleville, P., Tronc, E., Livage, J., 1992. Influence of Fe(II) on the formation of the spinel iron oxide in alkaline medium. *Clays Clay Miner.* 40, 531–539.
- Jolivet, J.P., Henry, M., Livage, J., 2000. Metal oxide chemistry and synthesis : from solution to solid state. J. Wiley and Sons, New York.
- Jones, D.L., 1974. The leaching of chalcopyrite. The University of British Columbia.
- Jones, D.L., Moore, R., 2001. The application of CESL process to laterites, in: Proceedings of ALTA Nickel Cobalt Conference. Melbourne, pp.412–423
- Jones, F., Ogden, M.I., Oliveira, A., Parkinson, G.M., Richmond, W.R., 2003. The effect of phosphonate-based growth modifiers on the morphology of hematite nanoparticles formed via acid hydrolysis of ferric chloride solutions. *Cryst. Eng. Comm.* 5, 159.
- Kan, S., Yu, S., Peng, X., Zhang, X., Li, D., Xiao, L., Zou, G., Li, T., 1996. Formation process of nanometer-sized cubic ferric oxide single crystals. *J. Colloid Interface Sci.* 178, 673–680.
- Kato, T., 1977. The crystal structures of jarosite and svanbergite. *Mineral. J.* 8, 419–430.
- Kawulka, P., Haffenden, W.J., Mackiw, V.N., 1975. Recovery of zinc from zinc sulphide by direct pressure leaching. US3867268.
- Kennedy, C.B., Scott, S.D., Ferris, F.G., 2004. Hydrothermal phase stabilization of 2-line

- ferrihydrite by bacteria. *Chem. Geol.* 212, 269–277.
- Kerfoot, D.G., Cordingley, P.D., 1997. The acid pressure leach process for nickel and cobalt laterite. Part II: Review of operations at Fort Saskatchewan, in: Cooper, W., Mihaylov, I. (Eds.), *Proceeding of Nickel Cobalt 97, Vol. II: Hydrometallurgy and Refining*. Sudbury, pp. 355–368.
- Kerfoot, D.G.E., Weir, D.R., 1988. The hydro and electrometallurgy of nickel and cobalt, in: *Proceedings of a Symposium at the 117th TMS Annual Meeting, Extractive metallurgy of nickel and cobalt*. Phoenix, pp. 241–267.
- Knight, R.J., Sylva, R.N., 1974. Precipitation in hydrolysed iron(III) solutions. *J. Inorg. Nucl. Chem.* 36, 591–597.
- Konishi, H., Xu, H., 2012. Nanostructures of natural iron oxide nanoparticles, in: *Nature's Nanostructures*. Pan Stanford, New York, pp. 75–114.
- Kostka, J.E., Luther, G.W., 1994. Partitioning and speciation of solid phase iron in salt marsh sediments. *Geochim. Cosmochim. Acta* 58, 1701–1710.
- Kovács, K., Kuzmann, E., Homonnay, Z., Vértes, A., Gunneriusson, L., Sandström, A., 2008. Mössbauer study of synthetic jarosites. *Hyperfine Interact.* 186, 69–73.
- Kubisz, J., 1969. Hydronium jarosite $[\text{H}_3\text{O}]\text{Fe}_3[(\text{SO}_4)_2(\text{OH})_6]$. *Prz. Geol.* 17(11), 583.
- Kubisz, J., 1964. Minerals of the alunite-jarosite group. *Polska Akad. Nauk Prace Geol.* 22, 1-90
- Kubota, N., Doki, N., Yokota, M., Sato, A., 2001. Seeding policy in batch cooling crystallization. *Powder Technol.* 121, 31–38.
- Kuhn, M.C., Arbiter, N., Kling, H., 1978. Physical and chemical separations via the Arbiter process, in: *Proceedings of the 11th International Mineral Processing Congress*. Cagliari, pp. 831–847.

- Kusik, C.L., Meissner, H.P., 1978. Electrolyte activity coefficients in inorganic processing. *Fundam. Asp. Hydrometall. Process. Symp. Ser.* 173, 14–19.
- Lahtinen, M., Svens, K., Lehtinen, L., 2006. Hematite versus jarosite precipitation in zinc production, in: *Proceedings of 3rd International Symposium on Hydrometallurgy, Montreal*, pp. 93–107.
- Leclerc, A., 1980. Room temperature Mössbauer analysis of jarosite-type compounds. *Phys. Chem. Miner.* 6, 327–334.
- Lee, G., Bigham, J.M., Faure, G., 2002. Removal of trace metals by coprecipitation with Fe, Al and Mn from natural waters contaminated with acid mine drainage in the Ducktown Mining District, Tennessee. *Appl. Geochemistry* 17, 569–581.
- Lee, J.B., 1981. Elevated temperature potential-pH diagrams for the chromium-water, titanium-water, molybdenum-water, and platinum-water systems. *Corrosion* 37, 467–481.
- Lemire, R.J., Berner, U., Musikas, C., Palmer, D.A., Taylor, P., Tochiyama, O., 2013. Chemical thermodynamics of iron Part 1, in: *Chemical Thermodynamics (13a)*. Nuclear Energy Agency, Paris, pp.163-231
- Lim, J., Pyun, J., Char, K., 2015. Recent approaches for the direct use of elemental sulfur in the synthesis and processing of advanced materials. *Angew. Chemie. Int. Ed.* 54, 3249–3258.
- Lin, X., Burns, R.C., Lawrence, G.A., 2003. Effect of cadmium(II) and anion type on the aging of ferrihydrite and its subsequent leaching under neutral and alkaline conditions. *Water. Air. Soil Pollut.* 143, 155–177.
- Lindsay, W.L., 1979. *Chemical equilibria in soils*. J.Wiley and Sons, New York.
- Liu, H., Li, P., Zhu, M., Wei, Y., Sun, Y., 2007. Fe(II)-induced transformation from ferrihydrite to lepidocrocite and goethite. *J. Solid State Chem.* 180, 2121–2128.

- Liu, H., Papangelakis, Vladimirov, G., Blakey, B.C., Alam, M.S., Singh, G., 2003. Solubility of hematite in H₂SO₄ solution at 230-270°C. *Can. Metall. Q.* 42(2), 199–208.
- Liu, H., Yang, L., Ma, M., Li, P., Wei, Y., 2010. The transformation of ferrihydrite in the presence of trace Fe(II): The effect of the ammonia, amine and the coordination ions of Fe(III). *J. Solid State Chem.* 183, 542–546.
- Liu, J., 2015. High temperature and high-pressure corrosion of titanium in hydrometallurgical applications. The University of British Columbia.
- Liu, Y., 2018. Critical concentration of Fe(III) required to passivate Ti. Personal Communication. Materials Engineering, The University of British Columbia, Vancouver, BC.
- Loan, M., Newman, O.G.M., Cooper, R.M.G., Farrow, J.B., Parkinson, G.M., 2006. Defining the paragoethite process for iron removal in zinc hydrometallurgy. *Hydrometallurgy* 81, 104–129.
- Loan, M., Parkinson, G.M., Newman, O.G.M., Farrow, J.B., 2002. Iron oxy-hydroxide crystallization in a hydrometallurgical residue. *J. Cryst. Growth* 235, 482–488.
- Loan, M., Pierre, T.G. St., Parkinson, G.M., Newman, O.G.M., Farrow, J.B., 2002. Identifying nanoscale ferrihydrite in hydrometallurgical residues. *JOM* 54, 40–43.
- Loan, M., Richmond, W.R., Parkinson, G.M., 2005. On the crystal growth of nanoscale schwertmannite. *J. Cryst. Growth* 275, 1875–1881.
- Lundström, M., Aromaa, J., Forsén, O., Hyvärinen, O., Barker, M.H., 2005. Leaching of chalcopyrite in cupric chloride solution. *Hydrometallurgy* 77, 89–95.
- Luther, G.W., Kostka, J.E., Church, T.M., Sulzberger, B., Stumm, W., 1992. Seasonal iron cycling in the salt-marsh sedimentary environment: the importance of ligand complexes with Fe(II) and Fe(III) in the dissolution of Fe(III) minerals and pyrite, respectively. *Mar. Chem.* 40, 81–

- Ma, C.C., Peres Jr., E.M., 1951. Corrosion resistance of anodized and unanodized titanium. *Ind. Eng. Chem.* 43, 675–679
- Machala, L., Zboril, R., Gedanken, A., 2007. Amorphous iron(III) oxide-a review. *J. Phys. Chem. B* 111, 4003–18.
- Majima, H., Awakura, Y., 1981. Measurement of the activity of electrolytes and the application of activity to hydrometallurgical studies. *Metall. Trans. B* 12, 141–147.
- Majima, H., Awakura, Y., Mishima, T., 1985. The Leaching of Hematite in Acid Solutions. *Metall. Trans. B* 16, 23–30.
- Majuste, D., Ciminelli, V.S.T., Eng, P.J., Osseo-Asare, K., 2013. Applications of in situ synchrotron XRD in hydrometallurgy: Literature review and investigation of chalcopyrite dissolution. *Hydrometallurgy* 131–132, 54–66.
- Marescotti, P., Carbone, C., Comodi, P., Frondini, F., Lucchetti, G., 2012. Mineralogical and chemical evolution of ochreous precipitates from the Libiola Fe–Cu-sulfide mine (Eastern Liguria, Italy). *Appl. Geochemistry* 27, 577–589.
- Marsden, J.O., Brewer, R.E., Hazen, N., 2003. Copper concentrate leaching developments by Phelps Dodge corporation., in: *Proceedings of 5th International Symposium on Hydrometallurgy*. Vancouver, pp. 1429–1446.
- Marsden, J.O., Wilmot, J.C., Green, C., Hazen, W.W., Baughman, D., 2010. Process for recovery of copper from copper-bearing material using pressure leaching, direct electrowinning and solution extraction. US7736487B2.
- Marsden, J.O., Wilmot, J.C., Hazen, N., 2007a. Medium-temperature pressure leaching of copper concentrates - Part I: chemistry and initial process development. *Miner. Metall. Process.* 24,

193–204.

Marsden, J.O., Wilmot, J.C., Hazen, N., 2007b. Medium-temperature pressure leaching of copper concentrates - Part II: development of direct electrowinning and an acid-autogenous process. *Miner. Metall. Process.* 24, 205–217.

Marsden, J.O., Wilmot, J.C., Mathern, D.R., 2007c. Medium-temperature pressure leaching of copper concentrates - Part III: commercial demonstration at Bagdad, Arizona. *Miner. Metall. Process.* 24, 218–225.

Marsden, J.O., Wilmot, J.C., Smith, R.J., 2007d. Medium-temperature pressure leaching of copper concentrates - Part IV: application at Morenci, Arizona. *Miner. Metall. Process.* 24, 226–236.

Martin, E.L., 1939. o-Phenylenediamine. *Org. Synth.* 19, 70–72.

Mathew, R.J., Papangelakis, V.G., Guerra, E., 2010. Interfacial phenomena in the sulfur-polytetrafluoroethylene system under hydrothermal conditions. *Miner. Eng.* 23, 1113–1119.

Matijević, E., Scheiner, P., 1978. Ferric hydrous oxide sols: III. Preparation of uniform particles by hydrolysis of Fe(III)-chloride, -nitrate, and -perchlorate solutions. *J. Colloid Interface Sci.* 63, 509–524.

Matsumoto, S., Koga, T., Fukai, K., Nakatani, S., 1980. Production of acicular ferric oxide. US4202871A.

Matsumoto, S., Koga, T., Fukai, K., Yamamoto, H., 1983. Method of producing single crystalline, acicular α -ferric oxide. US4414196A.

Matsushima, T., 1959. Viscosity of liquid sulfur. *Sci. Repts. Res. Inst., Tohoku Univ., Ser. A* 11, 474–481.

May, A., Sjöberg, J.J., Baglin, E.G., 1973. Synthetic argentojarosite. Physical properties and thermal behavior. *Am. Mineral.* 58, 936–941.

- McBriarty, M.E., Stubbs, J.E., Eng, P.J., Rosso, K.M., 2019. Reductive dissolution mechanisms at the hematite-electrolyte interface probed by *in Situ* X-ray scattering. *J. Phys. Chem. C* 123, 8077–8085.
- McCammion, C., 1995. Mössbauer spectroscopy of minerals, in: *Mineral physics and crystallography: A handbook of physical constants*. American Geophysical Union, pp. 332–347.
- McCarty, D.K., Moore, J.N., Marcus, W.A., 1998. Mineralogy and trace element association in an acid mine drainage iron oxide precipitate; comparison of selective extractions. *Appl. Geochemistry* 13, 165–176.
- McDonald, R.G., Muir, D.M., 2007a. Pressure oxidation leaching of chalcopyrite. Part I. Comparison of high and low temperature reaction kinetics and products. *Hydrometallurgy* 86, 191–205.
- McDonald, R.G., Muir, D.M., 2007b. Pressure oxidation leaching of chalcopyrite. Part II: Comparison of medium temperature kinetics and products and effect of chloride ion. *Hydrometallurgy* 86, 206–220.
- McKeague, J.A., Day, J.H., 1966. Dithionite- and oxalate-extractable Fe and Al as aids in differentiating various classes of soils. *Can. J. Soil Sci.* 46, 13–22.
- McNamara, J.H., Ahrens, W.A., Franek, J.G., 1980. A hydrometallurgical process for the extraction of copper. *CIM Bull.* 73, 201–204.
- Mehra, O.P., Jackson, M.L., 1960. Iron oxide removal from soils and clays by a dithionite-citrate system buffered with sodium bicarbonate, in: *Proceeding of 7th National Conference on Clays and Clay Minerals*. Washington, pp. 317–327.
- Mellor, J.W., 1932. *A comprehensive treatise on inorganic and theoretical chemistry*, Vol. XII. Longmans, Green and Co., London.

- Meng, X., Korfiatis, G.P., Christodoulatos, C., Bang, S., 2001. Treatment of arsenic in Bangladesh well water using a household co-precipitation and filtration system. *Water Res.* 35, 2805–2810.
- Meyer, B., 1964. Solid allotropes of sulfur. *Chem. Rev.* 64, 429–451.
- Michel, F.M., Ehm, L., Antao, S.M., Lee, P.L., Chupas, P.J., Liu, G., Strongin, D.R., Schoonen, M., Phillips, B.L., Parise, J.B., 2007. The structure of ferrihydrite, a nanocrystalline material. *Science* 316, 1726–1729.
- Mielczarek, E.V., McGrayne, S.B., 2000. *Iron, nature's universal element: Why people need iron and animals make magnets.* Rutgers university press, London.
- Miller, D.M., Dew, D.W., Norton, A.E., Cole, P.M., Benetis, G., 1997. The BioNIC process: description of the process and presentation of pilot plant results, in: Cooper, W.C., Mihaylov, I. (Eds.), *Proceedings of Nickel Cobalt 97, Vol. II: Hydrometallurgy and Refining.* Sudbury, pp. 369–379.
- Monhemius, J., 1977. Precipitation diagrams for metal hydroxides, sulfides, arsenates and phosphates. *Trans. Inst. Min. Metall.* 86, C202–C206.
- Morales, M.P., González-Carreño, T., Serna, C.J., 1992. The formation of α -Fe₂O₃ monodispersed particles in solution. *J. Mater. Res.* 7, 2538–2545.
- Morniroli, J.P., 2006. Introduction to Electron Diffraction, in: Weirich, T.E., Lábár, J.L., Zou, X. (Eds.), *NATO Science Series II: Mathematics, Physics and Chemistry.* Springer, Dordrecht, pp. 61–72.
- Morniroli, J.P., Steeds, J.W., 1992. Microdiffraction as a tool for crystal structure identification and determination. *Ultramicroscopy* 45, 219–239.
- Mössbauer, R.L., 2000. The discovery of the Mössbauer effect. *Hyperfine Interact.* 126, 1–12.

- Mossbauer, R.L., 1962. Recoilless nuclear resonance absorption of γ -radiation. *Science* 137, 731–738.
- Moyes, J., Sammut, D., Houllis, F., 2002. The Intec copper process: superior and sustainable metals production, in: *Proceedings of ALTA Copper Conference*. Melbourne, pp. 305–328.
- Muir, D.M., 2002. Basic principles of chloride hydrometallurgy, in: Peek, E., Van Weert, G. (Eds.) *Proceedings of 32nd annual Hydrometallurgical meeting : Chloride Metallurgy II*. Montreal, pp. 759–791.
- Mullin, J.W., 1993. *Crystallization*, 3rd Ed. Butterworth–Heinemann, Oxford.
- Murad, E., 1988. The Mössbauer spectrum of “well”-crystallized ferrihydrite. *J. Magn. Magn. Mater.* 74, 153–157.
- Murad, E., Cashion, J., 2011. *Mössbauer spectroscopy of environmental materials and their industrial utilization*. Springer, US.
- Murray, R.C., Cubicciotti, D., 1983. Thermodynamics of aqueous sulfur species to 300°C and potential-pH diagrams. *J. Electrochem. Soc.* 130, 866–869.
- Neaman, A., Waller, B., Mouele, F., Trolard, F., Bourrie, G., 2004. Improved methods for selective dissolution of manganese oxides from soils and rocks. *Eur. J. Soil Sci.* 55, 47–54.
- Nicoud, L., Licordari, F., Myerson, A.S., 2018. Estimation of the solubility of metastable polymorphs: A critical review. *Cryst. Growth Des.* 18, 7228–7237.
- Nyman, B., Aaltonen, A., Hultholm, S.E., Karpale, K., 1992. Application of new hydrometallurgical developments in the Outokumpu HIKO process. *Hydrometallurgy* 29, 461–478.
- Nyvt, J., 1995. The Ostwald rule of stages. *Cryst. Res. Technol.*, 30, 443–449.
- Ocaña, M., Morales, M.P., Serna, C.J., 1995. The growth mechanism of α -Fe₂O₃ ellipsoidal

- particles in solution. *J. Colloid Interface Sci.* 171, 85–91.
- Oenslager, G., 1933. Organic accelerators. *Ind. Eng. Chem.* 25, 232–237.
- Owusu, G., 1993. The role of surfactants in the leaching of zinc sulphide minerals at temperatures above the melting point of sulphur. The University of British Columbia.
- Ozaki, M., Kratochvil, S., Matijević, E., 1984. Formation of monodispersed spindle-type hematite particles. *J. Colloid Interface Sci.* 102, 146–151.
- Paikaray, S., Peiffer, S., 2012. Abiotic schwertmannite transformation kinetics and the role of sorbed As(III). *Appl. Geochemistry* 27, 590–597.
- Palmer, C.M., Johnson, G.D., 2005. The Activox process: Growing significance in the nickel industry. *J. Miner. Met. Mater. Soc.* 57, 40–47.
- Papangelakis, V.G., Blakey, B.C., Liao, H., 1994. Hematite solubility in sulphate process solutions, in: *Proceedings of International Symposium on Hydrometallurgy*. Cambridge, pp. 159–175.
- Parfitt, R.L., Childs, C.W., 1988. Estimation of forms of iron and aluminum - A review, and analysis of contracting soils by dissolution and Mössbauer methods. *Aust. J. Soil Res.* 26, 121–144.
- Park, B., Dempsey, B.A., 2005. Heterogeneous oxidation of Fe(II) on ferric oxide at neutral pH and a low partial pressure of O₂. *Environ. Sci. Technol.* 39, 6494–6500.
- Parkhurst, D.L., Appelo, C.A.J., 1999. User's Guide To PHREEQC (version 2) - A computer program for speciation, batch-reaction, one-dimensional transport, and inverse geochemical calculations, in: *U.S. Geological Survey Water-Resources Investigations Report 99-4259*. USGS, Denver.
- Pedersen, H.D., Postma, D., Jakobsen, R., Larsen, O., 2005. Fast transformation of iron

- oxyhydroxides by the catalytic action of aqueous Fe(II). *Geochim. Cosmochim. Acta* 69, 3967–3977.
- Peters, E., 1976. Direct Leaching of sulfides: Chemistry and applications. *Metall. Trans. B* 7, 505–517.
- Phillips, E.J.P., Lovley, D.R., 1987. Determination of Fe(III) and Fe(II) in oxalate extracts of sediment. *Soil Sci. Soc. Am. J.* 51, 938.
- Poulton, S.W., Canfield, D.E., 2005. Development of a sequential extraction procedure for iron: implications for iron partitioning in continentally derived particulates. *Chem. Geol.* 214, 209–221.
- Pourbaix, M., 1966. Atlas of electrochemical equilibria in aqueous solutions. Pergamon Press, Oxford.
- Punnoose, A., Phanthavady, T., Seehra, M.S., Shah, N., Huffman, G.P., 2004. Magnetic properties of ferrihydrite nanoparticles doped with Ni, Mo, and Ir. *Phys. Rev. B - Condens. Matter Mater. Phys.* 69.
- Qiang, Z., Chang, J.H., Huang, C.P., 2003. Electrochemical regeneration of Fe²⁺ in Fenton oxidation processes. *Water Res.* 37, 1308–1319.
- Rea, B.A., Davis, J.A., Waychunas, G.A., 1994. Studies of the reactivity of the ferrihydrite surface by Iron Isotopic Exchange and Mössbauer Spectroscopy. *Clays Clay Miner.* 42, 23–34.
- Raiswell, R., Canfield, D.E., Berner, R. a, 1994. A comparison of iron extraction methods for the determination of degree of pyritisation and the recognition of iron-limited pyrite formation. *Chem. Geol.* 111, 101–10.
- Reeves, N.J., Mann, S., 1991. Influence of inorganic and organic additives on the tailored synthesis of iron oxides. *J. Chem. Soc. Faraday Trans.* 87, 3875.

- Reid, M., 2005. Hematite Solubility in H₂SO₄ from 130-170°C and 230-270°C. The University of Toronto.
- Reid, M., Papangelakis, V.G., 2006. New data on hematite solubility in sulphuric acid solutions from 130 to 270°C., in: Proceedings of 3rd International Symposium on Iron Control in Hydrometallurgy. Montreal, pp. 673–686.
- Rhoton, F.E., Bigham, J.M., Norton, L.D., Smeck, N.E., 1981. Contribution of magnetite to oxalate-extractable iron in soils and sediments from the Maumee river basin of Ohio. Soil Sci. Soc. Am. J. 45, 645.
- Rickard, T.A., 1932. Man and metals. Whittlesey House, McGraw Hill.
- Riveros, P.A., Dutrizac, J.E., 1997. The precipitation of hematite from ferric chloride media. Hydrometallurgy 46, 85–104.
- Riveros, P.A., Dutrizac, J.E., Spencer, P., 2001. Arsenic disposal practices in the metallurgical industry. Can. Metall. Q. 40, 395–420.
- Robins, R.G., 1967. Hydrothermal precipitation in solutions of thorium nitrate, ferric nitrate and aluminum nitrate. J. Inorg. Nucl. Chem. 29, 431–435.
- Rolia, E., Dutrizac, J.E., 1984. The determination of free acid in zinc processing solutions. Can. Metall. Q. 23, 159–167.
- Rosen, M.J., 2004. Surfactants and interfacial phenomena, 3rd Ed. J. Wiley and Sons, New Jersey.
- Rothstein, Y., 2006. Spectroscopy of jarosite minerals and implications for the mineralogy of Mars. Mount Holyoke College, US.
- Rubisov, D.H., Papangelakis, V.G., 1999. The effect of acidity “at temperature” on the morphology of precipitates and scale during sulphuric acid pressure leaching of laterites, in: Proceedings of 29th Annual Hydrometallurgy Meeting. Quebec City, pp. 185–203.

- Rubisov, D.H., Papangelakis, V.G., 2000. Sulphuric acid pressure leaching of laterites - speciation and prediction of metal solubilities "at temperature." *Hydrometallurgy* 58, 13–26.
- Ruiz, M.C., Zapata, J., Padilla, R., 2007. Effect of variables on the quality of hematite precipitated from sulfate solutions. *Hydrometallurgy* 89, 32–39.
- Sahu, S.K., Asselin, E., 2011. Characterization of residue generated during medium temperature leaching of chalcopyrite concentrate under CESL conditions. *Hydrometallurgy* 110, 107–114.
- Salomon-de-Friedberg, H., Robinson, T., 2015. Tackling impurities in copper concentrates, in: *Proceedings of ALTA Conference*. Perth, pp. 406–415.
- Salomon-De-Friedberg, H., 2017. Impact of sulfur prills on the handling of elemental sulfur post autoclave discharge in a commercial plant. Personal Communication. Cominco Engineering Services Laboratory, Richmond, BC.
- Salomon-de-Friedberg, H., Jang, H.M., 2015. Process for recovery of copper from arsenic-bearing and/or antimony-bearing copper sulphide concentrates. US20150329937A1.
- Sapieszko, R.S., Matijević, E., 1980. Preparation of well-defined colloidal particles by thermal decomposition of metal chelates. I. Iron oxides. *J. Colloid Interface Sci.* 74, 405–422.
- Sasaki, K., Ootsuka, K., Tozawa, K., 1993. Hydrometallurgical studies on hydrolysis of ferric sulfate solutions at elevated temperatures. II. Equilibrium diagram in the system, ferric oxide-sulfuric acid, ($\text{Fe}_2\text{O}_3\text{-SO}_3\text{-H}_2\text{O}$), at elevated temperatures. *Shigen to Sozai* 109, 871–877.
- Sasowsky, I.D., Foos, A., Miller, C.M., 2000. Lithic controls on the removal of iron and remediation of acidic mine drainage. *Water Res.* 34, 2742–2746.
- Schindler, P., Michaelis, W., Feitknecht, W., 1963. Solubility products of metal oxides and hydroxides. The solubility of aged ferric hydroxide precipitates. *Helv. Chim. Acta* 46, 444–449.

- Schmidt, M., 1970. Sulfur-containing polymers. *Inorg. Macromol. Rev.* 1, 101–113.
- Schulze, D.G., 1981. Identification of soil iron oxide minerals by differential X-ray diffraction. *Soil Sci. Soc. Am. J.* 45, 437.
- Schweitzer, F.W., Livingstone, R., 1978. Duval's Clear hydrometallurgical process, in: Parker, P. (Ed.), *Chloride Electrometallurgy*. AIME, New York, pp. 221–228.
- Schwertmann, U., 1991. Solubility and dissolution of iron-oxides. *Plant Soil* 130, 1–25.
- Schwertmann, U., Cambier, P., Murad, E., 1985. Properties of goethites of varying crystallinity. *Clays Clay Miner.* 33, 369–378.
- Schwertmann, U., Cornell, R.M., 2000. *Iron oxides in the laboratory: Preparation and characterization*. J.Wiley and Sons, New York.
- Schwertmann, U., Friedl, J., Stanjek, H., 1999. From Fe(III) ions to ferrihydrite and then to hematite. *J. Colloid Interface Sci.* 209, 215–223.
- Schwertmann, U., Murad, E., 1983. Effect of pH on the formation of goethite and hematite from ferrihydrite. *Clays Clay Miner.* 31, 277–284.
- Schwertmann, U., Schulze, D.G., Murad, E., 1982. Identification of ferrihydrite in soils by dissolution kinetics, differential x-ray diffraction, and Mössbauer spectroscopy. *Soil Sci. Soc. Am. J.* 46, 869.
- Sergeeva, E.I., Suleimenov, O.M., Evstigneev, A.V., Khodakovskiy, I.L., 1999. Solubility of hematite, Fe₂O₃ at 200°C and the standard entropy of Fe³⁺ ion in aqueous solution. *Geochemistry Int.* 1218–1229.
- Shannon, R.D., 1976. Revised effective ionic radii and systematic studies of interatomic distances in halides and chalcogenides. *Acta Crystallogr. Sect. A Cryst. Physics, Diffraction, Theor. Gen. Crystallogr.* A32, 751–767.

- Shaw, R., Vance, S., Illescas, J., Dreisinger, D., Wassink, B., 2006. Ion exchange for iron impurity control in the base metal industry, in: Proceedings of 3rd International Symposium on Iron Control in Hydrometallurgy, Montreal, pp. 757–769.
- Shaw, S., Pepper, S.E., Bryan, N.D., Livens, F.R., 2005. The kinetics and mechanisms of goethite and hematite crystallization under alkaline conditions, and in the presence of phosphate. *Am. Mineral.* 90, 1852–1860.
- Sherman, D.M., 1987. Molecular orbital (SCF- $X\alpha$ -SW) theory of metal-metal charge transfer processes in minerals. I. Application to $Fe^{2+} \rightarrow Fe^{3+}$ charge transfer and “electron delocalization” in mixed-valence iron oxides and silicates. *Phys. Chem. Miner.* 14, 355–363.
- Silva, L.F.O., Sampaio, C.H., Guedes, A., Fdez-Ortiz de Vallejuelo, S., Madariaga, J.M., 2012. Multianalytical approaches to the characterisation of minerals associated with coals and the diagnosis of their potential risk by using combined instrumental microspectroscopic techniques and thermodynamic speciation. *Fuel* 94, 52–63.
- Simándi, L., Barna, T., Szeverenyi, Z., Nemeth, S., 1992. Homogeneous catalytic oxidation of o-substituted anilines with dioxygen in the presence of cobalt and manganese complexes. *Pure Appl. Chem.* 64, 1511–1518.
- Singer, D.A., 2017. Future copper resources. *Ore Geol. Rev.* 86, 271–279.
- Smiley, R.A., 2000. Phenylene and Toluenediamine, in: Ullmann’s encyclopedia of industrial chemistry. Wiley-VCH, Weinheim.
- Smith, S.J., Page, K., Kim, H., Campbell, B.J., Boerio-Goates, J., Woodfield, B.F., 2012. Novel synthesis and structural analysis of ferrihydrite. *Inorg. Chem.* 51, 6421–6424.
- Sofekun, G.O., Evoy, E., Lesage, K.L., Chou, N., Marriott, R.A., 2018. The rheology of liquid elemental sulfur across the λ -transition. *J. Rheol.* 62, 469–476.

- Sohnel, O., Garside, J., 1992. *Precipitation: Basic principles and industrial applications*. Butterworth-Heinemann, Oxford.
- Squire, E.N., 1975. Synthesis of aromatic amines by reaction of aromatic compounds with ammonia. 3929889A.
- Steeds, J.W., Morniroli, J.P., 1992. Selected area electron diffraction (SAED) and convergent beam electron diffraction (CBED). *Rev. Mineral. Geochemistry* 27, 37–84.
- Steeffel, C.I., Appelo, C.A.J., Arora, B., Jacques, D., Kalbacher, T., Kolditz, O., Lagneau, V., Lichtner, P.C., Mayer, K.U., Meeussen, J.C.L., Molins, S., Moulton, D., Shao, H., Šimůnek, J., Spycher, N., Yabusaki, S.B., Yeh, G.T., 2015. Reactive transport codes for subsurface environmental simulation. *Comput. Geosci.* 19 (3), 445–478.
- Steel, A., Hawboldt, K., Khan, F., 2010. Assessment of minerals and iron-bearing phases present in hydrometallurgical residues from a nickel sulfide concentrate and availability of residue associated metals. *Hydrometallurgy* 101, 126–134.
- Studel, R., Eckert, B., Okazaki, R., Takeda, N., Tokitoh, N., Wong, M.W., 2003. *Elemental sulfur and sulfur-rich compounds I*. Springer-Verlag, Berlin.
- Steyl, J.D., 2012. *Simulating the medium temperature chalcopyrite oxidation system in batch and continuous autoclaves*. Stellenbosch University.
- Stone, A.T., Morgan, J.J., 1987. Reductive dissolution of metal oxides., in: *Aquatic Surface Chemistry*. Wiley, pp. 221–254.
- Stumm, W., 1992. *Chemistry of the solid-water interface: Processes at the mineral-water and particle-water interface in natural systems*. J.Wiley and Sons, New York.
- Stumm, W., Furrer, G., Wieland, E., Zinder, B., 1985. The effects of complex-forming ligands on the dissolution of oxides and aluminosilicates. *NATO ASI Ser. Ser. C Math. Phys. Sci.* 149,

55–74.

Stumm, W., Morgan, J.J., 1996. Aquatic chemistry: Chemical equilibria and rates in natural waters, Environmental science and technology. J. Wiley and Sons, New York.

Sugimoto, T., Itoh, H., Mochida, T., 1998. Shape control of monodisperse hematite particles by organic additives in the gel-sol system. *J. Colloid Interface Sci.* 205, 42–52.

Sugimoto, T., Khan, M., Muramatsu, A., 1993. Preparation of monodisperse peanut-type α -Fe₂O₃ particles from condensed ferric hydroxide gel. *Colloids Surfaces A Physicochem. Eng. Asp.* 70, 167–169.

Sugimoto, T., Khan, M.M., Muramatsu, A., Itoh, H., 1993a. Formation mechanism of monodisperse peanut-type α -Fe₂O₃ particles from condensed ferric hydroxide gel. *Colloids Surfaces A Physicochem. Eng. Asp.* 79, 233–247.

Sugimoto, T., Muramatsu, A., 1996. Formation mechanism of monodispersed α -Fe₂O₃ particles in dilute FeCl₃ solutions. *J. Colloid Interface Sci.* 184, 626–638.

Sugimoto, T., Muramatsu, A., Sakata, K., Shindo, D., 1993. Characterization of hematite particles of different shapes. *J. Colloid Interface Sci.* 158(2), 420–428.

Sugimoto, T., Sakata, K., Muramatsu, A., 1993b. Formation mechanism of monodisperse pseudocubic α -Fe₂O₃ particles from condensed ferric hydroxide Gel. *J. Colloid Interface Sci.* 159, 372–382.

Sugimoto, T., Wang, Y., 1998. Mechanism of the shape and structure control of monodispersed α -Fe₂O₃ particles by sulfate ions. *J. Colloid Interface Sci.* 207, 137–149.

Sulzberger, B., Suter, D., Siffert, C., Banwart, S., Stumm, W., 1989. Dissolution of Fe(III) (hydr)oxides in natural waters; laboratory assessment on the kinetics controlled by surface coordination. *Mar. Chem.* 28, 127–144.

- Sung, W., Morgan, J.J., 1980. Kinetics and product of ferrous iron oxygenation in aqueous systems. *Environ. Sci. Technol.* 14, 561–568.
- Tamura, Y., Ito, K., Katsura, T., 1983. Transformation of γ -FeO(OH) to Fe₃O₄ by adsorption of iron(II) ion on γ -FeO(OH). *J. Chem. Soc., Dalt. Trans.* 189–194.
- Tamura, H., Goto, K., Nagayama, M., 1976. The effect of ferric hydroxide on the oxygenation of ferrous ions in neutral solutions. *Corros. Sci.* 16, 197–207.
- Taube, H., 1952. Rates and mechanisms of substitution in inorganic complexes in solution. *Chem. Rev.* 50, 69–126.
- Taylor, A., Jansen, M.L., 1999. Hydrometallurgical treatment fo copper sulphides – are we on the brink?, in: *Proceedings of ALTA Copper Conference*. Perth, pp. 6–24
- Taylor, R.M., 1959. Amorphous iron oxide in soils. *J. Soil Sci.* 10, 309–315.
- Tessier, A., Campbell, P.G.C., Bisson, M., 1979. Sequential extraction procedure for the speciation of particulate trace metals. *Anal. Chem.* 51, 844–851.
- Thomas, N.T., Nobe, K., 1969. Electrochemical behavior of titanium effect of pH and chloride ions. *J. Electrochem. Soc.* 116, 1748–1751.
- Torrent, J., Guzman, A.R., 1982. Crystallization of Fe(III)-oxides from ferrihydrite in salt solutions: osmotic and specific ion effects. *Clay Miner.* 17, 463–469.
- Towe, K.M., Bradley, W.F., 1967. Mineralogical constitution of colloidal “hydrous ferric oxides”. *J. Colloid Interface Sci.* 24, 384–392.
- Townsend, H.E., 1970. Potential-pH diagrams at elevated temperature for the system Fe-H₂O. *Corros. Sci.* 10, 343–358.
- Townsend, M., Longworth, G., Roudaut, E., 1986. Triangular-spin, kagome plane in jarosites.

- Phys. Rev. B 33, 4919–4926.
- Tozawa, K., Sasaki, K., 1986. Effect of coexisting sulphates on precipitation of ferric oxide from ferric sulphate solutions at elevated temperatures, in: Dutrizac, J.E. (Ed.), *Iron Control in Hydrometallurgy*. New York, pp. 454–476.
- Tronc, E., Belleville, P., Jolivet, J.P., Livage, J., 1992. Transformation of ferric hydroxide into spinel by Fe(II) adsorption. *Langmuir* 8, 313–319.
- Tufekci, N., Sarikaya, H.Z., Ozturk, I., 2000. An experimental study on iron removal with ferric sludge recycling. *Water Sci. Technol.* 42.
- Umetsu, Y., Tozawa, K., Sasaki, K., 1977. The hydrolysis of ferric sulfate solutions at elevated temperatures. *Can. Metall. Q.* 16, 111–117.
- Vandenbergh, R.E., De Grave, E., 2013. Application of Mössbauer Spectroscopy in Earth Sciences, in: *Mössbauer Spectroscopy*. Springer-Verlag, Berlin, pp. 91–97.
- Van Der Woude, J.H.A., Verhees, P., De Bruyn, P.L., 1983. Formation of colloidal dispersions from supersaturated iron(III) nitrate solutions. II. Kinetics of growth at elevated temperatures. *Colloids and Surfaces* 8, 79–92.
- Vizolyi, A., Veltman, H., Warren, I.H., Mackiw, V.N., 1967. Copper and elemental sulphur from chalcopyrite by pressure leaching. *JOM* 19, 52–59.
- Vogel, A.I., Furniss, B.S., 1989. *Vogel's textbook of practical organic chemistry*. Longman, New York.
- Vogt, P.F., Gerulis, J.J., 2000. Amines, aromatic, in: *Ullmann's encyclopedia of industrial chemistry*. Wiley-VCH, Weinheim, pp. 699–718.
- Vračar, R.Ž., Cerović, K.P., 1997. Kinetics of oxidation of Fe(II) ions by gaseous oxygen at high temperatures in an autoclave. *Hydrometallurgy* 44, 113–124.

- Vu, H.P., Shaw, S., Brinza, L., Benning, L.G., 2010. Crystallization of hematite (α -Fe₂O₃) under alkaline condition: The effects of Pb. *Cryst. Growth Des.* 10, 1544–1551.
- Wagman, D.D. et al., 1982. The NBS tables of chemical thermodynamic properties. American Institute of Physics, New York.
- Watanabe, T., Hirayama, T., Fukui, S., 1989. Phenazine derivatives as the mutagenic reaction product from o- or m-phenylenediamine derivatives with hydrogen peroxide. *Mutat. Res.* 227, 135–145.
- WD40. Retrieved from <https://en.wikipedia.org/wiki/WD-40>
- Weidenbach, M., Dunn, G., Teo, Y., 2016. Removal of impurities from copper sulfide mineral concentrates, in: *Proceedings of ALTA Conference*. Perth, pp. 335–351.
- Weigert, F.J., 1981. O-Phenylenediamine from sulfur, ammonia, and cyclohexane. *J. Org. Chem.* 46, 1936–1937.
- Williams, A.G.B., Scherer, M.M., 2004. Spectroscopic evidence for Fe(II)-Fe(III) electron transfer at the iron oxide-water interface. *Environ. Sci. Technol.* 38, 4782–4790.
- Wills, A.S., Harrison, A., Ritter, C., Smith, R.I., 2000. Magnetic properties of pure and diamagnetically doped jarosites: Model kagomé antiferromagnets with variable coverage of the magnetic lattice. *Phys. Rev. B* 61, 6156–6169.
- Woodfield, B.F., Liu, S., Boerio-Goates, J., Liu, Q., 2007. Preparation of uniform nanoparticles of ultra-high purity metal oxides, mixed metal oxides, metals, and metal alloys. EP1986804B1.
- Worthington, M.J.H., Kucera, R.L., Albuquerque, I.S., Gibson, C.T., Sibley, A., Slattery, A.D., Campbell, J.A., Alboaiji, S.F.K., Muller, K.A., Young, J., Adamson, N., Gascooke, J.R., Jampaiah, D., Sabri, Y.M., Bhargava, S.K., Ippolito, S.J., Lewis, D.A., Quinton, J.S., Ellis, A. V., Johs, A., Bernardes, G.J.L., Chalker, J.M., 2017. Laying waste to mercury: inexpensive

- sorbents made from sulfur and recycled cooking oils. *Chem. - A Eur. J.* 23(64), 16219–16230.
- Xia, G.X., Li, J.J., Shi, H.J., Yu, K.N., Gao, C.L., 1987. Preliminary studies on the physical chemistry of the acid pressure leaching of ZnS concentrates, in: Davies, G.A. (Ed.), *Separation Process in Hydrometallurgy*. Ellis Horwood, London, pp. 125–132.
- Yee, N., Shaw, S., Benning, L.G., Nguyen, T.H., 2006. The rate of ferrihydrite transformation to goethite via the Fe(II) pathway. *Am. Mineral.* 91, 92–96.
- Yishan, Z., Ruiying, A.I., Fengzhen, W., 1989. Solubility of the magnetite + hematite buffer assemblage and iron speciation in sodium chloride solutions at 300°C and 500 bars. *Geochim. Cosmochim. Acta* 53, 1875–1882.
- Yue, G., 2015. Speciation of the sulfuric acid-ferric sulfate-ferrous sulfate-water system and its application to chalcopyrite leaching kinetics up to 150°C. The University of British Columbia.
- Yue, G., Guezennec, A.-G., Asselin, E., 2016. Extended validation of an expression to predict ORP and iron chemistry: Application to complex solutions generated during the acidic leaching or bioleaching of PCBs, *Hydrometallurgy* 164, 334-342.
- Yue, G., Zhao, L., Olvera, O., Asselin, E., 2014. Speciation of the H₂SO₄-Fe₂(SO₄)₃-FeSO₄-H₂O system and development of an expression to predict the redox potential of the Fe³⁺/Fe²⁺ couple up to 150°C, *Hydrometallurgy* 147-148, 196-209.
- Zelany, L.W., Jackson, M.L., Lim, C.H., 1986. Oxides, hydroxides, and aluminosilicates, in: Klute, A. (Ed.), *Methods of Soil Analysis: Physical and Mineralogical Methods*. American Society of Agronomy, Inc., Madison, pp. 101–150.
- Žic, M., Ristić, M., Musić, S., 2011. Monitoring the hydrothermal precipitation of α-Fe₂O₃ from concentrated Fe(NO₃)₃ solutions partially neutralized with NaOH. *J. Mol. Struct.* 993, 115-119.

Appendices

Appendix A: Multi-acid digestion procedure

Equipment and acids required:

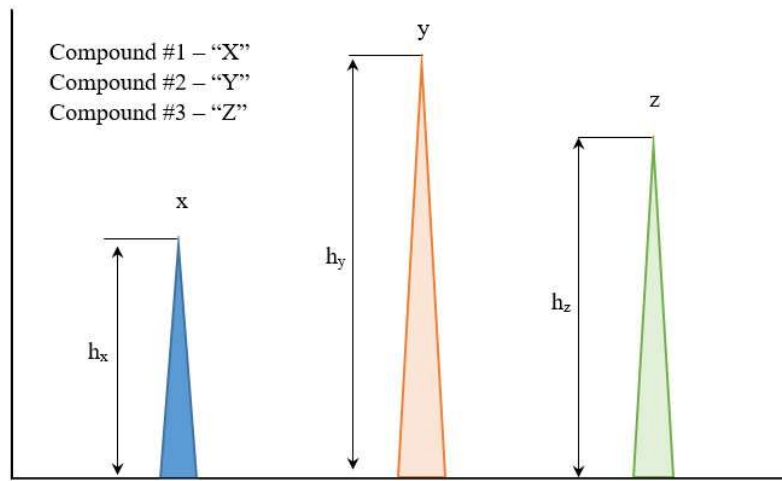
1. Analytical balance (0.0001 g precision)
2. Weigh-boat and spatula
3. 250 ml Teflon beakers and Teflon watch glasses
4. 100 ml volumetric flasks and rubber stoppers
5. Hotplate
6. Perchloric acid fume hood
7. Glass test tubes and test tube racks
8. Plastic funnel
9. Concentrated Hydrochloric acid (HCl) – ACS grade
10. Concentrated Nitric acid (HNO₃) - ACS grade
11. Concentrated perchloric acid (HClO₄) - ACS grade
12. Concentrated hydrofluoric acid (HF) - ACS grade
13. De-ionized distilled Water

Digestion test procedure:

1. Collect and label required Teflon beakers
2. Plug in the hot plate and set the dial setting at medium-high (~ 3.5) heat
3. Pre-heat the hotplate for about 15 minutes
4. Using an analytical balance weigh 0.20-0.50g (depending on concentration) of sample and/or standard
5. Record the mass to 4 decimal places

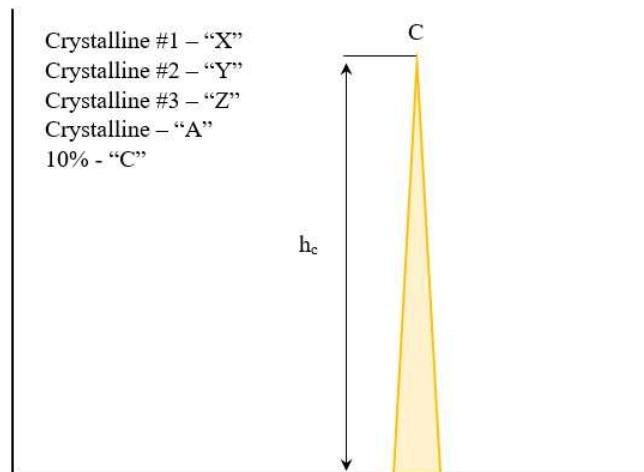
6. Add sample into 250 ml Teflon beakers
7. Turn on scrubber, ensure the perchloric acid fume hood air flow is in the proper range
8. Add 10 ml HCl and digest covered for 5 minutes, take off hot plate and cool down.
9. Rinse sides of the beaker with de-ionized distilled water
10. Add 10 ml HNO₃, 10 ml HClO₄ and 2 ml HF into Teflon beaker in order and digest covered with Teflon watch glass for 30 minutes.
11. Remove cover and rinse with de-ionized distilled water and boil down to low volume (~5ml) with thick fumes of HClO₄ evolving
12. Remove beaker off the hot plate and cool for 15 minutes
13. Add 3 ml HCl and 10 ml HNO₃ into the Teflon beaker
14. Cover with a Teflon watch glass and digest until the brown fumes disappear (~15 min)
15. Cool sample slightly and add ~30-40 ml of de-ionized distilled water
16. Boil for an additional 15 minutes.
17. Remove the beaker off the hot plate and cool to room temperature
18. Turn off scrubber
19. Transfer the solutions to 100 ml volumetric flasks quantitatively using de-ionized distilled water and a plastic funnel
20. Dilute to the mark with de-ionized distilled water, plug stopper and shake well
21. Transfer solution into labeled test tubes
22. Submit samples for analysis to ICP technician

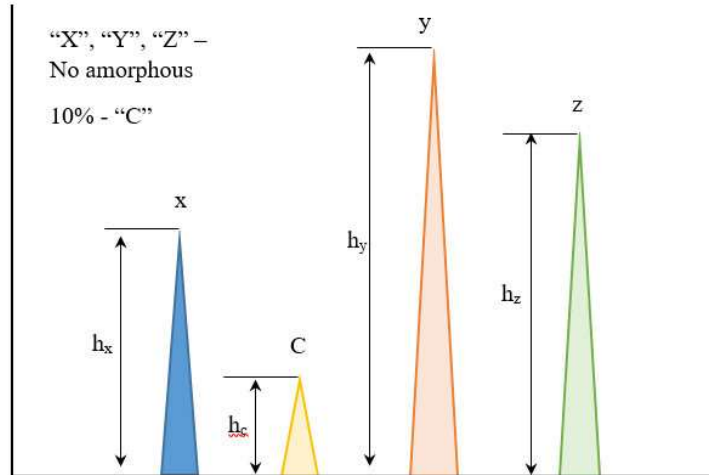
Appendix B: X-Ray amorphous determination scheme



$$h = h_x + h_y + h_z$$

$$\text{Concentration of "X"} = \frac{h_x}{h_x + h_y + h_z}$$





$$\text{Concentration of "C"} = \frac{h_c}{h_c + h_x + h_y + h_z} = 10\%$$

$$>5 - \frac{5}{0.85} \rightarrow 5 - \text{Cry X}$$

$$>50 - \frac{50}{0.85} \rightarrow 50 - \text{Cry Y}$$

$$>30 - \frac{30}{0.85} \rightarrow 30 - \text{Cry Z}$$

>100 \longrightarrow 15% Amorphous + 10% C

$$\text{Concentration of "C"} = \frac{h_c}{h_A + h_c + h_x + h_y + h_z}$$

$$h_c = 10\%$$

$$h_A = 15\%$$

$$h_x + h_y + h_z = 85\%$$

$$\text{Concentration of (x + y + z)} = \frac{h_x + h_y + h_z}{h_A + h_c + h_x + h_y + h_z} = 85\%$$

$$\text{Concentration of "C"} = \frac{h_c}{h_c+h_x+h_y+h_z} = 15\%$$

However, in reality, the concentration of "C" is 10%. Therefore, assuming that the amorphous material was crystalline and had given a peak of height h_A :

$$\text{The concentration of "C"} = \frac{h_c}{(h_c+h_x+h_y+h_z)+h_A} = 10\%$$

$$h_c = 0.15 (h_c + h_x + h_y + h_z)$$

$$h_c = 0.10 (h_c + h_x + h_y + h_z + h_A)$$

$$0.15 (h_c + h_x + h_y + h_z) = 0.10 (h_c + h_x + h_y + h_z + h_A)$$

$$0.15 (h_c + h_x + h_y + h_z) = 0.1 h_A$$

$$h_A = \frac{0.05}{0.1} (h_c + h_x + h_y + h_z)$$

$$\text{The concentration "A"} = \frac{h_A}{h_c+h_x+h_y+h_z+h_A}$$

Appendix C: Calculations for HaHC soluble and Cu extraction

The HaHC Soluble phase in Table 6.4 is calculated by summing the individual results and dividing this sum by the number of repeats (8 times)

Repeat no.	HaHC Soluble (wt%)					
	Test 1	Test 2	Test 3	Test 4	Test 5	Test 6
1	16.6	16.2	15.5	14.8	14.6	13.4
2	16.1	15.3	15.6	14.2	14.0	12.8
3	17.1	16.5	15.9	14.4	14.2	13.8
4	16.7	15.7	15.8	15.2	15.0	12.9
5	17.1	16.3	14.7	15.0	14.8	13.2
6	17.1	16.1	15.6	14.6	14.6	13.8
7	16.1	16.0	15.4	15.4	15.2	13.6
8	16.2	16.2	15.5	14.8	14.6	13.4
Average HaHC	16.6	16.0	15.5	14.8	14.6	13.4
Std Dev.	0.5	0.4	0.4	0.4	0.4	0.4
R. Std Dev.	3.0	2.6	2.6	2.9	2.9	3.1

The relative standard deviation (R. Std. Dev.) is expressed in percent and is obtained by multiplying the standard deviation by 100 and dividing this product by the average. $R. Std. Dev. = 100 * (Std Dev.) / (Average)$

The Cu extraction Table 6-4 is calculated by summing the individual results and dividing this sum by the number of repeats (3 times)

Repeat no	Cu Extn (%)					
	Test 1	Test 2	Test 3	Test 4	Test 5	Test 6
1	97.52	98.12	98.19	98.37	98.50	98.48
2	97.48	98.08	98.18	98.42	98.48	98.48
3	97.52	98.12	98.22	98.38	98.52	98.51
Average Cu extn.	97.52	98.11	98.20	98.39	98.50	98.49
Std Dev.	0.02	0.02	0.02	0.03	0.02	0.02
R. Std Dev.	0.02	0.02	0.02	0.03	0.02	0.02

Appendix D: X-Ray spectrum of ferrihydrite

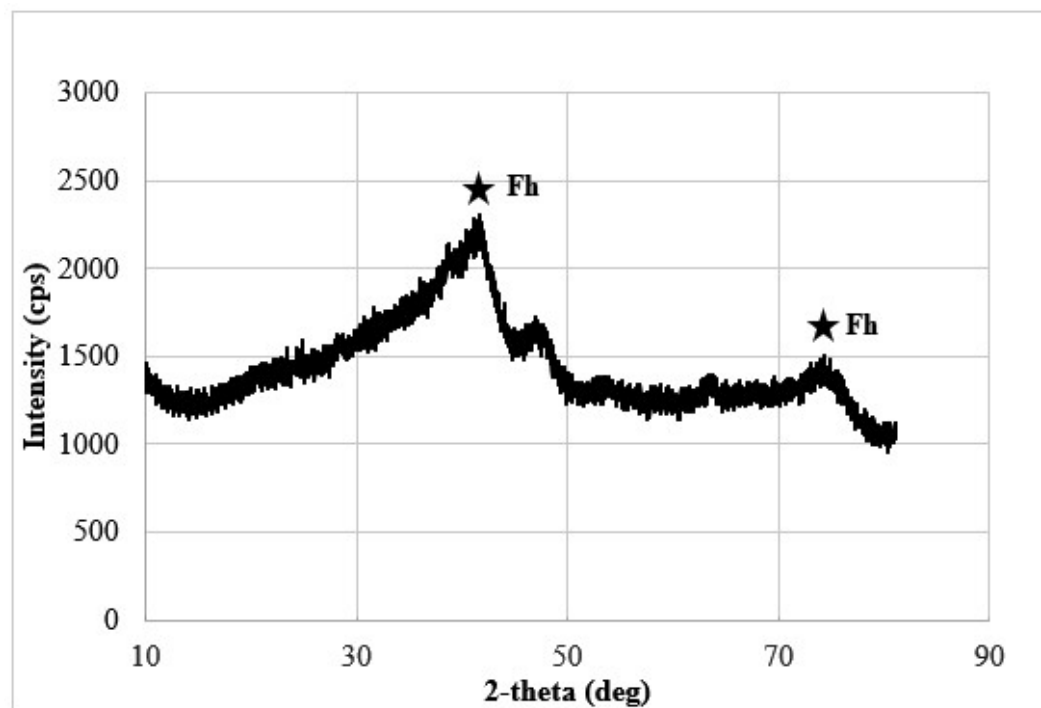


Figure D1: X-ray spectrum of 2 line-ferrihydrite (Fh) residue collected at $t = 0$, $T = 150^{\circ}\text{C}$ from a 10 g/L sulfuric acid – 12 g/L chloride solution

Appendix E: Ferrihydrite solubility

Solution Sample Volume (ml)

Sample ID	A0	A5	A10	Cu-A10	Ni-A10	A15	A20	A25
T0	4.0	5.2	5.4	4.8	6.2	5.2	5.0	5.2
T30	5.4	5.0	5.2	5.2	5.4	5.4	5.3	5.6
T60	5.4	5.8	6.0	6.4	5.6	6.2	5.8	5.6
T90	5.4	5.2	5.0	5.6	6.0	5.4	5.6	5.4
T120	5.0	5.2	5.8	5.4	6.2	5.4	5.4	5.2
T180	5.2	5.8	6.0	6.2	5.2	5.8	5.4	5.4
T240	5.0	6.0	6.0	5.6	5.6	5.2	5.6	5.0
T300	5.4	5.8	6.2	6.2	5.2	5.8	6.2	6.0
T360	5.4	5.2	6.0	5.8	5.2	5.4	5.2	5.4

Calculated Fe in Solution (g/L) by Mass Balance

Time (min)	A0	A5	A10	Cu-A10	Ni-A10	A15	A20	A25
0	0.0030	0.1650	0.7560	0.7130	0.5010	1.3400	3.2800	4.6600
30	0.0118	0.0994	0.4810	0.3720	0.4020	1.4500	2.2400	3.6200
60	0.0082	0.0477	0.2830	0.1580	0.2230	0.8210	1.5200	2.7400
90	0.0051	0.0391	0.1970	0.1490	0.1410	0.6060	1.2600	2.2000
120	0.0024	0.0351	0.1710	0.1260	0.1260	0.5390	1.0900	1.9900
180	0.0018	0.0324	0.1530	0.1130	0.1140	0.4810	1.0400	1.8100
240	0.0022	0.0306	0.1390	0.1040	0.1030	0.4330	0.9620	1.7100
300	0.0019	0.0293	0.1460	0.0944	0.0979	0.4330	0.9380	1.6900
360	0.0017	0.0274	0.1480	0.0881	0.0986	0.4270	0.9220	1.6800

Solution Fe Assay (ppm)

Sample ID	A0	A5	A10	Cu-A10	Ni-A10	A15	A20	A25
T0	3.02	165.0	756	713	501	1340	3280	4660
T30	11.8	99.4	481	372	402	1450	2240	3620
T60	8.24	47.7	283	158	223	821	1520	2740
T90	5.14	39.1	197	149	141	606	1260	2200
T120	2.35	35.1	171	126	126	539	1090	1990
T180	1.80	32.4	153	113	114	481	1040	1810
T240	2.22	30.6	139	104	103	433	962	1710
T300	1.90	29.3	146	94.4	97.9	433	938	1690
T360	1.66	27.4	148	88.1	98.6	427	922	1680

Dissolved Fe (%) in Solution

Time (min)	A0	A5	A10	Cu-A10	Ni-A10	A15	A20	A25
0	0.03	1.38	6.33	5.97	4.19	11.22	27.47	39.02
30	0.10	0.80	3.90	3.02	3.25	11.76	18.17	29.34
60	0.06	0.37	2.22	1.24	1.74	6.43	11.92	21.47
90	0.04	0.29	1.49	1.13	1.06	4.58	9.54	16.65
120	0.02	0.25	1.25	0.92	0.92	3.93	7.96	14.54
180	0.01	0.22	1.07	0.79	0.80	3.38	7.32	12.74
240	0.01	0.20	0.94	0.70	0.69	2.93	6.51	11.59
300	0.01	0.18	0.94	0.61	0.63	2.81	6.09	10.99
360	0.01	0.16	0.92	0.55	0.61	2.66	5.74	10.48

Ferrihydrite Solubility Fe Mass Balance (Initial Acid 0 g/L)

Solutions	sample	Assay	Fe out of the system for sample	Flush	Total Fe out	Volume of Solution in the system	Solution	Residue	Solution	
ID	ml	Fe (ppm)	Fe (mg)	Fe (mg)	Fe (mg)	(ml)	Fe (g)	Fe(g)	Fe (g/L)	
A0	T0	4.0	3.02	0.0121	0.0000	0.0121	484.0	0.0015	5.7885	0.0030
A0	T30	5.4	11.8	0.0637	0.0458	0.1096	466.6	0.0055	5.7829	0.0118
A0	T60	5.4	8.24	0.0445	0.0465	0.0910	449.2	0.0037	5.7791	0.0082
A0	T90	5.4	5.14	0.0278	0.0304	0.0581	431.8	0.0022	5.7768	0.0051
A0	T120	5.0	2.35	0.0118	0.0159	0.0277	414.8	0.0010	5.7758	0.0024
A0	T180	5.2	1.80	0.0094	0.0098	0.0192	397.6	0.0007	5.7751	0.0018
A0	T240	5.0	2.22	0.0111	0.0105	0.0216	380.6	0.0008	5.7742	0.0022
A0	T300	5.4	1.90	0.0103	0.0100	0.0202	363.2	0.0007	5.7735	0.0019
A0	T360	5.4	1.66	0.0090	0.0087	0.0176	345.8	0.0006	5.7729	0.0017

Ferrihydrite Solubility Fe Mass Balance (Initial Acid 5 g/L)

Solutions	sample	Assay	Fe out of the system for sample	Flush	Total Fe out	Volume of Solution in the system	Solution	Residue	Solution	
ID	ml	Fe (ppm)	Fe (mg)	Fe (mg)	Fe (mg)	(ml)	Fe (g)	Fe(g)	Fe (g/L)	
A5	T0	5.2	165.00	0.8580	0.0000	0.8580	482.8	0.0797	5.7095	0.1650
A5	T30	5.0	99.4	0.4970	0.5954	1.0924	465.8	0.0463	5.6621	0.0994
A5	T60	5.8	47.70	0.2767	0.3161	0.5927	448.0	0.0214	5.6401	0.0477
A5	T90	5.2	39.10	0.2033	0.2084	0.4117	430.8	0.0168	5.6229	0.0391
A5	T120	5.2	35.10	0.1825	0.1815	0.3640	413.6	0.0145	5.6080	0.0351
A5	T180	5.8	32.40	0.1879	0.1661	0.3540	395.8	0.0128	5.5948	0.0324
A5	T240	6.0	30.60	0.1836	0.1557	0.3393	377.8	0.0116	5.5829	0.0306
A5	T300	5.8	29.30	0.1699	0.1485	0.3184	360.0	0.0105	5.5720	0.0293
A5	T360	5.2	27.40	0.1425	0.1399	0.2823	342.8	0.0094	5.5624	0.0274

Ferrihydrite Solubility Fe Mass Balance (Initial Acid 10 g/L)

Solutions		sample	Assay	Fe out of the system for sample	Flush	Total Fe out	Volume of Solution in the system	Solution	Residue	Solution
ID		ml	Fe (ppm)	Fe (mg)	Fe (mg)	Fe (mg)	(ml)	Fe (g)	Fe(g)	Fe (g/L)
A10	T0	5.4	756.00	4.0824	0.0000	4.0824	484.6	0.3664	5.4196	0.7560
A10	T30	5.2	481.0	2.5012	1.0000	3.5012	469.4	0.2258	5.5607	0.4810
A10	T60	6.0	283.00	1.6980	2.0000	3.6980	453.4	0.1283	5.6580	0.2830
A10	T90	5.0	197.00	0.9850	3.0000	3.9850	438.4	0.0864	5.6997	0.1970
A10	T120	5.8	171.00	0.9918	4.0000	4.9918	422.6	0.0723	5.7127	0.1710
A10	T180	6.0	153.00	0.9180	5.0000	5.9180	406.6	0.0622	5.7219	0.1530
A10	T240	6.0	139.00	0.8340	6.0000	6.8340	390.6	0.0543	5.7289	0.1390
A10	T300	6.2	146.00	0.9052	7.0000	7.9052	374.4	0.0547	5.7274	0.1460
A10	T360	6.0	148.00	0.8880	8.0000	8.8880	358.4	0.0530	5.7281	0.1480

Ferrihydrite Solubility Fe Mass Balance (Initial Acid 15 g/L)

Solutions		sample	Assay	Fe out of the system for sample	Flush	Total Fe out	Volume of Solution in the system	Solution	Residue	Solution
ID		ml	Fe (ppm)	Fe (mg)	Fe (mg)	Fe (mg)	(ml)	Fe (g)	Fe(g)	Fe (g/L)
A15	T0	5.2	1340.00	6.9680	0.0000	6.9680	484.8	0.6496	5.1334	1.3400
A15	T30	5.4	1450.0	7.8300	1.0000	8.8300	469.4	0.6806	5.1005	1.4500
A15	T60	6.2	821.00	5.0902	2.0000	7.0902	453.2	0.3721	5.4108	0.8210
A15	T90	5.4	606.00	3.2724	3.0000	6.2724	437.8	0.2653	5.5184	0.6060
A15	T120	5.4	539.00	2.9106	4.0000	6.9106	422.4	0.2277	5.5554	0.5390
A15	T180	5.8	481.00	2.7898	5.0000	7.7898	406.6	0.1956	5.5866	0.4810
A15	T240	5.2	433.00	2.2516	6.0000	8.2516	391.4	0.1695	5.6123	0.4330
A15	T300	5.8	433.00	2.5114	7.0000	9.5114	375.6	0.1626	5.6179	0.4330
A15	T360	5.4	427.00	2.3058	8.0000	10.3058	360.2	0.1538	5.6259	0.4270

Ferrihydrite Solubility Fe Mass Balance (Initial Acid 20 g/L)

Solutions		sample	Assay	Fe out of the system for sample	Flush	Total Fe out	Volume of Solution in the system	Solution	Residue	Solution
ID		ml	Fe (ppm)	Fe (mg)	Fe (mg)	Fe (mg)	(ml)	Fe (g)	Fe(g)	Fe (g/L)
A20	T0	5.0	3280.00	16.4000	0.0000	16.4000	485.0	1.5908	4.1828	3.2800
A20	T30	5.3	2240.0	11.8720	1.0000	12.8720	469.7	1.0521	4.7250	2.2400
A20	T60	5.8	1520.00	8.8160	2.0000	10.8160	453.9	0.6899	5.0893	1.5200
A20	T90	5.6	1260.00	7.0560	3.0000	10.0560	438.3	0.5523	5.2277	1.2600
A20	T120	5.4	1090.00	5.8860	4.0000	9.8860	422.9	0.4610	5.3192	1.0900
A20	T180	5.4	1040.00	5.6160	5.0000	10.6160	407.5	0.4238	5.3556	1.0400
A20	T240	5.6	962.00	5.3872	6.0000	11.3872	391.9	0.3770	5.4016	0.9620
A20	T300	6.2	938.00	5.8156	7.0000	12.8156	375.7	0.3524	5.4248	0.9380
A20	T360	5.2	922.00	4.7944	8.0000	12.7944	360.5	0.3324	5.4448	0.9220

Ferrihydrite Solubility Fe Mass Balance (Initial Acid 25 g/L)

Solutions		sample	Assay	Fe out of the system for sample	Flush	Total Fe out	Volume of Solution in the system	Solution	Residue	Solution
ID		ml	Fe (ppm)	Fe (mg)	Fe (mg)	Fe (mg)	(ml)	Fe (g)	Fe(g)	Fe (g/L)
A25	T0	5.2	4660.00	24.2320	0.0000	24.2320	484.8	2.2592	3.5066	4.6600
A25	T30	5.6	3620.0	20.2720	1.0000	21.2720	469.2	1.6985	4.0702	3.6200
A25	T60	5.6	2740.00	15.3440	2.0000	17.3440	453.6	1.2429	4.5298	2.7400
A25	T90	5.4	2200.00	11.8800	3.0000	14.8800	438.2	0.9640	4.8111	2.2000
A25	T120	5.2	1990.00	10.3480	4.0000	14.3480	423.0	0.8418	4.9339	1.9900
A25	T180	5.4	1810.00	9.7740	5.0000	14.7740	407.6	0.7378	5.0375	1.8100
A25	T240	5.0	1710.00	8.5500	6.0000	14.5500	392.6	0.6713	5.1041	1.7100
A25	T300	6.0	1690.00	10.1400	7.0000	17.1400	376.6	0.6365	5.1364	1.6900
A25	T360	5.4	1680.00	9.0720	8.0000	17.0720	361.2	0.6068	5.1661	1.6800

Ferrihydrite Solubility Fe Mass Balance (Initial Acid 10 g/L with Cu ions)

Solutions		sample	Assay	Fe out of the system for sample	Flush	Total Fe out	Volume of Solution in the system	Solution	Residue	Solution
ID		ml	Fe (ppm)	Fe (mg)	Fe (mg)	Fe (mg)	(ml)	Fe (g)	Fe(g)	Fe (g/L)
Cu-A10	T0	4.8	713.00	3.4224	0.0000	3.4224	485.2	0.3459	5.4406	0.7130
Cu-A10	T30	5.2	372.0	1.9344	1.0000	2.9344	470.0	0.1748	5.6122	0.3720
Cu-A10	T60	6.4	158.00	1.0112	2.0000	3.0112	453.6	0.0717	5.7153	0.1580
Cu-A10	T90	5.6	149.00	0.8344	3.0000	3.8344	438.0	0.0653	5.7209	0.1490
Cu-A10	T120	5.4	126.00	0.6804	4.0000	4.6804	422.6	0.0532	5.7321	0.1260
Cu-A10	T180	6.2	113.00	0.7006	5.0000	5.7006	406.4	0.0459	5.7384	0.1130
Cu-A10	T240	5.6	104.00	0.5824	6.0000	6.5824	390.8	0.0406	5.7428	0.1040
Cu-A10	T300	6.2	94.40	0.5853	7.0000	7.5853	374.6	0.0354	5.7471	0.0944
Cu-A10	T360	5.8	88.10	0.5110	8.0000	8.5110	358.8	0.0316	5.7499	0.0881

Ferrihydrite Solubility Fe Mass Balance (Initial Acid 10 g/L with Ni ions)

Solutions		sample	Assay	Fe out of the system for sample	Flush	Total Fe out	Volume of Solution in the system	Solution	Residue	Solution
ID		ml	Fe (ppm)	Fe (mg)	Fe (mg)	Fe (mg)	(ml)	Fe (g)	Fe(g)	Fe (g/L)
Ni-A10	T0	6.2	501.00	3.1062	0.0000	3.1062	483.8	0.2424	5.5445	0.5010
Ni-A10	T30	5.4	402.0	2.1708	1.0000	3.1708	468.4	0.1883	5.5985	0.4020
Ni-A10	T60	5.6	223.00	1.2488	2.0000	3.2488	452.8	0.1010	5.6858	0.2230
Ni-A10	T90	6.0	141.00	0.8460	3.0000	3.8460	436.8	0.0616	5.7246	0.1410
Ni-A10	T120	6.2	126.00	0.7812	4.0000	4.7812	420.6	0.0530	5.7322	0.1260
Ni-A10	T180	5.2	114.00	0.5928	5.0000	5.5928	405.4	0.0462	5.7382	0.1140
Ni-A10	T240	5.6	103.00	0.5768	6.0000	6.5768	389.8	0.0401	5.7433	0.1030
Ni-A10	T300	5.2	97.90	0.5091	7.0000	7.5091	374.6	0.0367	5.7458	0.0979
Ni-A10	T360	5.2	98.60	0.5127	8.0000	8.5127	359.4	0.0354	5.7461	0.0986

Calculation of Ferric and Ferrous Ions

Time	Solution A0		A0 $\frac{\text{Ferric}_{Dissolved}}{\text{Ferrous}_{Nominal}}$	Fe ⁺²	Fe ⁺³
	Fe (g/L)	Fe (mg/L)		mg/L	mg/L
0	0.00302	3.02	0.28	2.36	0.66
30	0.0118	11.8	0.59	7.41	4.39
60	0.00824	8.24	0.78	4.62	3.62
90	0.00514	5.14	1.20	2.34	2.80
120	0.00235	2.35	1.74	0.86	1.49
180	0.0018	1.8	4.07	0.36	1.44
240	0.00222	2.22	12.20	0.17	2.05
300	0.0019	1.9	16.11	0.11	1.79
360	0.00166	1.66	16.11	0.10	1.56

Time	Solution A5		A5 $\frac{\text{Ferric}_{Dissolved}}{\text{Ferrous}_{Nominal}}$	Fe ⁺²	Fe ⁺³
	Fe (g/L)	Fe (mg/L)		mg/L	mg/L
0	0.165	165	8.26	17.83	147.17
30	0.0994	99.4	4.97	16.66	82.74
60	0.0477	47.7	3.95	9.63	38.07
90	0.0391	39.1	3.42	8.84	30.26
120	0.0351	35.1	3.42	7.94	27.16
180	0.0324	32.4	3.42	7.33	25.07
240	0.0306	30.6	2.96	7.73	22.87
300	0.0293	29.3	2.41	8.59	20.71
360	0.0274	27.4	1.79	9.82	17.58

Time	Solution A10		A10 $\frac{\text{Ferric}_{Dissolved}}{\text{Ferrous}_{Nominal}}$	Fe ⁺²	Fe ⁺³
	Fe (g/L)	Fe (mg/L)		mg/L	mg/L
0	0.756	756	4.07	149.16	606.84
30	0.481	481	2.63	132.35	348.65
60	0.283	283	1.90	97.57	185.43
90	0.197	197	1.84	69.26	127.74
120	0.171	171	1.84	60.12	110.88
180	0.153	153	1.84	53.79	99.21
240	0.139	139	1.84	48.87	90.13
300	0.146	146	1.84	51.33	94.67
360	0.148	148	1.84	52.04	95.96

Time	Solution A15		A15 $\frac{\text{Ferric}_{Dissolved}}{\text{Ferrous}_{Nominal}}$	Fe ⁺²	Fe ⁺³
	Fe (g/L)	Fe (mg/L)		mg/L	mg/L
0	1.34	1340	2.08	435.16	904.84
30	1.45	1450	1.40	603.99	846.01
60	0.821	821	1.36	348.20	472.80
90	0.606	606	1.32	261.64	344.36
120	0.539	539	1.28	236.86	302.14
180	0.481	481	1.28	211.38	269.62
240	0.433	433	1.24	193.64	239.36
300	0.433	433	1.24	193.64	239.36
360	0.427	427	1.24	190.96	236.04

Calculation of Ferric and Ferrous Ions

Time	Solution A20		A20 $\frac{\text{Ferric}_{Dissolved}}{\text{Ferrous}_{Nominal}}$	Fe ⁺²	Fe ⁺³
	Fe (g/L)	Fe (mg/L)		mg/L	mg/L
0	3.28	3280	10.92	275.22	3004.78
30	2.24	2240	1.63	850.57	1389.43
60	1.52	1520	1.36	644.66	875.34
90	1.26	1260	1.32	544.01	715.99
120	1.09	1090	1.09	521.88	568.12
180	1.04	1040	1.09	497.94	542.06
240	0.962	962	1.12	452.93	509.07
300	0.938	938	1.05	456.63	481.37
360	0.922	922	1.02	456.28	465.72

Time	Solution A25		A25 $\frac{\text{Ferric}_{Dissolved}}{\text{Ferrous}_{Nominal}}$	Fe ⁺²	Fe ⁺³
	Fe (g/L)	Fe (mg/L)		mg/L	mg/L
0	4.66	4660	1.74	1703.23	2956.77
30	3.62	3620	1.28	1590.81	2029.19
60	2.74	2740	1.12	1290.04	1449.96
90	2.2	2200	1.02	1088.74	1111.26
120	1.99	1990	0.90	1049.82	940.18
180	1.81	1810	0.81	999.83	810.17
240	1.71	1710	0.71	1001.73	708.27
300	1.69	1690	0.61	1046.77	643.23
360	1.68	1680	0.61	1040.57	639.43

Time	Solution Cu-A10		Cu-A10 $\frac{\text{Ferric}_{Dissolved}}{\text{Ferrous}_{Nominal}}$	Fe ⁺²	Fe ⁺³
	Fe (g/L)	Fe (mg/L)		mg/L	mg/L
0	0.713	713	1.02	352.85	360.15
30	0.372	372	2.56	104.55	267.45
60	0.158	158	64.01	2.43	155.57
90	0.149	149	96.67	1.53	147.47
120	0.126	126	96.67	1.29	124.71
180	0.113	113	96.67	1.16	111.84
240	0.104	104	96.67	1.06	102.94
300	0.0944	94.4	96.67	0.97	93.43
360	0.0881	88.1	96.67	0.90	87.20

Time	Solution Ni-A10		Ni-A10 $\frac{\text{Ferric}_{Dissolved}}{\text{Ferrous}_{Nominal}}$	Fe ⁺²	Fe ⁺³
	Fe (g/L)	Fe (mg/L)		mg/L	mg/L
0	0.501	501	10.92	42.04	458.96
30	0.402	402	186.85	2.14	399.86
60	0.223	223	167.42	1.32	221.68
90	0.141	141	158.47	0.88	140.12
120	0.126	126	127.22	0.98	125.02
180	0.114	114	117.16	0.96	113.04
240	0.103	103	117.16	0.87	102.13
300	0.0979	97.9	117.16	0.83	97.07
360	0.0986	98.6	117.16	0.83	97.77